Supersymmetric Field Theories, Scattering Amplitudes and the Grassmannian

GALLONI, DANIELE,STEFANO

Supersymmetric Field Theories, Scattering Amplitudes and the Grassmannian

Daniele Stefano Galloni

A Thesis presented for the degree of
Doctor of Philosophy

Institute for Particle Physics Phenomenology
Department of Physics
University of Durham
England

March 2015

To Catherine

For her endless love, support and encouragement

Supersymmetric Field Theories, Scattering Amplitudes and the Grassmannian

Daniele Stefano Galloni

Submitted for the degree of Doctor of Philosophy
March 2015

Abstract

In this thesis we carry out a detailed investigation of a class of four-dimensional $\mathcal{N} = 1$ gauge theories, known as Bipartite Field Theories (BFTs), and their utility in integrable systems and scattering amplitudes in 4-dimensional $\mathcal{N} = 4$ Super-Yang-Mills (SYM). We present powerful combinatorial tools for analyzing the moduli spaces of BFTs, and find an interesting connection with the matching and matroid polytopes, which play a central role in the understanding of the Grassmannian.

We use the tools from BFTs to construct (0+1)-dimensional cluster integrable systems, and propose a way of obtaining (1+1)- and (2+1)-dimensional integrable field theories.

Using the matching and matroid polytopes of BFTs, we analyze the singularity structure of planar and non-planar on-shell diagrams, which are central to modern developments of scattering amplitudes in $\mathcal{N} = 4$ SYM. In so doing, we uncover a new way of obtaining the positroid stratification of the Grassmannian.

We use tools from BFTs to understand the boundary structure of the amplituhedron, a recently found geometric object whose volume calculates the integrand of scattering amplitudes in planar $\mathcal{N} = 4$ SYM theory. We provide the most comprehensive study of the geometry of the amplituhedron to date.

We also present a detailed study of non-planar on-shell diagrams, constructing the on-shell form using two new, independent methods: a non-planar boundary measurement valid for arbitrary non-planar graphs, and a proposal for a combinatorial method to determine the on-shell form directly from the graph.

Declaration

The work in this thesis is based on research carried out at the Institute for Particle Physics Phenomenology, Department of Physics, Durham University, United Kingdom. No part of this thesis has been submitted elsewhere for any other degree or qualification and it is all my own work unless referenced to the contrary in the text.

Chapter 1 is based on text appearing in [1–6]. Chapter 2 is based on work done in [1, 3, 4, 6]. Chapter 3 is based on work done in [2]. Chapter 4 is primarily based on work in [3,6] and contains work also appearing in [4]. Chapter 5 is based on work in [5]. Chapter 6 is based on work in [6].

Acknowledgements

I am very grateful to several people for making this thesis possible. First, I would like to thank my supervisor Sebastián Franco, whose help and guidance were invaluable to the completion of the thesis. His understanding of physics, excellent research foresight and helpfulness in times of great need are all qualities I have hugely appreciated.

I would like to thank Alberto Mariotti, who is both a great friend and a fantastic collaborator. He has shown me that under the right conditions there is no distinction between fun and physics, and I owe to him countless hours of exciting research, discussions of physics, and of life.

Much of the research I have conducted has profited from wonderful collaborations. To this end I would like to also thank Yang-Hui He, Brenda Penante, Ander Retolaza, Rak-Kyeong Seong, Jaroslav Trnka, Angel Uranga and Congkao Wen for very fruitful discussions that led to the completion of a large number of articles. I would also like to thank my supervisor, Claude Duhr and Yang-Hui He for patiently writing many reference letters for me, and Céline Bœhm for valuable insights into aspects of academic life.

A special thank you to Nima Arkani-Hamed. I am especially indebted to his help and encouragement in the final stages of my doctorate, and together with Jaroslav Trnka for the discovery of the amplituhedron, which was one of the most enjoyable and interesting projects I've worked on.

I give enormous thanks to my parents for having given me everything. Their constant love and support has unfalteringly persisted throughout my life, and has ultimately given me the wonderful opportunities that I have so greatly enjoyed. I wish to also give enormous thanks to Michela, for being a wonderful person, close

family, and for having taught me much about life. An important thank you goes to my brother Alessandro, whose companionship through life has been crucial to me.

Finally I would like to express my most heartfelt thanks to Catherine, whose unconditional love and support not only made this thesis a reality, but have meant everything to me since the beginning. Her importance in the completion of my doctorate is inestimable.

Financial support for the duration of my doctorate was provided by the STFC, whom I gratefully acknowledge.

Contents

List of Figures

List of Tables

Chapter 1

Introduction

Quantum field theory (QFT) underlies our description of fields as diverse as particle physics, statistical mechanics and condensed matter physics. It leads to extremely precise predictions which are constantly tested experimentally. It is thus remarkable that despite QFT being such a fundamental and mature framework, our understanding of it is still currently making tremendous progress. This progress is occurring on multiple fronts, including holography, integrability and duality, to name a few.

Powerful mathematical and geometric ideas play a central role in some of the most recent developments. A common theme in recent years has been the definition of QFTs in terms of some underlying geometric or combinatorial object. In these constructions, it is often possible to build theories by assembling certain elementary geometric building blocks, which have gauge theory counterparts. Furthermore, gauge theory dualities such as Seiberg duality [7], S-duality [8] and mirror symmetry [9] are captured by basic transformations of the underlying geometric objects. Similar advances have also occurred in the computation of scattering amplitudes of QFTs, in particular planar maximally supersymmetric Super-Yang-Mills (SYM), where the scattering amplitude can be constructed by assembling elementary graphical building blocks, to form what are known as "on-shell diagrams". These developments have enabled drastic simplifications in the computation of various quantities of interest, as well as a deeper physical understanding of the dynamics that govern these theories.

Background to Bipartite Field Theories

In line with the modern developments outlined in the previous section, a new infinite class of 4-dimensional $\mathcal{N} = 1$ gauge theories was introduced by S. Franco [10]. Such theories are called Bipartite Field Theories (BFTs) [1, 10–13].[1] These theories are special in that they may be *defined* by a graphical object, a bipartite graph tiling an arbitrary Riemann surface.[2] BFTs draw power from their simplicity: their graphical description allows for combinatorial tools to compute quantities of interest. For example, the space of vanishing F-terms and D-terms, known as the moduli space, can be obtained with back-of-the-envelope calculations. Operations such as Seiberg duality, confinement, Higgsing, and integration of massive fields are neatly encoded in simple graphical manipulations.

Certain subclasses of BFTs have already appeared in the context of interesting physical systems. D3-branes probing toric Calabi-Yau 3-folds provide particularly important examples [15–19], in which the string-theoretic picture is dual to certain 4-dimensional $\mathcal{N} = 1$ quiver gauge theories, known as dimer models. Quiver gauge theories are thus named because of the graph typically used to represent their gauge-theory and matter-field content; each symmetry group of the theory is represented by a node, and arrows represent bifundamental matter fields, transforming in the fundamental representation of the node on the arrow's head, and in the anti-fundamental representation of the node on the arrow's tail. An example is provided in Figure 2.1.

Dimer models have been instrumental in the discovery of the first infinite families of explicit AdS/CFT dual pairs in 4 dimensions [17,20]. In addition, they provide the largest known classification of purely $\mathcal{N} = 1$ superconformal field theories (SCFTs) in 4 dimensions (cf. [21, 22]). They have also been utilized to construct duality-cascading models [23–27] and string-theoretic inflationary scenarios [28, 29].

Another interesting application of BFTs involves so-called cluster integrable

[1] A similar class of theories was simultaneously introduced in [14].

[2] A bipartite graph is a graph where the nodes are colored white or black, and white nodes are only connected to black nodes (and vice-versa).

systems [2, 30–32]. These applications were first discovered by Goncharov and Kenyon [33] and appeared in the mathematics literature, where they found a correspondence between dimer models and certain integrable models. The correspondence associates any dimer model on a torus to a (0+1)-dimensional quantum integrable system, which they dub a *cluster integrable system*.

More recently, BFTs have made much progress in the context of scattering amplitudes in 4-dimensional $\mathcal{N} = 4$ SYM [3, 5, 6, 34, 35]. These developments rely on the observation that the actual *structures* of BFTs have a very central role in the computation of scattering amplitudes in $\mathcal{N} = 4$ SYM. More precisely, a novel formulation of scattering amplitudes in $\mathcal{N} = 4$ SYM, involving a highly combinatorial object known as the Grassmannian, makes direct use of the combinatorics of the same bipartite graphs which define BFTs.

Many of the concepts in $\mathcal{N} = 4$ SYM, and importantly their generalizations beyond planar on-shell diagrams, have beautiful realizations in terms of BFTs. The investigation of the utility of BFTs in the area of scattering amplitudes is indeed one of the central goals of this thesis. The huge diversity of applications of BFTs suggests we are only scratching the surface of their potential utility. Additionally, BFTs may provide a more profound understanding of the physical connections between the areas of their applicability.

Introduction to Toric Geometry

The moduli space of BFTs is a space called a *toric* variety. This section will describe more precisely what this means, and illustrate extremely useful diagrams that completely encode the information of the toric variety in a simple and succinct way. These diagrams are known as *toric diagrams* and will be used very heavily in this thesis. To understand the tools and results of this thesis it is sufficient to know that it is *possible* to recover the algebraic-geometric information of a toric variety from the toric diagram, without needing to understand the precise details of this map. This section will nonetheless expound on this connection with a concrete example, providing useful context and understanding for the chapters to come.

Algebraic geometry can relate algebraic quantities, such as polynomials of variables, to geometric objects called *varieties*, which are similar to manifolds. Algebraic geometry appears naturally for vacua of supersymmetric theories; these moduli spaces are determined by the solution to the D-term and F-term constraints

$$D^a = \sum_i X_i^\dagger T^a X^i = 0 \tag{1.0.1}$$

$$F_i^\dagger = \frac{\partial W}{\partial X^i} = 0 \tag{1.0.2}$$

where the X_i are chiral superfields, W is the superpotential and T^a are the generators of the gauge group. The key point is that the vacuum can be described by a set of polynomial equations

$$p_1(z_1, z_2, \ldots) = 0 \quad p_2(z_1, z_2, \ldots) = 0 \quad \cdots \tag{1.0.3}$$

where the z_i are traces of polynomial functions of the fields X_i.

There are particular supersymmetric theories, known as toric quiver gauge theories, whose space of vacua is *toric*. We shall soon explain what this means. Much of this introduction to toric geometry is based on an excellent set of lecture notes by Cyril Closset [36].

Toric Varieties

A variety Σ is a simpler version of a manifold. Fundamentally, the difference is that it is possible to describe a variety through a set of equations of the form $f(z) = 0$:

$$\Sigma = \{z \in \mathbb{C}^n \mid f(z) = 0\} \ . \tag{1.0.4}$$

In general such manifolds can be very singular, but this can be greatly improved by limiting $f(z)$ to be a polynomial. *Toric* varieties are additionally limited to having rational coordinate transformations between different patches of the variety.

An important class of toric varieties consists of projective varieties. The most famous one is

$$\mathbb{C}P^n = \frac{\mathbb{C}^{n+1} \setminus 0}{\mathbb{C}^*} \tag{1.0.5}$$

where $\mathbb{C}^*$ is the action that multiplies all coordinates $x_i \in \mathbb{C}$ by λ:

$$\{x_1, \ldots, x_{n+1}\} \mapsto \{\lambda x_1, \ldots, \lambda x_{n+1}\} \tag{1.0.6}$$

One should think of $\mathbb{C}P^n$ as the space of lines going through the origin in $\mathbb{C}^{n+1}$. The coordinates on $\mathbb{C}P^n$ are

$$z_i^{(j)} = \frac{x_j}{x_i} \,, \tag{1.0.7}$$

and the coordinate transformations between patches are $z_i^{(j)}\left(z^{(k)}\right) = \frac{z_j^{(k)}}{z_i^{(k)}}$. There is no function $f(z)$ required to specify this space.

A toric variety is a generalization of a projective variety. It can be written as

$$X_T = \frac{\mathbb{C}^n \setminus Z_T}{(\mathbb{C}^*)^p \times \Gamma} \tag{1.0.8}$$

where Γ is some discrete group, typically $\mathbb{Z}_N$. A non-trivial Γ corresponds to orbifolding the theory. The action $(\mathbb{C}^*)^p$ acts on the coordinates by multiplying each coordinate by some power of λ. There are p different operations, each with a different λ_i. In order to have a well-defined action that can act non-trivially, we must remove a set of points Z_T. For $\mathbb{C}P^n$ this was simply done by removing the origin.

At this stage an example is very useful. Consider the conifold, usually denoted $\mathcal{C}_0$, defined by the equation

$$\mathcal{C}_0 = \{(z_1, z_2, z_3, z_4) \in \mathbb{C}^4 \mid z_1 z_2 - z_3 z_4 = 0\} \,. \tag{1.0.9}$$

The conifold can equally be described as

$$\mathcal{C}_0 = \frac{\mathbb{C}^4 \setminus Z_T}{\mathbb{C}^*} \,, \tag{1.0.10}$$

where the $\mathbb{C}^*$ action is

$$(x_1, x_2, x_3, x_4) \mapsto (\lambda x_1, \lambda^{-1} x_2, \lambda x_3, \lambda^{-1} x_4) \quad . \tag{1.0.11}$$

Notice that the action does not need to multiply the same power of λ to all coordinates. In this case $Z_T = \{x_1 = 0 = x_3\} \cup \{x_2 = 0 = x_4\}$.

We shall now see how these two apparently very different formulations of the conifold, i.e. (1.0.9) and (1.0.10), can be simply obtained through a study of the conifold's *toric diagram*.

The Projective Variety from the Toric Diagram

A toric diagram is determined by a set of points on a d-dimensional lattice $\mathbb{Z}^d$.[3] These points are expressed as a set of vectors $\{v_1, \ldots, v_n\}$, where $n \geq d$. For these vectors to specify a toric variety they will turn out to satisfy certain conditions. Before exploring these conditions, let us begin with a few definitions.

A *strongly convex rational cone* σ is the cone spanned by a subset of the vectors v_i. The "strongly convex" condition on the cone is that the cone should be "pointy", i.e. that $\sigma \cap (-\sigma) = \{0\}$. A *fan* is a collection of cones that pairwise share faces, where each face must also be a cone. In simple terms, a fan is simply a collection of cones stuck together.

The prescription for obtaining the projective description of the variety begins by associating a complex coordinate x to each lattice vector v. These n coordinates $\{x_1, \ldots, x_n\}$ will be subject to p different $\mathbb{C}^*$ actions, to give a variety of dimension $n - p = d$, which is the same as the dimension of the lattice $\mathbb{Z}^d$.

The specific $\mathbb{C}^*$ actions are determined by studying the different independent relations among the lattice vectors

$$\sum_{i=1}^{n} v_i Q_i^a = 0 \tag{1.0.12}$$

where Q_i^a are the coefficients of these linear combinations, and $a = 1, \ldots, p$. The way to translate the Q_i^a into the specific $\mathbb{C}^*$ action is simply by viewing the Q_i^a as charge vectors for the $\mathbb{C}^*$ action under consideration, i.e.

$$\{x_1, \ldots, x_n\} \mapsto \{\lambda^{Q_1^a} x_1, \ldots, \lambda^{Q_n^a} x_n\} \,. \tag{1.0.13}$$

From this it is also easy to find Z_T: for each subset of the lattice vectors $\{v_{i_1}, \ldots, v_{i_k}\}$ that do *not* form a cone of the original fan, there is a contribution $\{x_{i_1} = \cdots = x_{i_k} = 0\}$ to Z_T. Z_T is the union of all such contributions.

[3] As we shall soon see, if a space is Calabi-Yau these lattice points all live on a $(d-1)$-dimensional hypersurface. Strictly speaking, what is usually referred to as the toric diagram is a diagram of this hypersurface.

Example. Let us see how this procedure works for the conifold. The conifold is three-dimensional, and has a fan generated by the four vectors

$$v_1 = (0,0,1) \quad v_2 = (1,0,1) \quad v_3 = (1,1,1) \quad v_4 = (0,1,1) \quad , \tag{1.0.14}$$

which are illustrated in Figure 1.1. The fan is composed of one three-dimensional cone (pyramid-like), four two-dimensional cones (four faces), four one-dimensional cones (edges between the faces), and one zero-dimensional cone (the origin). Each

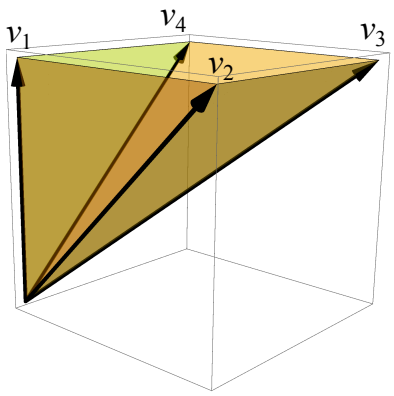

Figure 1.1: The fan for the conifold.

vector is associated to a variable x_i. Since we have four vectors in 3 dimensions, they are linearly related through the equation

$$v_1 - v_2 + v_3 - v_4 = 0 \ , \tag{1.0.15}$$

thus yielding the single charge vector $Q = (1,-1,1,-1)$. Hence, the $\mathbb{C}^*$ action is as given in (1.0.11). Since $\{v_1, v_3\}$ and $\{v_2, v_4\}$ are not cones of the original fan, $Z_T = \{x_1 = 0 = x_3\} \cup \{x_2 = 0 = x_4\}$, which finally completes the expression in (1.0.10)

The Algebraic Variety from the Toric Diagram

We have now seen how to obtain the expression of the projective variety (1.0.10) from the toric diagram. The aim of this section will be to obtain the equivalent algebraic formulation of the variety (1.0.9), i.e. the set of coordinates z and their constraints $f(z) = 0$, from the same toric diagram. We start by finding well-defined

coordinates z, which are invariant under the $\mathbb{C}^*$ action, analogously to (1.0.7) for the example of $\mathbb{C}P^n$. More generally we need to define each z as

$$z = x_1^{p_1} x_2^{p_2} \cdots x_n^{p_n} \quad \mapsto \quad \lambda^{\sum_i Q_i^a p_i} x_1^{p_1} x_2^{p_2} \cdots x_n^{p_n} = x_1^{p_1} x_2^{p_2} \cdots x_n^{p_n} \quad . \tag{1.0.16}$$

If we restrict ourselves to considering fans which are also cones, i.e. fans which are "pointy" as defined above, we see that some Q_i charges need to be negative. We can use this fact to restrict ourselves to only considering $p_i \geq 0$.

Hence, to have coordinates z invariant under the $\mathbb{C}^*$ action, we need to impose $\sum_i Q_i^a p_i = 0$. Because of the similarity to (1.0.12), it is natural to see p_i as an inner product between vectors w and v_i, where w is a vector in the "dual lattice". In this way the *dual cone*

$$\sigma^\vee = \{aw, a \in \mathbb{R}_{\geq 0}, \langle w, v_i \rangle \geq 0 \ \ \forall v_i \in \sigma\} \tag{1.0.17}$$

can be defined. Under this definition, each p_i for a given z is given by $p_i = \langle w, v_i \rangle$. In this way we see that each vector w in the dual cone is naturally associated to a corresponding z, much like $v_i \mapsto x_i$ in the previous section.

The w_i are generally not all independent: there are relations

$$\sum_i m_i w_i = \sum_j m_j w_j \quad , \quad m_i, m_j \in \mathbb{N} \quad . \tag{1.0.18}$$

These conditions can be easily translated into conditions for the variables z_i, by remembering that the w_i implicitly appear in (1.0.16), through the relation $p_i = \langle w, v_i \rangle$. Hence, the conditions are

$$\prod_i z_i^{m_i} = \prod_j z_j^{m_j} \quad \Rightarrow \quad f(z) = \prod_i z_i^{m_i} - \prod_j z_j^{m_j} = 0 \, . \tag{1.0.19}$$

Example. Let us return to the example of the conifold to illustrate the procedure. To find the dual variables z_i, the dual cone vectors w_k are needed. The dual cone will be the cone generated by vectors that can lie a maximum of $90\,^\circ$ from any v_i. From (1.0.14) we see that v_1 will restrict dual vectors to be in the upper-half space of $\mathbb{Z}^3$, v_2 will restrict to the same space but rotated one step in the x-direction, v_4 to the rotated space one step in the y-direction and v_3 will not impose any additional restriction. We thus have the dual vectors

$$w_1 = (1,0,0) \quad w_2 = (0,1,0) \quad w_3 = (-1,0,1) \quad w_4 = (0,-1,1) \quad . \tag{1.0.20}$$

The restrictions of v_2 and v_4 are seen in the third component of w_3 and w_4. It is easy to verify that these form a good choice for dual cone vectors: using $p_i = \langle w, v_i \rangle$, we obtain the coordinates $z_1 = x_2x_3$, $z_2 = x_3x_4$, $z_3 = x_1x_4$ and $z_4 = x_1x_2$, which are transparently invariant under the $\mathbb{C}^*$ action in (1.0.11). In this simple example we could equally have inferred the w_i from "guessing" the z_i.

There is only one relation between these vectors:

$$w_1 + w_3 = w_2 + w_4 \;\Rightarrow\; f(z) = z_1z_3 - z_2z_4 = 0 \;, \tag{1.0.21}$$

which is precisely (up to a trivial relabeling) the definition in (1.0.9).

Toric diagrams for Calabi-Yau manifolds

The moduli space of BFTs are toric varieties. Moreover, they are Calabi-Yau. We shall now see how the Calabi-Yau condition manifests itself at the level of the toric diagram.

A Calabi-Yau manifold has vanishing Ricci tensor. Combining the Calabi-Yau condition with toric varieties gives a toric Calabi-Yau variety, which satisfies the additional requirement that the powers of λ arising from the action $(\mathbb{C}^*)$ must all sum up to zero, i.e.

$$\sum_i Q_i^a = 0 \;. \tag{1.0.22}$$

A toric Calabi-Yau manifold is of complex dimension d, and will hence be described by d-dimensional vectors. The Calabi-Yau condition allows for a convenient simplification: through a suitable $SL(n, \mathbb{Z})$ transformation, it is possible to express the vectors v_i as $v_i = (\tilde{v}_i, 1)$. Hence, the fan can be projected down onto $\mathbb{Z}^{d-1}$ without losing any information.

As an example, the conifold is a toric Calabi-Yau variety. Its vectors in (1.0.14) can be projected down to the $\mathbb{Z}^2$ plane, to obtain the four points $(0,0)$, $(1,0)$, $(0,1)$, $(1,1)$. It is standard to draw lines along the outer edge of the toric diagram, to denote its boundaries.

Toric singularities

In algebraic geometry, a singularity is defined as a point on the variety at which the tangent space has a larger dimension than the variety. As an example, for the conifold we have $f(z) = z_1z_2 - z_3z_4 = 0$. At $z_1 = z_2 = z_3 = z_4 = 0$ the equations become trivial and the tangent space will have complex dimension 4; thus, there is a singularity here. In general we have a singularity when $\dim(T_zU) = \dim(U_z) + 1$, where U_z is the variety and T_zU is its tangent space at the point z.

A theorem in algebraic geometry states that for a cone σ, U_σ is non-singular iff σ is a simplex.[4] The theorem suggests a way to *resolve* toric singularities: by dividing the fan into simplices, and treating each simplex separately. This process is known as *simplicial decomposition*. On the toric diagram for Calabi-Yau 3-folds, this is equivalent to triangulating the diagram. Triangulation for the conifold is illustrated in Figure 1.2.

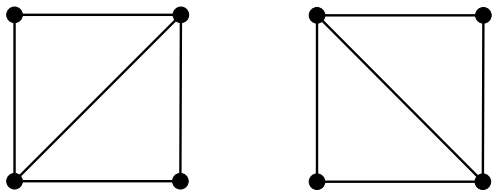

Figure 1.2: The conifold resolved in two different ways

There are two main ways to study a singularity: by resolution as in the above example, or deformation of the variety. This second method corresponds to slightly modifying the defining equation, e.g. modifying the conifold to $z_1z_2 - z_3z_4 = c$, $c \neq 0$. Deformations will not be treated here but there is much more to say about them; for a physicist-friendly account the reader is referred to [36]. Deformations will make a brief recurrence in Chapter 5.

The resolution of the singularity described above is an example of what is known as a "blow up".[5] This essentially replaces the singularity with a $\mathbb{C}P^m$, where m is

[4] We remind the reader that a simplex is the higher-dimensional analogue of a triangle.

[5] The mathematics literature distinguishes between "blow ups" and "small resolutions". Figure 1.2 shows an example of the latter.

smaller than the dimension of the variety. The blow up introduces new variables which give the singularity the structure of a $\mathbb{C}P^m$ but become redundant away from the singularity.

In the conifold example, $\mathcal{C}_0$ becomes two $\mathbb{C}^3$'s. The first one will have coordinates $\{z_1, z_3, y_1\}$ and the second will have coordinates $\{z_2, z_4, y_2\}$. Since together they form the conifold, we must have transition functions from one $\mathbb{C}^3$ to the other. The transition functions are given by

$$\frac{z_1}{z_2} = \frac{z_3}{z_4} \ , \ y_1 = \frac{1}{y_2} \ , \ z_1 y_1 = z_2 \ , \ \ldots \tag{1.0.23}$$

which are simply read off from the equations relating the vectors of the first cone with those of the second cone, analogously to (1.0.21). Note that this generates the defining equation for the conifold as well as equations for the new variables which give the singularity a $\mathbb{C}P^n$ structure.

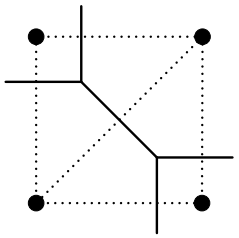

Figure 1.3: The (p, q) web for the resolved conifold. For clarity, the original lines (now dotted) have been included.

The (p, q) web. Of particular interest in the toric diagram is the (p, q) web [37]. It is the dual of the toric diagram; in practice this is a set of lines that cut across those of the resolved toric diagram. For the resolved conifold on the left in Figure 1.2, we have the (p, q) web shown in Figure 1.3. In Chapter 3, the importance of the (p, q) web will become clear when it appears as the backbone of the spectral curve associated to an integrable system.

Background to Scattering Amplitudes

Scattering amplitudes have undergone tremendous progress in the last two decades (see e.g. [38–44] and reviews [45–48]). This progress is especially impressive for amplitudes in planar 4-dimensional $\mathcal{N} = 4$ super Yang-Mills theory, where explicit results have been obtained up to high loop order [49–56]. Much of the recent progress in computing the scattering amplitudes relies on making the full symmetry group of the theory manifest. More specifically, it abandons Feynman diagrams as the basic terms from which the amplitudes are constructed, in favor of summing over terms which are manifestly invariant under the full symmetry group of $\mathcal{N} = 4$ SYM. While Feynman diagrams make the local description of amplitudes very manifest, they often hide important structures which are displayed by the full amplitude; for example, individual Feynman diagrams are not gauge invariant.

The construction of amplitudes through terms invariant under the full symmetry group can be systematized through the celebrated BCFW recursion relations [43, 44], which at tree-level construct n-point amplitudes by gluing together lower-point amplitudes. The BCFW recursion relations are not restricted to supersymmetric theories, and indeed form the fundaments of highly successful unitarity methods [38, 39].

At loop-level, restricting ourselves to $\mathcal{N} = 4$ supersymmetry, a similar set of recursion relations exists to construct the *integrand* of the amplitude [52].[6] Each term in these recursion relations is invariant under the full symmetry group of the theory, but is generally not local. The non-locality of each term is cancelled by the non-locality of other terms, to finally produce a local amplitude which is invariant under all symmetries of the theory.

An important question in the investigation of amplitudes is their singularity structure. Indeed, it was precisely a thorough understanding of this which enabled

[6] Much of the recent progress in scattering amplitudes, and indeed that which this thesis will focus on, is in constructing the integrand of the scattering amplitude. The integrated amplitude suffers from IR divergences and is a more complex object to compute and study. Thus, in the remainder of this thesis we shall continue to focus on understanding the integrand and its mathematical and physical structure.

the famous construction of the BCFW recursion relations. In fact, amplitudes in planar $\mathcal{N} = 4$ SYM are completely determined by their singularities, making their study highly relevant to recent developments. In this thesis we shall find BFTs to provide a very natural language in which these questions can be answered.

Symmetries of $\mathcal{N} = 4$ Super-Yang-Mills

Planar 4-dimensional $\mathcal{N} = 4$ Super-Yang-Mills enjoys a particularly large symmetry group. First, it has the conformal symmetry which acts on the spacetime variables x^μ. Moreover, there is a completely separate symmetry which acts on what are known as *dual variables* y^μ, defined through the relation

$$y_i^\mu - y_{i+1}^\mu = p_i^\mu \ , \tag{1.0.24}$$

where p_i^μ is the 4-momentum of the i^{th} particle. The integrand of the amplitude is invariant under conformal transformations of y_i^μ, and this symmetry is known as *dual conformal* symmetry [57, 58].

Finally, the fact that we have $\mathcal{N} = 4$ supersymmetry has very direct effects on the computation of scattering amplitudes. First, the set of diagrams which are $\mathcal{N} = 4$ symmetric is greatly reduced as compared to non-supersymmetric Yang-Mills. Furthermore, the evaluation of helicity sums over internal particles in the BCFW recursion relations is simplified. This is due to the fact that in $\mathcal{N} = 4$ it is possible to put all helicity states in a single multiplet, and the sum over helicities becomes a continuous Grassmann integral which scans over the multiplet.

All together, these symmetries form an infinite-dimensional symmetry known as the *Yangian* [59], allowing planar $\mathcal{N} = 4$ SYM to be integrable [60, 61]. This infinite symmetry is obscured in the standard Feynman diagram approach, while it is completely manifest in the newer, more mathematical formulation of amplitudes [34] (see also [52, 62–66] and recent work on a deformed version of the story [67–71]).

An important consequence of these symmetries is the *dlog form* of the integrand: the degrees of freedom X_i can all be written as $d\log(X_i) = \frac{dX_i}{X_i}$, times some delta functions. Singularities of the amplitude are obtained by shutting off these degrees of freedom, i.e. sending $X_i \to 0$. In physical terms, this corresponds to setting

propagators of a process on-shell, or considering collinear singularities. The *d*log structure has the effect of making all poles and subpoles of the amplitude integrand appear as simple poles. As an example, consider

$$\frac{dXdY}{XY(X+Y)} \,. \tag{1.0.25}$$

When we take the residue around the pole $X \to 0$, we obtain

$$\frac{dY}{Y^2} \,, \tag{1.0.26}$$

which is not a simple pole. This illustrates how non-simple poles can arise from an object that, at the outset, only appeared to have simple poles. Hence, we conclude that (1.0.25) cannot be rewritten as a *d*log form. The great achievement that made the *d*log structure of the integrand completely manifest was the use of *on-shell* diagrams [34], which we introduce in the next section.

Finally, we shall comment on the symmetries of non-planar amplitudes. Although there has been important progress in their study [72–76], they are far less well understood than amplitudes in the planar sector. Recently, building on the observation that the loop integrand in planar amplitudes has only logarithmic singularities and no poles at infinity, it has been conjectured that non-planar amplitudes share the same property [77]. Further evidence supporting this conjecture was provided in [78], where the *d*log form of the non-planar amplitude was found to hold to 3 loops.

On-Shell Diagrams

On-shell diagrams are extremely useful for studying scattering amplitudes, and provide a gateway for connecting amplitudes to the Grassmannian. In simple terms, the Grassmannian is the space of k-dimensional planes in n dimensions and is denoted $G(k,n)$. An element of $G(k,n)$ is a specific k-plane in n dimensions, and is conveniently described by its k basis vectors, juxtaposed to form a $k \times n$ matrix. We will present the Grassmannian in greater detail in Chapter 4. The Grassmannian description of scattering amplitudes enables the linearization of all the constraints of a given process, which in turn has the benefit of making the mathematical structure of the process very transparent.

General on-shell diagrams are constructed by gluing elementary three-point on-shell amplitudes together. For the three-point amplitude to be non-zero, the external particles cannot all have the same helicity. Hence, there are two possibilities: either we have a $(-,-,+)$ helicity configuration, or a $(+,+,-)$ configuration. The form is known as maximally helicity violating (MHV), and the latter is its conjugate $\overline{\text{MHV}}$.[7]

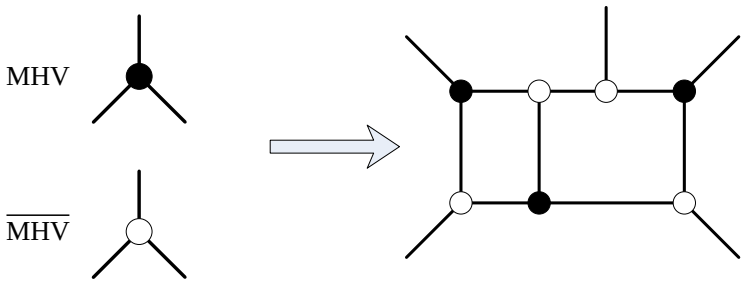

Figure 1.4: The construction of on-shell diagrams by gluing together 3-point amplitudes. MHV amplitudes are denoted by black nodes, $\overline{\text{MHV}}$ amplitudes are denoted by white nodes.

The vertex carries a helicity- and momentum-conserving delta function, and the diagrams constructed by gluing together all the three-point amplitudes are known as *on-shell diagrams*. Figure 1.4 illustrates an example of how 3-point amplitudes may be glued together to form an on-shell diagram. In these diagrams, all particles are on-shell. However, it is still possible to have unconstrained degrees of freedom, and the amplitude is obtained by integrating over these. An important result is that, in the planar limit, the all-loop integrand in planar $\mathcal{N} = 4$ SYM can be expressed in terms of on-shell diagrams [34, 52]. Moreover, the expression of the integrand in terms of on-shell diagrams makes the $d$log structure of the integrand completely manifest: it is simply the product of $d$log's of all the degrees of freedom of the diagram.

The on-shell diagrams are very closely tied to the BCFW recursion relations: each term in the recursion relations corresponds to a specific on-shell diagram. Since

[7]Since every three-point amplitude also carries a color factor, so does the on-shell diagram built from them. While important, the computation of this color factor falls beyond the scope of our discussions.

BCFW terms display the full Yangian invariance of the theory, each planar on-shell diagram is invariant under the Yangian.

The Amplituhedron

Separately, enormous progress has been achieved in the construction of a geometric object which simultaneously contains the information of all relevant planar on-shell diagrams for a given process [5, 79–83]. This object is known as the amplituhedron, and is a new algebraic geometric object which generalizes the positive Grassmannian and encodes scattering amplitudes in a maximally geometric way: they are simply given by its volume.

The amplituhedron is the missing link explaining how to combine Yangian invariant building blocks to give rise to the amplitude. The BCFW recursion relations are seen to be merely one way in which Yangian-invariant terms can be combined, and the combination of these terms is geometrically seen as a specific triangulation of the amplituhedron. However, there are different ways to triangulate the same object, each translating into a different representation of the amplitude. In this approach the standard pillars of quantum field theory like locality and unitarity are properties derived from the geometry of the amplituhedron. The existence of such a structure in planar $\mathcal{N} = 4$ SYM suggests that there might be a very different formulation of the field theory which does not use the standard Lagrangian description of physics.

The correspondence between scattering amplitudes and the amplituhedron has passed numerous tests, although it still remains conjectural and its study is in its infancy. In this thesis we introduce tools analyzing the amplituhedron and present the most comprehensive investigation of its geometry to date. A clear goal is to achieve a systematic understanding similar to the one available for cells in the positive Grassmannian [84]. Among other things, we expect our ideas to be instrumental in triangulating the amplituhedron, and hence contribute to its practical use in constructing scattering amplitudes. A beautiful interplay between experimental exploration of examples, discovery of new structures and theoretical new ideas has been a constant driving force for progress in the understanding of scattering amplitudes. It is reasonable to expect that the examples we study, and the ones which

will be studied in the future with the help of the tools we introduce, will nicely fit into this trend.

Outline

This thesis is divided into 5 chapters which together contain the main results from those publications completed during this doctorate related to the topics of BFTs, integrable systems, and scattering amplitudes [1–6].

Chapter 2 is devoted to the introduction of BFTs. Since these theories have benefited from continuous development over the years, the results of this chapter draw from numerous articles. The chapter begins with a short review of BFTs, primarily following [10], but importantly also identifies a new way of assigning gauge symmetries to the corresponding graphs, as was first found in our paper [1]. It also has an in-depth introduction to all of the necessary tools for the majority of the results in this thesis, the material from which was principally taken from our papers [1,3] but which also contains realizations from our papers [4,6]. Following the results in [1], this chapter also introduces: a new procedure for determining the Calabi-Yau moduli spaces of BFTs; a highly useful set of variables which are also used in Chapters 3 and 6; a detailed discussion of equivalences and reductions of BFTs; and a systematic BFT prescription for determining graph reductions, giving particular emphasis to theories associated to non-planar graphs. Following the results in [3], two very efficient algorithms are presented: a way of immediately obtaining the moduli space of BFTs, and a method to quickly determine the reducibility of BFTs.[8]

Chapter 3 displays our results in [2]: we initiate the study of how to extend the correspondence between dimer models and (0+1)-dimensional cluster integrable systems to (1+1) and (2+1)-dimensional continuous integrable field theories, addressing various points that are necessary for achieving this goal. These developments are quite separate from the main themes of this thesis, but are worthy of inclusion as they illustrate part of the large diversity of the applicability of BFTs. We first study

[8]Notably, we omitted from this thesis powerful tools for constructing new theories from given theories, which can be found in [1].

how to glue and split two integrable systems, from the perspective of the spectral curve, which in terms of the BFT corresponds to a resolution of the toric Calabi-Yau singularity, or equivalently a Higgsing in the gauge theory on the D3-brane probe. We identify a continuous parameter controlling the decoupling between the components and present two complementary methods for determining the dependence on this parameter of the dynamical variables of the integrable system. Interested in constructing systems with an infinite number of degrees of freedom, we study the combinatorics of integrable systems built up from a large number of elementary components, and introduce a toy model capturing important features expected to be present in a continuous reformulation of cluster integrable systems.

Chapter 4 studies the connection between BFTs and scattering amplitudes, following our results in [3]: we perform a detailed investigation of the combinatorial and geometric objects associated to on-shell diagrams. We mainly focus on their relation to polytopes and toric geometry, the Grassmannian and its stratification. Our work extends the current understanding of these connections along several important fronts, most notably eliminating restrictions imposed by planarity, positivity, reducibility and edge removability. We also present a map, known as the boundary measurement, between arbitrary non-planar graphs and elements of the Grassmannian, completing this picture by also including results from our later paper [6]. Because of the intimate relation between bipartite graphs and the Grassmannian, our results can be conversely regarded as an expansion in the understanding of the Grassmannian in terms of bipartite graphs.

Chapter 5 closely follows [5]: we initiate a comprehensive investigation of the geometry of the amplituhedron. We do so by introducing and studying its stratification, focusing on four-point amplitudes. The new stratification exhibits interesting combinatorial properties and positivity is neatly captured by permutations. As explicit examples, we find all boundaries for the two- and three-loop amplitudes and related geometries. We recover the stratifications of some of these geometries from the singularities of the corresponding integrands, providing a non-trivial test of the amplituhedron/scattering amplitude correspondence. We finally introduce a deformation of the stratification with remarkably simple topological properties.

Finally, Chapter 6 displays our results from [6], where we initiate a systematic study of non-planar on-shell diagrams in $\mathcal{N} = 4$ SYM and develop powerful technology for doing so. We use variables generalizing face variables, which make the $d\log$ form of the on-shell form explicit. We make significant progress towards a general classification of arbitrary on-shell diagrams. Interestingly, non-planar diagrams exhibit novel phenomena, such as the emergence of constraints on Plücker coordinates beyond Plücker relations when deleting edges. Finally, we introduce a prescription, applicable beyond the MHV case, for writing the on-shell form as a function of minors directly from the graph.

Chapter 2

Bipartite Field Theories

In this chapter we will introduce an important infinite class of $\mathcal{N} = 1$ quiver gauge theories, which are known as Bipartite Field Theories. We will also introduce the huge array of tools which will make frequent recurrence throughout this thesis.

2.1 Definition of BFTs

A BFT is a 4-dimensional $\mathcal{N} = 1$ quiver gauge theory, whose Lagrangian is defined in terms of a bipartite graph living on a Riemann surface, possibly containing boundaries. BFTs were first introduced in [10].[1] 4d $\mathcal{N} = 1$ supersymmetric gauge theories are determined by specifying the gauge symmetry group (vector superfields), matter content (chiral superfields), a real function of the chiral superfields (the Kähler potential) and a holomorphic function of the chiral superfields (the superpotential W). In this thesis we will focus on theories with canonical Kähler potential in the UV, so we will not mention it any longer.

We shall begin by defining the graph more precisely.

Bipartite Graphs. A graph is a collection of nodes and of edges connecting them. The graphs we consider have two types of nodes, distinguished by a white or black color. If white nodes are only connected to black nodes and vice-versa, the graph is

[1] Closely related theories were introduced in [14].

bipartite. We denote the number of edges connected to a given node as its *valence*. The framework discussed in this thesis deals with general bipartite graphs containing nodes of arbitrary valence.

In many applications, it can often be useful to consider embeddings of the graphs onto Riemann surfaces with boundaries. We shall call *planar* a graph which can be embedded on the disk without edges crossing. Instead, those graphs whose embedding involves edge crossings or multiple boundaries are referred to as *non-planar*.

We divide nodes into two distinct categories: *external* nodes are defined as those nodes which must lie on a boundary in any embedding of the graph, the remaining nodes are *internal*. We shall only consider monovalent external nodes.

Once an embedding of the graph on a Riemann surface is specified, one can define *faces* as those regions on the surface surrounded by edges and/or by boundaries. Faces are also divided in two categories: *internal faces* are those which are only surrounded by edges, and *external faces* are those whose perimeter includes at least one boundary.

The map defining a BFT in terms of a bipartite graph on a Riemann surface is as follows:

- **Faces:** each face represents a $U(N)$ symmetry group.[2] We shall soon describe how to identify the gauge symmetries from the global ones.

- **Edges:** each edge between faces i and j represents a chiral superfield X_{ij} transforming in the bifundamental representation of the two groups, $U(N)_i \times U(N)_j$, associated to the two faces adjacent to the edge (or adjoint representation if $i = j$). The chirality, i.e. orientation, of the bifundamental is such that it goes clockwise around white nodes and counter-clockwise around black nodes. Chiral fields associated to external legs, i.e. edges connected to external nodes, are taken to be non-dynamical.

[2]The case of general ranks, i.e. not equal for all faces, is extremely interesting. It is however not relevant for the questions discussed in this thesis, so we do not pursue it.

- **Nodes:** each k-valent node represents a superpotential term given by the trace of the product of k fields corresponding to edges terminating on the node. The clockwise or counter-clockwise orientation associated to nodes determines the cyclic ordering of fields in each superpotential term. The superpotential term bears a positive sign for white nodes and negative sign for black nodes. External nodes, by definition, do not map to any superpotential term.

The next section discusses in detail two possible ways of gauging the symmetries in these theories. These alternatives give rise to two independent classes of BFTs. As we will explain, for one of the possible gaugings the resulting theories are independent of any embedding of the bipartite graphs into a Riemann surface, in other words they can be defined without appealing to any Riemann surface at all. Keeping the two possibilities in mind, it is still useful to invoke an underlying Riemann surface in order to provide a unified presentation of the two classes of BFTs. The use of an embedding will also allow us to use a generalized notion of face variables, introduced in §2.5, which encode the degrees of freedom of the graph in the most succinct way.

2.1.1 Two Alternative Gaugings

One possible way of gauging the $U(N)$ symmetries of BFTs was considered in [10]. More careful thought reveals that there exists yet another natural way of gauging them, introduced for the first time in [1]. We refer to the two possibilities as gaugings 1 and 2 and present them below. Each gauging leads to a different class of consistent theories, expanding the realm of BFTs by effectively doubling it with respect to what was originally considered in [10].

Gauging 1. In this case, the $U(N)$ symmetries associated to *internal* faces of the graph are gauged. It is straightforward to see that bipartiteness guarantees that internal faces are even-sided. This implies that they are anomaly free and can be consistently gauged. The remaining symmetry groups are global. Note that external faces are generally not even-sided. We refer to the resulting class of gauge theories as BFT_1, and these are the ones considered when BFTs were introduced in [10].

The theories in this class are quiver gauge theories. Their quivers, including plaquettes representing the superpotential terms, are obtained by dualizing the bipartite graph [10], as illustrated in Figure 2.1. This quiver is such that its plaquettes, i.e. the minimal oriented closed loops, encode the terms in the superpotential of the BFT.

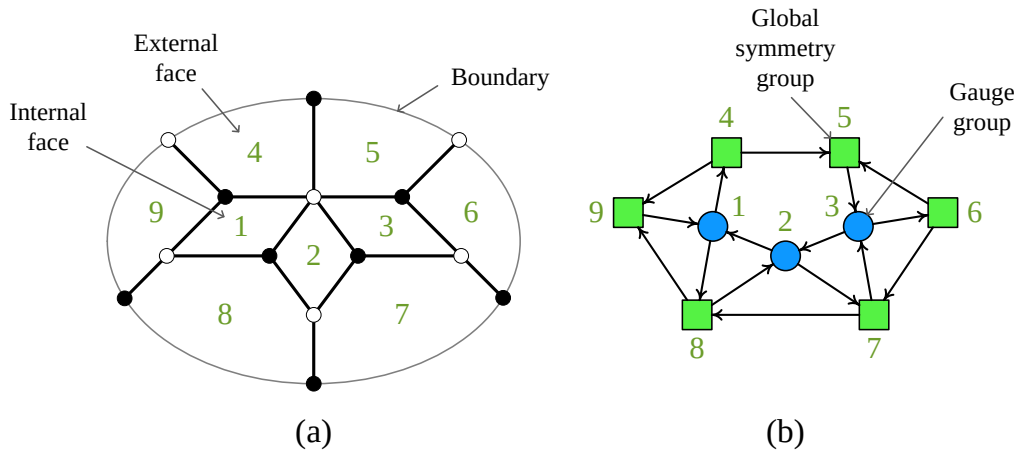

Figure 2.1: A bipartite graph on a disk and its dual quiver. Every plaquette in this quiver corresponds to a node in the original graph and hence a superpotential term.

Gauging 1 arises naturally when thinking about theories with a D-brane interpretation. Indeed, a subclass of BFT_1's has already appeared in this context in the literature, playing a prominent role. It corresponds to the 4d $\mathcal{N} = 1$ worldvolume theories on D3-branes probing toric Calabi-Yau 3-fold singularities. These theories are known as *dimer models*. For this subclass of theories, the Riemann surface is a 2-torus without boundaries [16]. In this context, the corresponding bipartite graphs are called *brane tilings* and have been the subject of extensive investigations [15–18, 85]. The correspondence between these gauge theories and bipartite graphs has indeed been instrumental in several important developments such as the determination of the superconformal field theories that are dual, via the AdS/CFT correspondence, to infinite families of Sasaki-Einstein manifolds [17, 20, 86]. More recently, a physical realization in terms of D3 and D7-branes on toric Calabi-Yau 3-folds has been introduced for a more general class of BFTs, which includes graphs with boundaries [13].

Gauging 2. Gauging 1 was motivated by both anomaly considerations and the analogy with theories with a known D-brane realization. However, our previous discussion makes it clear that the symmetries associated to internal faces are not the only ones that are automatically anomaly free. In fact, every closed path in the graph can be associated to an anomaly free symmetry. Those associated to linear combinations of faces are $U(N)$ symmetries. Other types of closed paths, such as the ones along the fundamental directions appearing when the underlying Riemann surface has genus greater than zero, correspond to $U(1)$ symmetries.[3] In general, only a minimal set of independent closed paths has to be gauged. Considering this gauging gives rise to a new class of theories which we call BFT_2, and first appeared in [1].

Gauging 2 extends gauging 1 by gauging some additional symmetries. While the quiver associated to gauging 1 still provides useful guidance, BFT_2's are not standard quiver theories since chiral fields can be charged under more than two gauge symmetries.

If we restrict ourselves to the Abelian case, where all the symmetries are $U(1)$, it is straightforward to see that the definition of Abelian BFT_2's is actually independent of any embedding of the bipartite graph into a Riemann surface. In fact, an underlying Riemann surface becomes unnecessary for defining this type of theory. However, removing the Riemann surface from the discussion is a step which needs to be approached with care, since it was not only used for identifying some of the gauge symmetries, but it was also necessary for providing nodes with an orientation that determines the chirality of fields. It is possible to define chirality without the need of a Riemann surface: one simply declares that for any gauge symmetry, the fields associated to edges alternate between being in the fundamental and antifundamental representations as one moves along the corresponding closed path.[4]

[3] Whether some of these symmetries can be consistently promoted to be non-Abelian is an interesting question that deserves further study. Moreover, it is natural to address this question in the context of a more general study in which arbitrary ranks for all symmetries are considered.

[4] An analogous chirality assignment is also possible for global symmetries associated to open paths in the graph.

The embedding-independence of BFT_2's will allow us to more naturally connect them to scattering amplitudes, since both types of objects only care about the connectivity of the graph. We shall see this connection utilized to great benefit in Chapters 4, 5 and 6, where the powerful machinery of BFTs is exported to provide new results in the novel setting of scattering amplitudes in 4-dimensional $\mathcal{N} = 4$ Super-Yang-Mills. The relevant BFTs in this context are classical and Abelian,[5] and are hence the theories we shall restrict ourselves to in the following sections.

For graphs on a disk there is no distinction between BFT_1 and BFT_2. The difference between the two gaugings arises in the presence of multiple boundaries and/or higher genus Riemann surfaces, as illustrated in Figure 2.2.

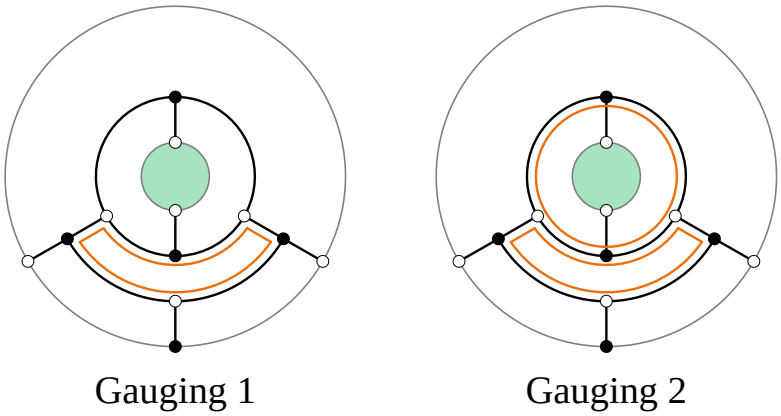

Figure 2.2: Difference between BFT_1 and BFT_2 in an example with two boundaries. The orange loops are those which are gauged in each gauging. The surface has genus $g = 0$ and hence there are no loops with non-trivial homology.

We refer those interested in extensive catalogues of explicit BFT examples to [1,10] for general BFTs and to [87–89] for higher genus examples without boundaries.

[5] Since we focus on classical theories, we do not worry about issues concerning the UV completion of Abelian BFTs.

2.2 Moduli Spaces

The *moduli space* is a fundamental object in the study of SUSY QFTs. It is the space of field configurations for which the scalar potential of the theory vanishes. Since the scalar potential is positive semi-definite in SUSY theories, the points where it vanishes correspond to absolute minima. Moreover, in SUSY theories such vacua are not isolated, and the moduli space becomes an interesting continuous geometry.

The scalar potential is a sum of two types of contributions: F-terms (associated to chiral superfields) and D-terms (associated to vector superfields). Every F- and D-term enters the scalar potential with squared absolute value and hence needs to independently vanish on the moduli space. We will not discuss the basics of F- and D-terms in this thesis. A remarkable feature of BFTs is that due to the very special structure of their superpotential, which follows from the bipartite graph as described by the dictionary given in §2.1, the determination of the moduli space reduces to a simple combinatorial problem.

As a first step towards a full investigation of BFTs, all our discussions of moduli spaces in the following sections are going to refer to the case where $N = 1$, i.e. all symmetries are $U(1)$. This simplification has various motivations. First, Abelian BFTs are relevant for the study of scattering amplitudes, which do not contain any parameter related to a non-trivial N. In fact, the scattering problem can be mapped to a $U(1)$ gauge theory living on the graph [34] which, in turn, is directly related to Abelian BFTs. This correspondence was studied for graphs on T^2 in [90, 91].

While in some cases, such as BFTs arising on stacks of D-branes, the moduli space of the non-Abelian theory is a symmetrized product of N copies of the Abelian one, a simple connection of this type need not hold for general BFTs. Elucidating the structure of the moduli space of non-Abelian BFTs is a very interesting question that certainly deserves to be studied in the future. We envision powerful tools such as those based on Hilbert series are going to be useful for this endeavour [92–95].

2.2.1 Master and Moduli Space

We shall now review the definition of the moduli spaces in terms of F- and D-term constraints. The classical moduli space can be constructed in two stages. First, we construct the space of vanishing F-terms, which is known as the *master space* of the theory [96–98]. In doing so, we only require the vanishing of the F-terms for fields associated to internal edges in the bipartite graph, without imposing zero F-terms for external edges. There are both geometric and physical reasons motivating this treatment, as explained in detail in [10], and discussed below.

Because fields are represented by edges in the graph, every internal edge X_0 appears in exactly two terms in the superpotential, which thus takes the general form

$$W = X_0 P_1(X_i) - X_0 P_2(X_i) + \dots , \tag{2.2.1}$$

where $P_1(X_i)$ and $P_2(X_i)$ represent products of bifundamentals fields. The F-term equation for every X_0 is given by

$$\partial_{X_0} W = 0 \quad \Longleftrightarrow \quad P_1(X_i) = P_2(X_i). \tag{2.2.2}$$

As mentioned above, we do not impose zero F-terms for external edges. Since these fields appear in a single superpotential term, setting their F-terms to zero would set to zero the products of fields they couple to, reducing the master space dramatically and potentially making it disappear. Also, in those BFTs with a D-brane embedding, the fields associated to external legs have a higher dimensional support and are hence naturally non-dynamical from a 4d viewpoint [13]. Being non-dynamical, these fields should be regarded as couplings in 4d. However, our treatment of external legs is instead to include them as continuous parameters in the master space. We can think of the resulting geometry as a *generalized master space*, which incorporates all possible values of the corresponding superpotential couplings. This approach is useful because the resulting space can be nicely treated in terms of toric geometry. In fact, if desired, it is straightforward to recover the standard master space, in which the values of these couplings are fixed, from the generalized one: we just consider slices of the toric generalized master space corresponding to

setting every external leg X_e to a fixed value $X_{e,0}$.

The *mesonic moduli space* [15, 16, 95, 99, 100] of the BFT, which we refer to just as the moduli space for brevity, is obtained by projecting the master space onto vanishing D-terms, of which we have one per gauge group. As we shall see, due to the restricted structure of BFTs arising from their definition in terms of bipartite graphs on Riemann surfaces, both the master and moduli spaces are toric Calabi-Yau manifolds [10, 35]. The precise CY for the moduli space will naturally depend on the choice of gauging.

In §2.4 we shall see that the master and moduli spaces of BFTs can be obtained using very powerful combinatorial machinery. Moreover, their toric diagrams form polytopes which we shall use as invaluable tools in the rest of this thesis.

2.3 Bipartite Technology

In this section we review the fundamental tools related to bipartite graphs which we shall make heavy use of throughout this thesis. We describe the notion of perfect matchings, perfect orientations and flows, which will later be used to easily obtain the master and moduli spaces.

Perfect Matchings. Perfect matchings are key combinatorial objects of bipartite graphs. A perfect matching is a sub-collection of edges such that every internal node is the endpoint of only one edge, while external nodes may or may not be contained in the perfect matching.[6] Usually, there are several ways to select sub-collections of edges with this property, and each of these is a different perfect matching, which we denote p_μ. An example of a bipartite graph and its perfect matchings is provided in Figure 2.3.

In §2.3.3 we will show how to find all perfect matchings for a given bipartite graph in a systematic way.

[6]Strictly speaking, this is known as an *almost perfect matching*. For brevity, we simply refer to these objects as perfect matchings in what follows.

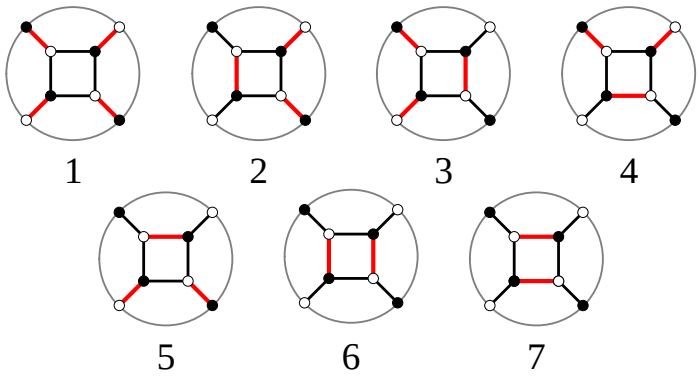

Figure 2.3: All seven perfect matchings for a bipartite graph with four external nodes. Edges in the perfect matchings are shown in red. The graph is embedded in a disk.

Perfect Orientations. A bipartite graph can equally be characterized by its perfect orientations. A perfect orientation is a way of assigning arrows to the edges of a graph in such a way that we have for nodes of valency v:

- **White node:** 1 incoming and $v-1$ outgoing arrows.
- **Black node:** 1 outgoing and $v-1$ incoming arrows.

Figure 2.4 provides an example of a perfect orientation for a bipartite graph on a disk, with 3-valent nodes.

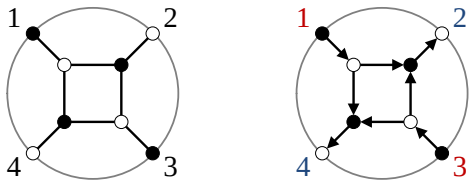

Figure 2.4: A bipartite graph and a possible perfect orientation. Sources are marked in red and sinks in blue.

Given a perfect orientation, external nodes can be naturally divided into *sources* and *sinks*, as shown in the figure. The number of elements in each of these two sets does not depend on the choice of the perfect orientation and is a characteristic of

the graph itself. Note that different perfect orientations on a given graph can give rise to the same sets of sources and sinks.

Flows. Given a graph and a perfect orientation, it is possible to specify the latter by listing all oriented non self-intersecting paths in it. We refer to such paths as *flows* and denote them as $\mathfrak{p}_\mu$. Flows may involve more than one disjoint component. These components can connect external nodes or correspond to closed loops. The trivial flow, i.e. the one which does not involve any edge of the graph, is also included.

2.3.1 Relation Between Perfect Orientations, Flows and Perfect Matchings

Perfect orientations are in bijection with perfect matchings. Given a perfect matching, the way to obtain the corresponding perfect orientation is to assign arrows to the edges as follows:

- Edges belonging to the perfect matching point from the black node to the white node.
- All other edges point out of white nodes and into black nodes.

Since a perfect matching only touches each internal node once, the above definition automatically satisfies the rules for arrows in a perfect orientation. Conversely, it is possible to obtain the perfect matching from a perfect orientation by selecting the incoming arrow for white nodes and the outgoing arrow for black nodes.

There is also a bijection between flows and perfect matchings. In order to find it, we begin by choosing a perfect matching p_{ref}, called the *reference perfect matching* (or just reference matching for short), and assigning to all of its edges an orientation that points from white nodes to black nodes. We orient the edges of all other perfect matchings in a similar way. Subtracting p_{ref} from all perfect matchings, i.e. reversing the arrows in p_{ref} before combining them, creates a set of oriented paths. These paths necessarily live in the perfect orientation associated to p_{ref}, because all arrows point out of white nodes and into black nodes except for the ones belonging

to p_{ref}, which have opposite orientation. These paths are thus precisely the flows in the perfect orientation defined by p_{ref}.

In summary, for each perfect matching there is an associated perfect orientation. The number of flows in each perfect orientation is equal to the number of perfect matchings, and they are found by subtracting the reference perfect matching from the corresponding perfect matchings. This is succinctly illustrated in Figure 2.5.

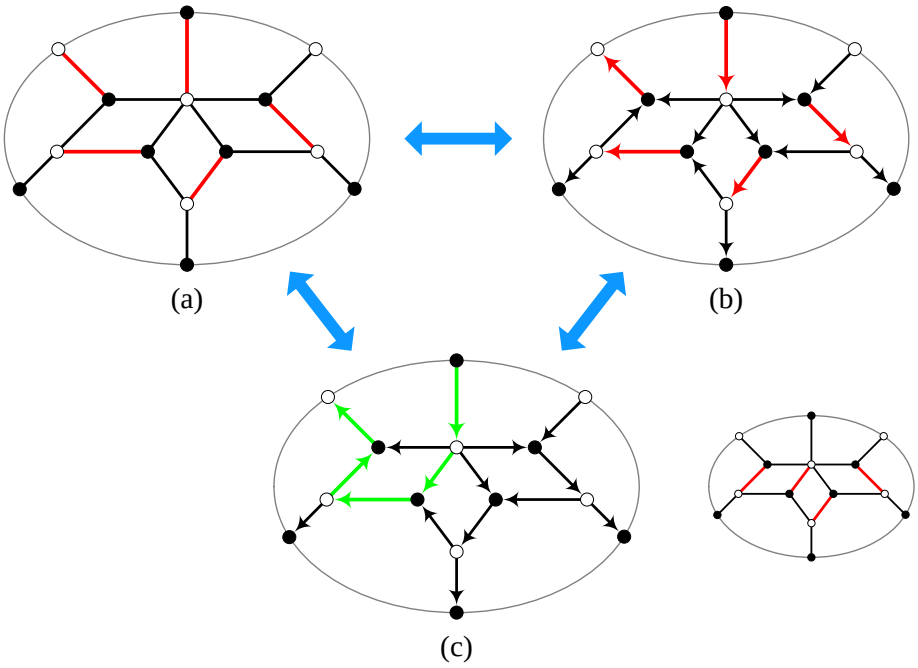

Figure 2.5: An example of: (a) a perfect matching, (b) the corresponding perfect orientation, and (c) a flow in this perfect orientation, corresponding to the perfect matching shown on the right.

2.3.2 Oriented Edge Weights

We will often be interested in relating edge weights, which strictly speaking have no associated orientation, to oriented paths. It is thus useful to devise a formalism that consistently deals with such a connection. We will refer to edge weights as X_i, where the index $i = 1, \ldots, E$ runs over all edges of the graph.

With the goal of describing oriented paths, we introduce new variables α_i, which are edge weights endowed with an orientation. In our convention the orientation goes

from white to black nodes. We can thus associate an *oriented perfect matching* $\tilde{p}_\mu$ to every perfect matching p_μ. The oriented perfect matching is given by the product of the α_i variables over all edges in the corresponding perfect matching. Figure 2.6 shows two perfect matchings p_3, p_4 and their corresponding oriented perfect matchings $\tilde{p}_3, \tilde{p}_4$.

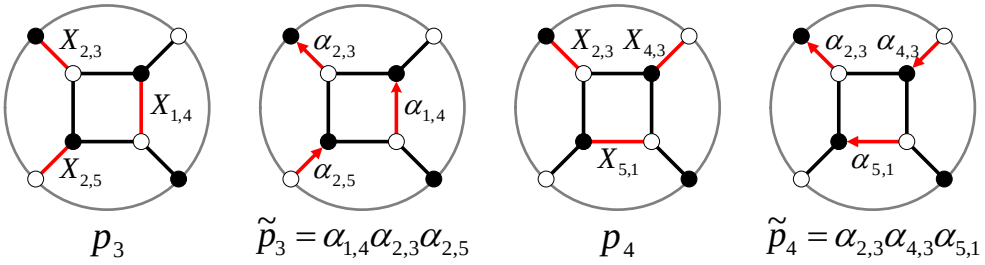

Figure 2.6: Example of ordinary perfect matchings p_i and oriented perfect matchings $\tilde{p}_i$. Edges $\alpha_{i,j}$ are oriented from white nodes to black nodes.

We can in fact write any oriented path on the graph as a product or ratio of these new variables: if a segment of the path goes from a white node to a black node, the relevant $\alpha_{i,j}$ contributes to the expression of the path in the numerator; if the segment goes from a black node to a white node, its $\alpha_{i,j}$ contributes to the denominator. In this parameterization all flows can be expressed as ratios $\mathfrak{p}_i = \tilde{p}_i/\tilde{p}_{\text{ref}}$, where $\tilde{p}_{\text{ref}}$ is the reference matching defining the underlying perfect orientation. An example is provided in Figure 2.7, where the perfect orientation corresponds to the perfect matching p_4, and the flow is $\mathfrak{p}_3 = \frac{\tilde{p}_3}{\tilde{p}_4} = \frac{\alpha_{2,5}\alpha_{1,4}}{\alpha_{5,1}\alpha_{4,3}}$. Note that the trivial flow is $\mathfrak{p}_{\text{ref}} = 1$.

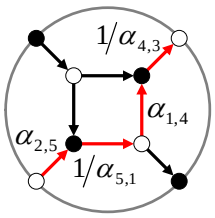

Figure 2.7: A flow in the perfect orientation corresponding to the reference perfect matching p_4. The flow shown is $\mathfrak{p}_3 = \frac{\tilde{p}_3}{\tilde{p}_4} = \frac{\alpha_{2,5}\alpha_{1,4}}{\alpha_{5,1}\alpha_{4,3}}$.

This parameterization is very convenient for the study of the connection between bipartite graphs and the Grassmannian, and will be extensively used in Chapters 4 and 6.

2.3.3 Finding Perfect Matchings

Flows, perfect orientations and perfect matchings contain equivalent combinatorial information about the bipartite graph. Among the three, perfect matchings are those which are obtained most efficiently. This is done using a generalization of Kasteleyn matrix techniques, which will be briefly outlined here. The reader is referred to [10] for a detailed discussion of these techniques.

The starting point for finding the perfect matchings is the construction of a weighted adjacency matrix, known as the *master Kasteleyn matrix* K_0. When there are multiple edges between two nodes their contributions are added. Denoting internal white and black nodes W_i and B_i, respectively, and external white and black nodes W_e and B_e, K_0 takes the form:

$$K_0 = \left(\begin{array}{c|c|c} & B_i & B_e \\ \hline W_i & * & * \\ \hline W_e & * & 0 \end{array}\right) . \tag{2.3.1}$$

The zero in the bottom-right corner arises because external nodes are only paired with internal nodes. K_0 is not necessarily square.

For any subsets $W_{e,del} \subseteq W_e$ and $B_{e,del} \subseteq B_e$ of the external nodes, we define the *reduced Kasteleyn matrix* $K_{(W_{e,del},B_{e,del})}$ as the matrix resulting from starting from K_0 and deleting the rows in $W_{e,del}$ and the columns in $B_{e,del}$.

All perfect matchings in the graph are given by the polynomial:[7]

$$\mathcal{P} = \sum_{W_{e,del},B_{e,del}} \text{perm } K_{(W_{e,del},B_{e,del})}, \tag{2.3.2}$$

where the sum runs over all possible subsets $W_{e,del}$ and $B_{e,del}$ of the external nodes such that the resulting reduced Kasteleyn matrices are square. Every term in this

[7]The permanent of a matrix is the determinant where all signs in the final expression are positive.

polynomial corresponds to the product of edges in a perfect matching.

Example. Let us see how this works in a specific example, shown in Figure 2.8. For this example we have

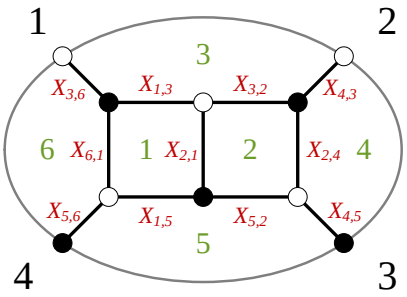

Figure 2.8: An example of a planar graph. Face labels are in green, edge labels in red, and external nodes in black. The labeling of external nodes will be useful when thinking about scattering amplitudes.

$$K_0 = \left(\begin{array}{ccc|cc} X_{3,2} & X_{2,1} & X_{1,3} & 0 & 0 \\ X_{2,4} & X_{5,2} & 0 & 0 & X_{4,5} \\ 0 & X_{1,5} & X_{6,1} & X_{5,6} & 0 \\ \hline 0 & 0 & X_{3,6} & 0 & 0 \\ X_{4,3} & 0 & 0 & 0 & 0 \end{array}\right) \tag{2.3.3}$$

which yields

$$\begin{aligned} \mathcal{P} =& X_{1,3}X_{1,5}X_{2,4} + X_{1,3}X_{1,5}X_{4,3}X_{4,5} + X_{1,3}X_{4,3}X_{5,2}X_{5,6} + X_{1,5}X_{3,2}X_{3,6}X_{4,5} \\ &+ X_{2,1}X_{2,4}X_{3,6}X_{5,6} + X_{2,1}X_{2,4}X_{6,1} + X_{3,2}X_{3,6}X_{5,2}X_{5,6} + X_{3,2}X_{5,2}X_{6,1} \\ &+ X_{2,1}X_{3,6}X_{4,3}X_{4,5}X_{5,6} + X_{2,1}X_{4,3}X_{4,5}X_{6,1} \ . \end{aligned} \tag{2.3.4}$$

Each term is equal to the product of edges in each perfect matching; counting the terms we see that we have 10 perfect matchings in this example.

2.4 Obtaining the Master and Moduli Spaces

We shall now use the combinatorial tools just presented to obtain the toric diagrams for the master and moduli space. Along the way, we will uncover two polytopes

which will be very important in this thesis: the matching and matroid polytopes.

2.4.1 Master Space

The characteristic polynomial in (2.3.2) contains all the information relating edges, i.e. bifundamental fields, to perfect matchings. This information can be equivalently recast in terms of an $(E \times c)$-dimensional *perfect matching matrix* P, where E is the number of edges X_i and c is the number of perfect matchings p_μ. The components of the matrix are defined as follows

$$P_{i\mu} = \begin{cases} 1 & \text{if } X_i \in p_\mu \\ 0 & \text{if } X_i \notin p_\mu \end{cases}$$

where $i = 1, \ldots, E$ and $\mu = 1, \ldots, c$. Viewing each column as the coordinate of a vertex, P specifies a polytope known as the *matching polytope* [101] and gives the toric diagram for the master space of the BFT.[8] This stems from the fact that the F-term equations are trivially satisfied with the following change of variables [10][9]

$$X_i = \prod_\mu p_\mu^{P_{i\mu}} \ . \tag{2.4.1}$$

Each perfect matching has a unique coordinate in the matching polytope, and their positions encode the linear relations between the p_μ variables associated to the F-term equations. In general, the polytopes we will define live in high-dimensional integer lattices. It is thus typically impractical to provide a graphical representation

[8]Note: This is the equivalent to the *coherent component* of the master space, and not the full master space. The full master space usually decomposes into smaller irreducible spaces, most of them being $\mathbb{C}^l$. The coherent component is the largest irreducible subspace of the full master space.

[9]It is important to emphasize the difference between (2.4.1) and the definition of oriented perfect matchings introduced in §2.3.2, which are given by $\tilde{p}_\mu = \prod_i \alpha_i^{P_{i\mu}}$. While edge weights are naturally interpreted as products of perfect matchings for solving F-term equations, oriented perfect matchings should be thought of as the product of oriented edge weights. In both cases, the object controlling the map is the P matrix. Avoiding inconsistencies associated with this subtle difference was one of the main reasons for introducing the concepts of oriented perfect matchings and edge weights.

of them. Instead, we will describe them in terms of matrices giving the position-vectors of points in them. From the toric diagram representation of the master space, it follows that the master space is a toric manifold. Moreover, it is CY [10, 35].

Example. Let us see how this works in practice in the example from Figure 2.8, whose perfect matchings are read off from (2.3.4). The perfect matching matrix becomes:

$$P = \left(\begin{array}{c|cccccccccc} & p_1 & p_2 & p_3 & p_4 & p_5 & p_6 & p_7 & p_8 & p_9 & p_{10} \\ \hline X_{1,3} & 1 & 1 & 1 & 0 & 0 & 0 & 0 & 0 & 0 & 0 \\ X_{1,5} & 1 & 1 & 0 & 1 & 0 & 0 & 0 & 0 & 0 & 0 \\ X_{2,4} & 1 & 0 & 0 & 0 & 1 & 1 & 0 & 0 & 0 & 0 \\ X_{3,2} & 0 & 0 & 0 & 1 & 0 & 0 & 1 & 1 & 0 & 0 \\ X_{2,1} & 0 & 0 & 0 & 0 & 1 & 1 & 0 & 0 & 1 & 1 \\ X_{5,2} & 0 & 0 & 1 & 0 & 0 & 0 & 1 & 1 & 0 & 0 \\ X_{6,1} & 0 & 0 & 0 & 0 & 0 & 1 & 0 & 1 & 0 & 1 \\ X_{3,6} & 0 & 0 & 0 & 1 & 1 & 0 & 1 & 0 & 1 & 0 \\ X_{4,5} & 0 & 1 & 0 & 1 & 0 & 0 & 0 & 0 & 1 & 1 \\ X_{4,3} & 0 & 1 & 1 & 0 & 0 & 0 & 0 & 0 & 1 & 1 \\ X_{5,6} & 0 & 0 & 1 & 0 & 1 & 0 & 1 & 0 & 1 & 0 \end{array}\right) \tag{2.4.2}$$

Generally, the matching polytope lives in a lower dimensional subspace of $\mathbb{Z}^E$ where E is the number of edges. This fact can be made explicit by row-reducing P, which for (2.4.2) results in the following matrix:

$$G_{\text{matching}} = \left(\begin{array}{cccccccccc} p_1 & p_2 & p_3 & p_4 & p_5 & p_6 & p_7 & p_8 & p_9 & p_{10} \\ \hline 1 & 0 & 0 & 0 & 0 & 0 & 0 & 0 & -1 & -1 \\ 0 & 1 & 0 & 0 & 0 & 0 & -1 & -1 & 1 & 1 \\ 0 & 0 & 1 & 0 & 0 & 0 & 1 & 1 & 0 & 0 \\ 0 & 0 & 0 & 1 & 0 & 0 & 1 & 1 & 0 & 0 \\ 0 & 0 & 0 & 0 & 1 & 0 & 0 & -1 & 1 & 0 \\ 0 & 0 & 0 & 0 & 0 & 1 & 0 & 1 & 0 & 1 \end{array}\right) . \tag{2.4.3}$$

From this we see that the toric diagram lives in 6 dimensions, indicating that the master space is a 6-dimensional toric variety. We can also see that the coordinates are not all independent: summing over all 6 rows of G_{matching} we obtain a row of 1's. This is simply the statement that the toric diagram lies on an 5-dimensional hypersurface at unit distance from the origin, which is nothing other than the condition for the toric variety to be CY. We deduce that we have the toric diagram of a 6d CY cone.

From now on we refer to the *dimension of the matching polytope* as the dimension of the hyperplane on which the points lie; in the example above this is 5 dimensions, while the dimension of the master space in this example is 6.

The matrix P is extremely useful, and will be much utilized throughout this thesis. It provides the fastest way to obtain the moduli space, as well as encodes the full singularity structure of BCFW terms for scattering amplitudes in $\mathcal{N} = 4$ SYM.

2.4.2 Moduli Space

We shall now move on to study the moduli space of BFTs. In order to construct the moduli space, the master space has to be projected onto gauge invariants. To this end, it is useful to introduce the gauge charge matrix $d_{G\times E}$ of the BFT, where G is the number of gauge groups and E is the number of fields.[10] This procedure was first introduced in [10]. The elements of the gauge charge matrix are

$$d_{aj} = \begin{cases} -1 & \text{if } X_j \text{ is fundamental to } U(N)_a \\ +1 & \text{if } X_j \text{ is anti-fundamental to } U(N)_a \\ 0 & \text{if } X_j \text{ is adjoint or neutral under } U(N)_a \end{cases}$$

where $a = 1, \ldots, G$ and $j = 1, \ldots, E$. Note that the number of fundamental and antifundamental fields for every gauge group is the same due to anomaly cancellation.

Each gauge group contributes with a D-term. D-terms can be encoded in a charge matrix Q^D, which is defined through the relation

$$d_{G\times E} = Q^D_{G\times c} \cdot P_{c\times E} \ . \tag{2.4.1}$$

This equation can be used to determine an assignation of $Q^D_{G\times c}$ charges on the perfect matchings. Since the system is not invertible, the resulting charges Q^D are generally not uniquely determined. The moduli space is however independent of the chosen solution.

Since we need to simultaneously impose the F- and D-terms, we also define the

[10] G clearly depends on whether one considers gauging 1 or 2.

matrix

$$Q^F = \ker(P_{c\times e}) \ . \tag{2.4.2}$$

The moduli space is also a toric CY manifold [10] and its toric diagram is obtained from the toric diagram of the master space by projecting it onto the null space of the matrix of gauge charges of the perfect matchings:

$$G = \ker \begin{pmatrix} Q^F \\ Q^D \end{pmatrix} . \tag{2.4.3}$$

Columns in the G matrix correspond to perfect matchings and contain the coordinates of the associated point in the toric diagram.

As already mentioned, the construction of the toric diagram of the moduli space has amounted to a *projection* of the coordinates in the matching polytope. Thus, while perfect matchings each had a unique coordinate in the matching polytope, there will typically be some identifications of perfect matchings under this projection, i.e. several perfect matchings will map to the same point in the toric diagram of the moduli space.

Gauging 2 will generally gauge more symmetries than gauging 1. Correspondingly, the toric diagram will generally have a smaller dimensionality. An extremely interesting result, proven in [1], is that the toric diagram of the moduli space, for gauging 2, forms another very important polytope, known as the *matroid polytope*. The matroid polytope is intimately related to the Grassmannian, and we shall make heavy use of this connection when exporting the tools of BFTs to scattering amplitudes.

Example. Let us compute the moduli space for the example in Figure 2.8. As remarked in §2.1.1, on the disk there is no difference between gauging 1 and gauging 2. We can then take the two internal faces f_1 and f_2 to be our gauge symmetries $U(1)_1$ and $U(1)_2$, respectively. The charge matrix $d_{2\times 11}$ for this example is

$$d = \left(\begin{array}{c|cc} & U(1)_1 & U(1)_2 \\ \hline X_{1,3} & 1 & 0 \\ X_{1,5} & 1 & 0 \\ X_{2,4} & 0 & 1 \\ X_{3,2} & 0 & -1 \\ X_{2,1} & -1 & 1 \\ X_{5,2} & 0 & -1 \\ X_{6,1} & -1 & 0 \\ X_{3,6} & 0 & 0 \\ X_{4,5} & 0 & 0 \\ X_{4,3} & 0 & 0 \\ X_{5,6} & 0 & 0 \end{array}\right) \quad \Rightarrow \quad Q^D = \left(\begin{array}{cccccccccc} p_1 & p_2 & p_3 & p_4 & p_5 & p_6 & p_7 & p_8 & p_9 & p_{10} \\ \hline 0 & 0 & 1 & 1 & 0 & 0 & 0 & -1 & -1 & 0 \\ 0 & 0 & 0 & 0 & 0 & 1 & 0 & -1 & 0 & 0 \end{array}\right) \tag{2.4.4}$$

where our choice for Q^D is not unique. Using (2.4.2) to find Q^F, we obtain the moduli space toric diagram from (2.4.3):

$$G_{\text{moduli}} = \left(\begin{array}{ccc|cc|c|c|cc|c} p_1 & p_6 & p_8 & p_2 & p_{10} & p_3 & p_4 & p_5 & p_7 & p_9 \\ \hline 0 & 0 & 0 & 1 & 1 & 0 & 0 & -1 & -1 & 0 \\ 0 & 0 & 0 & 0 & 0 & 1 & 0 & 1 & 1 & 1 \\ 1 & 1 & 1 & 0 & 0 & 1 & 0 & 1 & 1 & 0 \\ 0 & 0 & 0 & 0 & 0 & -1 & 1 & 0 & 0 & 0 \end{array}\right) \tag{2.4.5}$$

where we have grouped together those perfect matchings with the same coordinates, i.e. those which are identified under the projection. Here we see that the moduli space toric diagram is composed of 6 points and is a 4-dimensional CY cone, and that the projection caused some points to have multiplicities greater than 1.

Let us see what the matroid polytope formed by these points is. The polytope is the convex hull of the coordinates in (2.4.5), which is most easily obtained by translating the coordinates such that one vertex will be at the origin, and row-reducing. Doing this we obtain

$$G_{\text{matroid}} = \left(\begin{array}{ccc|cc|c|c|cc|c} p_1 & p_6 & p_8 & p_2 & p_{10} & p_3 & p_4 & p_5 & p_7 & p_9 \\ \hline 0 & 0 & 0 & 1 & 1 & 0 & 0 & -1 & -1 & 0 \\ 0 & 0 & 0 & 0 & 0 & 1 & 0 & 1 & 1 & 1 \\ 0 & 0 & 0 & 0 & 0 & 0 & 1 & 1 & 1 & 1 \end{array}\right) \tag{2.4.6}$$

This polytope is of sufficiently low dimensionality to draw, and is illustrated in Figure 2.9.

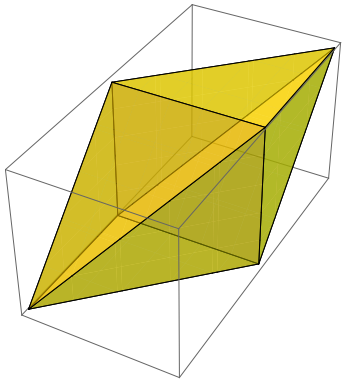

Figure 2.9: Matroid polytope for the example in Figure 2.8.

2.4.3 A Fast Algorithm for Finding the Moduli Space

Here we introduce a practical implementation of the ideas in previous sections leading to an efficient algorithm for the determination of the matroid polytope of a bipartite graph, which was introduced for the first time in [3]. This method stems from the realization that the projection from the matching to the matroid polytope corresponds to projecting away the gauge degrees of freedom, which are the ones typically associated to internal edges. We remind the reader that the polytope formed by the toric diagram of the moduli space is the matroid polytope *only under gauging 2*.

In fact, for gauging 2, it is only the external edges which define the matroid polytope. In analogy to the matching polytope, this correspondence implies that the matroid polytope is given by a *reduced perfect matching matrix*, with columns given by perfect matchings but rows only associated to external edges. Denoting external edges $X_i^{(e)}$ and perfect matchings p_μ, we have:

$$G_{\text{matroid},i\mu} = \begin{cases} 1 & \text{if} \quad X_i^{(e)} \in p_\mu \\ 0 & \text{if} \quad X_i^{(e)} \notin p_\mu \end{cases} . \tag{2.4.1}$$

From this equation it is clear that to obtain the toric diagram for the moduli space under gauging 2, all we need to do is take the matrix P and discard all rows that do not correspond to external edges. Those perfect matchings which only differ by internal edges will thus be identified.

Example. For the example in Figure 2.8 this is very easy to do: from (2.4.2) we simply extract the final 4 rows, to obtain the matroid polytope

$$G_{\text{matroid}} = \left(\begin{array}{c|cccccccccc} & p_1 & p_2 & p_3 & p_4 & p_5 & p_6 & p_7 & p_8 & p_9 & p_{10} \\ \hline X_{3,6} & 0 & 0 & 0 & 1 & 1 & 0 & 1 & 0 & 1 & 0 \\ X_{4,5} & 0 & 1 & 0 & 1 & 0 & 0 & 0 & 0 & 1 & 1 \\ X_{4,3} & 0 & 1 & 1 & 0 & 0 & 0 & 0 & 0 & 1 & 1 \\ X_{5,6} & 0 & 0 & 1 & 0 & 1 & 0 & 1 & 0 & 1 & 0 \end{array}\right). \tag{2.4.2}$$

This can be row-reduced to the form

$$G_{\text{matroid}} = \left(\begin{array}{ccc|ccc|cc|c} p_1 & p_6 & p_8 & p_2 & p_{10} & p_3 & p_4 & p_5 & p_7 & p_9 \\ \hline 0 & 0 & 0 & 1 & 1 & 0 & 0 & -1 & -1 & 0 \\ 0 & 0 & 0 & 0 & 0 & 1 & 0 & 1 & 1 & 1 \\ 0 & 0 & 0 & 0 & 0 & 0 & 1 & 1 & 1 & 1 \end{array}\right) \tag{2.4.3}$$

which is indeed identical to (2.4.6), as required. This example illustrates that on the disk gauging 1 and gauging 2 are equivalent.

2.5 Loop Variables

In this section we begin by introducing canonical variables capturing the degrees of freedom of arbitrary graphs in the most succinct way possible. Associating variables to faces has huge advantages in relating a subclass of BFTs to integrable systems, as elucidated in Chapter 3, as well as understanding the structure of scattering amplitudes, as discussed in Chapters 4 and 6. Intrinsically, graphs have no notion of faces; they only arise after we have specified an embedding for the graph. The variables we will now present should be seen as a generalization of the face variables for planar graphs, and are valid for arbitrary graphs on arbitrary Riemann surfaces. They constitute an important step towards a unified understanding of non-planar scattering amplitudes, as well as provide an alternative route to the master and moduli spaces we have introduced above. This section is mostly based on the ideas in [1] where the generalized face variables were first introduced; related ideas which emphasize slightly different aspects can be found in [35].

The first step in the construction of the face variables is to embed the graph into a (possibly bordered) Riemann surface. Once this is done, we can associate to the

diagram F faces, B boundaries and a genus g. These ingredients are sufficient to construct the basis, as follows:

- **Faces:** A variable f_i, $i = 1, \ldots, F$, is introduced for every path going clockwise around a face, either internal or external. Faces are expressed as products of oriented edge weights as described in §2.3.2. Face variables satisfy

$$\prod_{i=1}^{F} f_i = 1.$$

  Hence, one of the face variables can always be expressed in terms of the others. For graphs with boundaries, which are the relevant ones for scattering, a useful convention is to discard one of the external faces.

- **Paths between boundaries:** For $B \geq 1$, it is necessary to introduce $B - 1$ paths, which we call b_a, $a = 1, \ldots, B-1$, stretching between different boundary components. The particular choice of these $B - 1$ paths is unimportant.

- **Fundamental cycles:** For genus g we need to consider α_ν and β_ν pairs of variables, $\nu = 1, \ldots g$, associated to the fundamental cycles in the underlying Riemann surface.

The paths b_a, α_ν and β_ν are expressed as products of oriented edge weights in the same way as for f_i.

For brevity, in what follows we will commonly refer to all the above paths as face variables.

2.5.1 Master Space from Flows

As for perfect matchings, every flow $\mathfrak{p}_\mu$ maps to a point in the matching polytope. To translate perfect matchings into flows, we need to first pick a perfect orientation using a reference matching p_{ref} and study all flows $\mathfrak{p}_\mu = \tilde{p}_\mu / \tilde{p}_{\text{ref}}$. Alternative choices of p_{ref} lead to trivial modifications of the polytopes. Flows can be fully specified by expanding them in terms of the face variables described above. The coordinate for $\mathfrak{p}_\mu$ in the matching polytope is then simply given by the vector of powers of the face

variables required to specify $\mathfrak{p}_\mu$ [1]:

$$\begin{aligned}\mathfrak{p}_\mu &= \prod_{i=1}^{F-1} f_i^{x_{i,\mu}} \prod_{j=1}^{B-1} b_j^{y_{j,\mu}} \prod_{k=1}^{g} \alpha_k^{z_{k,\mu}} \beta_k^{w_{k,\mu}} \\ &\longmapsto \underline{\text{Coordinate in Matching Polytope}} : \\ &\qquad (x_{1,\mu}, \ldots, x_{F-1,\mu}, y_{1,\mu}, \ldots, y_{B-1,\mu}, z_{1,\mu}, \ldots, z_{g,\mu}, w_{1,\mu}, \ldots, w_{g,\mu})\end{aligned} \tag{2.5.1}$$

As already noted above, the face variables are the most succint way of containing all degrees of freedom of the graph. This is reflected in the fact that the dimension of the matching polytope is the number of independent face variables [1], i.e.

$$\begin{aligned} B \neq 0 : &\qquad d_{\text{matching}} = F + B + 2g - 2 \\ B = 0 : &\qquad d_{\text{matching}} = F + 2g - 1 \end{aligned} \tag{2.5.2}$$

where we have distinguished the cases with and without boundaries. Because of the Calabi-Yau condition, the matching polytope lives in one dimension lower than the master space, hence

$$\begin{aligned} B \neq 0 : &\qquad d_{\text{master}} = F + B + 2g - 1 \\ B = 0 : &\qquad d_{\text{master}} = F + 2g \quad . \end{aligned} \tag{2.5.3}$$

Since every flow has a unique description in terms of face variables it will be mapped to a unique point in the matching polytope.

We will make ample use of flows when we construct a map between bipartite graphs and the Grassmannian in Chapter 4.

Example. Let us return to our example in Figure 2.8. There we have 6 faces, 5 of which are independent, and no paths b_a, α_ν or β_ν. The faces are written as

$$f_1 = \frac{\alpha_{2,1}\alpha_{6,1}}{\alpha_{1,3}\alpha_{1,5}} \quad f_2 = \frac{\alpha_{3,2}\alpha_{5,2}}{\alpha_{2,1}\alpha_{2,4}} \quad f_3 = \frac{\alpha_{1,3}\alpha_{4,3}}{\alpha_{3,2}\alpha_{3,6}} \quad f_4 = \frac{\alpha_{2,4}}{\alpha_{4,3}\alpha_{4,5}} \quad f_5 = \frac{\alpha_{1,5}\alpha_{4,5}}{\alpha_{5,2}\alpha_{5,6}} \ . \tag{2.5.4}$$

If we choose the reference matching $p_{\text{ref}} = p_1$ we obtain the flows

$$\begin{aligned}
\mathfrak{p}_1 &= 1 & \mathfrak{p}_6 &= \frac{\alpha_{2,1}\alpha_{6,1}}{\alpha_{1,3}\alpha_{1,5}} = f_1 \\
\mathfrak{p}_2 &= \frac{\alpha_{4,3}\alpha_{4,5}}{\alpha_{2,4}} = \frac{1}{f_4} & \mathfrak{p}_7 &= \frac{\alpha_{3,2}\alpha_{3,6}\alpha_{5,2}\alpha_{5,6}}{\alpha_{1,3}\alpha_{1,5}\alpha_{2,4}} = \frac{1}{f_3 f_4 f_5} \\
\mathfrak{p}_3 &= \frac{\alpha_{4,3}\alpha_{5,2}\alpha_{5,6}}{\alpha_{1,5}\alpha_{2,4}} = \frac{1}{f_4 f_5} & \mathfrak{p}_8 &= \frac{\alpha_{3,2}\alpha_{5,2}\alpha_{6,1}}{\alpha_{1,3}\alpha_{1,5}\alpha_{2,4}} = f_1 f_2 \\
\mathfrak{p}_4 &= \frac{\alpha_{3,2}\alpha_{3,6}\alpha_{4,5}}{\alpha_{1,3}\alpha_{2,4}} = \frac{1}{f_3 f_4} & \mathfrak{p}_9 &= \frac{\alpha_{2,1}\alpha_{3,6}\alpha_{4,3}\alpha_{4,5}\alpha_{5,6}}{\alpha_{1,3}\alpha_{1,5}\alpha_{2,4}} = \frac{1}{f_2 f_3 f_4^2 f_5} \\
\mathfrak{p}_5 &= \frac{\alpha_{2,1}\alpha_{3,6}\alpha_{5,6}}{\alpha_{1,3}\alpha_{1,5}} = \frac{1}{f_2 f_3 f_4 f_5} & \mathfrak{p}_{10} &= \frac{\alpha_{2,1}\alpha_{4,3}\alpha_{4,5}\alpha_{6,1}}{\alpha_{1,3}\alpha_{1,5}\alpha_{2,4}} = \frac{f_1}{f_4}
\end{aligned} \tag{2.5.5}$$

which translate into the following coordinates for the matching polytope:

$$G_{\text{matching}} = \left(\begin{array}{c|cccccccccc} & \mathfrak{p}_1 & \mathfrak{p}_2 & \mathfrak{p}_3 & \mathfrak{p}_4 & \mathfrak{p}_5 & \mathfrak{p}_6 & \mathfrak{p}_7 & \mathfrak{p}_8 & \mathfrak{p}_9 & \mathfrak{p}_{10} \\ \hline x_1 & 0 & 0 & 0 & 0 & 0 & 1 & 0 & 1 & 0 & 1 \\ x_2 & 0 & 0 & 0 & 0 & -1 & 0 & 0 & 1 & -1 & 0 \\ x_3 & 0 & 0 & 0 & -1 & -1 & 0 & -1 & 0 & -1 & 0 \\ x_4 & 0 & -1 & -1 & -1 & -1 & 0 & -1 & 0 & -2 & -1 \\ x_5 & 0 & 0 & -1 & 0 & -1 & 0 & -1 & 0 & -1 & 0 \end{array}\right) , \tag{2.5.6}$$

where we can easily confirm that the dimension of the matching polytope is indeed 5, as expected from (2.5.2). Translating all coordinates (2.4.3) such that p_1 is at the origin, and row-reducing both (2.4.3) and (2.5.6) will yield identical expressions, thus confirming that the two polytopes are identical.

2.5.2 Moduli Space from Flows

Going from the master to the moduli space will depend on our choice of gauging. We shall treat the two gaugings separately.

Gauging 1. Here the gauge symmetries correspond to internal faces of the graph. The resulting projection simply amounts to dropping the coordinates associated to (independent) internal f_i's. The dimension of the moduli space is then [1]

$$\begin{aligned} B \neq 0: &\qquad d_{\text{moduli}} = F_e + B + 2g - 1 \\ B = 0: &\qquad d_{\text{moduli}} = 2g + 1 \quad , \end{aligned} \tag{2.5.1}$$

where F_e is the number of external faces. Notice that, while all internal faces are independent for $B \neq 0$, only $F - 1$ of them are independent for $B = 0$. Under gauging 1, flows that differ by internal faces will project down to the same point in the moduli space toric diagram.

Example. Returning to our example, the moduli space is simply obtained by ignoring x_1 and x_2, i.e.

$$G_{\text{moduli}} = \left(\begin{array}{c|cccccccccc} & \mathfrak{p}_1 & \mathfrak{p}_2 & \mathfrak{p}_3 & \mathfrak{p}_4 & \mathfrak{p}_5 & \mathfrak{p}_6 & \mathfrak{p}_7 & \mathfrak{p}_8 & \mathfrak{p}_9 & \mathfrak{p}_{10} \\ \hline x_3 & 0 & 0 & 0 & -1 & -1 & 0 & -1 & 0 & -1 & 0 \\ x_4 & 0 & -1 & -1 & -1 & -1 & 0 & -1 & 0 & -2 & -1 \\ x_5 & 0 & 0 & -1 & 0 & -1 & 0 & -1 & 0 & -1 & 0 \end{array}\right) , \tag{2.5.2}$$

which upon row-reduction yields (2.4.6) and (2.4.3), as required.

Gauging 2. Under gauging 2 all internal loops are gauged: all internal faces, fundamental cycles α_ν and β_ν, and any product of external faces which encloses a boundary. As is made clear from the efficient method to determine the matroid polytope in §2.4.3, what specify the coordinates of flows in the matroid polytope are the external edges. Hence,

$$d_{\text{matroid}} = n_e - 1 \quad \Rightarrow \quad d_{\text{moduli}} = n_e \tag{2.5.3}$$

where n_e is the number of external edges. Under this gauging, flows are identified according to which sources and sinks they use [1]. In particular, for graphs without boundaries gauging 2 identifies all flows, i.e. the matroid polytope simply becomes a single point.

2.5.3 Moduli Space from Source Sets

A corollary of the above is that we may construct the matroid polytope from the source sets of the perfect orientations. Indeed, this is the definition of the matroid polytope, which can be encoded in the matrix S as follows: denoting the external edges by $X_i^{(e)}$ and the source sets of the perfect orientations by s_μ, we have

$$S_{i\mu} = \begin{cases} 1 & \text{if} \quad X_i^{(e)} \in s_\mu \\ 0 & \text{if} \quad X_i^{(e)} \notin s_\mu \end{cases} \tag{2.5.1}$$

where i runs over the external edges and μ runs over the source sets of the various perfect orientations.

Example. Using again the example in Figure 2.8, we have the source sets encoded in $S_{i\mu}$ as follows:

$$S = \left(\begin{array}{c|cccccccccc} & p_1 & p_2 & p_3 & p_4 & p_5 & p_6 & p_7 & p_8 & p_9 & p_{10} \\ \hline 1 & 1 & 1 & 1 & 0 & 0 & 1 & 0 & 1 & 0 & 1 \\ 2 & 1 & 0 & 0 & 1 & 1 & 1 & 1 & 1 & 0 & 0 \\ 3 & 0 & 1 & 0 & 1 & 0 & 0 & 0 & 0 & 1 & 1 \\ 4 & 0 & 0 & 1 & 0 & 1 & 0 & 1 & 0 & 1 & 0 \end{array}\right), \tag{2.5.2}$$

where the row-numbering refers to the black labels in Figure 2.8 and denotes the source set for the perfect orientation associated to p_μ. It is easy to check that this is indeed the same polytope as the one in (2.4.6), (2.4.3) and (2.5.2).

2.6 BFT Perspective on Graph Equivalence and Reduction

Based on the BFT interpretation of graphs it is possible to introduce a natural notion of *graph equivalence*. We say that:

Two graphs are equivalent iff
the corresponding BFTs have the same moduli space.

Of course the equivalence classes resulting from this definition depend on the specific gauging under consideration. This definition was already advocated in [10], after noting that the moduli space is a natural geometric object that remains invariant under certain class of moves and reductions that are reviewed in §2.6.1 and §2.6.2.

On-shell diagrams for scattering amplitudes in $\mathcal{N} = 4$ play an important role when thinking about applications of BFTs. In this context, one needs to consider gauging 2. Two on-shell diagrams are considered equivalent if they parametrize the same region of the Grassmannian. As we shall see in Chapter 4, for graphs on a disk the BFT definition of graph equivalence is completely equivalent to the definition of equivalence for on-shell diagrams. For non-planar diagrams, the BFT definition remains a necessary condition, and can be augmented by an additional condition involving the linear dependences of points in the matching polytope.

Often we encounter situations where two diagrams are equivalent despite appearing drastically different in complexity. This leads us to the notion of *reduced* graphs: a graph is reduced if its matching polytope has the smallest possible dimension within a given equivalence class. Expressed differently, a graph is reduced if it has the minimum number of loops. From a BFT point of view, a reduced graph has the minimal gauge symmetry. Reduced graphs in a given equivalence class are not unique, since they are defined up to equivalence moves. Reduced graphs are of

particular interest. For example, they play a central role in the context of scattering, giving the simplest expressions for the integrand [34].

There are two natural questions that arise in connection with graph equivalence and reducibility:

- How can one identify efficiently whether two graphs are equivalent?
- How can one determine whether the graph is reduced?

These two questions have elegant answers, which make excellent use of the BFT tool kit, and will be the topic of the next sections.

2.6.1 Equivalence Moves

For BFTs the equivalences of the moduli space can be neatly encoded as simple operations of the graph. Figure 2.10 shows two basic transformations that can be applied to arbitrary bipartite graphs on arbitrary surfaces, which preserve the moduli space and do not alter the number of face variables. These equivalences are irrespective of gauging, as their field-theoretic interpretations makes clear. Here we summarize a more detailed discussion, which can be found in [10, 14]:

(a) Integrating out massive fields, which appear in the graph as bivalent nodes. This equivalence move is also known as the merge-expand move, and can be performed in either direction, since the moduli space will not depend on these massive fields. If the bivalent node is attached to an external edge, we simply turn both edges into a single external edge.

(b) Seiberg duality [7, 99, 100, 102–105] on an $N_f = 2N_c$ gauge group. This transformation is also known as a square move, urban renewal, or spider move. Let us emphasize that this rule correctly describes Seiberg duality even for faces adjacent to external ones; there is no limitation of any sort in the type of $N_f = 2N_c$ gauge groups that can be dualized.

Seiberg duality requires the theory to be non-Abelian, i.e. to have $N > 1$. In any case, the square move preserves the moduli space of the BFT even

for $N = 1$ and hence leads to equivalent graphs. Turning this around, the coincidence of the Abelian moduli space of two BFTs is a necessary condition for the corresponding non-Abelian theories to be related by Seiberg duality.

For BFT_2's, the operation in Figure 2.10(b) can actually be performed on any closed loop involving four edges in the graph.

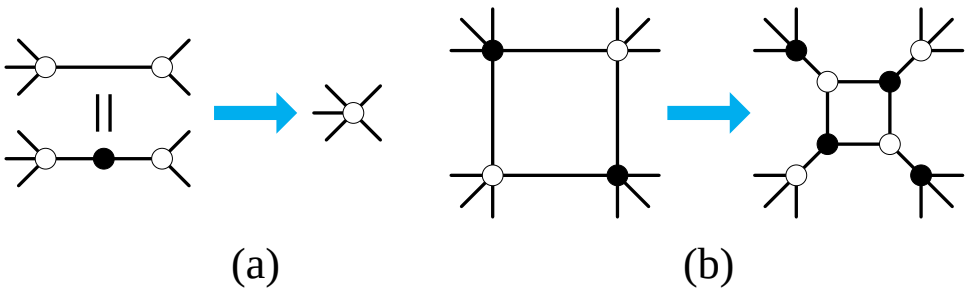

Figure 2.10: Graphical equivalences of bipartite graphs. They correspond to: (a) integrating out massive fields, and (b) Seiberg duality on an $N_f = 2N_c$ gauge group.

It is an amazing result that on-shell diagrams in scattering amplitudes have precisely the same equivalences as those shown in Figure 2.10; we shall return to this in Chapter 4.

2.6.2 Reductions

There are also operations which decrease the number of loops, and hence can be used to reduce graphs. These operations leave the moduli space intact, but decrease the dimension of the master space. These operations are illustrated in Figure 2.11, whose interpretation is found in [10, 14] and summarized here:

(c) Confinement of an $N_f = N_c$ gauge group, staying on a branch of moduli space on which mesons do not get expectation values. This operation is often called a bubble reduction.

Again, since we restrict ourselves to Abelian theories, the coincidence of the Abelian moduli space is a necessary condition for the interpretation of confinement in the non-Abelian theory.

(d) Higgsing a bifundamental field [106], by turning on a vev for that scalar. This corresponds to the deletion of that edge, which merges two faces into a single larger face.

We note that (c) can be seen as a subclass of (d), and we shall therefore restrict ourselves to only discussing (d), which is more general.

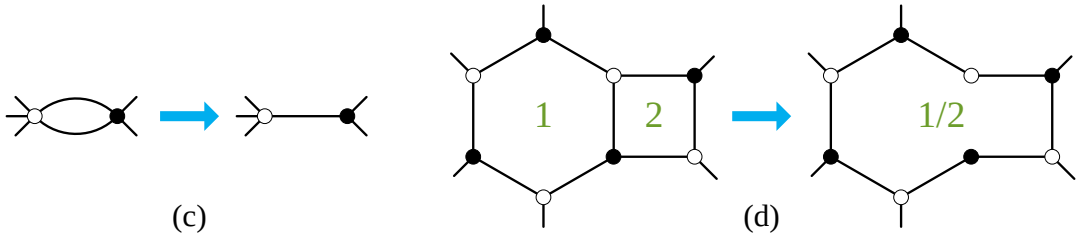

Figure 2.11: Reductions of the graph: (c) corresponds to confinement, (d) corresponds to Higgsing, i.e. to turning on a vev for a bifundamental scalar, resulting in the merging of two faces.

Only the removal of internal edges may preserve the moduli space. The possibility of reducing graphs by removing edges was first discovered and investigated in the language of leading singularities in scattering amplitudes [34].

Deleting an edge associated to the field X_i will force the elimination of all perfect matchings which utilized that edge, i.e. of all perfect matchings p_μ with $P_{i\mu} = 1$. We can declare the moduli space to be invariant if, after the reduction, there is at least one perfect matching for every point in the original toric diagram of the moduli space, i.e. if the toric diagram for the moduli space remains intact. If on the other hand we have killed perfect matchings such that some point in the moduli space no longer exists, because we have killed all perfect matchings which contributed to that point, the operation is not considered a reduction of the original graph.

It's important to emphasize that in the context of scattering amplitudes, operations (a) and (b) always produce equivalent on-shell diagrams, but the invariance under more general edge removals (d) requires both the invariance of the matroid polytope, as well as an additional condition on the linear dependences of points in the matching polytope. We shall return to this point in Chapters 4 and 6.

One can scan over all edges of the graph and individually determine whether their removal constitutes a reduction. Iterating this process, it is possible to determine all combinations of edges that can be simultaneously removed. Reduced graphs are reached when deleting edges without eliminating points in the toric diagram is no longer feasible.

The procedure outlined above makes it possible to identify all combinations of vevs that produce reduced graphs. Some of these sets of vevs can lead to different reduced graphs. Whenever this happens, the original graph has multiple reductions. In the language of scattering amplitudes, this phenomenon is a manifestation of having multiple leading singularities. An attractive feature of the BFT approach is that multiple reductions can be systematically identified.

Example. Let us verify that the equivalence moves and reductions shown above preserve the moduli space. We will again use the example in Figure 2.8, whose toric diagram for the moduli space is given by (2.4.2).[11] The operations we will perform are shown in Figure 2.12, which were first presented in [10].

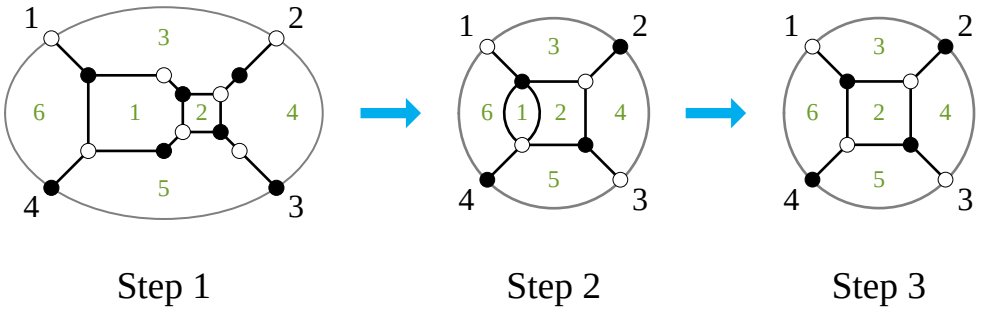

Figure 2.12: A reduction of the example in Figure 2.8.

Step 1: Here we have performed a square move on face 2. The resulting graph has 9 perfect matchings, which we denote q_μ. Following §2.4.3, we obtain the moduli

[11] Strictly speaking, (2.4.2) gives its matroid polytope; the moduli space is at unit distance from the origin.

space

$$G_{\text{matroid}} = \left(\begin{array}{c|c|c|c|c|c|c|c|c} q_1 & q_2 & q_4 & q_3 & q_5 & q_6 & q_8 & q_7 & q_9 \\ \hline 1 & 0 & 0 & 1 & 0 & 0 & 0 & 1 & 0 \\ 1 & 0 & 0 & 0 & 1 & 1 & 1 & 1 & 0 \\ 0 & 0 & 0 & 0 & 1 & 1 & 1 & 1 & 1 \\ 0 & 0 & 0 & 1 & 0 & 0 & 0 & 1 & 1 \end{array}\right), \tag{2.6.1}$$

which is indeed equivalent to that of (2.4.2), modulo multiplicities of the lattice points.

Step 2: This step consists of integrating out the massive fields, as shown in Figure 2.10(a). The graph still has 9 perfect matchings, denoted r_μ. The moduli space is now

$$G_{\text{matroid}} = \left(\begin{array}{c|c|c|c|c|c|c|c|c} r_1 & r_8 & r_9 & r_2 & r_3 & r_4 & r_5 & r_6 & r_7 \\ \hline 0 & 0 & 0 & 1 & 0 & 1 & 0 & 0 & 1 \\ 0 & 0 & 0 & 1 & 0 & 1 & 1 & 1 & 0 \\ 0 & 0 & 0 & 0 & 1 & 1 & 1 & 1 & 0 \\ 0 & 0 & 0 & 0 & 1 & 1 & 0 & 0 & 1 \end{array}\right), \tag{2.6.2}$$

which can again be seen to not have changed.

Step 3: The final step is in performing a bubble reduction on face 1. We obtain a diagram often referred to as the square box, whose seven perfect matchings p_μ are illustrated in Figure 2.3. The moduli space is given by

$$G_{\text{matroid}} = \left(\begin{array}{c|c|c|c|c|c|c} p_1 & p_2 & p_3 & p_4 & p_5 & p_6 & p_7 \\ \hline 1 & 0 & 1 & 1 & 0 & 0 & 0 \\ 1 & 1 & 0 & 1 & 0 & 0 & 0 \\ 1 & 1 & 0 & 0 & 1 & 0 & 0 \\ 1 & 0 & 1 & 0 & 1 & 0 & 0 \end{array}\right), \tag{2.6.3}$$

which, again, has not changed.

Finding the reduction for this example was rather laborious: it required us to perform two equivalence moves, and finally a bubble reduction. In the next section we will construct an efficient way for finding the Higgsing that corresponds to this reduction, thus circumventing the need for all intermediate steps. The tools presented there will also enable us to confirm that Step 3 has brought us to a *reduced* diagram, and hence the simplest possible diagram for this moduli space.

2.6.3 An Efficient Approach to Reducibility

Determining whether a bipartite graph is reduced is an important question for various applications. For planar graphs, there is a combinatorial diagnostic for reducibility based on zig-zag paths (see e.g. [34] and references therein). Determining zig-zags and their properties can however be rather impractical. Furthermore, whether and how this method generalizes to non-planar graphs is currently unknown. In this section we introduce an alternative test for reducibility, which first appeared in [3], with two salient features: it is straightforward to implement and it applies to both planar and non-planar BFTs. Non-planar scattering amplitudes are also subject to an additional condition, as we shall explain in Chapters 4 and 6.

It is by now clear that the matroid polytope is the central player for determining graph equivalence and hence reducibility. As already discussed in §2.6.2, to check the full reducibility we would need to attempt to Higgs every internal edge, each time removing those perfect matchings which utilized the edge in question, and check whether the multiplicity of any point in the matroid polytope becomes zero.

For gauging 2, where the matroid polytope is quickly obtained using the procedure in §2.4.3, there is an extremely efficient matrix implementation to determine reducibility, which tells us which edges may be removed without having to try them all out.

The procedure begins with the perfect matching matrix P, in terms of which the effects of edge removal are very transparent. We now define a new matrix $\mathscr{P}$, by multiplying the entries of P associated to each point π_α in the matroid polytope (which may or may not have higher multiplicity than one) as follows:

$$\mathscr{P}_{i\alpha} \equiv \prod_{p_\mu \in \pi_\alpha} P_{i\mu} \ . \tag{2.6.1}$$

This results in a new $E \times n_p$ matrix $\mathscr{P}$, where E is the number of edges, as it is for P, and n_p is the number of distinct points in the matroid polytope.

A vanishing entry $\mathscr{P}_{i\alpha} = 0$ implies that the removal of the edge X_i preserves the point α in the matroid polytope, albeit not necessarily its multiplicity. Similarly, $\mathscr{P}_{i\alpha} = 1$ signifies that the removal of X_i kills all perfect matchings at point π_α.

The construction of $\mathscr{P}$ is very efficient given P and immediately displays the reducibility of a graph: if $\mathscr{P}$ has a row of zeroes, the graph is reducible since it is possible to remove the corresponding edge while preserving all points in the matroid polytope.

Example. Let us illustrate this construction for the example in Figure 2.8. We reorder the columns of the perfect matching matrix in (2.4.2), grouping together those columns which project down to the same point in the matroid polytope:

$$P = \left(\begin{array}{c|ccc|cc|c|c|cc|c} & \pi_1 & & & \pi_2 & & \pi_3 & \pi_4 & \pi_5 & & \pi_6 \\ & p_1 & p_6 & p_8 & p_2 & p_{10} & p_3 & p_4 & p_5 & p_7 & p_9 \\ \hline X_{1,3} & 1 & 0 & 0 & 1 & 0 & 1 & 0 & 0 & 0 & 0 \\ X_{1,5} & 1 & 0 & 0 & 1 & 0 & 0 & 1 & 0 & 0 & 0 \\ X_{2,4} & 1 & 1 & 0 & 0 & 0 & 0 & 0 & 1 & 0 & 0 \\ X_{3,2} & 0 & 0 & 1 & 0 & 0 & 0 & 1 & 0 & 1 & 0 \\ X_{2,1} & 0 & 1 & 0 & 0 & 1 & 0 & 0 & 1 & 0 & 1 \\ X_{5,2} & 0 & 0 & 1 & 0 & 0 & 1 & 0 & 0 & 1 & 0 \\ X_{6,1} & 0 & 1 & 1 & 0 & 1 & 0 & 0 & 0 & 0 & 0 \\ \hline X_{3,6} & 0 & 0 & 0 & 0 & 0 & 0 & 1 & 1 & 1 & 1 \\ X_{4,5} & 0 & 0 & 0 & 1 & 1 & 0 & 1 & 0 & 0 & 1 \\ X_{4,3} & 0 & 0 & 0 & 1 & 1 & 1 & 0 & 0 & 0 & 1 \\ X_{5,6} & 0 & 0 & 0 & 0 & 0 & 1 & 0 & 1 & 1 & 1 \end{array}\right). \tag{2.6.2}$$

The horizontal line separates the internal edges from the external ones.[12]

We now construct the matrix $\mathscr{P}$, as dictated by (2.6.1):

$$\mathscr{P} = \left(\begin{array}{c|cccccc} & \pi_1 & \pi_2 & \pi_3 & \pi_4 & \pi_5 & \pi_6 \\ \hline X_{1,3} & 0 & 0 & 1 & 0 & 0 & 0 \\ X_{1,5} & 0 & 0 & 0 & 1 & 0 & 0 \\ X_{2,4} & 0 & 0 & 0 & 0 & 0 & 0 \\ X_{3,2} & 0 & 0 & 0 & 1 & 0 & 0 \\ X_{2,1} & 0 & 0 & 0 & 0 & 0 & 1 \\ X_{5,2} & 0 & 0 & 1 & 0 & 0 & 0 \\ X_{6,1} & 0 & 0 & 0 & 0 & 0 & 0 \\ \hline X_{3,6} & 0 & 0 & 0 & 1 & 1 & 1 \\ X_{4,5} & 0 & 1 & 0 & 1 & 0 & 1 \\ X_{4,3} & 0 & 1 & 1 & 0 & 0 & 1 \\ X_{5,6} & 0 & 0 & 1 & 0 & 1 & 1 \end{array}\right). \tag{2.6.3}$$

[12]This organization of rows and columns in P is not obligatory, but it is convenient for simplifying our analysis.

This matrix contains rows of zeroes, so we conclude the graph is reducible: $X_{2,4}$ or $X_{6,1}$ can be removed without eliminating points from the matroid polytope. As can be verified by Figure 2.8, the removal of either of these edges will yield the square box in Step 3 of Figure 2.12, after the trivial operation described in §2.6.1 (a).

Removable edges. Finally, we remark that $\mathscr{P}$ is also useful for finding those edges which, in the language of [34], are *removable edges*. Removable edges are defined as those which, starting from a reduced graph, yield a reduced graph after being removed.[13] In order to identify removable edges, we first generate a new perfect matching matrix P' from P, by removing the putative removable edge k and every column μ for which $P_{k\mu} = 1$. Next, we construct the corresponding $\mathscr{P}'$ matrix. Removable edges are those whose $\mathscr{P}'$ does not display reducibility.

2.7 Conclusions

This chapter carried out a comprehensive study of BFTs, considerably extending the understanding of these theories in various directions. We recognized that there are two natural ways of assigning gauge symmetries to BFTs, which implies that in fact there are two classes of gauge theories that can be associated to bipartite graphs. BFT_1's require specifying an embedding of the graph into a Riemann surface for their definition, while BFT_2's do not need a Riemann surface at all. The two classes of theories are interesting in their own right and find applications in different contexts. For example, a subclass of BFT_1's arises on D3-branes over toric CY 3-folds, while BFT_2's are related to scattering amplitudes.

Several alternative approaches for connecting BFTs and the toric CYs that correspond to their master and moduli spaces were discussed. For planar BFTs, this perspective allowed us to identify the toric diagram of the master and moduli spaces

[13] It is important not to confuse these edges with the ones discussed so far, i.e. those edges which constitute a reduction: removing the edges highlighted by $\mathscr{P}$ could produce a graph which may be subject to further reductions, and hence isn't reduced. Also, removable edges exist on graphs which are already reduced.

with the matching and matroid polytopes, respectively. The vast array of tools needed to perform these calculations was introduced.

We next investigated an array of graph transformations, interpreted as integration of massive fields, Seiberg duality, confinement, and reduction by Higgsing. We introduced detailed and efficient procedures for determining the equivalence between two theories as well as their reductions.

Notably, this thesis will leave out the investigation of the string theory embedding of BFTs, which was elucidated in [13].

Our work suggests several directions for future investigation of BFTs, regarding their properties and applications. It is also desirable to understand the physical origin of the connections between the different contexts in which BFTs appear. Below we collect some interesting open questions and thoughts on how to address them.

- *Superconformal Invariance:* It is interesting to investigate whether, and under which conditions, BFTs give rise to superconformal fixed points. In the case of BFT_1's, it is indeed possible to map the R-charges of fields to angles in the isoradial or rhombus embeddings of the graph [18, 107, 108].[14] In such embeddings, the vanishing of individual beta functions for gauge and superpotential couplings translates into zero local curvature. For BFT_1's it thus becomes natural to expect CFTs whenever the embedded graph has vanishing curvature everywhere.

  It would also be interesting to revisit the question of conformal invariance while allowing different ranks for gauge and global symmetry groups.

- *Gauge Theory and Reducibility:* From a BFT viewpoint, the reduction of degrees of freedom associated to graph reductions is strongly reminiscent of an RG flow. It would be interesting to determine whether this connection is indeed true. If so, it would provide an alternative perspective on reduced graphs, which would be mapped to fixed points of the RG flow.

[14] BFT_2's are independent of a Riemann surface embedding and hence there is no simple graphical translation of R-charges and beta functions.

- *Detailed Investigation of Non-Abelian BFTs:* The Abelian version of BFTs is sufficient for certain applications, such as scattering amplitudes, and also captures some features, like the connection by moves and bubble reductions, that are also present for non-Abelian theories. Having said that, it is extremely interesting to perform a more detailed study of non-Abelian BFTs. We envision that powerful tools such as Hilbert series [92–95] and the superconformal index [109–111] can provide an interesting window into the dynamics of the general theories.

Chapter 3

Towards the Continuous Limit of Cluster Integrable Systems

As mentioned in Chapter 2, a subclass of BFT_1's known as *dimer models* are defined by bipartite tilings of the torus without boundaries, and have played an important role in the creation of infinite classes of AdS/CFT duals. In this chapter we will show how dimer models are connected to a (0+1)-dimensional integrable system, and how to utilize this connection to construct integrable systems of infinite size, paving the way for generating continuous (1+1)-dimensional integrable field theories.

3.1 Newton Polynomial and Toric Diagrams

Let us begin by applying some of the technology of Chapter 2 to study the generic structure of the moduli space of dimer models. We start by recalling that the relevant gauging for dimer models is gauging 1, i.e. the one for which only internal faces are gauged. We shall primarily be interested in expressing the moduli space using the loop variables from §2.5, as these variables play an important role in the associated integrable system [31,33], as will be clear presently. Dimer models require face variables f_i, and the fundamental cycles of the torus α and β. Recall that every flow is expressed as a product of these variables (only $F-1$ faces are required). Since all faces are gauge groups here, the coordinate in the moduli space toric diagram associated to $\mathfrak{p}_\mu$ is simply read off from the powers of α and β required to express the

flow. This information is neatly captured by the so-called *Newton or characteristic polynomial*

$$P_N(\alpha,\beta) = \sum_\mu \mathfrak{p}_\mu = \sum_\mu c_\mu \, \alpha^{v_1^{(\mu)}} \beta^{v_2^{(\mu)}} \ , \tag{3.1.1}$$

which will play in an important role in this chapter. The points in the toric diagram of the moduli space are simply given by the set of different powers $\{(v_1^{(\mu)}, v_2^{(\mu)})\}$. The coefficients c_μ are simply products of face variables f_i.

We see that the toric diagram is specified by 2-dimensional lattice points; these will often be shown pictorially in this chapter. As we shall see, the shape of the toric diagram is intimately related to the spectral curve of the associated integrable system, and will be of great importance in our analysis. Furthermore, points in the toric diagram (which are constituted by perfect matchings) are related to conserved charges of the integrable system.[1]

In this chapter we shall only be interested in the moduli space toric diagram, rather than that of the master space; any mention of the toric diagram implicitly refers to the 2-dimensional object just described.

3.2 Dimer Models and Cluster Integrable Systems

A remarkable correspondence linking dimer models to an infinite class of integrable systems, denoted *cluster integrable systems*, was recently introduced in [33]. We now provide a brief review of the correspondence.

The Poisson manifold of the integrable system is parametrized by oriented loops on the dimer tiling. The face variables f_i, α and β are the natural variables of the cluster integrable system. Their Poisson brackets are given by

$$\{f_i, f_j\} = \epsilon_{f_i,f_j} \, f_i f_j \quad , \quad \{\alpha,\beta\} = 1 + \epsilon_{\alpha,\beta} \quad , \quad \{\alpha, f_i\} = \epsilon_{\alpha,f_i} \quad , \quad \{\beta, f_i\} = \epsilon_{\beta,f_i} \tag{3.2.1}$$

[1] From a gauge theory perspective, these points are also related to mesonic and baryonic symmetries in the theory. While this is a very interesting topic, its review falls beyond the scope of this thesis; the interested reader is referred to [18] for an excellent presentation of these ideas.

where $\epsilon_{x,y}$ is the number of edges on which the x and y loops overlap, with orientation. Then, ϵ_{f_i,f_j} is simply the antisymmetric oriented adjacency matrix that counts the number of arrows between gauge groups in the quiver dual to the dimer tiling.

The integrable system can be quantized replacing the Poisson brackets by a q-deformed algebra, which takes the form

$$X_i X_j = q^{n_{ij}} X_j X_i \,, \tag{3.2.2}$$

where $X_i = e^{x_i}$, q is a complex number with $|q| = 1$ and $n_{ij} = \{x_i, x_j\}/(x_i x_j)$.

In [33], it was shown that the commutators defined by (3.2.2) and (3.2.1) give rise to a (0+1)-dimensional quantum integrable system, whose conserved charges are:

- **Casimirs:** they commute with everything and are given by the ratio between contributions associated to consecutive points on the boundary of the toric diagram.
- **Hamiltonians:** they commute with each other and correspond to the internal points in the toric diagram.

The toric diagram of the Calabi-Yau 3-fold associated to the dimer model gives rise to a Riemann surface of genus equaling to the number of internal points. The equation for this surface is the zero locus of the Newton polynomial:

$$P_N(\alpha, \beta) = 0 \,. \tag{3.2.3}$$

This Riemann surface is indeed the *spectral curve* of the integrable system.

The full Poisson manifold of the integrable system is obtained by gluing different patches via cluster transformations, equivalently Seiberg duality in the associated quiver gauge theories.

3.3 Gluing and Splitting

In this section we discuss the decomposition of a spectral curve into pieces and the reverse procedure of gluing spectral curves. This process also arises in a different

context: the desingularization, or Higgsing, of a Calabi-Yau space. The intimate connection between the decomposition of integrable systems and Higgsing will be the topic of forthcoming sections.

3.3.1 Spectral Curves

Let us consider the splitting process

$$\Sigma \longrightarrow \Sigma_1 + \Sigma_2 \ , \tag{3.3.1}$$

where Σ is the "parent" spectral curve and $\Sigma_{1,2}$ are the two daughters. In this process we elongate certain throats of Σ until it breaks into two pieces. Since the spectral curve is a thickening of the (p, q)-web [37, 112], which is the graph-dual to the toric diagram, the connecting throats are dual to segments joining points of the toric diagram along the boundary between the daughters, as shown in Figure 3.1.

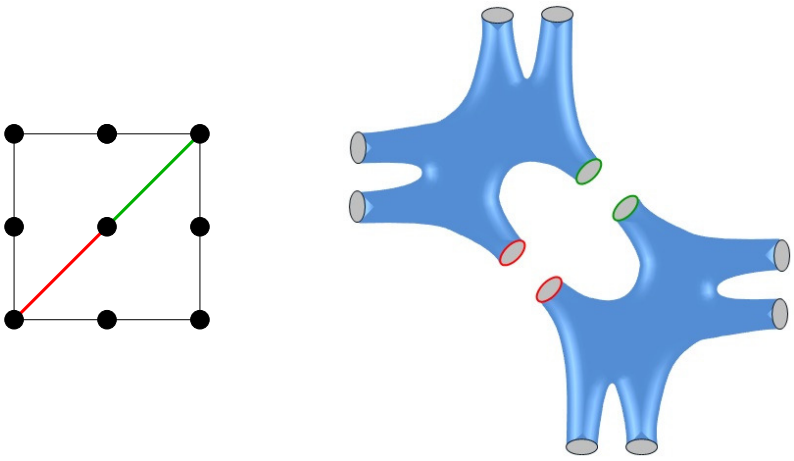

Figure 3.1: A toric diagram split along the red and green lines. This causes the splitting of Σ into two daughters.

The separation between components of the spectral curve is achieved by tuning the coefficients c_μ in the characteristic polynomial (3.1.1). In the limit of large distance between components, the c_i's scale differently with respect to the separation and develop a hierarchical structure.

In the limit of infinite separation the splitting of the spectral curve into two pieces is naturally expected to reduce to the sum of the integrable systems associated to

the two components. In §3.4 and §3.5, we provide a detailed explanation of how this intuition is realized.

Taking the splitting process to an extreme we obtain a decomposition of any Riemann surface into a collection of *trinions*, i.e. spheres with three punctures. Any such decomposition is in one-to-one correspondence with triangulations of the toric diagram. Each triangle gives rise to a trinion. Their number is thus equal to twice the area of the toric diagram, which in turn is equal to the number of gauge groups in the associated quiver gauge theory. These decompositions allow us to see the full integrable system continuously emerge from the combination of trivial integrable systems associated to trinions. Figure 3.2 shows a possible triangulation of a toric diagram and its corresponding trinion decomposition.

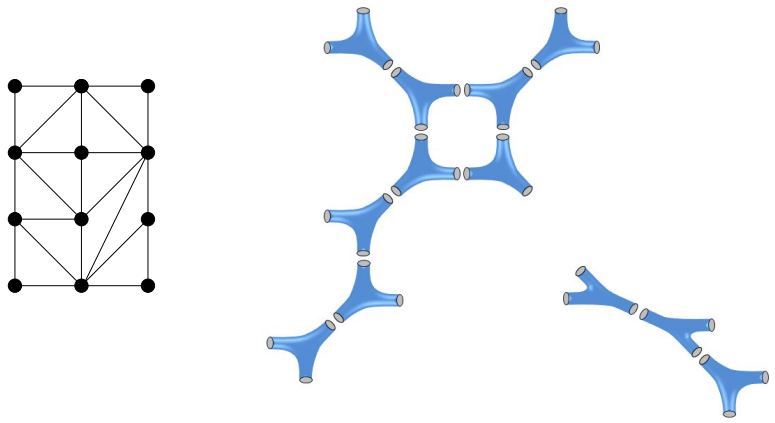

Figure 3.2: A general triangulation of the toric diagram and the corresponding trinion decomposition of the spectral curve.

A standard method in real ("tropical") geometry to visualize Riemann surfaces, which will prove useful in later sections, is the so-called *amœba projection*:

$$\mathcal{A} \ : \ (\alpha, \beta) \mapsto (\log|\alpha|, \log|\beta|) \, . \tag{3.3.2}$$

The amœba can be thought of as a thickening of the graph-dual of the toric diagram, i.e. we can draw the (p, q)-web from D and this will constitute the "spine" of the amœba. In the actual plot, the "tentacles" which tend to infinity will have their directions given by the (p, q)-vectors which are normal to the toric diagram. The

resulting object will look very similar to Σ; explicit examples of this are found in Figure 3.10 and Figure 3.13.

As explained in the introduction, what we ultimately wish to study is the integrable system that emerges in the continuous limit where we glue a countably infinite number of toric sub-diagrams, or equivalently, spectral curves. We conjecture that, depending on how we assemble these building blocks, the integrable systems with an infinite number of degrees of freedom that are generated by this procedure are (1+1)- or (2+1)-dimensional integrable field theories. Figure 3.3 shows a number of elementary spectral curves glued to generate a (1+1)-dimensional theory.

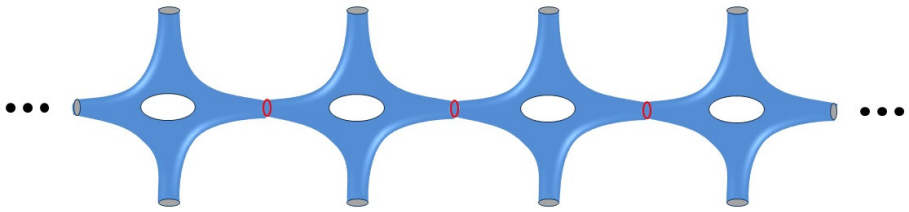

Figure 3.3: Combining an infinite number of elementary spectral curves to generate a (1+1)-dimensional theory. By performing a similar gluing along the vertical direction we expect to generate a (2+1)-dimensional theory.

3.3.2 Partial Resolution of Calabi-Yau Singularities and Higgsing

The splitting and gluing of Riemann surfaces of the type discussed in §3.3.1 also plays an important role in the context of partial resolutions of toric singular Calabi-Yau 3-folds. We now review how to split toric diagrams from geometric, gauge theoretic and dimer model perspectives. In §3.4 we elaborate on the intimate connections with the (de)composition of integrable systems.

Geometrically, the partial resolution of a toric singularity corresponds to the process illustrated in Figure 3.1: one takes the toric diagram and divides it into components.[2] For concreteness, we will focus on the case in which we split the toric

[2]In the dual cone picture of the toric variety, this is the process of stellar division [113].

diagram into two parts, to which we shall refer as the parent with two daughters. It is possible to deal with more components by iteration of this procedure.[3]

Let us now describe the resolution from the perspective of the quiver theory on the worldvolume of D3-brane probes. This is technology dating back to the early days of studying quiver gauge theories from toric Calabi-Yau singularities [100,103,114,115]. The starting point is a set of $N = n_1+n_2$ D3-branes on the parent singularity. All chiral fields in the parent quiver are $(n_1 + n_2) \times (n_1 + n_2)$ matrices. The parent singularity is then resolved into two daughter singularities containing n_1 and n_2 D3-branes, respectively. As a result, we obtain two decoupled quiver gauge theories, whose gauge group ranks are given by n_1 and n_2. From a gauge theory viewpoint, this resolution corresponds to turning on non-zero vacuum expectation values (vevs) for some block sub-matrices in the scalar components of these fields. Fields charged under gauge groups in both quivers have masses controlled by the expectation values and decouple from the low energy theory.

A pictorial representation of this process is given in Figure 3.4. One could envisage, of course, the reverse process of gluing to produce a more singular parent. This should correspond to an un-Higgsing mechanism (q.v. [106]). We will illustrate these ideas with explicit examples in §3.5.

For our purposes, it is sufficient to focus on the simple case in which $n_1 = n_2 = 1$. We focus on diagonal vevs of the form

$$\langle X_{ij} \rangle = \begin{pmatrix} X_{ij}^{(1)} & 0 \\ 0 & X_{ij}^{(2)} \end{pmatrix} , \tag{3.3.1}$$

for the field X_{ij} in the parent theory. We will stick to this case throughout the chapter. Resolutions generally involve turning on several non-zero expectation values simultaneously. We restrict to the case in which all non-zero vevs have the same magnitude, which will turn out to control the distance between the daughter singularities.[4] The acquisition of vevs in this fashion will split the parent theory into its

[3]Not all decompositions can be reduced to a sequence of binary splittings. A necessary condition is that, at each step, the toric diagrams of the daughters are convex.

[4]Theories with different vevs give rise to multiple energy scales. If these scales are hierarchically separated, the Higgsing process can be studied sequentially.

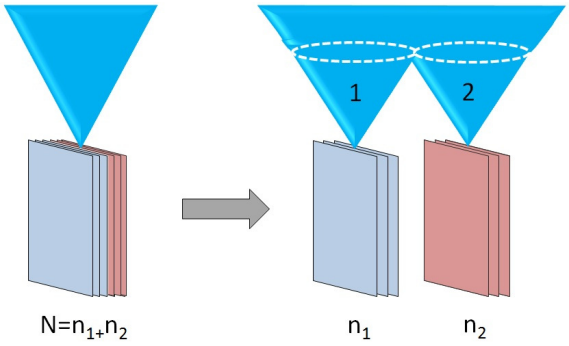

Figure 3.4: The resolution of the parent singularity with parallel coincident $N = n_1 + n_2$ D3-branes (on the left) results in two daughter theories with n_1 and n_2 D3-brane respectively. The blue cone signifies the Calabi-Yau singularity at the tip of which the D3-branes sit.

two daughters.

Resolution in the Dimer Model

One of the greatest computational challenges to the resolution of toric singularities by D3-branes was the identification of which fields in the parent acquire non-zero vevs [100, 103]. This issue was resolved by the dimer model representation of toric quiver gauge theories [15, 16, 19]. Dimer models are extremely useful for identifying the non-zero vevs that are necessary in order to achieve a given resolution. An elegant description of general partial resolutions, exploiting the map between the dimer model and a tiling of the spectral curve, was introduced in [116]. We now briefly review this procedure.

Like perfect matchings, zig-zag paths play a prominent role in connecting dimer models to geometry. They are defined as paths that alternate between turning maximally right and maximally left at consecutive nodes in the bipartite tiling. Each edge, then, has exactly two oppositely oriented zig-zag paths, criss-crossing before heading to nodes of opposite color, weaving an intertwined pattern on the torus. For consistent gauge theories, these zig-zag paths never intersect themselves and form closed loops wrapping (p, q)-cycles on the torus.

The *untwisting map* is an operation on zig-zag paths that exchanges the criss-

cross on the torus, with faces on a different Riemann surface. This Riemann surface turns out to be precisely the spectral curve Σ. Conversely, the zig-zag paths on Σ, when untwisted, are the faces of the original 2-torus. We refer the reader to [19] for a detailed explanation of the untwisting map whose effect on zig-zag paths of both $\mathbb{T}^2$ and Σ is summarized below.

$\mathbb{T}^2$		Σ
zig-zag path	$\leftrightarrow$	face = puncture
face = gauge group	$\leftrightarrow$	zig-zag path

We note that the untwisting map does not change the graph, only the *embedding* of the graph.

Starting from the parent spectral curve Σ, we elongate one or several internal throats that connect the two daughters, Σ_1 and Σ_2. The daughters then decouple in the limit in which these throats become infinitely long. From the viewpoint of the daughters, these throats become new external legs, i.e. new punctures. Following the map above, the appearance of new punctures translates to the appearance of new zig-zag paths on $\mathbb{T}^2$.

This can easily be implemented in terms of dimer tilings. We consider one copy of the original dimer tiling on $\mathbb{T}^2$ for each of the two daughters. On each copy, we draw the zig-zag paths associated to the original punctures that will end up on the corresponding component. Next, we introduce the paths which are the complement to these zig-zag paths in the original set. These new paths correspond to the new punctures that are generated in the splitting process.

In order for the new paths to become actual zig-zag paths, some edges must be removed from the daughter tilings. The bifundamentals on the tiling that do not have any paths running over them are removed. These are precisely the ones that acquire non-zero vevs in the Higgsing. Generally, different edges are removed from the tiling of the first and second daughter. This is the manifestation, in dimer language, of the matrix vevs $X_{ij}^{(1)}$ and $X_{ij}^{(2)}$ in (3.3.1) being different. In §3.5, we present explicit examples illustrating this procedure.[5]

[5]Bivalent nodes might be generated when removing edges. They correspond to massive fields

From the perspective of the daughter integrable systems, the generation of new punctures corresponds to the appearance of new Casimir operators, because each daughter-toric-diagram will have new external legs.

Perfect Matching Perspective. As we recall from §2.6.2, when Higgsing the rule for removing perfect matchings is simple: every perfect matching containing an edge corresponding to a field with a non-zero vev must be eliminated. Since the untwisting map turns the tiling on $\mathbb{T}^2$ into a tiling on Σ, we can gain an alternative understanding of which perfect matchings will survive the Higgsing process on each daughter. The difference between two adjacent perfect matchings in the toric diagram, say p and p', creates a flow on Σ. Once Σ has been split, certain 1-cycles will no longer be able to exist. If the difference between two perfect matchings is contained in any of the sub-dimers, both perfect matchings will survive in the corresponding component of the daughter singularity. On the other hand, if the difference is not contained in any sub-dimer, one or both of the perfect matchings will not survive the Higgsing process.

In general, there are multiple ways of Higgsing fields X_{ij} that will result in the same splitting of $\Sigma \to \Sigma_1 + \Sigma_2$. In §3.5, we will discuss the issue of multiple solutions for an explicit example in detail.

3.4 A Continuous Control Parameter

As we have already mentioned, the splitting of the spectral curve follows from certain hierarchies between the coefficients in the characteristic polynomial. These hierarchies are controlled by a continuous parameter, which we will denote Λ; in quiver language it is connected to the non-zero expectation values of bifundamental fields.

In this section, we introduce two complementary approaches for determining the precise dependence of Λ on the coefficients of $P_N(\alpha, \beta)$ that achieves a given $\Sigma \to \Sigma_1 + \Sigma_2$ decomposition.

---

that can be integrated out [16].

3.4.1 Scalings from VEVs

Without loss of generality, we can identify Λ with the non-zero vevs, i.e. $\langle X_{ij}^{(a)} \rangle = \Lambda$. The coefficients in $P_N(\alpha, \beta)$ are polynomials in the f_i variables, corresponding to closed loops with vanishing homology on the dimer tiling. Recalling §2.5, we can write any loop in terms of oriented edges in the tiling. We can thus obtain the Λ-scaling of any loop from its expression in terms of the product of edge variables. The conclusion is that we obtain the following factors when X_{ij} develops an expectation value $\langle X_{ij} \rangle = \Lambda$:

- Scaling Λ for each $\alpha_{i,j}$ appearing in the numerator of the path, where $\alpha_{i,j}$ is an oriented edge variable.
- Scaling Λ^{-1} for each $\alpha_{i,j}$ appearing in the denominator of the path.

We obtain

$$\begin{array}{rccccc} \underline{\text{for a } f_i \text{ cycle}}: & \Lambda & \text{for each} & \langle X_{ji} \rangle & = & \Lambda \\ & \Lambda^{-1} & \text{for each} & \langle X_{ij} \rangle & = & \Lambda \end{array} \tag{3.4.1}$$

where the subindices indicate gauge groups connected by bifundamentals. We show some examples in Figure 3.5.

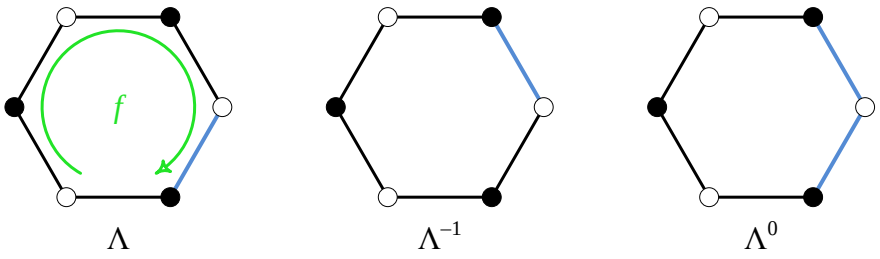

Figure 3.5: Examples of Λ scalings of a f_i cycle. We indicate the edge associated with a field with a non-zero vev in blue.

Notice that we have not specified on which of the two daughter components, which have different sets of non-zero vevs, the scalings in (3.4.1) must be calculated. However, on physical grounds, it is clear that determining the scaling in any of the two daughters leads to the same result. We shall present explicit examples which will illustrate this in §3.5.

3.4.2 Scalings from the Spectral Curve

Let us now introduce an alternative method for determining the Λ scalings directly associated with a decomposition of the spectral curve in an algorithmic fashion, wherein we obtain a set of explicit Diophantine inequalities which needs to be solved. Since it is only the powers of α and β that specify the toric diagram point, we can write (3.1.1) as

$$P_N(\alpha,\beta) = \sum_i \alpha^{v_1^{(i)}} \beta^{v_2^{(i)}} \left(\sum_\mu c_\mu \right) = \sum_i \alpha^{v_1^{(i)}} \beta^{v_2^{(i)}} \left(\sum_\mu \prod_{j=1}^{F-1} f_j^{x_{j,\mu}^{(i)}} \right) \tag{3.4.1}$$

where i ranges over the distinct points in the toric diagram, and μ over those flows that contribute to that specific point. Hence, we see that the i^{th} term's coefficient is expressed as a sum of terms, where each term is a product of faces f_j required to express a given flow $\mathfrak{p}_\mu$.

Now, when we Higgs, the coefficients c_μ separate into two categories: those which belong to flows that survive the Higgsing, which we shall denote $c_\mu^{(s)}$, and those which do not, which we denote $c_\mu^{(h)}$:

$$P_N(\alpha,\beta) = \sum_i \alpha^{v_1^{(i)}} \beta^{v_2^{(i)}} \left(\sum_\mu c_\mu^{(s)} + \sum_\nu c_\nu^{(h)} \right) \tag{3.4.2}$$

where μ and ν range over the appropriate values.

Now, let us introduce the scalings (we can take, without loss of generality, the powers κ_j to be integers):

$$f_j \longrightarrow \Lambda^{\kappa_j} \ , \qquad \kappa_j \in \mathbb{Z} \tag{3.4.3}$$

and substitute back into (3.4.2) to give

$$P_N(\alpha,\beta) = \sum_i \alpha^{v_1^{(i)}} \beta^{v_2^{(i)}} \left(\sum_\mu \Lambda^{\sum_{j=1}^{F-1} \kappa_j x_{j,\mu}^{(i)}} + \sum_\nu \Lambda^{\sum_{j=1}^{F-1} \kappa_j x_{j,\nu}^{(i)}} \right) \ . \tag{3.4.4}$$

It is now clear what has to occur: for the $c_\mu^{(s)}$'s to survive, they must have the same order in Λ; those which do not, must have strictly lower order. In other words, for each i, we must have $\sum_{j=1}^{F-1} \kappa_j x_{j,\mu_1}^{(i)} = \sum_{j=1}^{F-1} \kappa_j x_{j,\mu_2}^{(i)} = \ldots \equiv C$. This C must be strictly greater than each of $\sum_{j=1}^{F-1} \kappa_j x_{j,\nu}^{(i)}$. Finally, we recall that $\prod_{j=1}^{F} f_j = 1$,

so that $\sum_{j=1}^{F} \kappa_j = 0$. Since we know which flows survive a given Higgsing, we can determine a priori which terms must have a relative Λ suppression.

In summary, we have the following set of Diophantine inequalities in κ: for each $i = 1, 2, \ldots, t$ where t is the number of points in the toric diagram,

$$\begin{aligned} C &= \sum_{j=1}^{F-1} \kappa_j x_{j,\mu}^{(i)} \text{ for each } \mathfrak{p}_\mu \text{ that survives} \\ C &> \sum_{j=1}^{F-1} \kappa_j x_{j,\nu}^{(i)} \text{ for each } \mathfrak{p}_\mu \text{ that does not survive} \\ 0 &= \sum_{j=1}^{F} \kappa_j \ . \end{aligned} \tag{3.4.5}$$

3.5 Explicit Examples

Having abstractly discussed how the splitting should work by obtaining the weights of the variables either from the acquisition of vevs in the dimer or from the coefficients in the spectral curve, we can now illustrate our proposal in detail with some explicit examples. In this section, we will first study the cone over the double zeroth Hirzebruch surface, i.e. the "double F_0", and then the space known as $Y^{4,0}$. These will give ample demonstration of our technique.

3.5.1 Double F_0

Let us consider a $\mathbb{Z}_2$ orbifold of F_0, whose toric diagram is shown in Figure 3.7, to which we refer as the double F_0 theory. Figure 3.6 shows the corresponding tiling, where we draw the unit cell of the torus with a dotted line. We see that there are 8 gauge groups, twice that of F_0, and 16 bifundamental fields which we shall denote as X_{ij} in standard nomenclature, signifying the field corresponding to the edge bounding face i and face j in Figure 3.6. The superpotential terms are all quartic and can also be instantly read off from the figure. We wish to consider the decomposition of this geometry into two copies of F_0, as shown in Figure 3.7.

Using the ideas of [116], which were summarized in §3.3.2, we conclude there are four possible sets of expectation values leading to the same desired decomposition

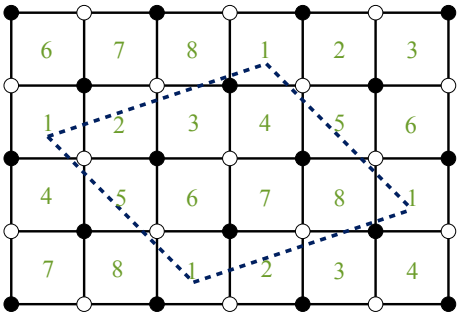

Figure 3.6: Tiling for the double F_0 theory.

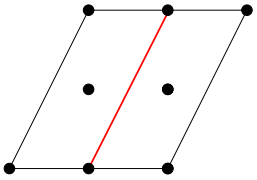

Figure 3.7: Toric diagram for the double F_0. The red line indicates how we split it into two components.

of the geometry. They are:

Higgsing 1:	$X^{(1)}_{41}, X^{(1)}_{12}, X^{(1)}_{85}, X^{(1)}_{56}$ $X^{(2)}_{83}, X^{(2)}_{32}, X^{(2)}_{47}, X^{(2)}_{76}$	**Higgsing 2:**	$X^{(1)}_{34}, X^{(1)}_{41}, X^{(1)}_{78}, X^{(1)}_{85}$ $X^{(2)}_{32}, X^{(2)}_{25}, X^{(2)}_{76}, X^{(2)}_{61}$
Higgsing 3:	$X^{(1)}_{27}, X^{(1)}_{78}, X^{(1)}_{63}, X^{(1)}_{34}$ $X^{(2)}_{25}, X^{(2)}_{54}, X^{(2)}_{61}, X^{(2)}_{18}$	**Higgsing 4:**	$X^{(1)}_{12}, X^{(1)}_{27}, X^{(1)}_{56}, X^{(1)}_{63}$ $X^{(2)}_{18}, X^{(2)}_{83}, X^{(2)}_{54}, X^{(2)}_{47}$

(3.5.1)

In the above we have separated the 8 fields of the parent theory that get a non-zero vev into its two daughters, which following the notation in (3.3.1) we denote by superscripts (1) and (2) respectively. We see that each daughter contains four fields with non-zero vevs. From these non-zero vevs and the rule prescribed in (3.4.1), we

determine the weights of our f_i variables for the four Higgsings:

Higgsing	f_1	f_2	f_3	f_4	f_5	f_6	f_7	f_8
1	1	Λ	1	Λ^{-1}	1	Λ	1	Λ^{-1}
2	Λ	1	Λ^{-1}	1	Λ	1	Λ^{-1}	1
3	1	Λ^{-1}	1	Λ	1	Λ^{-1}	1	Λ
4	Λ^{-1}	1	Λ	1	Λ^{-1}	1	Λ	1

(3.5.2)

What is happening in the field theory, as graphically depicted by the dimer, is shown in Figure 3.8. In each of the four Higgsings, we separate the parent dimer model into the complementary dimers of the two daughters, (1) on the left and (2) on the right. In order to facilitate comparison with the original parent tiling, we have not integrated out massive fields. If we do so, we obtain the square lattice characteristic of F_0.

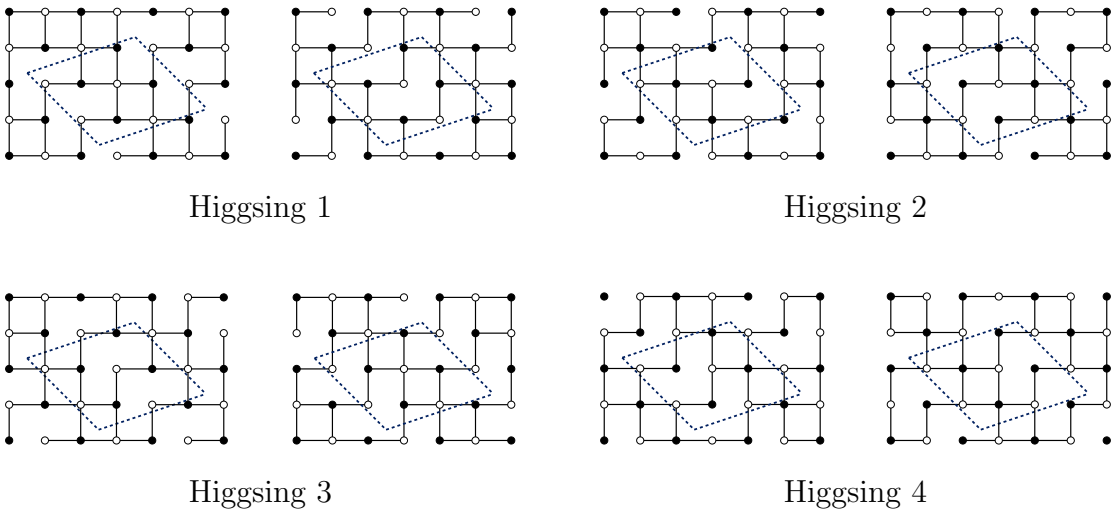

Figure 3.8: Dimer models for the four Higgsings of the double F_0 theory into two daughter F_0 theories.

The weights associated to different Higgsings are simply related by an overall shift, which follows from the fact that the Higgsed tilings are also connected by shifts and rotations as shown in Figure 3.8.

The Integrable System

We now investigate the effect of continuously splitting the spectral curve, equivalently Higgsing, on the integrable system. In this process some contributions to

conserved charges, more specifically the perfect matchings which are removed by the Higgsing, are continuously suppressed until the theory reduces to two decoupled integrable systems.

We can also determine the Λ-scaling of f_i variables by analyzing the behavior of coefficients of the spectral curve. Indeed, we can find the weights in (3.5.2) independently by the procedure outlined in §3.4.2. Reassuringly, the results of using this method agree in all examples with the ones obtained from (3.4.1).

The tables below present the information in the integrable system for the double F_0 theory. The (v_1, v_2) row refers to the coefficient for the $\alpha^{v_1}\beta^{v_2}$ term in the Newton polynomial. For each of the Higgsings, we underline the contributions that survive in the $\Lambda \to \infty$ limit. The third column shows the surviving leading Λ dependence of the coefficients in the characteristic polynomial.

Higgsing 1: Let us begin with Higgsing 1 and discuss it in a little more detail. For each point in the toric diagram, here given as an integer 2-vector, we can specify the coefficient in terms of the f_i variables within the spectral curve using the technique of [31], as reviewed in §3.2. The number of terms will correspond to the number of perfect matchings for the point. Let us take the $(1, 1)$ point of the toric diagram as an example, which is an internal point with 8 perfect matchings; the term in the spectral curve will be

$$\left(f_1 f_3 f_4 + f_3 f_4 + \underline{f_3} + \underline{1} + f_6^{-1} + \underline{f_5^{-1} f_6^{-1} f_8^{-1}} + \underline{f_1 f_2 f_3 f_4} + f_5^{-1} f_6^{-1}\right) \alpha\beta \ ,$$

where we have underlined the terms which survive the Higgsing. The ones that do not survive can be immediately determined: they are the ones containing edges corresponding to fields with non-zero vevs.

In terms of (3.4.5), this means the weights $f_j \to \Lambda^{\kappa_j}$ must be such that $\kappa_3 = 0 = -\kappa_5 - \kappa_6 - \kappa_8 = \kappa_1 + \kappa_2 + \kappa_3 + \kappa_4$ coming from the underlined terms and that they must all be strictly greater than any of $\{\kappa_1+\kappa_2+\kappa_3 \ , \kappa_3+\kappa_4 \ , -\kappa_6 \ , -\kappa_5-\kappa_6\}$ coming from the non-underlined terms. This thus constitutes one of the inequalities. We do this for each of the 8 points in the toric diagram and combine all these relations, supplementing by the inequality that $\sum_{j=1}^{8} \kappa_j = 0$, and solve the resulting system over the integers. We will find precisely the first row of the solution table in (3.5.2). In

the table below, we also include, for reference, the final leading order weight for the surviving terms. For the $(1,1)$ term above, this is just 0, hence the entry $\Lambda^0 = 1$ in the third column. These results are in full agreement with those derived using (3.5.2) and (3.4.1). In the examples that follow, we have independently determined the Λ-scalings using both methods and confirmed their agreement.

(v_1, v_2)	Loops	
$(0,0)$	$\underline{1}$	1
$(1,0)$	$1 + \underline{f_1 f_2 f_5 f_6}$	Λ^2
$(2,0)$	$\underline{f_1 f_2 f_5 f_6}$	Λ^2
$(1,1)$	$f_1 f_3 f_4 + f_3 f_4 + \underline{f_3} + \underline{1} + f_6^{-1}$ $+\underline{f_5^{-1} f_6^{-1} f_8^{-1}} + \underline{f_1 f_2 f_3 f_4} + f_5^{-1} f_6^{-1}$	1
$(2,1)$	$f_1 f_3 + \underline{f_1 f_8^{-1}} + \underline{f_8^{-1}} + f_1 + f_6^{-1} f_8^{-1}$ $+f_6^{-1} f_7^{-1} f_8^{-1} + \underline{f_1 f_2 f_3 f_5} + \underline{f_1 f_2 f_3}$	Λ
$(1,2)$	$\underline{f_3 f_4 f_5^{-1} f_6^{-1}}$	Λ^{-2}
$(2,2)$	$f_1 f_3 f_4 f_6^{-1} + \underline{f_3 f_5^{-1} f_6^{-1} f_8^{-1}}$	1
$(3,2)$	$\underline{f_1 f_3 f_6^{-1} f_8^{-1}}$	1

(3.5.3)

Higgsing 2: We can now perform a similar analysis for the second Higgsing and obtain:

(v_1, v_2)	Loops	
$(0,0)$	$\underline{1}$	1
$(1,0)$	$1 + \underline{f_1 f_2 f_5 f_6}$	Λ^2
$(2,0)$	$\underline{f_1 f_2 f_5 f_6}$	Λ^2
$(1,1)$	$\underline{f_1 f_3 f_4} + f_3 f_4 + f_3 + \underline{1} + \underline{f_6^{-1}}$ $+f_5^{-1} f_6^{-1} f_8^{-1} + \underline{f_1 f_2 f_3 f_4} + f_5^{-1} f_6^{-1}$	1
$(2,1)$	$f_1 f_3 + \underline{f_1 f_8^{-1}} + f_8^{-1} + \underline{f_1} + f_6^{-1} f_8^{-1}$ $+\underline{f_6^{-1} f_7^{-1} f_8^{-1}} + \underline{f_1 f_2 f_3 f_5} + f_1 f_2 f_3$	Λ
$(1,2)$	$\underline{f_3 f_4 f_5^{-1} f_6^{-1}}$	Λ^{-2}
$(2,2)$	$\underline{f_1 f_3 f_4 f_6^{-1}} + f_3 f_5^{-1} f_6^{-1} f_8^{-1}$	1
$(3,2)$	$\underline{f_1 f_3 f_6^{-1} f_8^{-1}}$	1

(3.5.4)

Higgsing 3: So too we can now study the third Higgsing, confirming our results:

(v_1, v_2)	Loops	
$(0,0)$	$\underline{1}$	1
$(1,0)$	$\underline{1} + f_1 f_2 f_5 f_6$	1
$(2,0)$	$\underline{f_1 f_2 f_5 f_6}$	Λ^{-2}
$(1,1)$	$\underline{f_1 f_3 f_4} + \underline{f_3 f_4} + f_3 + 1 + \underline{f_6^{-1}}$ $+ f_5^{-1} f_6^{-1} f_8^{-1} + f_1 f_2 f_3 f_4 + \underline{f_5^{-1} f_6^{-1}}$	Λ
$(2,1)$	$\underline{f_1 f_3} + f_1 f_8^{-1} + f_8^{-1} + \underline{f_1} + \underline{f_6^{-1} f_8^{-1}}$ $+ \underline{f_6^{-1} f_7^{-1} f_8^{-1}} + f_1 f_2 f_3 f_5 + f_1 f_2 f_3$	1
$(1,2)$	$\underline{f_3 f_4 f_5^{-1} f_6^{-1}}$	Λ^2
$(2,2)$	$\underline{f_1 f_3 f_4 f_6^{-1}} + f_3 f_5^{-1} f_6^{-1} f_8^{-1}$	Λ^2
$(3,2)$	$\underline{f_1 f_3 f_6^{-1} f_8^{-1}}$	1

(3.5.5)

Higgsing 4: Finally, we complete the story with the last Higgsing:

(v_1, v_2)	Loops	
$(0,0)$	$\underline{1}$	1
$(1,0)$	$\underline{1} + f_1 f_2 f_5 f_6$	1
$(2,0)$	$\underline{f_1 f_2 f_5 f_6}$	Λ^{-2}
$(1,1)$	$f_1 f_3 f_4 + \underline{f_3 f_4} + \underline{f_3} + 1 + f_6^{-1}$ $+ \underline{f_5^{-1} f_6^{-1} f_8^{-1}} + f_1 f_2 f_3 f_4 + \underline{f_5^{-1} f_6^{-1}}$	Λ
$(2,1)$	$\underline{f_1 f_3} + f_1 f_8^{-1} + \underline{f_8^{-1}} + f_1 + \underline{f_6^{-1} f_8^{-1}}$ $+ f_6^{-1} f_7^{-1} f_8^{-1} + f_1 f_2 f_3 f_5 + \underline{f_1 f_2 f_3}$	1
$(1,2)$	$\underline{f_3 f_4 f_5^{-1} f_6^{-1}}$	Λ^2
$(2,2)$	$f_1 f_3 f_4 f_6^{-1} + \underline{f_3 f_5^{-1} f_6^{-1} f_8^{-1}}$	Λ^2
$(3,2)$	$\underline{f_1 f_3 f_6^{-1} f_8^{-1}}$	1

(3.5.6)

Amœba Projections

As reviewed in §3.3.1, amœba plots provide a simple way of visualizing the spectral curves. Thus, we can explicitly verify that a large value of Λ does indeed have the

desired effect on the parent spectral curve, as an additional check that the scalings we obtained indeed give rise to elongations leading to the desired splitting of Σ.

Let the Λ-weights for each point in the toric diagram be given by the third column in the tables above. The leading behavior in Λ coincides for Higgsings 1 and 2 and for Higgsings 3 and 4. Furthermore, the two pairs are related to each other by a 180° rotation, as shown in Figure 3.9.

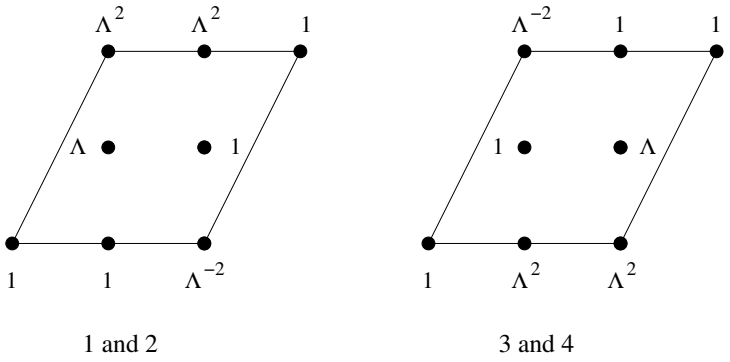

Figure 3.9: The corresponding weights of the coefficients in the Newton polynomial for Higgsings 1 and 2 are connected to those of Higgsings 3 and 4 by a 180° rotation of the corresponding toric diagram.

We see that, in perfect agreement, the amœba projections exhibit the corresponding behavior. Figure 3.10 shows the amœbas for the four Higgsings for large Λ. Indeed, the amœbas for the four models coincide, up to a trivial shift on the (x, y) plane. This results from the simple relation between their scalings as given by Figure 3.9. Furthermore, we see that the thin spine in the center controls precisely the splitting of the double F_0 into her two daughter F_0 theories. The holes in the spectral curve associated to internal points in the toric diagram have zero size in Figure 3.10. This is due to the particular choice of coefficients in the characteristic polynomial. These coefficients can be varied at will without modifying their Λ-scaling and hence preserving the splitting.

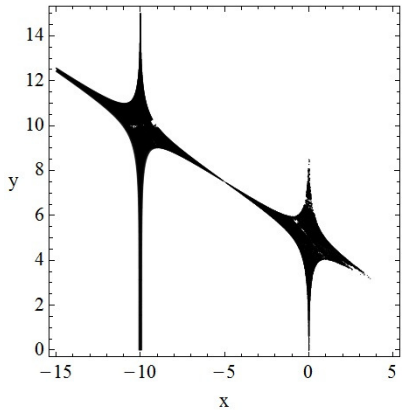

Higgsings 1 and 2

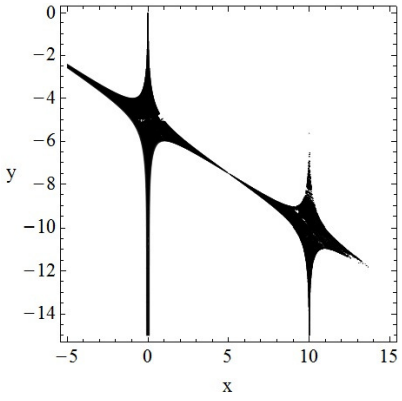

Higgsings 3 and 4

Figure 3.10: Amœba plots for the 4 possible Higgsings with Λ set to the numerical value of e^5. The patchy appearance of these and subsequent amoeba plots, with some missing points in their interior, is due to the fact that we determine them numerically.

3.5.2 $Y^{4,0}$

Fortified by the consistency of our story for double F_0, let us move on to another non-trivial example. We now consider $Y^{4,0}$, whose corresponding integrable system has been worked out in [31]. We remind the reader of the dimer model in Figure 3.11. This is a theory with 8 gauge group factors, quartic superpotential terms and 16 fields, which we suggestively label as V_{ij}, $\tilde{V}_{ij}$ and H_{ij} in accordance with their vertical and horizontal orientation. The toric diagram is shown in Figure 3.12, with 7 points.

We now study the two splittings depicted in Figure 3.12. We will refer to them as Higgsings 1 and 2. Specifically, the acquisition of vevs is as follows:

$$\begin{array}{lll} \underline{\textbf{Higgsing 1:}} & H_{32}^{(1)}, H_{65}^{(1)}, H_{14}^{(1)}, H_{87}^{(1)} & \underline{\textbf{Higgsing 2:}} \quad V_{51}^{(1)}, V_{73}^{(1)}, \tilde{V}_{26}^{(1)}, \tilde{V}_{48}^{(1)} \\ & H_{34}^{(2)}, H_{67}^{(2)}, H_{12}^{(2)}, H_{85}^{(2)} & \tilde{V}_{51}^{(2)}, \tilde{V}_{73}^{(2)}, V_{26}^{(2)}, V_{48}^{(2)} \end{array} \tag{3.5.1}$$

We remark that the black and white nodes are exchanged with respect to [31]. This is of course only a matter of convention. As in the previous example, the choice of vevs leading to each splitting is not unique. Having already illustrated this possibility with the splitting of double F_0 to two F_0's, we focus on the vevs given in (3.5.1) for convenience.

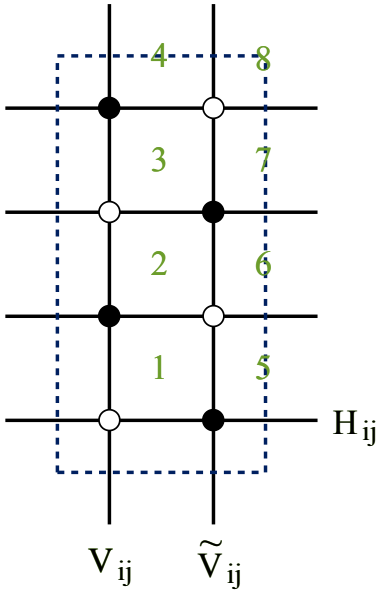

Figure 3.11: Tiling for $Y^{4,0}$.

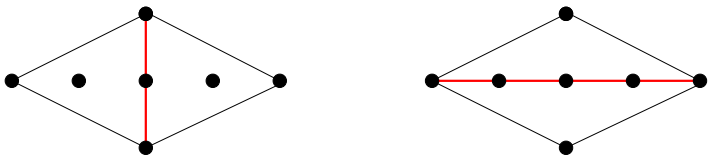

Higgsing 1 Higgsing 2

Figure 3.12: Toric diagram for $Y^{4,0}$, showing the two splittings that we will investigate. The splitting is indicated by the red line.

Once again, we determine the Λ-scalings associated to both decompositions using the methods of §3.4, i.e. both the rule in (3.4.1) and the algorithm in §3.4.2, which yield identical results. We obtain:

Higgsing	f_1	f_2	f_3	f_4	f_5	f_6	f_7	f_8
1	Λ^{-1}	Λ	Λ^{-1}	Λ	Λ	Λ^{-1}	Λ	Λ^{-1}
2	Λ	Λ^{-1}	Λ	Λ^{-1}	Λ^{-1}	Λ	Λ^{-1}	Λ

(3.5.2)

Higgsing 1: We follow the notation in the previous examples, write the coefficients in terms of the f_i variables and underline the terms which survive. We tabulate this for each point, and in the third column write the overall leading behavior in Λ for

the terms which survive.

(v_1, v_2)	Loops	
$(0,0)$	$\underline{1}$	1
$(-1,0)$	$\underline{f_4} + f_4 f_8 + \underline{f_4 f_7 f_8} + f_3 f_4 f_7 f_8$ $+\underline{f_1^{-1} f_5^{-1} f_6^{-1}} + f_1^{-1} f_5^{-1} + \underline{f_1^{-1}} + 1$	Λ
$(-2,0)$	$f_1^{-1} f_5^{-1} f_4 + f_4 f_8 + f_1^{-1} f_4 f_8 + f_1^{-1} f_5^{-1} f_4 f_8$ $+f_1^{-1} f_5^{-1} f_6^{-1} f_4 f_8 + f_4 f_7 f_8 + \underline{f_1^{-1} f_4 f_7 f_8} + f_1^{-1} f_5^{-1} f_4 f_7 f_8$ $+f_3 f_4 f_7 f_8 + f_1^{-1} f_3 f_4 f_7 f_8 + f_1^{-1} f_5^{-1} f_3 f_4 f_7 f_8 + f_1^{-1} f_5^{-1} f_6^{-1}$ $+f_1^{-1} f_5^{-1} + f_3 f_4^2 f_7 f_8 + \underline{f_4 f_1^{-1} f_5^{-1} f_6^{-1}} + f_3 f_4^2 f_7 f_8^2$	Λ^2
$(-3,0)$	$f_1^{-1} f_5^{-1} f_4 f_8 + \underline{f_1^{-1} f_5^{-1} f_6^{-1} f_4 f_8} + \underline{f_1^{-1} f_5^{-1} f_4 f_7 f_8}$ $+f_1^{-1} f_5^{-1} f_3 f_4 f_7 f_8 + \underline{f_1^{-1} f_5^{-1} f_3 f_4^2 f_7 f_8} + f_3 f_4^2 f_7 f_8^2$ $+\underline{f_1^{-1} f_3 f_4^2 f_7 f_8^2} + f_1^{-1} f_5^{-1} f_3 f_4^2 f_7 f_8^2$	Λ
$(-4,0)$	$\underline{f_1^{-1} f_5^{-1} f_3 f_4^2 f_7 f_8^2}$	1
$(-2,1)$	$\underline{f_1^{-1} f_4 f_7 f_8}$	Λ^2
$(-2,-1)$	$\underline{f_2 f_3 f_4^2 f_7 f_8}$	Λ^2

(3.5.3)

Higgsing 2: Likewise, we tabulate the result for Higgsing 2 and obtain:

(v_1, v_2)	Loops	
$(0,0)$	$\underline{1}$	1
$(-1,0)$	$f_4 + \underline{f_4 f_8} + f_4 f_7 f_8 + \underline{f_3 f_4 f_7 f_8}$ $+f_1^{-1} f_5^{-1} f_6^{-1} + \underline{f_1^{-1} f_5^{-1}} + f_1^{-1} + \underline{1}$	1
$(-2,0)$	$f_1^{-1} f_5^{-1} f_4 + \underline{f_4 f_8} + f_1^{-1} f_4 f_8 + \underline{f_1^{-1} f_5^{-1} f_4 f_8}$ $+f_1^{-1} f_5^{-1} f_6^{-1} f_4 f_8 + f_4 f_7 f_8 + f_1^{-1} f_4 f_7 f_8 + f_1^{-1} f_5^{-1} f_4 f_7 f_8$ $+\underline{f_3 f_4 f_7 f_8} + f_1^{-1} f_3 f_4 f_7 f_8 + \underline{f_1^{-1} f_5^{-1} f_3 f_4 f_7 f_8} + f_1^{-1} f_5^{-1} f_6^{-1}$ $+\underline{f_1^{-1} f_5^{-1}} + f_3 f_4^2 f_7 f_8 + f_4 f_1^{-1} f_5^{-1} f_6^{-1} + \underline{f_3 f_4^2 f_7 f_8^2}$	1
$(-3,0)$	$\underline{f_1^{-1} f_5^{-1} f_4 f_8} + f_1^{-1} f_5^{-1} f_6^{-1} f_4 f_8 + f_1^{-1} f_5^{-1} f_4 f_7 f_8$ $+\underline{f_1^{-1} f_5^{-1} f_3 f_4 f_7 f_8} + f_1^{-1} f_5^{-1} f_3 f_4^2 f_7 f_8 + \underline{f_3 f_4^2 f_7 f_8^2}$ $+f_1^{-1} f_3 f_4^2 f_7 f_8^2 + \underline{f_1^{-1} f_5^{-1} f_3 f_4^2 f_7 f_8^2}$	1
$(-4,0)$	$\underline{f_1^{-1} f_5^{-1} f_3 f_4^2 f_7 f_8^2}$	1
$(-2,1)$	$\underline{f_1^{-1} f_4 f_7 f_8}$	Λ^{-2}
$(-2,-1)$	$\underline{f_2 f_3 f_4^2 f_7 f_8}$	Λ^{-2}

(3.5.4)

Figure 3.13 shows the amœbas corresponding to the scalings in (3.5.3) and (3.5.4), confirming they produced the desired splitting.

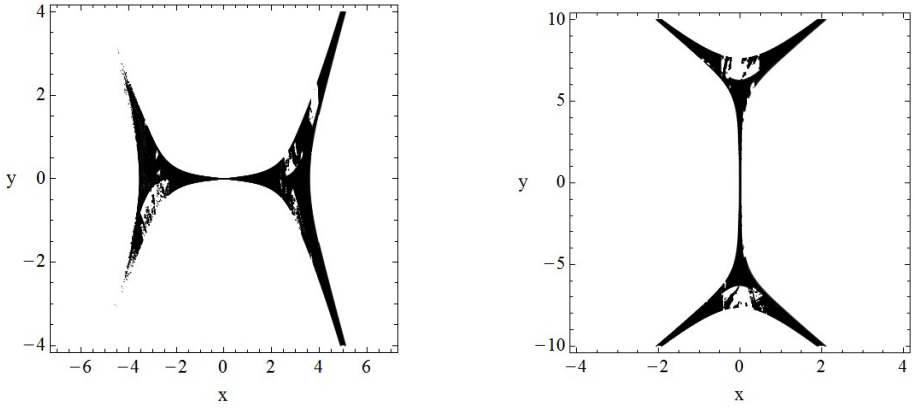

Higgsing 1 Higgsing 2

Figure 3.13: Amœba plots for Higgsings 1 and 2 of $Y^{4,0}$ at $\Lambda = e^3$.

3.6 Combining Multiple Components

In the previous sections, we have explained how to split integrable systems. Reversing the logic, we also understand how to glue them. We have identified a continuous parameter Λ that controls the distance between components of the spectral curve. This parameter manifests itself in the associated quivers as non-zero vevs and suppresses certain contributions in the integrable system. We can now proceed towards our goal of understanding the continuous limit of these systems.

3.6.1 Combinatorics of a Large Number of Components

Let us focus on the case in which we combine an infinite number of identical components Σ_0 along a single direction, effectively generating a new continuous dimension. The amœba projection suggests a natural way to approach the continuum: we consider all components equally separated in the amœba and then send the number of components N contained in a finite interval of length L to infinity. More concretely, defining $\Lambda \equiv e^{\alpha}$, we consider the limit

$$N \to \infty, \qquad \alpha \to 0, \qquad L = N\alpha \text{ fixed.} \tag{3.6.1}$$

This will give us a (1+1)-dimensional integrable system from the continuous limit of an infinite number of (0+1)-dimensional ones. In principle, it seems possible to do the same in both the x and y directions, generating a (2+1)-dimensional integrable field theory in the process.

Before studying this limit, let us investigate how the number of contributions to Hamiltonians behaves for large N. Following the dictionary in §3.2, this number corresponds to the multiplicity of perfect matchings associated to internal points in the toric diagram.[6]

Gluing N copies of an integrable system corresponds to considering a certain $\mathbb{Z}_N$ orbifold of the basic theory. In dimer model language, this corresponds to enlarging the unit cell by a factor of N. While the number of points in the toric diagram grows linearly with N, their multiplicity grows much faster. Let us illustrate this growth in some explicit examples.

$Y^{N,0}$. The cone over $Y^{N,0}$ is the $\mathbb{Z}_N$ orbifold of the conifold with toric diagram given by Figure 3.14.

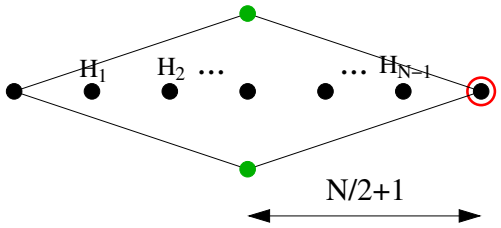

Figure 3.14: Toric diagram for $Y^{N,0}$ for even N. The red circle indicates the reference perfect matching and the green dots correspond to cycles with windings $(-N/2-1, 1)$ and $(-N/2-1, -1)$, which are fixed by the Casimirs.

The integrable system for this geometry was determined in [31] using the prescription in [33], where it was identified with the N-site relativistic periodic Toda chain. Our goal in this section is to investigate its behavior for large N.

[6]Casimirs are given by ratios of external points in the toric diagram. Hence, the same ideas apply independently to their numerator and denominator.

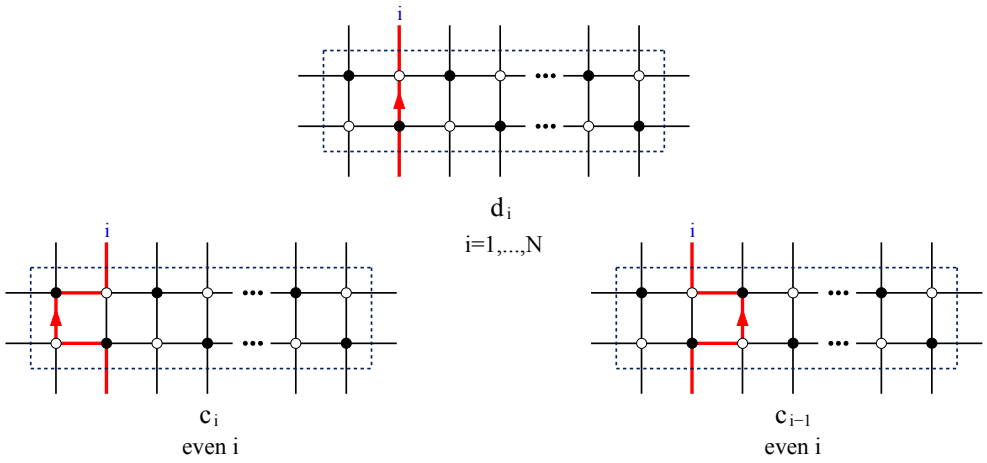

Figure 3.15: A convenient set of cycles for $Y^{N,0}$ with even N. The cycles of type c only exist for even i.

For simplicity, let us focus on the case of even N. A similar analysis is possible for odd N. It turns out that the resulting integrable system is considerably simplified when considering the basis of cycles given in Figure 3.15, instead of using the standard face variables from §2.5.[7] In terms of this basis, the Hamiltonians become

$$H_n = \sum \prod_{n \text{ factors}} \underbrace{d_i\, c_j}\quad . \tag{3.6.2}$$

The problem of finding the Hamiltonians is thus reduced to the combinatorics of non-intersecting paths, which can be used to immediately determine the multiplicity of internal points in the toric diagram. A closed expression for this multiplicity was derived in [117] by using a Potts-model-like description for the dimers, and via a recursion relation that was obtained from a map to a 1-dimensional monomer-dimer system. The final result for the multiplicity of the n^{th} internal point is

$$\sum_{i=0}^{n} \frac{N}{N-i} \binom{n}{i} \binom{N-i}{n}\,, \tag{3.6.3}$$

which applies for both even and odd N.

[7] Figure 3.15 shows $2N$ cycles. The two additional cycles that are necessary to form a basis, are fixed by the Casimirs and hence not important in our discussion. They correspond to the green dots in Figure 3.14.

It is interesting to visualize how these multiplicities are distributed over the toric diagram and how the distribution approaches some limit shape after appropriate normalization. This is shown in Figure 3.16.

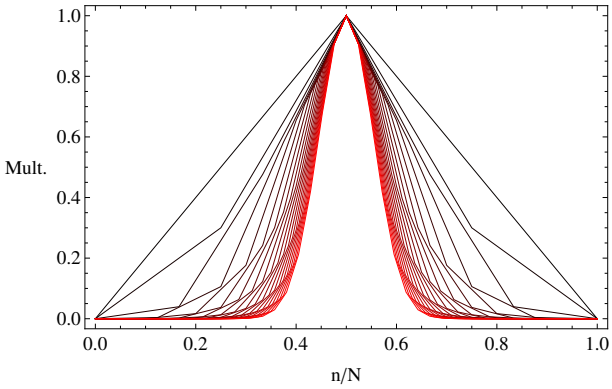

Figure 3.16: Normalized multiplicity of perfect matchings for the internal points of the $Y^{N,0}$ theory. We have also normalized the length of the toric diagram to 1. We show results for $N = 2a$, $a = 1, \ldots, 20$ (black to red).

Multiple F_0. Similarly, we can investigate the generalization of the model considered in §3.5.1 to N copies of F_0. Figure 3.17 shows its toric diagram.

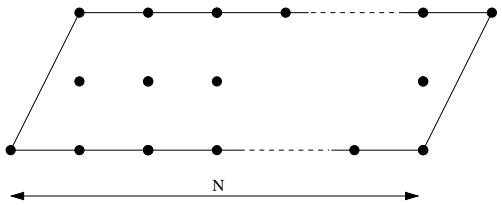

Figure 3.17: Toric diagram for the N F_0 model.

In this case, it is also possible to find closed formulas for the multiplicities of all points in the toric diagram. They are

$$\text{Boundary points: } \binom{N}{m} \qquad \text{Internal points: } 2\binom{2N}{2n-1} \tag{3.6.4}$$

where N is the number of F_0's that have been glued together and $m \in \{0, N\}$ and $n \in \{1, N\}$ index points on the boundary and in the interior of the toric diagram, respectively.

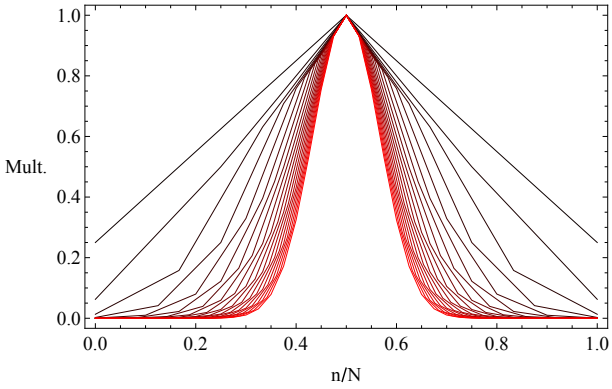

Figure 3.18: Normalized multiplicity of perfect matchings for the internal points of the multiple F_0 theory. We have also normalized the length of the toric diagram to 1. We show results for $N = 2a + 1$, $a = 0, \ldots, 20$ (black to red).

These two examples illustrate a general behavior of large-N models: an explosive growth in the number of perfect matchings associated to a given point in the toric diagram, which translates into a huge number of contributions for each conserved charge. It thus becomes clear that a continuous reformulation of cluster integrable systems is desirable in order to deal with their large-N limit. In the next section we take the first steps towards such a reformulation.

3.6.2 A Toy Model for the Continuous Limit

The two examples considered in the previous subsection share some common characteristics. In both of them, the n^{th} Hamiltonian corresponds to the sum over all possible positions on the tiling of n paths, subject to the constraint of not overlapping over edges. Furthermore, these paths are of a very specific type: they cross the tiling along the short direction of the unit cell and are *almost straight*. By this we mean that these paths are almost localized along the long direction of the unit cell. Figure 3.15 shows the explicit form of these paths for $Y^{N,0}$ and (3.6.2) gives the corresponding Hamiltonians. It is natural to assume that this structure is generic when

gluing N copies of a cluster integrable system with a genus-1 spectral curve.[8] In this section, we introduce a toy model with these properties, which we expect captures the main features of a continuous reformulation of cluster integrable systems.

Let us consider a system in the $x \in [0, L]$ interval and introduce a path z winding vertically at $x = 0$.

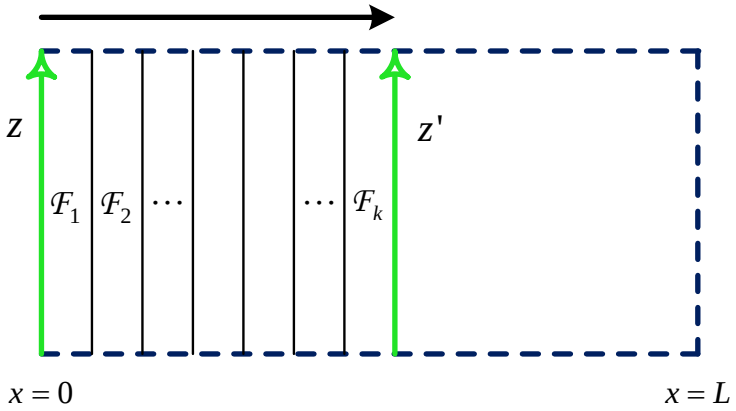

Figure 3.19: A toy model for the continuous limit of cluster integrable systems. The path z can be shifted by multiplying it by all the $\mathcal{F}_i$'s contained in the strip between its initial and final positions.

We can shift z horizontally by multiplying it by all the f_i variables contained in the strip between $x = 0$ and its final position.

$$z \to \prod_{i \in \text{strip}} \mathcal{F}_i \, z \,. \tag{3.6.1}$$

Here $\mathcal{F}_i$ stands in general for a product of f_i's contained in a slice of the tiling. The explicit form of $\mathcal{F}_i$ is controlled by the details of the specific tiling under consideration. Combining n paths and summing over their positions k_i, $i = 1, \ldots, n$, we obtain

$$H_n = \left(\prod_{i=1}^{n} \sum_{k_i < k_{i+1}} \prod_{j=0}^{k_i} \mathcal{F}_j \right) z^n \,, \tag{3.6.2}$$

[8] Attaching N copies of a genus-N spectral curve results in $g\,N$ Hamiltonians. We expect the resulting theories to obey a similar structure.

which we have suggestively called H_n, since it has the expected structure for Hamiltonian operators.[9] We can readily generalize this expression in the continuous limit, obtaining

$$H_n = \left(\prod_{i=1}^{n} \int_{x_{i-1}}^{L} dx_i \, e^{\int_0^{x_i} dy \ln \mathcal{F}(y)} \right) z^n \,, \tag{3.6.3}$$

where $x_0 \equiv 0$. While we have derived (3.6.3) under rather basic assumptions that try to capture the most basic features observed in explicit examples, we expect it displays the main aspects of the actual continuous limit of cluster integrable systems. We leave a detailed investigation of this limit in explicit models for future work.

3.7 Conclusions

We have taken the initial steps in extending the correspondence between dimer models and (0+1)-dimensional cluster integrable systems to continuous (1+1)- and (2+1)-dimensional integrable theories. In order to understand the transition between discrete and continuous theories, it is necessary to have a certain notion of distance between elementary constituents, or "lattice spacing", such that the continuous theory emerges when it is sent to zero. We identified such a continuous parameter controlling the distance between daughters from the perspectives of both spectral curves and the resolution of Calabi-Yau singularities, equivalently the Higgsing of quivers. Furthermore, we introduced two procedures for determining the integrable system dependence on this parameter, whose effect is to suppress certain contributions to conserved charges, making them vanish in the infinite separation limit.

We then explored the integrable systems that are constructed by combining a large number of components, equivalently by gluing a large number of toric diagrams. More concretely, we studied, in explicit examples, the behavior of the number of contributions to individual Hamiltonians as the number of components grows. These

[9] Strictly speaking, Hamiltonians might also contain an n-independent power of the cycle orthogonal to z, as dictated by the position of the corresponding internal point in the toric diagram. This fact can be trivially incorporated into our expressions so, for simplicity, we omit it from our discussion.

contributions are in one-to-one correspondence with perfect matchings of the underlying dimer model. For this reason, their number diverges much more rapidly than the number of components, begging for an alternative continuous formulation of cluster integrable systems. We also observed that each Hamiltonian is given by the contributions of a number of simple paths summed over all their possible positions on the dimer tiling. We used these insights to develop a toy model that we expect reproduces the basic features of the continuous limit of cluster integrable systems.

Interestingly, our investigation of the continuous merging of integrable systems has also resulted in a novel understanding of (un)Higgsing in quiver theories and the associated desingularization of the corresponding Calabi-Yau spaces. Thus, we have added a new angle of attack to the classical subject of D-brane resolution of singularities. We have realized that when one refines the coefficients of the spectral curve into polynomials in loop variables, the Higgsing/resolution simply corresponds to establishing a consistent scale Λ dictating which terms should survive or be suppressed. Therefore, we have effectively generated a new algorithm, outlined in §3.4.2, for systematically studying all partial resolutions for a given toric diagram. It would be worthwhile to exploit this procedure for classifying all consistent daughter theories for a given parent.

What we have touched upon is, of course, only the beginning of a program. The natural question that arises now is how to extend our continuous toy model to theories that are actually constructible from dimers. For example, attempting to recover simple integrable field theories such as Toda theories would be an obvious next step. Given the simplifications afforded by dimer models, we expect it should be possible to construct increasingly more elaborate integrable field theories.

We envision many applications of dimer models to continuous theories, such as the study of integrability preserving lower-dimensional impurities or interfaces between different integrable field theories. Indeed, in light of the correspondence with dimer models, the often difficult condition of integrability simply amounts to checking whether the field theory results from the infinite limit of consistent toric diagrams, i.e. that they are given by convex lattice polygons.

Chapter 4

The Geometry of On-Shell Diagrams

In this chapter we will explore the connection between BFTs and scattering amplitudes. After introducing the necessary mathematical concepts which will play a crucial role in this and subsequent chapters, we will show how to map BFTs to the Grassmannian, and show how the matching and matroid polytopes are sufficient for obtaining the entire singularity structure of on-shell diagrams.

Since our methods don't have any intrinsic restriction to planarity, i.e. graphs that can be embedded on a disk without edge crossings, they allow us to initiate the study of non-planar on-shell diagrams, which will be the topic of Chapter 6.

4.1 The Grassmannian and its Decompositions

A central object in recent developments in scattering amplitudes is the Grassmannian [34]. In this section we review basic aspects about the Grassmannian and its stratifications. We refer the interested reader to [84, 118–121] for more comprehensive discussions.

4.1.1 Definition

The Grassmannian $G_{\mathbb{R}}(k, n)$ is the space of k-dimensional planes in n dimensions that pass through the origin. Elements of $G(k, n)$ are typically represented by $k \times n$

matrices where the plane is the span of the k n-dimensional row vectors. The action of $\mathrm{GL}(k)$ on the basis vectors leaves the plane invariant, so the Grassmannian is the space of $k \times n$ matrices C modulo $\mathrm{GL}(k)$. The $\mathrm{GL}(k)$ invariance can be used to fix any k columns to form a $k \times k$ identity sub-matrix, e.g. for $G(2,4)$ we can fix C to the form

$$C = \begin{pmatrix} 1 & 0 & -c_3 & -c_4 \\ 0 & 1 & c_1 & c_2 \end{pmatrix} \quad , \tag{4.1.1}$$

where the signs have been introduced for later convenience. When mapping bipartite graphs to the Grassmannian, we will see that columns in this matrix correspond to external nodes and rows correspond to those external nodes which are sources in a given perfect orientation. From here on, we will always present elements of the Grassmannian in a form that has fixed the $\mathrm{GL}(k)$ invariance.

4.1.2 Plücker Coordinates

The degrees of freedom of C can alternatively be expressed by its $k \times k$ minors Δ_I, where I is a set with k elements describing which columns participate in the minor; these are known as Plücker coordinates. These minors are invariant under the action of $\mathrm{SL}(k)$ and scale by a common factor under $\mathrm{GL}(k)$. Since there are $\binom{n}{k}$ of these, it induces the Plücker embedding of the Grassmannian $G(k,n) \hookrightarrow \mathbb{RP}^{\binom{n}{k}-1}$. The minors are not all independent, they satisfy relations known as the Plücker relations

$$\sum_{i=1}^{k+1} (-1)^{i-1} \Delta_{J_1 \cup a_i} \, \Delta_{J_2 \setminus a_i} = 0, \tag{4.1.2}$$

where J_1 is any $(k-1)$-element subset of $\{1,\ldots,n\}$, J_2 is any $(k+1)$-element subset of $\{1,\ldots,n\}$ and a_i is the i^{th} element of J_2. In each term, a_i is removed from J_2 and appended to the right of J_1. In this embedding, the Grassmannian is simply the subvariety described by the Plücker relations. For the example of $G(2,4)$ above, we have

$$\begin{array}{lllllllll} \Delta_{12} & = & 1 & \Delta_{14} & = & c_2 & \Delta_{24} & = & c_4 \\ \Delta_{13} & = & c_1 & \Delta_{23} & = & c_3 & \Delta_{34} & = & c_1 c_4 - c_2 c_3 \end{array} \tag{4.1.3}$$

and the single relation $\Delta_{14}\Delta_{23} - \Delta_{13}\Delta_{24} + \Delta_{12}\Delta_{34} = 0$. The totally non-negative Grassmannian $G_{\geq 0}(k,n)$ is given by those matrices C with all $\Delta_I \geq 0$.

4.1.3 Schubert Decomposition

There are many ways to decompose the Grassmannian into (possibly overlapping) sets, according to certain properties. Schubert cells[1] Ω_I are defined as those $C \in G(k,n)$ where Δ_I is the first non-zero Plücker coordinate, counted in lexicographic order[2], i.e.

$$\Omega_I = \{C \in G(k,n) \mid \Delta_I \text{ is the lexicographically minimal non-zero Plücker coordinate}\}. \tag{4.1.4}$$

For example,

$$C = \begin{pmatrix} 1 & 0 & 0 & -c_4 \\ 0 & 1 & c_1 & c_2 \end{pmatrix} \in \Omega_{12}, \tag{4.1.5}$$

because there is no other non-zero Plücker coordinate with smaller lexicographic ordering than $I = 12$. The cyclically shifted Schubert cell $\Omega_I^{(i)}$ is defined similarly, but the lexicographic order is cyclically shifted to begin the counting at i, e.g. for the same example in (4.1.5), $C \in \Omega_{12}$ but also $C \in \Omega_{24}^{(2)}$ because the order is shifted to $2 < 3 < 4 < 1$, and since $\Delta_{23} = 0$, the lexicographically smallest (with respect to the shifted order) non-zero Δ_I is now $I = 24$. Similarly, $C \in \Omega_{34}^{(3)}$ and $C \in \Omega_{41}^{(4)}$.

Note that in each shifted Schubert cell $\Omega_I^{(i)}$ the Plücker coordinates lexicographically larger (with respect to the shifted order i) than I are free to be zero or non-zero.

The permuted Schubert cell Ω_I^w is defined as in (4.1.4), except that the lexicographic order is with respect to a permuted order $w(1) < w(1) < \cdots < w(n)$, where $w \in S_n$.

4.1.4 Positroid Stratification

The positroid stratification of the Grassmannian $G(k,n)$ introduced by Postnikov [84] defines each stratum as

$$S_{\mathcal{I}} = \bigcap_{i=1}^{n} \Omega_{I_i}^{(i)}, \tag{4.1.6}$$

where $\mathcal{I} = \{I_1, \ldots, I_n\}$, and I_i specifies which Plücker coordinates are non-zero, only looking at those which are lexicographically minimal with respect to each shifted

[1] A cell is homeomorphic to an open ball and must have Euler number 1.

[2] Lexicographic order is $1 < 2 < 3 < 4$, e.g. $1243 < 1324$, analogous to alphabetical order.

cyclic ordering starting at i. Note in particular that the Plücker coordinates lexicographically smaller with respect to each shifted order must be zero, following the definition of the Schubert decomposition. For the example in (4.1.5), the non-zero Plücker coordinates are Δ_{12}, Δ_{13}, Δ_{14}, Δ_{24} and Δ_{34}. With respect to the first order $i = 1$, the lexicographically minimal one is Δ_{12}; for $i = 2$ the minimal one is Δ_{24}; for $i = 3$, Δ_{34}; and finally for $i = 4$, $\Delta_{41} = -\Delta_{14}$. Hence, this element of the Grassmannian is in the positroid stratum

$$S_{\mathcal{I}} = \{C \in G(2,4) \mid \Delta_{12} \neq 0, \Delta_{24} \neq 0, \Delta_{34} \neq 0, \Delta_{14} \neq 0\} \quad . \tag{4.1.7}$$

where $\Delta_{23} = 0$ and we do not specify whether Δ_{13} is vanishing or not. Instead, consider the following stratum

$$S_{\mathcal{I}} = \{C \in G(2,4) \mid \Delta_{14} \neq 0, \Delta_{24} \neq 0\} \quad . \tag{4.1.8}$$

This stratum contains those matrices for which lexicographically smaller Plücker coordinates with respect to each shifted order are set to zero. For the shifted order $i = 1$, we note that $\Delta_{12} = 0$ and $\Delta_{13} = 0$ since they are lexicographically smaller than Δ_{14}. For the shifted order $i = 2$, $\Delta_{23} = 0$ since it is lexicographically smaller than Δ_{24}. For the shifted order $i = 3$, we additionally have $\Delta_{34} = 0$ since it is lexicographically smaller than Δ_{14} (along with Δ_{31} and Δ_{32}). Finally $\Delta_{41} \neq 0$ is the lexicographically smallest with respect to the shifted order $i = 4$. So a matrix belonging to this positroid stratum is for instance

$$\begin{pmatrix} c_1 & 1 & 0 & 0 \\ 0 & 0 & 0 & 1 \end{pmatrix} \in S_{\mathcal{I}} = \{C \in G(2,4) \mid \Delta_{14} \neq 0, \Delta_{24} \neq 0\} \quad . \tag{4.1.9}$$

Since a positroid stratum is in general more restricted than a Schubert cell, the positroid stratification refines the Schubert decomposition.

4.1.5 Matroid Stratification

In order to describe this stratification, we have first to introduce the concept of *matroids*. The study of matroids is the analysis of an abstract theory of dependences. We refer the interested reader to [120] for a comprehensive introduction; here we review only some basic aspects.

Definition of a Matroid. A matroid of rank k on a set $[n] \equiv \{1, \ldots, n\}$ is a non-empty collection $\mathcal{M} \subset \binom{[n]}{k}$ of k-element subsets in $[n]$, called *bases* of $\mathcal{M}$, that satisfy the *exchange axiom*:

For any $I, J \in \mathcal{M}$ and $i \in I$, there exists a $j \in J$ such that $(I \setminus \{i\}) \cup \{j\} \in \mathcal{M}$.

Matroid Polytope. We can construct a polytope which efficiently encodes the linear dependencies among the bases of a matroid. Given a matroid $\mathcal{M}$ of rank k on a set $[n]$, the matroid polytope $\mathcal{P}(\mathcal{M})$ is the convex hull of the indicator vectors of the bases of $\mathcal{M}$

$$\mathcal{P}(\mathcal{M}) = \text{convex}\{e_I \ : \ I \in \mathcal{M}\}$$

where by e_I we denote $e_I = \sum_{i \in I} e_i$ for any $I \in \mathcal{M}$, and $\{e_1, \ldots, e_n\}$ is the standard Euclidean basis of $\mathbb{R}^n$. Linear relations among matroid bases translate into linear relations between position vectors of points in the matroid. The construction of matroid polytopes in the context of BFTs was discussed in detail in §2.4.2.

Matroid Stratification. Now we can discuss the matroid stratification of the Grassmannian $G(k, n)$, which further refines the positroid stratification. Let $\mathcal{M} \subset \binom{[n]}{k}$ be a matroid. A matroid stratum is defined as follows

$$S_{\mathcal{M}} = \{C \in G(k, n) \mid \Delta_I \neq 0 \text{ if and only if } I \in \mathcal{M}\} \ . \tag{4.1.10}$$

Note that each stratum is defined by which Plücker coordinates are non-zero and which ones are zero; here all Plücker coordinates are specified. This stratification can also be expressed as the common refinement of the $n!$ permuted Schubert cells Ω_I^w.

To give an example for $G(2, 4)$, the positroid given in (4.1.7) only contains one matroid stratum, $\{12, 13, 14, 24, 34\}$, which corresponds to elements $C \in G(2, 4)$ with $\{\Delta_{12} \neq 0, \Delta_{13} \neq 0, \Delta_{14} \neq 0, \Delta_{24} \neq 0, \Delta_{34} \neq 0, \Delta_{23} = 0\}$; the matrix (4.1.5) belongs to this matroid stratum. Note that there is no matroid stratum $\{12, 14, 24, 34\}$, i.e. where only $\Delta_{13} = 0 = \Delta_{23}$. Indeed we observe that this object does not satisfy the exchange axiom and hence is not a matroid: choosing $I = 34$ and $J = 12$, for $i = 4$ there is no $j \in J$ such that $(I \setminus \{i\}) \cup \{j\} = \{3\} \cup \{j\}$ is in $\mathcal{M}$. We can equivalently deduce this from the Plücker relation $\Delta_{14}\Delta_{23} - \Delta_{13}\Delta_{24} + \Delta_{12}\Delta_{34} = 0$, which

in this case reduces to $\Delta_{12}\Delta_{34} = 0$, which is not compatible with both $\Delta_{12} \neq 0$ and $\Delta_{34} \neq 0$.

4.1.6 Positroid Cells

Postnikov showed that intersecting the matroid stratification with the totally non-negative Grassmannian $G_{\geq 0}(k, n)$ gives a cell decomposition of $G_{\geq 0}(k, n)$ [84]. Only one matroid stratum in each positroid stratum has a non-empty intersection with $G_{\geq 0}(k, n)$, and it is this intersection which is the positroid cell.[3] Equivalently, the positroid cell decomposition of $G_{\geq 0}(k, n)$ can be obtained as the intersection of the positroid stratification with the totally non-negative Grassmannian $G_{\geq 0}(k, n)$. This cell is the only one for which non-negative Plücker coordinates are compatible with the Plücker relations.

The positroid cell whose Plücker coordinates are all different from zero (and positive) is the top-dimensional cell, which we refer to as the top-cell. Postnikov showed that the positroid cells are indexed by ⅃ diagrams and planar bipartite graphs [84].

4.1.7 Perfect Matchings and Plücker Coordinates

In §2.5.3 we observed that different perfect matchings can give rise to perfect orientations with the same source set and hence provide multiple "contributions" to a given matroid element. This phenomenon manifests as non-trivial multiplicities for points in the matroid polytope. We are now ready to explain in what sense these objects contribute to the same matroid element in more detail.

Matroid elements $\{i_1 \dots i_k\}$ are in one-to-one correspondence with Plücker coordinates $\Delta_{i_1 \dots i_k}$ which, in turn, are given by minors of the Grassmannian matrix C. As a result, every perfect matching is mapped to a specific Plücker coordinate [35, 84, 101, 122]. In summary, each point in the matroid polytope is associated with a single Plücker coordinate, but may get contributions from multiple perfect matchings.

[3] These are called cells since they are homeomorphic to an open ball of appropriate dimension.

For the example in §2.5.3, (2.5.2) implies the following relation between perfect matchings and Plücker coordinates:

Plücker coordinate	Δ_{12}	Δ_{13}	Δ_{14}	Δ_{23}	Δ_{24}	Δ_{34}
Perfect matchings	p_1, p_6, p_8	p_2, p_{10}	p_3	p_4	p_5, p_7	p_9

We shall see this relation become even more precise after discussing the boundary measurement in §4.3.

4.2 Scattering Amplitudes

In this section we briefly review some of the recent results in scattering amplitudes which are relevant to this thesis. For a broad introduction to the subject, the interested reader is directed to an excellent review by Elvang and Huang [48]. For the specific applications of the Grassmannian and the results in this chapter, a detailed discussion can be found in [34, 62].

4.2.1 The Grassmannian in Scattering Amplitudes

The leading singularity of a scattering amplitude is obtained by cutting internal propagators, i.e. setting them on-shell, until there remain no integrals left to integrate over.[4]

It is an extremely interesting result that leading singularities in $\mathcal{N} = 4$ SYM are given by contour integrals over the Grassmannian [62]. In fact, we can write *any loop amplitude* of planar $\mathcal{N} = 4$ SYM as a contour integral over the Grassmannian, or a sum over such integrals.

Each process in $\mathcal{N} = 4$ SYM scattering amplitudes is specified by the number of external particles n, the number of negative-helicity[5] particles k, and the loop level L. Since treating all particles as incoming instead of outgoing does not change the physics of the process, the amplitude for k and $n - k$ helicities must be equal.

[4] Contrary to what their name suggests, leading singularities are finite quantities.

[5] The standard convention is to treat all particles as outgoing.

It is a well-known result that if all particles have the same helicity, the amplitude must be zero, i.e. the amplitude is zero for $k = 0$ and $k = n$. Also, the amplitude is zero for $k = 1$ and $k = n - 1$, except for 3-point amplitudes, which will soon be explained to be important in constructing general amplitudes. Hence, the smallest value for k to generate a non-trivial process is $k = 2$; these are known as *maximally helicity violating* (MHV) amplitudes. For $k > 2$ the amplitude is said to be a N^{k-2}MHV amplitude.

The Grassmannian $G(k, n)$ also has a $k \leftrightarrow (n - k)$ symmetry, since a k-plane in n dimensions can equally be specified by the space normal to that plane. Hence, the Grassmannian $G(k, n)$ is equal to $G(n-k, n)$. This analogy to scattering amplitudes has its origin in the fact that the Grassmannian specifies the scattering amplitude. More precisely, N^{k-2}MHV leading singularities are given by [62]:

$$\mathcal{L}_{k,n} = \int_{\Gamma_{k,n}} \frac{d^{k\times n}C}{\mathrm{Vol}(\mathrm{GL}(k))} \frac{\prod_{\alpha=1}^{k} \delta^{4|4}\left(C_{\alpha a}\mathcal{W}^a\right)}{(1\cdots k)(2\cdots k+1)\cdots(n\cdots k-1)}\,, \tag{4.2.1}$$

where $\Gamma_{k,n}$ is the contour, i.e. a prescription for which particular combination of $k\times k$ consecutive minors of the matrix C must be set to zero in order to compute the residues, and $\mathcal{W}^a$ encode the kinematical data in terms of supertwistors. Here and in what follows, $(i_1, \ldots, i_k)$ denotes the minor corresponding to columns $i_1, \ldots, i_k$, i.e. $(i_1, \ldots, i_k) \equiv \Delta_{i_1,\ldots,i_k}$.

4.2.2 On-Shell Diagram Formalism

The emergence of the Grassmannian in the context of scattering amplitudes was fully understood with the introduction of the *on-shell diagram* formalism [34], which is valid beyond leading singularities. In this section, we briefly review the main properties of planar on-shell diagrams, with the aim of introducing the basic concepts that will be generalized in coming sections to the non-planar case. For a detailed presentation, we refer the reader to the original work [34].

On-shell diagrams are graphs constructed by connecting vertices which represent three-point amplitudes along edges that represent on-shell momenta. There are two types of (non-vanishing) three-point amplitudes, A_3^{MHV} and $A_3^{\overline{\mathrm{MHV}}}$, which are

represented by black and white vertices, respectively. Nodes are glued together via the integration over the on-shell phase space of the (super) momentum associated to the edge shared by two vertices.[6] We note that the graphs constructed in this way will in general not be bipartite, but will be bicolored. We can turn bicolored graphs into bipartite graphs simply by performing the merge/expand move introduced in §2.6.1(a).

In the Grassmannian formulation, A_3^{MHV} is given by an integral over $G(2,3)$ while $A_3^{\overline{\text{MHV}}}$ corresponds to an integral over $G(1,3)$. As vertices are glued together, they give rise to a larger Grassmannian $G(k,n)$. For a trivalent on-shell diagram with n_B internal black nodes, n_W internal white nodes and n_I internal edges, the value of k is given by

$$k \;=\; 2n_B + n_W - n_I. \tag{4.2.2}$$

The number of degrees of freedom d of a general on-shell diagram is obtained by starting from the edge weights and subtracting the GL(1) gauge redundancy associated to every internal node. This means that for a diagram with E edges and N internal nodes, we have

$$d = E - N. \tag{4.2.3}$$

This expression is completely general. However, it is often significantly more convenient to express the degrees of freedom of the graph in terms of the face variables introduced in §2.5. In particular, it turns out that the degrees of freedom of an on-shell diagram are equal to the dimension of the matching polytope as given in (2.5.2), i.e.

$$d = d_{\text{matching}} = F + B + 2g - 2\ , \tag{4.2.4}$$

which despite appearances is independent of the embedding, and is manifestly valid also for non-planar on-shell diagrams.

[6]Following a standard approach in the combinatorics literature, we choose to include external nodes at the endpoints of legs of on-shell diagrams. We would like to emphasize that we are dealing with ordinary on-shell diagrams and that such external nodes have no physical significance. They are both useful bookkeeping devices when performing the transformations in §2.6.1, as well as make the connection with BFTs more transparent.

Generalizing (4.2.1) beyond leading singularities, every on-shell diagram, either planar or non-planar, is associated to a differential form

$$\left(\prod_{\text{int. nodes } v} \frac{1}{\text{Vol}(\text{GL}(1)_v)}\right)\left(\prod_{\text{edges } X_e} \frac{dX_e}{X_e}\right)\prod_{\alpha=1}^{k}\delta^{4|4}\left(C_{\alpha a}\mathcal{W}^a\right), \tag{4.2.5}$$

where the first product is taken over all internal nodes. We will refer to the form excluding the δ-functions as the *on-shell form* Ω corresponding to a given on-shell diagram. The full on-shell form associated to a d-dimensional *planar* on-shell diagram in terms of edge or face variables is of the "$d\log$" form [34]

$$\Omega = \frac{dX_1}{X_1}\frac{dX_2}{X_2}\cdots\frac{dX_d}{X_d} = \frac{df_1}{f_1}\frac{df_2}{f_2}\cdots\frac{df_d}{f_d}. \tag{4.2.6}$$

In Chapter 6 we will see that for non-planar diagrams a very similar formula holds, which makes full use of the generalized face variables from §2.5. We note that expressing the on-shell form in terms of edge weights requires using the GL(1) redundancies to identify d independent variables; this task is bypassed when using face variables.

When the dimension of the graph coincides with the maximal dimension of $G(k,n)$, i.e. $d = k(n-k)$, the on-shell form is said to be top-dimensional. If the dimension of the graph is larger than the dimension of $G(k,n)$, the graph may be reduced into a graph of dimension $d \leq k(n-k)$. The precise details of equivalence and reductions in the context of scattering amplitudes will be elucidated in §4.4.

If the dimension of the graph is smaller than the dimension of $G(k,n)$, (4.2.6) arises as a certain *residue* of the right-hand side of (4.2.1) (which we note is valid beyond leading singularities); the residue is taken around the vanishing of those minors which disappear once those graphical degrees of freedom have been turned off.

4.2.3 Stratification and Singularity Structure of On-Shell Diagrams

The delta functions in (4.2.5) impose $2n-4$ kinematical constraints on the external data. Hence, depending on the degrees of freedom in the matrix C, i.e. on d,

different situations arise. If $d = 2n - 4$ the integral over the differential form is fully localized, and the result is an ordinary function of the external data; this is the so-called leading singularity. If $d < 2n - 4$ we have more constraints than degrees of freedom, so the leftover constraints impose conditions on the external data; this is a singularity. If $d > 2n - 4$ there are some degrees of freedom left unfixed by the delta functions which can be integrated over.

Moreover, reducibility of diagrams is closely tied to the existence of $d\log$ factors in the on-shell form Ω which involve variables that appear nowhere else in the integrand; these degrees of freedom are precisely the degrees of freedom associated with *bubbles*, which were introduced in §2.6.2(c).

Understanding the singularity structure of the differential forms associated to on-shell diagrams is of great physical interest. For instance, in the case of planar $\mathcal{N} = 4$ SYM, the study of such singularities is connected to a generalization of the BCFW recursion relation which fully determines the scattering amplitudes to all loop orders [34, 43, 44].

Given a differential form related to an on-shell diagram, the singularity structure contains the information of the residues at the poles of the differential form, which are generally located at some $X_i = 0$.[7] These singularities correspond to elements in the Grassmannian where the number of degrees of freedom in the matrix C has been reduced, by turning off some X_i.

The singularity structure can be organized in a layered partially ordered set (poset). At the top level we have the original on-shell diagram and the associated differential form. At the next level, there are the differential forms obtained at the poles of the original one, with one less degree of freedom, and so on. This procedure continues until it reaches the trivial configuration with no poles left. We provide graphical realizations of this in §4.5, cf. Figure 4.8.

In terms of the Grassmannian element determining the differential form, the number of degrees of freedom in C is reduced by one when going from one level of the poset to the next one. In terms of the bipartite graph, each step coincides

[7] Many coordinate charts $\vec{X}$ are necessary to cover all the poles of the differential form.

with the removal of so-called *removable edges*, which are those which yield reduced subgraphs where $d \to d-1$. A quick way to identify removable edges was already discussed in §2.6.3.

In summary, given a differential form related to an on-shell diagram, its singularity structure can be understood from the corresponding bipartite graph by decomposing the graph into subgraphs by removing only removable edges. This provides a lattice of subgraphs, whose corresponding differential forms are the singularities of the original differential form, organized by number of degrees of freedom.

In the planar case, if the original graph is top-dimensional, this graph decomposition is equivalent to the positroid stratification of the associated Grassmannian. In §4.5, we will introduce a natural generalization of this decomposition which also applies to the non-planar graphs.

4.3 Boundary Measurement for Arbitrary On-Shell Diagrams

In this section we introduce how to map the graphical information of an on-shell diagram to the corresponding element of the Grassmannian. This map is known as the *boundary measurement*, and maps the edge weights of a bipartite graph with k sources and n external vertices to an element of $G(k,n)$. As is clear from (4.2.1) and (4.2.5), the boundary measurement is an important ingredient in the study of on-shell diagrams.

The boundary measurement was first constructed for planar graphs by Postnikov [84] and for the annulus by Gekhtman, Shapiro and Vainshtein [123]. After a quick review of the basics of how the boundary measurement works, we shall follow [3] and [6] and show how to generalize the boundary measurement to arbitrary on-shell diagrams. This will be particularly useful when computing non-planar scattering amplitudes in Chapter 6.

Strictly speaking, the boundary measurement is independent of the embedding. However, as in previous sections, considering an explicit embedding will turn out to extremely useful. More importantly, we can regard on-shell diagrams that do not

admit a genus-zero embedding as inherently demanding a higher genus treatment.

4.3.1 General Strategy

The first step in the construction is to pick a perfect orientation of the diagram. For n external nodes and k sources in the perfect orientation, the entries C_{ij} in the matrix $C \in G(k,n)$ take the general form

$$C_{ij}(X) = \sum_{\Gamma \in \{i \rightsquigarrow j\}} (-1)^{s_\Gamma} \prod_{e \in \Gamma} X_e \ , \tag{4.3.1}$$

where i runs over the sources, j runs over all external nodes and Γ is a flow in the perfect orientation going from i to j. In simple terms, the entries C_{ij} are sums of connected oriented paths that flow from source i to the external node j. The orientation of the edges is determined by the perfect orientation. Moreover, each of these paths is multiplied by a sign $(-1)^{s_\Gamma}$, whose determination constitutes the main challenge when generalizing the boundary measurement, and which will be discussed at length in the next sections.

The entries which contain paths that go from a source to the same source are always equal to 1. Some entries are 0, representing the fact that sometimes it is impossible to flow from a source to a given external node. In particular, there are no oriented flows between two sources. The location of 1's and 0's depends on the chosen perfect orientation, and this choice precisely translates to a choice of $\mathrm{GL}(k)$ gauge symmetry of $G(k,n)$, since we see that there is always a $k \times k$ identity sub-matrix associated to the source nodes.

The paths contributing to entries in C can be identified with *single component* flows, which we recall can be expressed in terms of oriented edge variables, and take the form $\mathfrak{p}_\mu = \tilde{p}_\mu / \tilde{p}_{\text{ref}}$ for some oriented perfect matching $\tilde{p}_\mu$. In the presence of loops in the perfect orientation, C_{ij} will typically receive an infinite number of contributions, each consisting of a path multiplied by an ever larger number of loops. This infinite contribution is resummed and expressed in the generic form $\frac{\mathfrak{p}_\mu}{1-\mathfrak{p}_{\text{loop}}}$.

There is an extremely efficient matrix implementation to construct a matrix $\mathcal{M}^C$, which is identical to C except for the signs $(-1)^{s_\Gamma}$, which is known as the path matrix. This technique is reviewed in Appendix A.1.

Conditions on the Boundary Measurement. In order to have a well-defined boundary measurement we impose two conditions. The first is that for graphs on a disk, the Plücker coordinates should be manifestly positive for positive edge weights. This is simply the statement that planar on-shell diagrams are in one-to-one with positroid cells, as discovered by Postnikov [84]. We shall soon discuss how to arrange the signs $(-1)^{s_\Gamma}$ in order to achieve this.

The second condition is that the Plücker coordinates must be written as sums of flows (which are equivalent to perfect matchings), with coefficients ± 1. This is the statement that the matroid polytope as constructed using flows is indeed equivalent to the matroid polytope associated to the Grassmannian. Expressed differently, it ensures that §4.1.7 is true. Notice that while the entries in C are linear combinations of flows, the fact that Plücker coordinates, i.e. the determinants of its $k \times k$ submatrices, are sums of very specific sets of flows is a highly non-trivial property.

Satisfying both conditions for arbitrary non-planar on-shell diagrams is particularly complicated, and we shall see that the prescription for assigning the signs $(-1)^{s_\Gamma}$ is fine-tuned precisely to achieve this.

4.3.2 Boundary Measurement on the Disk

In order to gain familiarity with the full boundary measurement, we review the original construction of the boundary measurement, which was only valid for planar graphs embedded on a disk [84], i.e. on a surface with genus $g = 0$ and $B = 1$ boundaries.

In order to construct a matrix with definite non-negative minors, we have to modify some signs in the entries of $\mathcal{M}^C$, so as to map $\mathcal{M}^C \mapsto C \in G(k, n)$. To do this we first introduce an overall sign $(-1)^{s(i,j)}$ to the entry $\mathcal{M}^C_{i,j}$, where $s(i, j)$ is the number of sources strictly between i and j, neglecting periodicity. Secondly, we introduce a (-1) factor to every loop. These two modifications conspire in such a way to obtain a matrix C whose minors are all non-negative, and moreover such that its minors remain simple sums of flows.

Example. We now provide an example to illustrate this method. We begin with the diagram displayed in Figure 4.1, and the perfect orientation associated to the reference matching consisting of edges $X_{1,2}, X_{1,4}$.

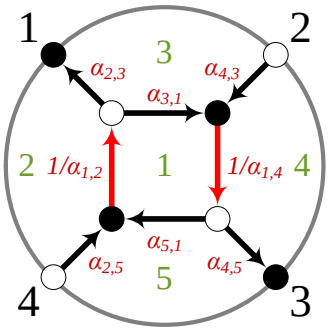

Figure 4.1: Bipartite graph for the top-cell of $G(2,4)$. The reference perfect matching is shown in red. Arrows indicate the corresponding perfect orientation.

The relevant subset of the path matrix, choosing the clockwise ordering of external nodes starting at the edge $X_{2,3}$, is

$$\mathcal{M}^C = \left(\begin{array}{c|cccc} & 1 & 2 & 3 & 4 \\ \hline 2 & \frac{\alpha_{2,3}\alpha_{4,3}\alpha_{5,1}}{\alpha_{1,2}\alpha_{1,4}\left(1-\frac{\alpha_{3,1}\alpha_{5,1}}{\alpha_{1,2}\alpha_{1,4}}\right)} & 1 & \frac{\alpha_{4,3}\alpha_{4,5}}{\alpha_{1,4}\left(1-\frac{\alpha_{3,1}\alpha_{5,1}}{\alpha_{1,2}\alpha_{1,4}}\right)} & 0 \\ 4 & \frac{\alpha_{2,3}\alpha_{2,5}}{\alpha_{1,2}\left(1-\frac{\alpha_{3,1}\alpha_{5,1}}{\alpha_{1,2}\alpha_{1,4}}\right)} & 0 & \frac{\alpha_{2,5}\alpha_{3,1}\alpha_{4,5}}{\alpha_{1,2}\alpha_{1,4}\left(1-\frac{\alpha_{3,1}\alpha_{5,1}}{\alpha_{1,2}\alpha_{1,4}}\right)} & 1 \end{array}\right)$$

$$= \left(\begin{array}{c|cccc} & 1 & 2 & 3 & 4 \\ \hline 2 & \frac{\mathfrak{p}_4}{1-\mathfrak{p}_7} & 1 & \frac{\mathfrak{p}_2}{1-\mathfrak{p}_7} & 0 \\ 4 & \frac{\mathfrak{p}_3}{1-\mathfrak{p}_7} & 0 & \frac{\mathfrak{p}_5}{1-\mathfrak{p}_7} & 1 \end{array}\right), \tag{4.3.2}$$

where the labeling of perfect matchings follows that of Figure 2.3. This example has a loop in the perfect orientation, which manifests itself as several terms in the denominator, as explained above and in Appendix A.1.

We proceed in modifying the signs of the matrix $\mathcal{M}^C$ to obtain the element of the totally non-negative Grassmannian. The $(-1)^{s(i,j)}$ factor implies that we have to multiply the entry $\mathcal{M}^C_{4,1}$ by (-1), since between 1 and 4 we have precisely one source, i.e. node 2. The (-1) factor for loops amounts to replacing $\mathfrak{p}_7 \to -\mathfrak{p}_7$. These

two operations map $\mathcal{M}^C$ into the relevant element of the Grassmannian $C \in G(2,4)$:

$$C = \left(\begin{array}{c|cccc} & 1 & 2 & 3 & 4 \\ \hline 2 & \frac{\alpha_{2,3}\alpha_{4,3}\alpha_{5,1}}{\alpha_{1,2}\alpha_{1,4}\left(1+\frac{\alpha_{3,1}\alpha_{5,1}}{\alpha_{1,2}\alpha_{1,4}}\right)} & 1 & \frac{\alpha_{4,3}\alpha_{4,5}}{\alpha_{1,4}\left(1+\frac{\alpha_{3,1}\alpha_{5,1}}{\alpha_{1,2}\alpha_{1,4}}\right)} & 0 \\ 4 & -\frac{\alpha_{2,3}\alpha_{2,5}}{\alpha_{1,2}\left(1+\frac{\alpha_{3,1}\alpha_{5,1}}{\alpha_{1,2}\alpha_{1,4}}\right)} & 0 & \frac{\alpha_{2,5}\alpha_{3,1}\alpha_{4,5}}{\alpha_{1,2}\alpha_{1,4}\left(1+\frac{\alpha_{3,1}\alpha_{5,1}}{\alpha_{1,2}\alpha_{1,4}}\right)} & 1 \end{array}\right)$$
$$= \left(\begin{array}{c|cccc} & 1 & 2 & 3 & 4 \\ \hline 2 & \frac{f_1 f_3}{1+f_1} & 1 & \frac{1}{f_4(1+f_1)} & 0 \\ 4 & -\frac{1}{f_2(1+f_1)} & 0 & \frac{1}{f_2 f_3 f_4(1+f_1)} & 1 \end{array}\right). \tag{4.3.3}$$

where in the second equality we have expressed the degrees of freedom using loop variables.

The maximal minors of $C \in G(k,n)$ are the Plücker coordinates Δ_I. For this example the Plücker coordinates are:

$$\begin{aligned} \Delta_{12} &= \frac{1}{f_2(1+f_1)} = \frac{\mathfrak{p}_3}{1+\mathfrak{p}_7} & \Delta_{23} &= \frac{1}{f_2 f_3 f_4(1+f_1)} = \frac{\mathfrak{p}_5}{1+\mathfrak{p}_7} \\ \Delta_{13} &= \frac{1}{f_2 f_4(1+f_1)} = \frac{\mathfrak{p}_1}{1+\mathfrak{p}_7} & \Delta_{24} &= 1 \\ \Delta_{14} &= \frac{f_1 f_3}{1+f_1} = \frac{\mathfrak{p}_4}{1+\mathfrak{p}_7} & \Delta_{34} &= \frac{1}{f_4(1+f_1)} = \frac{\mathfrak{p}_2}{1+\mathfrak{p}_7} \end{aligned} \tag{4.3.4}$$

Several remarks are in order. First, all the minors of C have the form of sums of flows, divided by possible loops, thanks to non-trivial cancellations. Secondly, all minors are non-zero, reflecting the fact that the element of the Grassmannian associated to C has maximal dimension $k(n-k) = 4$. This can be independently verified by counting the number of independent face variables, which in this case is four. Thirdly, all minors are manifestly positive, for positive edge weights.

The attentive reader may notice that the reference matching $\tilde{p}_6$ doesn't seem to appear in (4.3.4). This is simply due to the fact that, being the reference matching, it has been divided out in all the Plücker coordinates; this is closely related to having chosen a GL(k) gauge. In order to recover a transparent relation between Plücker coordinates and perfect matchings we need to multiply by those perfect matchings which have the same source sets as this perfect orientation, in this case $(\tilde{p}_6 + \tilde{p}_7)$.

This yields the required map

$$\Delta_{12} \leftrightarrow \tilde{p}_3 \ , \ \ \Delta_{13} \leftrightarrow \tilde{p}_1 \ , \ \ \Delta_{14} \leftrightarrow \tilde{p}_4 \ , \ \ \Delta_{23} \leftrightarrow \tilde{p}_5 \ , \ \ \Delta_{24} \leftrightarrow \tilde{p}_6 + \tilde{p}_7 \ , \ \ \Delta_{34} \leftrightarrow \tilde{p}_2 \ . \tag{4.3.5}$$

4.3.3 Boundary Measurement on Arbitrary Genus-Zero Diagrams

Non-planar graphs can also be mapped to elements of the Grassmannian. In this section we demonstrate the subtleties that need to be addressed by a non-planar boundary measurement, and the prescription to implement them introduced in [3]. We shall restrict our discussion to graphs with genus zero and multiple boundaries. For cases on the annulus, a well-defined map to the Grassmannian already exists [123]; the one presented here reduces to the known cases on the annulus and the disk in the cases with two boundaries or one boundary, respectively, and can be seen as a generalization of them.

It is important to note that in the non-planar case the Plücker coordinates are no longer positive definite, given positive edge weights. Thus, the image of the map is no longer restricted to the positive part of the Grassmannian. However, the prescription we provide is a generalization of the known boundary measurements, and hence recovers manifest positivity on the disk.

As in the planar boundary measurement, for a given perfect orientation, the matrix entries C_{ij} of the element of the Grassmannian are composed of paths connecting the k sources to the n external nodes. Insisting on the conditions in §4.3.1, in particular that minors of C be expressed as sums of flows, typically requires a delicate assignation of signs in the matrix entries C_{ij}. There are two principal sources of difficulty:

- The ordering of external nodes determines the position of the corresponding columns in C, thus affecting the signs associated with minors involving that column.

- Each loop gives a (-1) sign to a given flow in C_{ij}. We will need a more general prescription for counting loops.

For compatibility with the known planar boundary measurement, we will also need to keep the sign $(-1)^{s(i,j)}$ introduced in §4.3.2 that is given to a matrix entry C_{ij}.

To address both issues, we introduce *cuts* between boundaries. These cuts might cross over some of the edges of the graph. Figure 4.2 shows two examples with $B = 2$ and their respective cuts.[8]

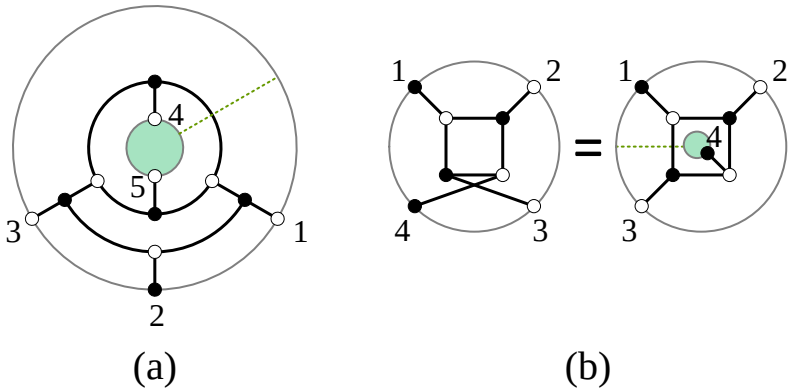

Figure 4.2: (a) A graph with two boundaries. The cut is represented by the green dotted line. (b) Crossing external legs can be eliminated by introducing a new boundary.

Prescription for Ordering the External Nodes. The ordering prescription for the external nodes is fixed by creating a path along the cuts and boundaries, in a way which is reminiscent of the computation of residues in complex analysis: we start at an arbitrary point on one of the boundaries, and follow the boundary until reaching a cut. Then we follow the cut to the next boundary, follow the boundary to the next cut, and so on, until reaching the original starting point. This should be done without ever crossing over any cuts or boundaries. An example of this, taken from [3], is given in Figure 4.3. External nodes are labeled according to the order in which they appear along the path.

We note that this ordering recovers the cyclic labeling of external indices for planar graphs, as well as the canonical ordering on the annulus as given in [123].

[8]Figure 4.2(b) illustrates how crossing external legs can be traded with additional boundaries.

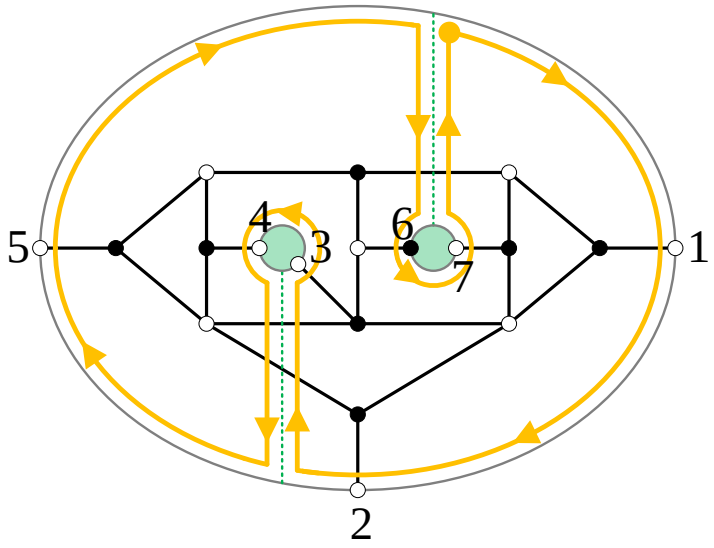

Figure 4.3: Labeling of external nodes by following boundaries and cuts. The cuts are represented by green dotted lines.

Prescription for Counting Loops. Matrix entries C_{ij} are composed of paths from source i to node j. To count loops for each path, we first *close the path* by starting from the sink and following a succession of boundaries and cuts in order to get from the sink to the source. In general, the loop that is thus created has self-intersections. The *rotation number* r of the loop is defined as the number of full clockwise revolutions of the loop minus the number of full counter-clockwise revolutions. The sign assigned to each path is $(-1)^{r+1}$. Note that this sign automatically accounts for the sign (-1) given to loops in the original boundary measurement described in §4.3.2. Figure 4.4 provides two examples where the rotation number is computed.

The cut essentially measures the non-planarity of a path, by counting how many times it goes around the non-trivial direction of the annulus. For this reason, it is heuristically clear that the results cannot depend on the choice of cut. This is shown to be the case in [123].

For computational convenience, there is a significantly faster way to compute the signs $(-1)^{r+1}$, valid on any graph embedded on genus $g = 0$, which does not involve drawing and analyzing the path. Each time a path runs across a cut, it picks up a

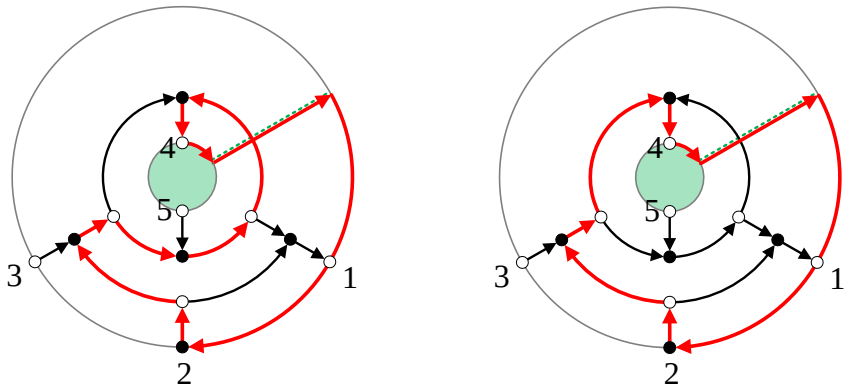

Figure 4.4: The path is closed using cuts and boundaries. The example on the left has $r = 0$ and gives a sign (-1) to this contribution in C_{24}. The example on the right has $r = 1$ and gives no additional signs to this contribution in C_{24}.

minus sign iff it is going between two boundaries that can only be reached using this cut. Each entry in C is specified by its source and sink; it is easy then to identify which cuts are going to be actively used in this matrix entry. Thus, each matrix entry activates sign flips for only those edges that run across the relevant cuts. In addition to these signs, it is necessary to add signs to closed loops that are present in the perfect orientation. From a computational standpoint, it is then only necessary to provide information on how nodes are distributed over the different boundaries, which cuts are activated by each pair of boundaries, and which edges are crossed by the respective cuts.

For reference, the examples in Figure 4.2(a) and Figure 4.3 are explicitly computed in [3].

4.3.4 Boundary Measurement for Arbitrary On-Shell Diagrams

We are finally ready to present the full boundary measurement for arbitrary on-shell diagrams embedded on surfaces of arbitrary genus and number of boundaries. As is

made clear in multiple examples in [6], the difficulty of generalizing the prescription to higher genus is in computing the rotation number when closing the flow into a loop. For example, it is sometimes possible for a loop to avoid the cut by circling around a non-trivial loop α_i or β_i of the surface, thus avoiding a crucial minus sign needed to preserve the map between Plücker coordinates and perfect matchings. The prescription we are about to illustrate addresses this. It can also have additional interesting consequences however, such as producing additional signs for flows even in the absence of cuts, as is demonstrated in Appendix A.2.

Following [6], in order to extend the boundary measurement to higher genus, we propose an explicit prescription for constructing the loop: it should be closed *within the unit cell*. This is done as follows: every time a flow goes around a non-trivial loop and thus uses the periodicity of the Riemann surface, we connect its exit and entry points of the unit cell. This procedure is illustrated in Figure 4.5 for genus $g = 1$. This process creates a closed loop which is entirely contained inside the unit cell, whose rotation number r is used to determine the combinatorial sign $(-1)^{r+1}$ associated to the corresponding flow.

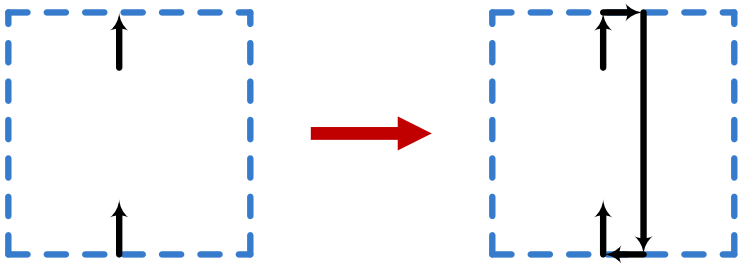

Figure 4.5: A schematic representation of how to close a flow within the unit cell in the case of a torus.

We emphasize that this prescription is a proposal, and it would be desirable to develop a proof for it and to consider its dependence on things such as the choice of unit cell. In order to arrive to it we have considered several explicit examples, like the ones presented in this thesis, and verified that it works, as opposed to other ways of determining the rotation numbers.

Summary of the Method

In summary, the construction of the most general boundary measurement is the following:

- Embed the on-shell diagram on a surface. Since the choice of surface is irrelevant, it is convenient to embed it on a surface of genus zero, if possible, and with the fewest possible number of boundaries.

- Choose cuts. Label the n external nodes according to the prescription illustrated in Figure 4.3.

- Choose a perfect orientation, which determines a source set made out of k external nodes.

- Construct a $k \times n$ matrix $\mathcal{M}^C$, with entries equal to the sum of connected oriented paths from source i to external node j. To construct $\mathcal{M}^C$ it is convenient to follow the algorithm reviewed in Appendix A.1. So far we have not introduced any signs $(-1)^{s_\Gamma} = (-1)^{s(i,j)}(-1)^{r+1}$.

- Give an overall sign $(-1)^{s(i,j)}$ to matrix entries $\mathcal{M}^C_{ij}$.

- For each contribution to $\mathcal{M}^C_{ij}$, close the path using the boundaries and cuts. Every time the path goes around a non-trivial direction of the higher-genus surface, close the path analogously to Figure 4.5. Count the rotation number r of the resulting loop, and assign a $(-1)^{r+1}$ to this contribution in $\mathcal{M}^C_{ij}$. For graphs embedded on a surface of genus zero, it is not necessary to draw the path: knowledge of which edges and cuts are used is sufficient, as described at the end of §4.3.3. We have now completed the map to the Grassmannian $\mathcal{M}^C \mapsto C \in G(k,n)$.[9]

Our boundary measurement applies to arbitrary genus, reducing to the already known prescription on genus-zero graphs. For illustrative purposes and to provide

[9]Whether this way of assigning signs is unique is an interesting question, beyond the scope of this thesis.

evidence supporting our proposal, we shall now present a $g = 1$ example. Appendix A.2 additionally presents a $g = 2$ example with a single boundary and hence no cuts, illustrating that in general it is necessary to have $(-1)^{r+1}$ signs even in the absence of cuts.

A Genus-One Example. Let us explore the genus-one on-shell diagram presented in Figure 4.6, where we have drawn the perfect orientation associated to the reference perfect matching $\tilde{p}_4 = \alpha_{1,3}\alpha_{4,2}\alpha_{4,5}\alpha_{7,3}\alpha_{7,6}$. This diagram does not admit a $g = 0$ embedding. The figure also shows the cut we have chosen, and the correspondingly correctly labeled external nodes.

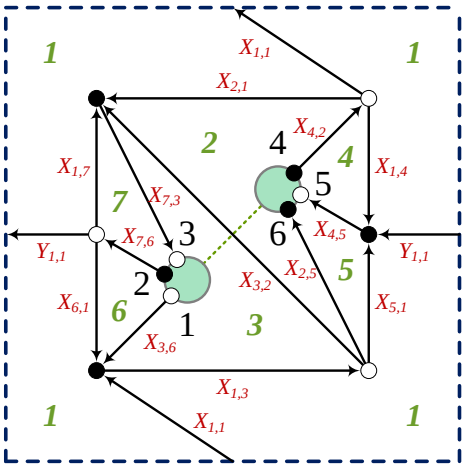

Figure 4.6: A reduced on-shell diagram embedded into a torus with two boundaries. This graph cannot be embedded on any surface with $g = 0$. The dotted line represents the cut.

This diagram has 34 perfect matchings; the corresponding flows in the perfect orientation under consideration and their source sets are

$$\mathfrak{p}_1 = \frac{\alpha_{1,4}\alpha_{1,7}}{\alpha_{4,2}\alpha_{4,5}\alpha_{7,3}\alpha_{7,6}} \quad \{1,3,5\} \qquad \mathfrak{p}_{18} = \frac{\alpha_{2,5}\alpha_{3,6}\alpha'_{1,1}}{\alpha_{1,3}\alpha_{4,5}\alpha_{7,6}} \quad \{4,5,6\}$$

$$\mathfrak{p}_2 = \frac{\alpha_{1,4}}{\alpha_{4,2}\alpha_{4,5}} \quad \{1,2,5\} \qquad \mathfrak{p}_{19} = \frac{\alpha_{2,1}\alpha_{2,5}\alpha_{3,6}}{\alpha_{1,3}\alpha_{4,2}\alpha_{7,3}} \quad \{2,3,6\}$$

$$\mathfrak{p}_3 = \frac{\alpha_{1,7}}{\alpha_{7,3}\alpha_{7,6}} \quad \{1,3,4\} \qquad \mathfrak{p}_{20} = \frac{\alpha_{2,1}\alpha_{2,5}\alpha_{3,6}\alpha'_{1,1}}{\alpha_{1,3}\alpha_{4,2}\alpha_{4,5}\alpha_{7,3}\alpha_{7,6}} \quad \{3,5,6\}$$

$$\mathfrak{p}_4 = 1 \quad \{1,2,4\} \qquad \mathfrak{p}_{21} = \frac{\alpha_{2,5}\alpha_{6,1}}{\alpha_{1,3}\alpha_{7,6}} \quad \{1,4,6\}$$

$$\mathfrak{p}_5 = \frac{\alpha'_{1,1}}{\alpha_{4,5}\alpha_{7,6}} \quad \{1,4,5\} \qquad \mathfrak{p}_{22} = \frac{\alpha_{1,1}\alpha_{2,5}}{\alpha_{1,3}\alpha_{4,2}} \quad \{1,2,6\}$$

$$\mathfrak{p}_6 = \frac{\alpha_{2,1}}{\alpha_{4,2}\alpha_{7,3}} \quad \{1,2,3\} \qquad \mathfrak{p}_{23} = \frac{\alpha_{2,1}\alpha_{2,5}\alpha_{6,1}}{\alpha_{1,3}\alpha_{4,2}\alpha_{7,3}\alpha_{7,6}} \quad \{1,3,6\}$$

$$
\begin{aligned}
\mathfrak{p}_7 &= \frac{\alpha_{2,1}\alpha'_{1,1}}{\alpha_{4,2}\alpha_{4,5}\alpha_{7,3}\alpha_{7,6}} && \{1,3,5\} & \qquad \mathfrak{p}_{24} &= \frac{\alpha_{1,1}\alpha_{2,5}\alpha'_{1,1}}{\alpha_{1,3}\alpha_{4,2}\alpha_{4,5}\alpha_{7,6}} && \{1,5,6\}\\
\mathfrak{p}_8 &= \frac{\alpha_{1,4}\alpha_{1,7}\alpha_{2,5}\alpha_{3,6}}{\alpha_{1,3}\alpha_{4,2}\alpha_{4,5}\alpha_{7,3}\alpha_{7,6}} && \{3,5,6\} & \qquad \mathfrak{p}_{25} &= \frac{\alpha_{3,2}\alpha_{3,6}}{\alpha_{1,3}\alpha_{7,3}} && \{2,3,4\}\\
\mathfrak{p}_9 &= \frac{\alpha_{1,4}\alpha_{2,5}\alpha_{3,6}}{\alpha_{1,3}\alpha_{4,2}\alpha_{4,5}} && \{2,5,6\} & \qquad \mathfrak{p}_{26} &= \frac{\alpha_{3,6}\alpha_{5,1}}{\alpha_{1,3}\alpha_{4,5}} && \{2,4,5\}\\
\mathfrak{p}_{10} &= \frac{\alpha_{1,4}\alpha_{2,5}\alpha_{6,1}}{\alpha_{1,3}\alpha_{4,2}\alpha_{4,5}\alpha_{7,6}} && \{1,5,6\} & \qquad \mathfrak{p}_{27} &= \frac{\alpha_{3,2}\alpha_{3,6}\alpha'_{1,1}}{\alpha_{1,3}\alpha_{4,5}\alpha_{7,3}\alpha_{7,6}} && \{3,4,5\}\\
\mathfrak{p}_{11} &= \frac{\alpha_{1,4}\alpha_{3,2}\alpha_{3,6}}{\alpha_{1,3}\alpha_{4,2}\alpha_{4,5}\alpha_{7,3}} && \{2,3,5\} & \qquad \mathfrak{p}_{28} &= \frac{\alpha_{2,1}\alpha_{3,6}\alpha_{5,1}}{\alpha_{1,3}\alpha_{4,2}\alpha_{4,5}\alpha_{7,3}} && \{2,3,5\}\\
\mathfrak{p}_{12} &= \frac{\alpha_{1,4}\alpha_{3,2}\alpha_{6,1}}{\alpha_{1,3}\alpha_{4,2}\alpha_{4,5}\alpha_{7,3}\alpha_{7,6}} && \{1,3,5\} & \qquad \mathfrak{p}_{29} &= \frac{\alpha_{3,2}\alpha_{6,1}}{\alpha_{1,3}\alpha_{7,3}\alpha_{7,6}} && \{1,3,4\}\\
\mathfrak{p}_{13} &= \frac{\alpha_{1,7}\alpha_{2,5}\alpha_{3,6}}{\alpha_{1,3}\alpha_{7,3}\alpha_{7,6}} && \{3,4,6\} & \qquad \mathfrak{p}_{30} &= \frac{\alpha_{5,1}\alpha_{6,1}}{\alpha_{1,3}\alpha_{4,5}\alpha_{7,6}} && \{1,4,5\}\\
\mathfrak{p}_{14} &= \frac{\alpha_{1,1}\alpha_{1,7}\alpha_{2,5}}{\alpha_{1,3}\alpha_{4,2}\alpha_{7,3}\alpha_{7,6}} && \{1,3,6\} & \qquad \mathfrak{p}_{31} &= \frac{\alpha_{1,1}\alpha_{3,2}}{\alpha_{1,3}\alpha_{4,2}\alpha_{7,3}} && \{1,2,3\}\\
\mathfrak{p}_{15} &= \frac{\alpha_{1,7}\alpha_{3,6}\alpha_{5,1}}{\alpha_{1,3}\alpha_{4,5}\alpha_{7,3}\alpha_{7,6}} && \{3,4,5\} & \qquad \mathfrak{p}_{32} &= \frac{\alpha_{1,1}\alpha_{5,1}}{\alpha_{1,3}\alpha_{4,2}\alpha_{4,5}} && \{1,2,5\}\\
\mathfrak{p}_{16} &= \frac{\alpha_{1,1}\alpha_{1,7}\alpha_{5,1}}{\alpha_{1,3}\alpha_{4,2}\alpha_{4,5}\alpha_{7,3}\alpha_{7,6}} && \{1,3,5\} & \qquad \mathfrak{p}_{33} &= \frac{\alpha_{1,1}\alpha_{3,2}\alpha'_{1,1}}{\alpha_{1,3}\alpha_{4,2}\alpha_{4,5}\alpha_{7,3}\alpha_{7,6}} && \{1,3,5\}\\
\mathfrak{p}_{17} &= \frac{\alpha_{2,5}\alpha_{3,6}}{\alpha_{1,3}} && \{2,4,6\} & \qquad \mathfrak{p}_{34} &= \frac{\alpha_{2,1}\alpha_{5,1}\alpha_{6,1}}{\alpha_{1,3}\alpha_{4,2}\alpha_{4,5}\alpha_{7,3}\alpha_{7,6}} && \{1,3,5\}
\end{aligned}
\tag{4.3.6}
$$

We are now ready to construct the corresponding element of the Grassmannian. The first step is to introduce the positivity signs $(-1)^{s(i,j)}$ in $\mathcal{M}^C$, which yields the following preliminary matrix

$$
\left(\begin{array}{c|cccccc}
 & 1 & 2 & 3 & 4 & 5 & 6\\ \hline
1 & 1 & 0 & -\mathfrak{p}_{25} & 0 & \mathfrak{p}_{26} & \mathfrak{p}_{17}\\
2 & 0 & 1 & \mathfrak{p}_3+\mathfrak{p}_{29} & 0 & -\mathfrak{p}_5-\mathfrak{p}_{30} & -\mathfrak{p}_{21}\\
4 & 0 & 0 & \mathfrak{p}_6+\mathfrak{p}_{31} & 1 & \mathfrak{p}_2+\mathfrak{p}_{32} & \mathfrak{p}_{22}
\end{array}\right). \tag{4.3.7}
$$

It is straightforward to verify that the minors of this matrix are not linear combinations with coefficients ± 1 of all the flows with the corresponding source sets; the signs in (4.3.7) do not produce the necessary cancellations.

Figure 4.7 shows the closed loops associated to each flow and the corresponding $(-1)^{r+1}$ sign arising from our prescription. We see that only the flow $\mathfrak{p}_{31}$ picks up an additional minus sign. After including it, we obtain the Grassmannian matrix

$$
C = \left(\begin{array}{c|cccccc}
 & 1 & 2 & 3 & 4 & 5 & 6\\ \hline
1 & 1 & 0 & -\mathfrak{p}_{25} & 0 & \mathfrak{p}_{26} & \mathfrak{p}_{17}\\
2 & 0 & 1 & \mathfrak{p}_3+\mathfrak{p}_{29} & 0 & -\mathfrak{p}_5-\mathfrak{p}_{30} & -\mathfrak{p}_{21}\\
4 & 0 & 0 & \mathfrak{p}_6-\mathfrak{p}_{31} & 1 & \mathfrak{p}_2+\mathfrak{p}_{32} & \mathfrak{p}_{22}
\end{array}\right). \tag{4.3.8}
$$

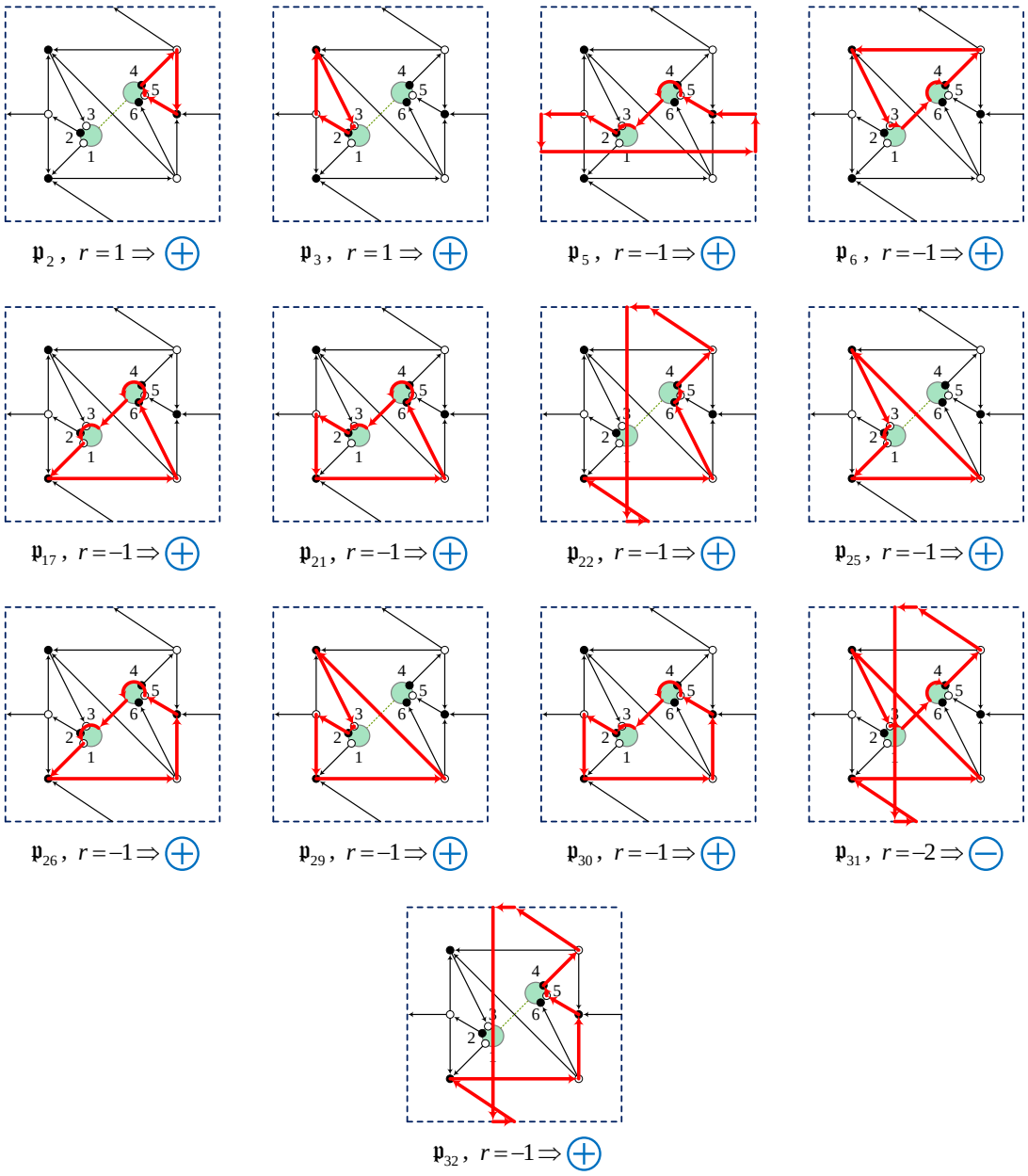

Figure 4.7: Completion of flows into loops inside the unit cell for the example in Figure 4.6, their rotation numbers and the resulting signs.

This gives rise to the cancellations required to obtain the Plücker coordinates

$$\begin{aligned}
\Delta_{1,2,3} &= \mathfrak{p}_6 - \mathfrak{p}_{31} & \Delta_{2,3,4} &= \mathfrak{p}_{25} \\
\Delta_{1,2,4} &= 1 & \Delta_{2,3,5} &= \mathfrak{p}_{11} + \mathfrak{p}_{28} \\
\Delta_{1,2,5} &= \mathfrak{p}_2 + \mathfrak{p}_{32} & \Delta_{2,3,6} &= \mathfrak{p}_{19} \\
\Delta_{1,2,6} &= \mathfrak{p}_{22} & \Delta_{2,4,5} &= \mathfrak{p}_{26} \\
\Delta_{1,3,4} &= \mathfrak{p}_3 + \mathfrak{p}_{29} & \Delta_{2,4,6} &= \mathfrak{p}_{17} \\
\Delta_{1,3,5} &= \mathfrak{p}_1 + \mathfrak{p}_7 + \mathfrak{p}_{12} + \mathfrak{p}_{16} - \mathfrak{p}_{33} + \mathfrak{p}_{34} & \Delta_{2,5,6} &= \mathfrak{p}_9 \\
\Delta_{1,3,6} &= \mathfrak{p}_{14} + \mathfrak{p}_{23} & \Delta_{3,4,5} &= \mathfrak{p}_{15} - \mathfrak{p}_{27} \\
\Delta_{1,4,5} &= \mathfrak{p}_5 + \mathfrak{p}_{30} & \Delta_{3,4,6} &= \mathfrak{p}_{13} \\
\Delta_{1,4,6} &= \mathfrak{p}_{21} & \Delta_{3,5,6} &= \mathfrak{p}_8 + \mathfrak{p}_{20} \\
\Delta_{1,5,6} &= \mathfrak{p}_{10} - \mathfrak{p}_{24} & \Delta_{4,5,6} &= \mathfrak{p}_{18}
\end{aligned} \tag{4.3.9}$$

A quick comparison with (4.3.6) will show that the Plücker coordinates are indeed expressed as a sum of those flows whose source set is the index of the Plücker coordinate, as desired. We note that this example not only is reduced and non-planarizable, but also has multiple boundaries, constituting a rather non-trivial check of our proposal.

4.4 Scattering Amplitude Perspective on Equivalence and Reduction

There are an infinite number of on-shell diagrams. It is thus desirable to come up with a classification of them, i.e. to endow this plethora of diagrams with some structure and order. Such a classification is achieved by identifying equivalence classes of diagrams, which are related by equivalence moves and reductions, as for BFTs. Graph equivalences and reductions are well understood for planar graphs [34]. In particular, they are *all* captured by and can be defined in terms of the operations discussed in §2.6. The realm of non-planar graphs will turn out to be more complicated, since the edge-deletion operation in §2.6.2 is not guaranteed to be a reduction—though all reductions are guaranteed to be of the form of an edge deletion. In this section we will take important steps towards developing a systematic and combinatorial approach, based on the generalized matching and

matroid polytopes, to the classification of general on-shell diagrams, including non-planar ones. For this purpose, it is convenient to define:

- **Region matching:** This term indicates the case in which the regions of the Grassmannian parametrized by different on-shell diagrams coincide. Two necessary conditions in order for two on-shell diagrams to be equivalent are region matching and having the same number of degrees of freedom.
- **Reduction:** An on-shell diagram B is a reduction of an on-shell diagram A, if it is obtained from A by deleting edges and it covers the same region of the Grassmanian as A.

For amplitudes, reducibility is essentially the statement that there exists a variable transformation in (4.2.5) such that one or more variables only appear in the $d\log$ form. In particular, these variables are absent from the matrix C. The idea of reduction leads to the concept of a *reduced graph*:

- **Reduced graph:** A graph is reduced if it is impossible to remove edges from it while covering the same region of the Grassmannian.

The importance of reduced graphs stems from the fact that there are a finite number of them for every scattering process and they contain all information required for addressing certain questions, e.g. determining leading singularities.

Let us be specific about the difference between planar and non-planar diagrams. For planar diagrams, the region of the Grassmannian covered by the graph is fully determined by specifying the non-vanishing Plücker coordinates. Expressed differently, to know which region of the Grassmannian is covered by the degrees of freedom of the on-shell diagram, through the boundary measurement we have introduced in the previous section, it is sufficient to know which points in the matroid polytope are present.

For non-planar diagrams, it is in general not sufficient to simply know which points in the matroid polytope are present, or equivalently which Plücker coordinates are non-zero: it is possible that constraints between Plücker coordinates beyond Plücker relations might exist. These new relations are discussed in detail in §6.4.

Finally, let us mention that non-planar diagrams exhibit additional new features, such as having non-unique reductions [1, 124]. This does not modify the definition

of reductions, but is rather a consequence of the definition.

4.4.1 Combinatorial Implementation in Terms of Polytopes

The characterization of on-shell diagrams outlined above has a powerful implementation in terms of matching and matroid polytopes. First, we note that for diagrams that do not admit constraints among Plücker coordinates beyond the Plücker relations, the matroid polytope is already a perfect diagnostic for graph-equivalence and reducibility. Hence, all of the discussion in §2.6 applies directly to all such diagrams; in particular, the efficient approach to reducibility can be used without modifications.

In the presence of new constraints, preserving the matroid polytope is a necessary but not sufficient condition for ensuring graph-equivalence and reductions. As we shall see in §6.4, these new constraints are completely characterized by the matching polytope. Hence, in order to determine whether two diagrams are move-equivalent or related by a reduction, we must:

- Ensure that the matroid polytope is preserved, *and*
- Use the matching polytope to determine whether the two diagrams are subject to the same constraints among Plücker coordinates.

Together, these two conditions can check the move-equivalence or reduction between any pair on-shell diagrams. In particular, cases without new constraints among Plücker coordinates, e.g. all planar diagrams and a vast proportion of non-planar diagrams, are diagnosed by the same two conditions, with the second condition being trivially satisfied.

4.5 Singularity Structure of On-shell Diagrams: New Methods

We have studied how the degrees of freedom of the on-shell diagram are mapped to elements of the Grassmannian. These then appear in the on-shell form whose

integration yields the corresponding scattering amplitude. As already explained in §4.2.3, the full singularity structure of the amplitude is obtained by starting from a reduced graph, and sequentially deleting removable edges.

From a mathematical viewpoint such a decomposition is interesting because, for planar graphs, it corresponds to the positroid stratification of the totally non-negative Grassmannian. Recall that the positroid stratification can also be regarded as the intersection between the matroid stratification and the totally non-negative Grassmannian. More generally, as we discuss in §4.5.2, for arbitrary graphs the decomposition considered in this section can be regarded as a *partial matroid decomposition*, which we shall call the *combinatorial decomposition*. This will allow us to go beyond the positive regions of the Grassmannian, which are specific to the planar diagrams.

The combinatorial decomposition stratifies a region or cell in the Grassmannian into its constituent lower-dimensional components, and can be seen as characterizing the entire boundary structure of this region. In this way it provides a detailed geometric characterization of the Grassmannian element.

The combinatorial decomposition can be nicely visualized in terms of a poset, in which every node corresponds to a reduced graph and arrows indicate the deletion of a removable edge. For planar graphs, every site in the poset corresponds to a positroid stratum, represented by a specific matroid stratum. Figure 4.8 presents the simple example of the positroid decomposition of the top-cell of $G(2,4)$, obtained by this procedure.[10]

In the following sections we shall show that the combinatorial decomposition of the Grassmannian can be obtained in a different but very efficient way, which makes heavy use of the geometry already associated to the graphs [3]. This alternative way of stratifying the Grassmannian element is computationally very powerful, and never makes explicit use of Plücker coordinates, removable edges or reducibility. It is deeply motivated by thinking of graphs and geometry in terms of BFTs, and works for all on-shell diagram that do not admit new constraints among Plücker

[10]In the physics literature, the positroid stratification of $G(2,4)$ has appeared in [34].

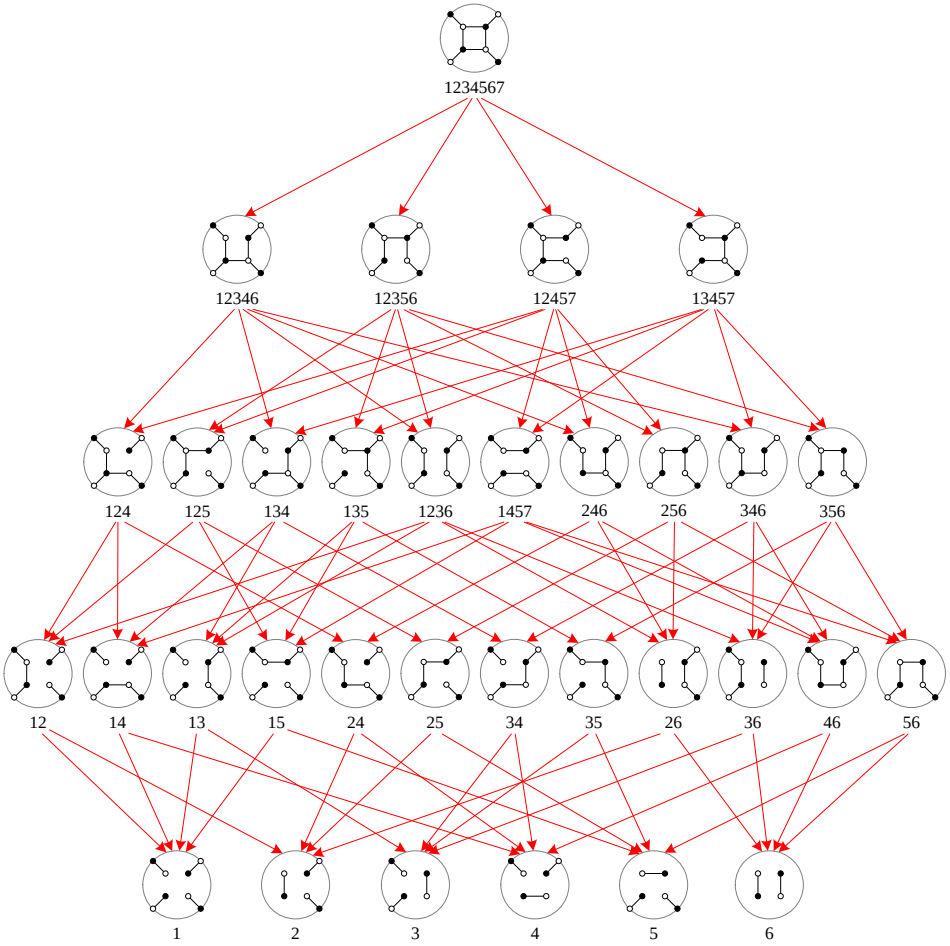

Figure 4.8: Positroid decomposition of $G(2,4)$. Each site corresponds to a positroid stratum, and we indicate the associated graph and surviving perfect matchings.

coordinates.

4.5.1 Combinatorial Decomposition Via Polytopes

We will first apply our ideas to planar graphs, which are well-known to experts. We shall then move on to treating the non-planar case, which deserves a detailed study of its own, since it remains relatively unexplored.

Step 1: Edge Removal. The first step of the process corresponds to removing every possible equivalence class of edges of the graph, one at a time. Two edges are considered equivalent if they participate in the same set of perfect matchings.

Edges can become equivalent *after* removing other edges and the associated perfect matchings. This process terminates when the surviving graph coincides with a perfect matching of the original one, i.e. to a vertex in the matching polytope. Notice that *any* edge can be removed, i.e. there is no restriction to removable edges. The graphs generated by this procedure and their relations can be organized into an Eulerian poset, which is different from the poset discussed in the previous section.

Interestingly, removing edges is equivalent to constructing the *face lattice*[11] of the matching polytope [101]. Let us explain in more detail the structure of the poset for the matching polytope. Consider a matching polytope of dimension d_{matching}. Its boundary has dimension equal to $(d_{\text{matching}} - 1)$ and is a union of facets. Each facet is defined as the intersection of the boundary with a $(d_{\text{matching}} - 1)$-dimensional hyperplane. In turn, each of these facets has a $(d_{\text{matching}} - 2)$-dimensional boundary, which can also be decomposed into faces, and so on. The face lattice of the matching polytope is generated by iterating the boundary operator until reaching 0-dimensional faces.

In this approach, faces are directly determined from the positions of points in the matching polytope. Computer applications constructing the set of faces for arbitrary polytopes are publicly available, see e.g. Polymake [125]. Contrary to the method based on removing edges, Polymake only requires a single bipartite graph at the initial step, for determining the matching polytope.

Example. Let us consider the planar graph associated to the top-cell of $G(2,4)$, which is shown in Figure 4.1. The matching polytope has seven different points corresponding to its perfect matchings and is given by the following perfect matching matrix

$$P = \left(\begin{array}{c|ccccccc} & p_1 & p_2 & p_3 & p_4 & p_5 & p_6 & p_7 \\ \hline X_{1,2} & 0 & 1 & 0 & 0 & 0 & 1 & 0 \\ X_{1,4} & 0 & 0 & 1 & 0 & 0 & 1 & 0 \\ X_{3,1} & 0 & 0 & 0 & 0 & 1 & 0 & 1 \\ X_{5,1} & 0 & 0 & 0 & 1 & 0 & 0 & 1 \\ X_{2,3} & 1 & 0 & 1 & 1 & 0 & 0 & 0 \\ X_{2,5} & 1 & 0 & 1 & 0 & 1 & 0 & 0 \\ X_{4,5} & 1 & 1 & 0 & 0 & 1 & 0 & 0 \\ X_{4,3} & 1 & 1 & 0 & 1 & 0 & 0 & 0 \end{array}\right). \tag{4.5.1}$$

[11] In the face lattice we do not include the empty set.

This matrix defines a 4d polytope, as becomes clear by row-reduction.

Let us briefly discuss the relation between edge removal and lower-dimensional faces of the matching polytope. Recall that removing an edge X_i results in eliminating the perfect matchings p_μ for which the corresponding entry $P_{i\mu}$ is equal to 1. In this example, we obtain eight different subgraphs at the first level, corresponding to eight 3d faces. We then continue removing additional edges, successively obtaining lower-dimensional faces until reaching the vertices of the matching polytope, which correspond to the 7 perfect matchings. The resulting face lattice is shown in Figure 4.10.

Step 2: Identification. The final step in the combinatorial decomposition involves identifying perfect matchings associated to the same point in the matroid polytope, equivalently to the same Plücker coordinate. This results in the identification, or more precisely merging, of nodes in the poset for the face lattice of the matching polytope we constructed in the previous section.

The identification of perfect matchings can give rise to two qualitatively different types of identifications. We refer to them as *horizontal* and *vertical* identifications, following their effect on points on the poset. They are defined as follows:

- **Horizontal identifications:** they merge nodes in the poset that sit at the same level. Their effect on the matching polytope is to identify different faces without affecting their dimensionalities.

- **Vertical identifications:** from the viewpoint of the poset, they merge nodes at different levels. They identify different points in a given face of the matching polytope and result in a lower-dimensional one.

Figure 4.9 shows simple examples of each class of identification at the level of the matching polytope. We emphasize that this figure is only schematic; generally, more than two perfect matchings can be simultaneously involved in identifications, and the identification of faces will in general produce an object which can no longer be seen as a polytope.

This approach to decomposition makes certain general properties of the final poset obtained after identifications rather clear. In particular:

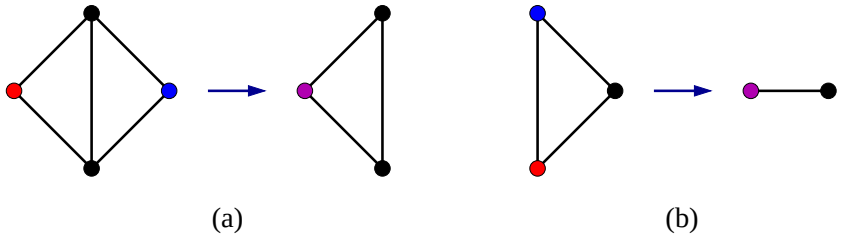

Figure 4.9: Two types of identifications: (a) horizontal and (b) vertical. Here we show the action on points in the matching polytope. Points, i.e. perfect matchings, to be identified are shown in blue and red. Purple dots indicate the resulting points after identification.

- The number of levels is equal to the dimensions of the matching polytope of a reduced graph in the equivalence class of the starting point plus one. This number is invariant under graph equivalence, and does not depend on the initial graph being reduced.

- The number of sites in the lowest level of the poset is equal to the number of points in the matroid polytope.

Finally, we note that the combinatorial decomposition does not require irreducibility at any step. Not only is restricting to removable edges, i.e. to reduced graphs at intermediate steps, not necessary, but the starting point also does not need to be a reduced graph. In [3] we illustrated this point with the example of the reducible graph in Figure 2.8, which as shown in §2.6.2 reduces to Figure 4.1.

Example. Returning to the $G(2,4)$ example, the matroid polytope in this case is given by:

$$G_{\text{matroid}} = \left(\begin{array}{c|ccccccc} & p_1 & p_2 & p_3 & p_4 & p_5 & p_6 & p_7 \\ \hline X_{2,3} & 1 & 0 & 1 & 1 & 0 & 0 & 0 \\ X_{2,5} & 1 & 0 & 1 & 0 & 1 & 0 & 0 \\ X_{4,5} & 1 & 1 & 0 & 0 & 1 & 0 & 0 \\ X_{4,3} & 1 & 1 & 0 & 1 & 0 & 0 & 0 \end{array}\right). \tag{4.5.2}$$

The 7 perfect matchings are mapped to 6 points, with p_6 and p_7 becoming coincident. Figure 4.10 shows the face lattice for the matching polytope. Colored nodes

need to be merged with some of the white ones, following the identification of p_6 and p_7: green and blue nodes are subject to horizontal and vertical identifications, respectively. White nodes correspond to the nodes in Figure 4.8. It is straightforward to verify that the entire structure of Figure 4.8, i.e. including its arrows, is recovered by the identifications.

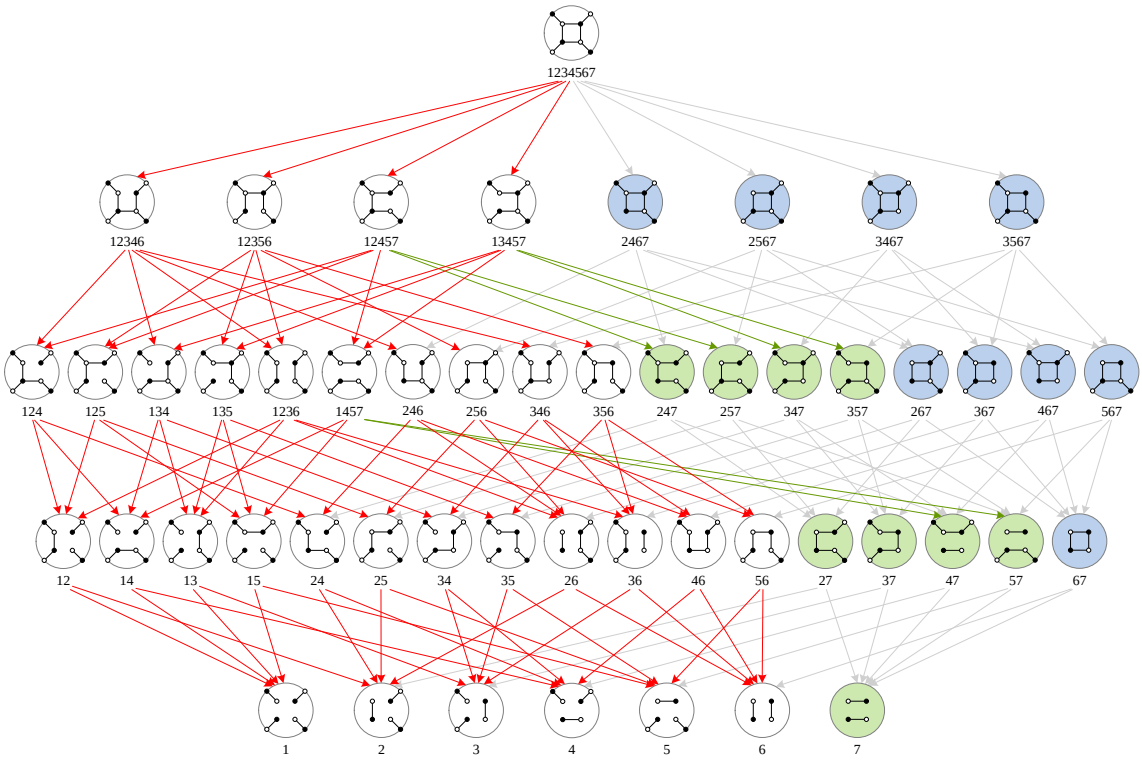

Figure 4.10: Face lattice of the matching polytope for the graph in Figure 4.1. At each point, we indicate the corresponding graph and the surviving perfect matchings. When p_6 and p_7 are identified, green and blue nodes in the poset are subject to horizontal and vertical identifications, respectively.

4.5.2 Relation to the Matroid Stratification

In the previous section we introduced the combinatorial decomposition of a bipartite diagram and discussed different implementations.

Here we consider another natural decomposition we can relate to a bipartite graph, which is the matroid stratification of the associated Grassmannian element, and comment on their relation. As was made clear in §4.1.7, and further emphasized

in the construction of the boundary measurement, perfect matchings p_μ are associated to the Plücker coordinates Δ_I whose index I is the source set of the perfect orientation of p_μ, i.e. $\Delta_I \leftrightarrow \{p_\mu^I\}$.

In this way it is possible to translate sites in the combinatorial decomposition to matroid strata. However, generally not all matroid strata can be generated by removing edges from a fixed starting graph. The combinatorial decomposition can thus be regarded as a *partial matroid decomposition*. In Appendix A.3, we speculate on possible ways to achieve the complete matroid stratification in terms of bipartite graphs.

In practical terms, the combinatorial decomposition is given by the intersection between the matroid stratification and the lattice generated by all possible edge removals. For planar graphs, this reduction can be alternatively obtained by intersecting the matroid stratification with the totally non-negative Grassmannian, as explained in §4.1.6.

Example. Returning to the example in Figure 4.8, we can read off the relation between Plücker coordinates and perfect matchings from (4.3.4). Using the figure, the matroid strata we are left with are

$d=4$	$\{12,13,14,23,24,34\}$
$d=3$	$\{12,13,14,23,24\},\{12,13,14,24,34\},$ $\{12,13,23,24,34\},\{13,14,23,24,34\}$
$d=2$	$\{12,13,14\},\{12,13,23\},\{12,14,24\},\{12,23,24\},\{13,14,34\},\{13,23,34\},$ $\{14,24,34\},\{23,24,34\},\{12,13,24,34\},\{13,14,23,24\},$
$d=1$	$\{12,13\},\{12,14\},\{12,23\},\{12,24\},\{13,14\},\{13,23\},\{13,34\},\{14,24\},$ $\{14,34\},\{23,24\},\{23,34\},\{24,34\},$
$d=0$	$\{12\},\{13\},\{14\},\{23\},\{24\},\{34\},$

(4.5.3)

where we have used the Plücker relation

$$\Delta_{12}\,\Delta_{34}+\Delta_{23}\,\Delta_{14}=\Delta_{13}\,\Delta_{24} \tag{4.5.4}$$

in order to recognize the dimension of each matroid stratum and to arrange it at the correct level. The only matroid strata which do not appear are $\{12,13,14,23,34\}$, $\{12,14,23,24,34\}$ and $\{12,14,23,34\}$.

The table in (4.5.3) is indeed the positroid stratification depicted in Figure 4.11, which is identical to Figure 4.8. For each graph we show its matroid labels (dark green) and its positroid labels (light green).

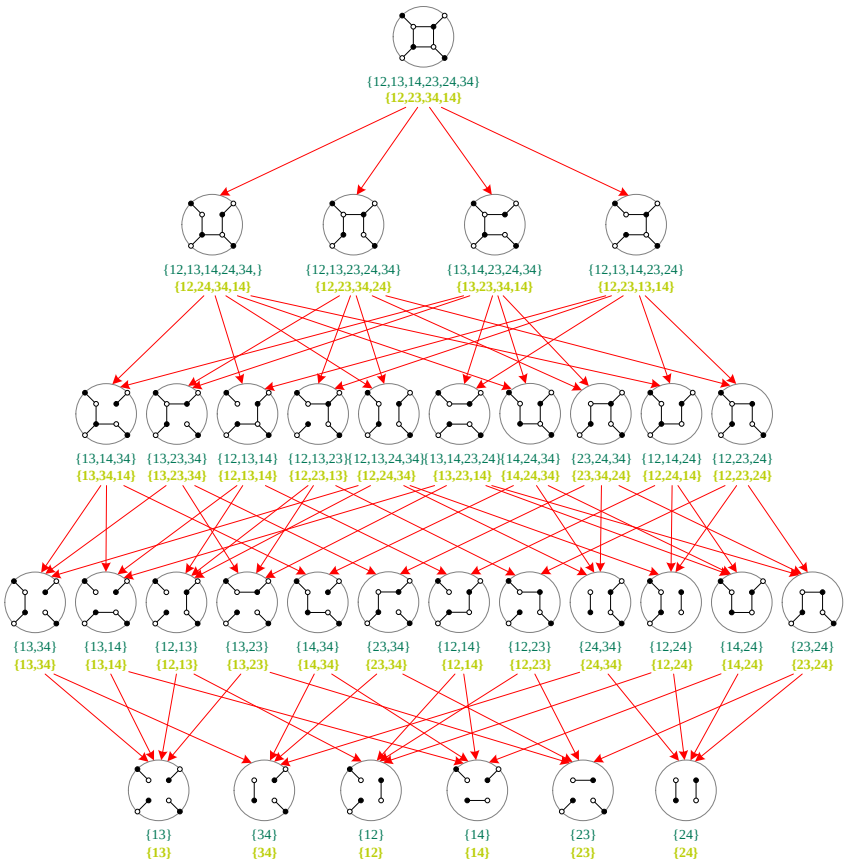

Figure 4.11: Positroid stratification of $G(2,4)$. Each graph maps to a matroid stratum whose matroid is indicated in dark green. The positroid stratum containing the matroid stratum is shown in light green. We see that all positroid strata are present, and no two graphs are in the same positroid stratum.

4.5.3 Combinatorial Decomposition of Non-Planar Graphs

In this section we will apply the techniques introduced in §4.5.1 to a non-planar diagram. We present in detail an example and construct its decomposition. As we will see, the combinatorial decomposition of non-planar on-shell diagrams does not correspond to the positroid stratification of the Grassmannian, but is still a subset of the matroid stratification. Appendix A.3 collects some ideas about how the full

matroid stratification might be achieved by combining different graphs. Additional examples can be found in [3].

Example: Graph on the Annulus. We begin by illustrating our techniques with the example displayed in Figure 4.12. This example has 15 perfect matchings.

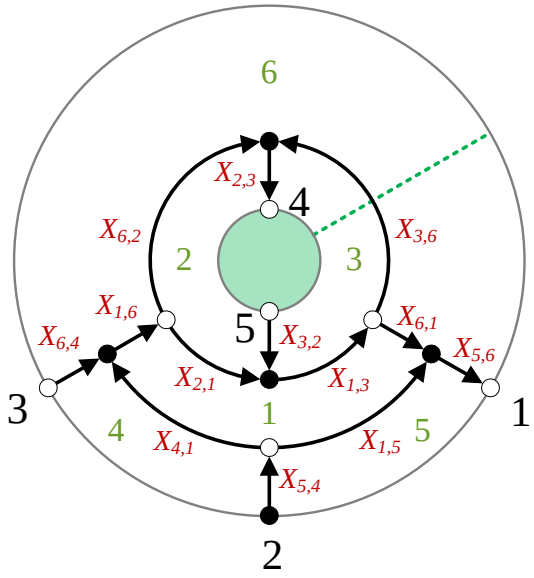

Figure 4.12: A non-planar graph for a top-dimensional region of $G(3,5)$. The cut is indicated by a green dotted line. Arrows show the perfect orientation associated to the perfect matching p_1, which contains edges $X_{1,3}$, $X_{1,6}$, $X_{2,3}$ $X_{5,4}$ and $X_{5,6}$.

The matching polytope is given by

$$P = \left(\begin{array}{c|cccccccccccccc} & p_1 & p_2 & p_3 & p_4 & p_5 & p_6 & p_7 & p_8 & p_9 & p_{10} & p_{11} & p_{12} & p_{13} & p_{14} & p_{15} \\ \hline X_{1,3} & 1 & 1 & 1 & 1 & 1 & 0 & 0 & 0 & 0 & 0 & 0 & 0 & 0 & 0 & 0 \\ X_{1,6} & 1 & 1 & 0 & 0 & 0 & 1 & 1 & 1 & 0 & 0 & 0 & 0 & 0 & 0 & 0 \\ X_{3,6} & 0 & 0 & 0 & 0 & 0 & 0 & 1 & 1 & 0 & 0 & 1 & 0 & 1 & 0 & 1 \\ X_{6,1} & 0 & 0 & 0 & 0 & 0 & 1 & 0 & 0 & 1 & 1 & 0 & 1 & 0 & 1 & 0 \\ X_{1,5} & 0 & 1 & 0 & 0 & 1 & 0 & 0 & 1 & 0 & 0 & 0 & 0 & 0 & 0 & 1 \\ X_{2,1} & 0 & 0 & 0 & 0 & 0 & 0 & 0 & 0 & 1 & 1 & 1 & 0 & 1 & 0 & 1 \\ X_{4,1} & 0 & 0 & 0 & 1 & 0 & 0 & 0 & 0 & 0 & 1 & 0 & 0 & 1 & 1 & 0 \\ X_{6,2} & 0 & 0 & 1 & 1 & 1 & 0 & 0 & 0 & 0 & 0 & 0 & 1 & 0 & 1 & 0 \\ \hline X_{2,3} & 1 & 1 & 0 & 0 & 0 & 1 & 0 & 0 & 1 & 1 & 0 & 0 & 0 & 0 & 0 \\ X_{5,4} & 1 & 0 & 1 & 0 & 0 & 1 & 1 & 0 & 1 & 0 & 1 & 1 & 0 & 0 & 0 \\ X_{5,6} & 1 & 0 & 1 & 1 & 0 & 0 & 1 & 0 & 0 & 0 & 1 & 0 & 1 & 0 & 0 \\ X_{3,2} & 0 & 0 & 0 & 0 & 0 & 1 & 1 & 1 & 0 & 0 & 0 & 1 & 0 & 1 & 0 \\ X_{6,4} & 0 & 0 & 1 & 0 & 1 & 0 & 0 & 0 & 1 & 0 & 1 & 1 & 0 & 0 & 1 \end{array}\right) \tag{4.5.5}$$

and is 6-dimensional. The matroid polytope is given by the last 5 lines of P and has dimension 4. This example has 10 non-vanishing Plücker coordinates, and the following Plücker relations:

$$\Delta_{125}\Delta_{134} - \Delta_{124}\Delta_{135} + \Delta_{123}\Delta_{145} = 0 \ , \quad \Delta_{125}\Delta_{234} - \Delta_{124}\Delta_{235} + \Delta_{123}\Delta_{245} = 0 \ ,$$
$$\Delta_{135}\Delta_{234} - \Delta_{134}\Delta_{235} + \Delta_{123}\Delta_{345} = 0 \ , \quad \Delta_{145}\Delta_{234} - \Delta_{134}\Delta_{245} + \Delta_{124}\Delta_{345} = 0 \ ,$$
$$\Delta_{145}\Delta_{235} - \Delta_{135}\Delta_{245} + \Delta_{125}\Delta_{345} = 0$$

of which only 3 are independent.

The face lattice of the matching polytope contains 412 elements of various dimensions; it is therefore very impractical to draw the full poset. Below we present the first level in detail; subsequent levels follow analogously.

First Level: Dimension 5. This example has 13 edges. We now proceed by removing them to obtain the first level of the face lattice of the matching polytope, which contains the following faces:

Removed edge	Face
$X_{1,3}$	$p_6, p_7, p_8, p_9, p_{10}, p_{11}, p_{12}, p_{13}, p_{14}, p_{15}$
$X_{1,6}$	$p_3, p_4, p_5, p_9, p_{10}, p_{11}, p_{12}, p_{13}, p_{14}, p_{15}$
$X_{3,6}$	$p_1, p_2, p_3, p_4, p_5, p_6, p_9, p_{10}, p_{12}, p_{14}$
$X_{6,1}$	$p_1, p_2, p_3, p_4, p_5, p_7, p_8, p_{11}, p_{13}, p_{15}$
$X_{1,5}$	$p_1, p_3, p_4, p_6, p_7, p_9, p_{10}, p_{11}, p_{12}, p_{13}, p_{14}$
$X_{2,1}$	$p_1, p_2, p_3, p_4, p_5, p_6, p_7, p_8, p_{12}, p_{14}$
$X_{4,1}$	$p_1, p_2, p_3, p_5, p_6, p_7, p_8, p_9, p_{11}, p_{12}, p_{15}$
$X_{6,2}$	$p_1, p_2, p_6, p_7, p_8, p_9, p_{10}, p_{11}, p_{13}, p_{15}$
$X_{2,3}$	$p_3, p_4, p_5, p_7, p_8, p_{11}, p_{12}, p_{13}, p_{14}, p_{15}$
$X_{5,4}$	$p_2, p_4, p_5, p_8, p_{10}, p_{13}, p_{14}, p_{15}$
$X_{5,6}$	$p_2, p_5, p_6, p_8, p_9, p_{10}, p_{12}, p_{14}, p_{15}$
$X_{3,2}$	$p_1, p_2, p_3, p_4, p_5, p_9, p_{10}, p_{11}, p_{13}, p_{15}$
$X_{6,4}$	$p_1, p_2, p_4, p_6, p_7, p_8, p_{10}, p_{13}, p_{14}$

(4.5.6)

where the faces in the table show the surviving perfect matchings after removal of the corresponding edge. In order to find the decomposition we are interested in, we proceed by identifying perfect matchings which have the same coordinate in the

matroid polytope, as explained in §4.5.1. This can be done by looking at (4.5.5) and is:

$$\{p_1\}\quad\{p_2,p_{10}\}\quad\{p_3,p_{11}\}\quad\{p_4,p_{13}\}\quad\{p_5,p_{15}\}\quad\{p_6\}\quad\{p_7\}\quad\{p_8,p_{14}\}\quad\{p_9\}\quad\{p_{12}\}\,. \tag{4.5.7}$$

The faces then become:

Removed edge	Face	Plücker Coordinates
$X_{1,3}$	$p_6,p_7,p_8,p_9,p_{10},p_{11},p_{12},p_{13},p_{15}$	$\Delta_{123},\Delta_{234},\Delta_{134},\Delta_{125},\Delta_{135},\Delta_{245},\Delta_{124},\Delta_{345},\Delta_{145}$
$X_{3,6}$	$p_1,p_2,p_3,p_4,p_5,p_6,p_9,p_{12},p_{14}$	$\Delta_{235},\Delta_{135},\Delta_{245},\Delta_{345},\Delta_{145},\Delta_{123},\Delta_{125},\Delta_{124},\Delta_{134}$
$X_{1,5}$	$p_1,p_3,p_4,p_6,p_7,p_9,p_{10},p_{12},p_{14}$	$\Delta_{235},\Delta_{245},\Delta_{345},\Delta_{123},\Delta_{234},\Delta_{125},\Delta_{135},\Delta_{124},\Delta_{134}$
$X_{2,1}$	$p_1,p_2,p_3,p_4,p_5,p_6,p_7,p_8,p_{12}$	$\Delta_{235},\Delta_{135},\Delta_{245},\Delta_{345},\Delta_{145},\Delta_{123},\Delta_{234},\Delta_{134},\Delta_{124}$
$X_{4,1}$	$p_1,p_2,p_3,p_5,p_6,p_7,p_8,p_9,p_{12}$	$\Delta_{235},\Delta_{135},\Delta_{245},\Delta_{145},\Delta_{123},\Delta_{234},\Delta_{134},\Delta_{125},\Delta_{124}$
$X_{6,2}$	$p_1,p_2,p_6,p_7,p_8,p_9,p_{11},p_{13},p_{15}$	$\Delta_{235},\Delta_{135},\Delta_{123},\Delta_{234},\Delta_{134},\Delta_{125},\Delta_{245},\Delta_{345},\Delta_{145}$
$X_{1,6}$	$p_3,p_4,p_5,p_9,p_{10},p_{12},p_{14}$	$\Delta_{245},\Delta_{345},\Delta_{145},\Delta_{125},\Delta_{135},\Delta_{124},\Delta_{134}$
$X_{6,1}$	$p_1,p_2,p_3,p_4,p_5,p_7,p_8$	$\Delta_{235},\Delta_{135},\Delta_{245},\Delta_{345},\Delta_{145},\Delta_{234},\Delta_{134}$
$X_{2,3}$	$p_3,p_4,p_5,p_7,p_8,p_{12}$	$\Delta_{245},\Delta_{345},\Delta_{145},\Delta_{234},\Delta_{134},\Delta_{124}$
$X_{5,4}$	p_2,p_4,p_5,p_8	$\Delta_{135},\Delta_{345},\Delta_{145},\Delta_{134}$
$X_{5,6}$	$p_2,p_5,p_6,p_8,p_9,p_{12}$	$\Delta_{135},\Delta_{145},\Delta_{123},\Delta_{134},\Delta_{125},\Delta_{124}$
$X_{3,2}$	p_1,p_2,p_3,p_4,p_5,p_9	$\Delta_{235},\Delta_{135},\Delta_{245},\Delta_{345},\Delta_{145},\Delta_{125}$
$X_{6,4}$	p_1,p_2,p_4,p_6,p_7,p_8	$\Delta_{235},\Delta_{135},\Delta_{345},\Delta_{123},\Delta_{234},\Delta_{134}$

(4.5.8)

In the table above we show the surviving perfect matchings after removing the corresponding edge in the graph, and after the identifications in (4.5.7). We also show the non-vanishing Plücker coordinates for each subgraph.

As a consequence of the identifications, the faces in the lower half of the table are of dimension lower than 5 and get identified with other lower-dimensional ones, i.e. they are subject to vertical identifications. This can be deduced by counting the surviving Plücker coordinates and relevant Plücker relations (4.5.6). Hence $X_{1,6}$, $X_{6,1}$, $X_{2,3}$, $X_{5,4}$, $X_{5,6}$, $X_{3,2}$ and $X_{6,4}$ are not removable edges. For the remaining 6 boundaries there is no horizontal identification at this level, so the 6 removable edges are $X_{1,3}$, $X_{3,6}$, $X_{1,5}$, $X_{2,1}$, $X_{4,1}$ and $X_{6,2}$. The removal of any of these edges yields a 5-dimensional element of the Grassmannian. Each of these corresponds to a differential form which is a singularity in the sense explained in §4.2.3. Moreover,

each of the boundaries also corresponds to a matroid stratum with 9 elements each, where the elements are given by the indices of the Plücker coordinates in (4.5.8).

Full Combinatorial Decomposition. To represent the boundaries of the entire poset, we group the elements in each level of the poset by how many perfect matchings they have, thus presenting the information of each level by pairs of numbers, where the first specifies the number of faces of a certain type and the second specifies the type. For example, 14[6] means there are 14 faces, each containing 6 perfect matchings. This information is presented in Table 4.1.

d	**Faces of matching polytope**
5	1[8], 2[9], 8[10], 2[11]
4	11[5] 14[6], 23[7], 12[8]
3	67[4], 46[5], 13[6]
2	112[3], 19[4]
1	67[2]
0	15[1]

Table 4.1: Faces of the matching polytope. At each level of dimension d, a pair of numbers $m[n]$ indicates that there are m boundaries consisting of n perfect matchings.

After the identification (4.5.7), 272 of the faces get identified with other boundaries, to yield a poset with 140 elements, described by Table 4.2. It is straightforward to verify that these tables agree with the detailed analysis of the first level presented before.

As a further check, using the methods introduced in §2.6.3 and applying the identification (4.5.7) it is straightforward to check that Table 4.2 is consistent with the poset obtained by deleting only removable edges.

d	**Matroids**
5	6[9]
4	5[6], 6[7], 6[8]
3	5[4], 5[24], 6[6]
2	30[3], 12[4]
1	30[2]
0	10[1]

Table 4.2: Matroids in the decomposition of the diagram shown in Figure 4.12. At each level, a pair of numbers $m[n]$ indicates that there are m matroids consisting of n bases.

4.5.4 Non-Eulerian Posets

The face lattice of a convex polytope is a graded poset. Moreover this poset is Eulerian, which means that the number of elements of even dimension is one more than the number of elements of odd dimension, i.e.

$$\sum_{i=0}^{d}(-1)^i N_B^{(i)} = 1, \tag{4.5.9}$$

where d is the dimension of the polytope and $N_B^{(i)}$ is the number of faces of the polytope of dimension i.[12] This quantity is known as the *Euler number*.

As a check that the face lattice of the matching polytope for non-planar graphs can be obtained through successive edge removal, we evaluate the Eulerian number in the previous example:

$$\sum_{i=0}^{6}(-1)^i N_B^{(i)} = 15 - 67 + 131 - \ldots + 1 = 1\ . \tag{4.5.10}$$

While the positroid stratification was shown to be Eulerian [126], for non-planar cases the combinatorial decomposition is in general not Eulerian. The example

[12]If we were to include the empty set in our face lattice, the number of boundaries would sum to 0 rather than 1.

above is an excellent confirmation of this fact:

$$\sum_{i=0}^{6}(-1)^i N_B^{(i)} = 10 - 30 + 42 - \ldots + 1 = -1 \,. \tag{4.5.11}$$

In [3] we provide an additional example where the Euler number is seen to be 14. The appearance of non-Eulerian posets should not be surprising: due to the nature of the identifications involved in the combinatorial decomposition, the resulting poset will in general not describe the face lattice of a geometric polytope.

4.6 Conclusions

We presented a detailed investigation of the geometric and combinatorial structures, which are ingrained in $\mathcal{N} = 4$ SYM scattering amplitudes at a fundamental level. Such objects become manifest when formulating gauge theories in terms of on-shell diagrams, equivalently bipartite graphs. We extended these correspondences along various directions, most notably by the inclusion of non-planarity. The new structures we uncovered are natural candidates to arise in scattering amplitudes beyond the planar limit.

As part of our investigation, we introduced a new combinatorial decomposition of the Grassmannian, which reduces to its positroid stratification for planar graphs. We explained how this decomposition can be directly obtained from the matching and matroid polytopes.

We also extended the boundary measurement, which maps bipartite graphs to the Grassmannian, to graphs on surfaces of arbitrary genus and arbitrary number of boundaries.

Our work suggests that general bipartite graphs, i.e. including non-planar ones, can lead to a more refined description of the Grassmannian. It would be extremely interesting to continue investigating, along the lines of Appendix A.3, how they can be exploited for the matroid stratification of the Grassmannian.

Chapter 5

Anatomy of the Amplituhedron

This chapter initiates a comprehensive investigation of the geometry of the amplituhedron, a recently found geometric object whose volume calculates the integrand of scattering amplitudes in planar $\mathcal{N} = 4$ SYM theory.

5.1 The Amplituhedron

In this section we provide a brief introduction to the amplituhedron. We refer the reader to [79, 80] for further details.

5.1.1 Tree-Level Amplituhedron

The amplituhedron is a generalization of the positive Grassmannian conjectured to give all scattering amplitudes in planar $\mathcal{N} = 4$ SYM theory when integrated over with an appropriate volume form. The amplituhedron can be regarded as a generalization of the interior of a set of n vertices Z^I of dimension $(k + 4)$, where $(k+2)$ is the number of negative-helicity gluons, $I = 1, 2, \ldots, k+4$, and n is the total number of external gluons. In this notation, $k = 0$ corresponds to MHV amplitudes, contrary to our definition in Chapter 4. This shift by $k \to k - 2$ will simplify many of the expressions in this chapter; we hope the reader will not be confused by it. These vertices can be combined into a matrix Z^I_a, where $a = 1, 2, \ldots, n$. In order to have a notion of interior we need vertices to be ordered in a specific way. In the familiar 2-dimensional case of polygons, vertices must be cyclically ordered to avoid

the crossing of external edges connecting consecutive vertices. The generalization of this cyclicity constraint takes the form of a positivity condition on the matrix Z_a^I: all maximal minors of Z_a^I must be positive, i.e. $Z_a^I \in M_+(4+k,n)$ where $M_+(4+k,n)$ is the space of positive $(4+k)\times n$ matrices.

External vertices form a polytope. For $k=1$ we consider a point in the interior of this polytope, which corresponds to a linear combination of the external vertices, where the coefficients must be positive. Each of these points will be considered projectively, and can thus be seen as 1-planes (or lines) in $k+4$ dimensions. For general k, we consider a k-plane and impose positivity conditions on the matrix of coefficients of its expansion in terms of external points. Explicitly, a k-plane Y in the interior of the tree-level amplituhedron is given by

$$Y = C \cdot Z\,, \tag{5.1.1}$$

where Z is the $(k+4)\times n$ matrix of external vertices, C is a $k\times n$ matrix in $G_+(k,n)$, and Y is the tree-level amplituhedron interior, given by a $k\times(k+4)$ matrix.[1] We are not imposing positivity on each of the k rows of the matrix C, but a condition on how the rows of C interact with each other such that minors are positive. As a result, the amplituhedron is *not* simply given by k copies of "the interior of the vertices", but it is a more complicated geometric object. We can also think of the amplituhedron as a map:

$$G_+(k,n) \xrightarrow{Z} G(k,k+4)\,. \tag{5.1.2}$$

The GL(k) degree of freedom of the Grassmannian, which acts on C, must also apply to Y, thus implying that the matrix $Y \in G(k,k+4)$.

[1] A warning to the reader: whenever we refer to the positive Grassmannian $G_+(k,n)$, we mean the totally non-negative Grassmannian. The boundaries of this space arise when the positive degrees of freedom become zero. Similarly, we will use positive as a synonym of non-negative and emphasize when a given quantity is not zero. This slight abuse of terminology will persist throughout; we hope it will not cause any confusion.

5.1.2 Loop Geometry

Each point of the tree-level amplituhedron spans a k-plane in $(k+4)$ dimensions; the full amplituhedron spans all possible k-planes in $(k+4)$ dimensions. For each point, the transverse space is 4-dimensional and this is where the loop-level part of the amplituhedron lives. The degrees of freedom of each loop span a 2-plane in this transverse space. Let us start our discussion with the $k=0$ case, which at tree-level is given by the empty projective space $\mathbb{P}^3$, since Y is 0-dimensional. At loop level, it corresponds to what we call the pure *loop geometry*. In this case, every loop $\mathcal{L}_{(i)}$ is a different linear combination of the external vertices, which lies in $\mathbb{P}^3$:

$$\mathcal{L}_{(i)} = D_{(i)} \cdot Z \,, \tag{5.1.3}$$

where the Z's are 4-dimensional vectors, $D_{(i)} \in G_+(2,n)$ maps the vertices in Z to the transverse space, and so $\mathcal{L}_{(i)} \in G(2,4)$. Multiple loops are implemented by increasing the number of matrices $D_{(i)}$:

$$\begin{pmatrix} \mathcal{L}_{(1)} \\ \mathcal{L}_{(2)} \\ \vdots \\ \mathcal{L}_{(L)} \end{pmatrix} = \begin{pmatrix} D_{(1)} \\ D_{(2)} \\ \vdots \\ D_{(L)} \end{pmatrix} \cdot Z \,. \tag{5.1.4}$$

The matrices $D_{(i)}$ satisfy *extended positivity* conditions, i.e. for any subset of them we define

$$D_{(ij)} = \begin{pmatrix} D_{(i)} \\ D_{(j)} \end{pmatrix}, \qquad D_{(ijk)} = \begin{pmatrix} D_{(i)} \\ D_{(j)} \\ D_{(k)} \end{pmatrix}, \text{ etc.} \tag{5.1.5}$$

and demand all maximal minors of each of these extended matrices to be positive, namely $D_{(ij)} \in M_+(4,n)$, $D_{(ijk)} \in M_+(6,n)$, etc. In general, $D_{(a_1 \cdots a_m)} \in M_+(2m,n)$. These conditions apply only for $m \leq n/2$. In the special case of $n=4$ and arbitrary L, the only surviving conditions are mutual positivities: $D_{(ij)} \in M_+(4,n)$ for all pairs of i and j.

5.1.3 The Full Amplituhedron

To obtain the full amplituhedron for any n, k, L, we combine the tree-level space and the loop space into a larger matrix

$$\begin{pmatrix} \mathcal{L}_{(1)} \\ \mathcal{L}_{(2)} \\ \vdots \\ \mathcal{L}_{(L)} \\ \hline Y \end{pmatrix} = \begin{pmatrix} D_{(1)} \\ D_{(2)} \\ \vdots \\ D_{(L)} \\ \hline C \end{pmatrix} \cdot Z \tag{5.1.6}$$

or more neatly

$$\mathcal{Y} = \mathcal{C} \cdot Z \,, \tag{5.1.7}$$

where $\mathcal{C}$ is the $(k + 2L) \times n$ matrix specifying the set of $(k + 2L)$ different linear combinations of external vertices, and $\mathcal{Y}$ is the full amplituhedron interior. Here the positivity condition for $\mathcal{C}$ is not the same as the one for C: $\mathcal{C} \notin G_+(k+2L, n)$ (in fact, $k + 2L$ may be much larger than n). As for the pure loop geometry, the positivity condition is now an extended positivity. The requirements are that the combination of C with any subset of the $D_{(i)}$ matrices is positive, i.e. all their maximal minors are positive, as long as the matrix has at least as many columns as rows, i.e. that

$$\Big(C\Big) \,, \left(\frac{D_{(1)}}{C}\right) \,, \cdots \,, \left(\frac{D_{(L)}}{C}\right) \,, \left(\frac{\begin{matrix} D_{(1)} \\ D_{(2)} \end{matrix}}{C}\right) \,, \cdots \tag{5.1.8}$$

are all positive, where we stop stacking $D_{(i)}$'s onto C when the resulting matrix has more rows than columns. Note that there is no condition that only relates the various $D_{(i)}$'s to each other, except in the absence of C, i.e. for $k = 0$. This novel space inhabited by $\mathcal{C}$, characterized by the extended positivity, is denoted $G_+(k, n; L)$.

5.1.4 The Scattering Amplitude

The scattering amplitude is obtained by integrating over all of the degrees of freedom of the amplituhedron, with a specific form constrained to have *logarithmic singularities* on the boundaries of the space. This form is the amplitude integrand,

and can in principle be constructed using methods such as Feynman diagrams, unitary cuts or BCFW recursion relations. For arbitrary numbers of particles and loops such methods become very laborious, and it would be desirable to construct the integrand directly from the definition of the amplituhedron. There are several strategies for doing this: the first one is to try to triangulate the amplituhedron in terms of smaller elementary spaces which have trivial $d\log$ forms. Recursion relations via on-shell diagrams provide examples of such triangulations, where the rules for triangulating are dictated by the physics rather than the amplituhedron geometry.[2] Another strategy is to nail down the integrand directly, by requiring that all spurious singularities (which do not correspond to amplituhedron boundaries) cancel. In either approach, an understanding of the boundary structure of the space will be crucial for systematically constructing the integrand form.

5.2 Stratification of the Amplituhedron: Loop Geometry

In this section we develop tools for *stratifying* the amplituhedron, by which we mean finding its boundary structure.

In this chapter, we focus our attention on the $k = 0$ case, i.e. on the pure *loop geometry*, and also restrict to $n = 4$. For $k = 0$, the matrix C disappears, and we are only left with the $D_{(i)}$ matrices:

$$\mathcal{C} = \begin{pmatrix} D_{(1)} \\ D_{(1)} \\ \vdots \\ D_{(L)} \end{pmatrix} . \tag{5.2.1}$$

The structure at loop level is rather non-trivial due to the extended positivity condition imposed on matrices. Note that $\mathcal{C}$ is *not* an element of the positive Grassmannian, except for $L = 1$.

[2] See [82] for alternative diagrammatic tools for addressing this problem and [127] for interesting new ideas on the computation of volumes of polytopes associated to scattering amplitudes.

For $n = k + 4$, the positivity of external data, encoded in the matrix Z, is trivial and the stratification of the amplituhedron corresponds to the stratification of $\mathcal{C}$.[3] Even in this simplified situation, the geometry of the amplituhedron will exhibit extraordinary richness. For general n, the process we will discuss can be regarded as the stratification of $G_+(0, n; L)$ rather than the stratification of the amplituhedron. Independently of its relation to the amplituhedron, the stratification of $G_+(0, n; L)$ is an interesting geometric question in its own right.

5.2.1 The Degrees of Freedom of $\mathcal{C}$

Each $D_{(i)} \in G_+(2, n)$ has $2(n-2)$ degrees of freedom, best parametrized by its 2×2 minors, i.e. its Plücker coordinates. There are $\binom{n}{2}$ different Plücker coordinates $\Delta_I^{(i)}$. As discussed in §4.1, the $\Delta_I^{(i)}$'s are not all independent but are subject to Plücker relations. $\mathcal{C}$ gets a contribution from each $D_{(i)}$, giving a total of $2L(n-2)$ degrees of freedom.

Note that extended positivity, despite imposing a condition on the degrees of freedom of different $D_{(i)}$, does not decrease the dimension, for the simple reason that it is just an inequality and cannot determine any Plücker coordinate in terms of the others. This is akin to the fact that the restriction to the positive Grassmannian, i.e. that $\Delta_I^{(i)} > 0$, does not create new relations between the coordinates $\Delta_I^{(i)}$, but simply constrains them to be positive.

However, extended positivity can restrict the allowed domain of the $\Delta_I^{(i)}$ further than the simple $\Delta_I^{(i)} > 0$ condition. This additional restriction can in certain cases be quite non-trivial, and may even split the domain into disjoint *regions*. Later in this section, we will introduce a *mini stratification* of $\mathcal{C}$ which is insensitive to this subtlety, and a *full stratification* which refines the mini stratification and fully accounts for it. The full stratification in effect counts all domain regions of the amplituhedron.

Regardless of which stratification we are interested in, for the purposes of count-

[3] This follows directly from the fact that when Z is a square matrix we may choose a basis for which Z equals the unit matrix. Then from (5.1.7) we see that $\mathcal{Y} = \mathcal{C} \cdot Z = \mathcal{C}$.

ing dimensions we only count the number of independent equalities between various $\Delta_I^{(i)}$'s. For example, when $\mathcal{C}$ is top-dimensional the only relations come from the Plücker relations which are independently present in each $D_{(i)}$, e.g. for $i = 1$ there is a Plücker relation between various $\Delta_I^{(1)}$'s, for $i = 2$ there is a separate Plücker relation between the $\Delta_J^{(2)}$'s, but we cannot write any $\Delta_I^{(1)}$ in terms of $\Delta_J^{(2)}$'s.

5.2.2 Extended Positivity and Boundaries

For $k = 0$, extended positivity enforces the condition that all $D_{(i)}$ are positive, as well as all subsets of them when stacked onto each other, i.e. that

$$\left(D_{(i)}\right), \begin{pmatrix} D_{(i)} \\ D_{(j)} \end{pmatrix}, \cdots \tag{5.2.2}$$

are all positive. This translates into various conditions on the Plücker coordinates. To unify the conditions it is convenient to define $2m \times 2m$ minors $\Delta_I^{(i_1,\ldots,i_m)}$, $m = 1, \ldots, L$, which are all the maximal minors when stacking the matrices $D_{i_1}, \ldots D_{i_m}$.[4] First, all $\Delta_I^{(i)}$ must be positive. Extended positivity also requires the $\Delta_I^{(i_1,\ldots,i_m)}$'s, which are polynomials of order m in the $\Delta_I^{(i)}$'s, to be positive. In order to emphasize the contrast with Plücker coordinates $\Delta_I^{(i)}$, we will often refer to the $m > 1$ minors as *non-minimal minors*.

For a given number of loops L, there are $\binom{L}{m}$ ways of choosing m matrices $D_{(i)}$ to form a $\Delta_J^{(i_1,\ldots,i_m)}$. For each of these choices, there are $\binom{n}{2m}$ ways of choosing the set J of $2m$ columns out of all the n external nodes. Hence, the number of non-minimal minors becomes

$$\sum_{m=2}^{m\leq n/2} \binom{L}{m}\binom{n}{2m}. \tag{5.2.3}$$

These larger minors are not all independent, there are Plücker-like relations among them.

Boundaries of $\mathcal{C}$ are reached by killing degrees of freedom in it by setting minors to zero. In other words, $\Delta_I^{(i_1,\ldots,i_m)} \geq 0$ has its boundary when $\Delta_I^{(i_1,\ldots,i_m)} = 0$. The

[4] This notation includes the 2×2 Plücker coordinates. In order to maintain an economic notation, we use a single subindex I to indicate the set of columns in the larger minors.

more complicated inequalities arising from minors with $m > 1$ give rise to relations between $\Delta_I^{(i)}$'s. Each independent relation of this form reduces the degrees of freedom by 1. A more precise characterization of boundaries is given below, when we discuss the stratification.

Labels. To every boundary we can associate the corresponding list of vanishing $\Delta_I^{(i_1,\ldots,i_m)}$. In each list, all $\Delta_I^{(i_1,\ldots,i_m)}$, i.e. for both $m = 1$ and $m > 1$, are treated *democratically*. We will refer to such lists of minors as *labels*. The minors which are not in the label are not vanishing. Labels are very useful for characterizing boundaries and other configurations of minors, although they do not fully specify them.

These labels will form the basis of the mini stratification described in §5.2.3, which will only distinguish elements in the stratification by them. However, motivated by the physical problem of using the amplituhedron to identify all possible singularities of the integrand, we will refine this counting in §5.2.4 by noticing that there are several independent domain regions for each label, or equivalently by identifying *independent* solutions consistent with a given label.[5] It is thus important to emphasize that, generally, *labels do not fully specify boundaries*.

However, labels are still subject to interesting restrictions, since not every arbitrary set of minors can be set to zero. There are two sources of hindrance:

- Plücker relations relate different $\Delta_I^{(i)}$'s and hence it is sometimes impossible to kill a given Plücker coordinate without some other coordinate also becoming zero. The same is in fact true for all $\Delta_I^{(i_1,\ldots,i_m)}$'s: they are not all independent, since there are Plücker-like relations between them. As a result, it is not possible to *exclusively* set any arbitrary combination of $\Delta_I^{(i_1,\ldots,i_m)}$'s to zero.

- Relations belonging to different levels of minors may be incompatible, i.e. the full extended positivity can become impossible to satisfy, despite only

[5] As will become clearer in §5.2.4, and exemplified in §5.5.2, the definition automatically accounts for the information about the sequence or path in which minors are turned off to reach a given boundary.

being given in terms of inequalities. This is because the relations arising from non-minimal minors typically contain positive and negative terms, and the sum must be non-negative. When all the Plücker coordinates are turned on, extended positivity is easily satisfied. On the contrary if, for example, we kill a subset such that only the negative terms survive, we can no longer satisfy positivity. Similarly, setting a $\Delta_I^{(i_1,\ldots,i_m)}$ to zero becomes impossible if only positive terms in it are turned on. We shall later see explicit examples of both of these occurrences.

From the above discussion we conclude that while Plücker relations and their generalizations for $m > 1$ may invalidate boundaries in an automatic way, extended positivity does so more aggressively: it imposes by hand an ulterior check to determine whether a given boundary exists or not. This is analogous to what happens when imposing positivity on the Grassmannian: $G(k,n) \to G_+(k,n)$ kills "by hand" a subset of boundaries. In our case, we go from $G(k,n;L) \to G_+(k,n;L)$. For the tree-level case $G_+(k,n;0) \equiv G_+(k,n)$, it is a beautiful result that certain potential boundaries[6] are removed in such a way so as to generate an Eulerian poset [126].

5.2.3 Mini Stratification

As mentioned above, the full stratification of the amplituhedron counts all independent solutions for a given positivity-preserving label. At this point in our discussion, it is natural to define an unrefined counting, which we call *mini stratification*, which serves as a close proxy of the full stratification introduced in next section. The mini stratification corresponds to only considering the labels of the boundaries. This counting can be used to generate a label stratification, in which multiple solutions for a given label are collapsed into a single point, which is assigned the highest dimension of all these solutions. In other words, the mini stratification combines boundaries into equivalence classes determined by the labels. For brevity, we will simply refer to these equivalence classes as the boundaries of the mini stratification.

While the mini stratification does not capture the full singularity structure of

[6]By this we mean configurations in which some minors vanish.

the amplitude, it is valuable for various reasons. First, it provides a rather complete geometric characterization of the amplituhedron. More importantly, as we discuss in §5.4, its value follows from the fact that it admits a very efficient combinatorial implementation. We will present examples of the mini stratification in §5.5 and §5.6.

5.2.4 Full Stratification

As already discussed above, labels only include information on which minors are vanishing and which are non-vanishing. Their level of refinement is identical to that of the matroid strata for $G_+(k,n)$. It is often possible, however, that there are disjoint regions of domain for the minimal minors $\Delta_I^{(i)}$ which satisfy the equalities of a given label, i.e. that there are multiple solutions to the set of equalities described by the label.

We are thus naturally led to the definition of a *region*, which is a set of equalities and inequalities for the $\Delta_I^{(i_1,\ldots,i_m)}$, $m = 1,\ldots,L$, which has a unique solution. In general, the equalities and inequalities needed to describe a region are more than those specifying a label: given the label, we must also specify which of the solutions the region refers to. In the future, when we refer to a boundary of $G_+(k,n;L)$ we will mean a region as defined here. The *full stratification* is defined as the stratification which distinguishes all such regions. This suggests a natural extension of the labels introduced in the last section, to which we refer as *extended labels*. Extended labels correspond to specifying not only the vanishing $\Delta_I^{(i_1,\ldots,i_m)}$'s but also all other relations between minors. Such an extended label then fully specifies a given boundary. While the mini stratification is based on labels, the full stratification uses extended labels.

For concreteness, let us focus on $n = 4$, for which all non-minimal minors are 4×4. Consider one such minor which, without loss of generality, we can assume to be $\Delta_{1234}^{(1,2)}$.[7] When all $\Delta_I^{(i)}$ are turned on, $\Delta_{1234}^{(1,2)}$ can be expressed in terms of Plücker coordinates as follows:

$$\Delta_{1234}^{(1,2)} = \Delta_{12}^{(1)}\Delta_{34}^{(2)} + \Delta_{23}^{(1)}\Delta_{14}^{(2)} + \Delta_{34}^{(1)}\Delta_{12}^{(2)} + \Delta_{14}^{(1)}\Delta_{23}^{(2)} - \Delta_{13}^{(1)}\Delta_{24}^{(2)} - \Delta_{24}^{(1)}\Delta_{13}^{(2)}\,. \quad (5.2.4)$$

[7] The simplest situation in which such a minor arises is for 2-loops, i.e. $G_+(0,4;2)$. In this case, this is the only non-minimal minor.

After using the Plücker relations $\Delta^{(i)}_{12}\Delta^{(i)}_{34} + \Delta^{(i)}_{23}\Delta^{(i)}_{14} = \Delta^{(i)}_{13}\Delta^{(i)}_{24}$ for $i = 1, 2$, this can be turned into the convenient form

$$\begin{aligned}\Delta^{(1,2)}_{1234} &= \frac{\left(\Delta^{(1)}_{12}\Delta^{(2)}_{13} - \Delta^{(1)}_{13}\Delta^{(2)}_{12}\right)\left(\Delta^{(1)}_{13}\Delta^{(2)}_{34} - \Delta^{(1)}_{34}\Delta^{(2)}_{13}\right)}{\Delta^{(1)}_{13}\Delta^{(2)}_{13}} \\ &+ \frac{\left(\Delta^{(1)}_{23}\Delta^{(2)}_{13} - \Delta^{(1)}_{13}\Delta^{(2)}_{23}\right)\left(\Delta^{(1)}_{13}\Delta^{(2)}_{14} - \Delta^{(1)}_{14}\Delta^{(2)}_{13}\right)}{\Delta^{(1)}_{13}\Delta^{(2)}_{13}} \,. \end{aligned} \tag{5.2.5}$$

If we now turn off $\Delta^{(1)}_{23} = \Delta^{(1)}_{14} = 0$, we obtain

$$\Delta^{(1,2)}_{1234} = \frac{\left(\Delta^{(1)}_{12}\Delta^{(2)}_{13} - \Delta^{(1)}_{13}\Delta^{(2)}_{12}\right)\left(\Delta^{(1)}_{13}\Delta^{(2)}_{34} - \Delta^{(1)}_{34}\Delta^{(2)}_{13}\right)}{\Delta^{(1)}_{13}\Delta^{(2)}_{13}} - \frac{\Delta^{(1)}_{13}\Delta^{(2)}_{23}\Delta^{(2)}_{14}}{\Delta^{(2)}_{13}} \tag{5.2.6}$$

The mini stratification label for this is simply $\{\Delta^{(1)}_{14}, \Delta^{(1)}_{23}\}$, which is the full set of vanishing minors. All other $\Delta^{(i)}_I$'s are strictly positive. However, we notice that there are two regions in which we may satisfy $\Delta^{(1,2)}_{1234} > 0$:

- **Region 1:** $\left(\Delta^{(1)}_{12}\Delta^{(2)}_{13} - \Delta^{(1)}_{13}\Delta^{(2)}_{12}\right) > 0$ and $\left(\Delta^{(1)}_{13}\Delta^{(2)}_{34} - \Delta^{(1)}_{34}\Delta^{(2)}_{13}\right) > 0$
- **Region 2:** $\left(\Delta^{(1)}_{12}\Delta^{(2)}_{13} - \Delta^{(1)}_{13}\Delta^{(2)}_{12}\right) < 0$ and $\left(\Delta^{(1)}_{13}\Delta^{(2)}_{34} - \Delta^{(1)}_{34}\Delta^{(2)}_{13}\right) < 0$

These two regions are very easy to understand: denoting $x \equiv \left(\Delta^{(1)}_{12}\Delta^{(2)}_{13} - \Delta^{(1)}_{13}\Delta^{(2)}_{12}\right)$, $y \equiv \left(\Delta^{(1)}_{13}\Delta^{(2)}_{34} - \Delta^{(1)}_{34}\Delta^{(2)}_{13}\right)$ and $k \equiv \frac{\Delta^{(1)}_{13}\Delta^{(2)}_{23}\Delta^{(2)}_{14}}{\Delta^{(2)}_{13}}$, we have the simple condition that

$$\Delta^{(1,2)}_{1234} \geq 0 \quad \Leftrightarrow \quad xy \geq k \quad (k > 0) \tag{5.2.7}$$

which on the x–y plane simply corresponds to two regions whose boundary is the hyperbolic curve $xy = k$. Here we see that to specify the regions within this label, all we need to do is additionally specify the sign of x and y. The relations specifying regions 1 and 2 are explicit examples of the type of relations included in extended labels.

In this example, if we go to a different label where we have also shut off $\Delta^{(1,2)}_{1234}$, i.e. $\{\Delta^{(1)}_{14}, \Delta^{(1)}_{23}, \Delta^{(1,2)}_{1234}\}$, we again have two regions: $xy = k$ with $x, y > 0$, and $xy = k$ with $x, y < 0$.

The full stratification contains all possible poles of the integrand. In fact, it is even more refined than the integrand: while there are several different integrand poles that correspond to the same label in the mini stratification, here it sometimes

happens that there are several regions contained within the same integrand pole. The example above is an instance where this happens: as will be clear in subsequent sections, the pole of the integrand when we set $\Delta_{23}^{(1)} = \Delta_{14}^{(1)} = 0$ is

$$\frac{\langle AB34\rangle\langle CD12\rangle + \langle AB12\rangle\langle CD34\rangle}{\langle ABCD\rangle\langle AB12\rangle\langle AB34\rangle\langle CD12\rangle\langle CD14\rangle\langle CD23\rangle\langle CD34\rangle}\,. \tag{5.2.8}$$

We have just shown that this object is composed of two disjoint regions. Provided the amplituhedron proposal holds, identifying those regions in the full stratification which correspond to the same integrand pole exactly reproduces the pole structure of the integrand.

5.2.5 Summary of the Method and Structure of the Stratification

In this section we summarize the general procedure for stratifying $\mathcal{C} \in G_+(0, n; L)$. As stated earlier, in this thesis we will almost exclusively focus on the case of $k = 0$, $n = 4$ and arbitrary L. This case is particularly simple owing to the fact that for $n = 4$ the Z_I matrix can be chosen to be diagonal, and hence trivial, thus positivity of external data becomes unimportant and the stratification of $G_+(0, 4; L)$ actually coincides with the one for the loop amplituhedron.[8]

As previously mentioned, every boundary of $G_+(0, n; L)$ has an associated label, i.e. a list of vanishing minors. For any given label, there is one boundary (or region) for each independent solution giving rise to it, in general specified by some additional inequalities.

All minors should be treated democratically. When implementing the stratification, however, it is natural to give the Plücker coordinates $\Delta_I^{(i)}$ a special treatment. The reasons for this choice include the facts that every minor $\Delta_I^{(i_1,\ldots,i_m)}$ is an order m polynomial in $\Delta_I^{(i)}$'s and, as we discussed in §4.1.7, the $\Delta_I^{(i)}$'s are related to perfect matchings of simply connected graphs. Moreover, the Plücker coordinates for each

[8]The case of $k > 0$ is further complicated by the fact that the minors of the $D_{(i)}$ matrices do not have a definite sign, and tuning these to zero does not constitute a boundary of the amplituhedron. Boundaries are only obtained by shutting off degrees of freedom that have a definite sign.

$D_{(i)}$ scale with a common factor under the GL(2) acting on $D_{(i)}$. The dimension of each boundary is given by the number of degrees of freedom in the $\Delta_I^{(i)}$'s:

$$d = N_{\Delta_I} - N_{\text{rel}} - L\,, \tag{5.2.9}$$

where N_{Δ_I} is the number of non-vanishing $\Delta_I^{(i)}$ on the boundary and N_{rel} is the number of independent equations relating the $\Delta_I^{(i)}$.[9] These equations may be Plücker relations or follow from non-minimal minors that have been independently set to zero on a given boundary. In the mini stratification, each label is assigned the dimension of the top-dimensional region associated to it.

In this way we split the positivity constraint on the matrix $\mathcal{C}$ in two:

- $\Delta_I^{(i)} \geq 0$.
- Larger minors $\Delta_I^{(i_1,\ldots,i_m)}$, expressed as sums of products of $\Delta_I^{(i)}$, also satisfy $\Delta_I^{(i_1,\ldots,i_m)} \geq 0$.

The aforementioned distinction between Plücker coordinates and non-minimal minors leads us to a natural separation of the stratification of $G_+(0,n;L)$ into two stages. First, we obtain all possible sets of vanishing Plücker coordinates $\Delta_I^{(i)}$, subject to extended positivity conditions. At this step larger minors are not set to zero, unless they trivially vanish as a result of the vanishing Plücker coordinates. If we are considering the full stratification, some of these configurations can be further divided in different regions, specified by inequalities among the non-vanishing Plücker coordinates. Next, we introduce for each of these elements a further structure corresponding to the vanishing of non-minimal minors. This second stage reduces the dimension of boundaries by imposing constraints on the non-vanishing $\Delta_I^{(i)}$'s. Depending on whether we are interested in the mini or the full stratification, it is implemented slightly differently.

The first stage in the stratification thus corresponds to the following two steps:

[9] The subtraction of L degrees of freedom follows from the fact that Plücker coordinates are projectively defined.

1. Classify potential boundaries according only to the vanishing Plücker coordinates. This corresponds to independently performing the positroid stratification of each $D_{(i)}$, i.e. of each $G_+(2,n)$.

2. Some of these collections violate the extended positivity of the larger minors $\Delta_I^{(i_1,\ldots,i_m)} \geq 0$ and are thus removed. The surviving collections of $\Delta_I^{(i)}$ represent all the labels of $G_+(0,n;L)$ for which non-minimal minors can be non-negative.

Step 1 produces the L^{th} power of the positroid stratification of $G_+(2,n)$ and is independent of what type of stratification we are considering. We will denote the numbers of potential boundaries with dimension d obtained at this first step as $\mathbb{N}^{(d)}$, where d is determined using (5.2.9). Step 2 represents a further refinement of this decomposition, removing some of the potential boundaries obtained at step 1 by demanding extended positivity. We refer to the number of remaining boundaries as $\mathcal{N}^{(d)}$. These boundaries can be organized in a poset that we denote Γ_0, where the top element corresponds to all minors non-vanishing. Every element in Γ_0 is associated to a set of vanishing $\Delta_I^{(i)}$'s. In the case of the full stratification, this information might not uniquely fix the element of Γ_0, due to the multiplicity of regions. A combinatorial approach for constructing Γ_0 in the mini stratification will be introduced in §5.4.

Independently of whether we are constructing the mini or the full stratification, for each element in Γ_0 there are, generally, multiple boundaries, which arise from setting to zero non-minimal minors which are not automatically vanishing due to vanishing Plücker coordinates. The procedure for systematically constructing these boundaries is:

3. For each element of Γ_0 and its collections of surviving $\Delta_I^{(i)}$, we first classify non-minimal minors $\Delta_I^{(i_1,\ldots,i_m)} \geq 0$, $m > 1$, into three categories:

   (i) Those that are trivially zero given the list of vanishing $\Delta_I^{(i)}$.

   (ii) Those that are manifestly positive, because only positive terms are turned on by the given collection of non-zero $\Delta_I^{(i)}$.

   (iii) Those that have both positive and negative terms turned on.

4. Given the previous classification, for each element of Γ_0 the additional boundary structure is obtained by turning off combinations of type (iii) $\Delta_I^{(i_1,\ldots,i_m)}$. Additionally, for the full stratification we may sometimes obtain additional boundaries from type (i) non-minimal minors. The mini and the full stratifications differ in the structure arising from this step.

This new set of boundaries can be nicely captured by additional posets Γ_1 emanating from every point in Γ_0. It is important to emphasize that, in general, each point in Γ_0 can have a different Γ_1. In addition, the explicit form of Γ_0 and the Γ_1's generally depends on whether we are considering the mini or full stratification. The top element of each Γ_1 is characterized by having all non-minimal minors of types (ii) and (iii) non-vanishing. Figure 5.1 shows a cartoon of the structure of the full stratification poset.

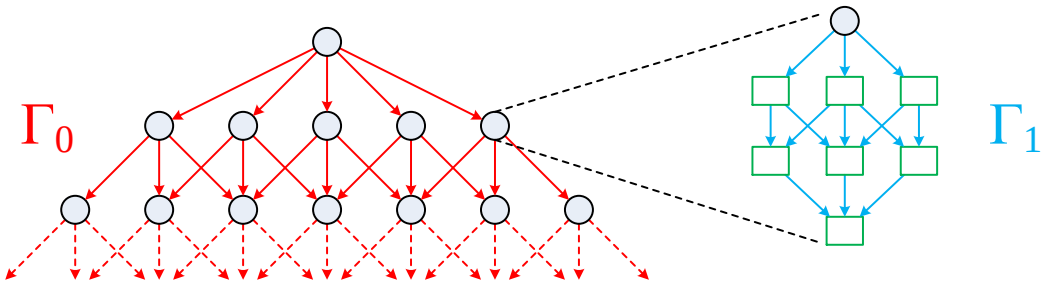

Figure 5.1: A natural decomposition of the poset associated to the stratification. Γ_0 corresponds to 2×2 minors and Γ_1 corresponds to non-minimal ones.

Note that the construction of the Γ_1's requires caution. First, not all type (iii) minors can always be set to zero. Non-minimal minors are in general not independent and it is necessary to explicitly check whether it is possible to shut them off while preserving the positivity of the type (ii) and type (iii) larger minors and of the Plücker coordinates $\Delta_I^{(i)}$. This becomes particularly important when trying to turn off combinations of them. Moreover, if considering the full stratification, for every label we should consider all separate regions. Finally, the computation of the dimension of the boundaries via (5.2.9) can be subtle. The vanishing of the larger minors should be taken into account as extra relations among Plücker coordinates,

and hence contribute to $N_{\rm rel}$ in (5.2.9), only if they are independent from the other conditions, i.e. Plücker relations plus the possible vanishing of other larger minors. Explicit examples of all these issues are given in §5.5.

5.3 Simple Examples: Basic Properties

This section further illustrates some of the basic properties of positivity in terms of simple examples.

5.3.1 Stratification of $G_+(0,n;1) = G_+(2,n)$

Let us first consider the 1-loop geometry. A top-dimensional cell of $G_+(0,n,1) \equiv G_+(2,n)$ has all $\binom{n}{2} = \frac{1}{2}n(n-1)$ Plücker coordinates turned on. There are $(\frac{n^2}{2} - \frac{n}{2} - 2n + 3)$ independent Plücker relations; together with the GL(2) invariance which removes one extra degree of freedom by rescaling the coordinates, we get

$$\frac{1}{2}n(n-1) - (\frac{n^2}{2} - \frac{n}{2} - 2n + 3) - 1 = 2(n-2) \tag{5.3.1}$$

degrees of freedom. Boundaries are obtained by setting some Δ_I's to zero in a way that is compatible with the Plücker relations and $\Delta_J > 0$. Since in this case there are no non-minimal minors, there is no distinction between mini and full stratification. An example is provided in Figure 4.11, where we illustrate the stratification of $G_+(2,4)$.

Some remarks are already in order:

- At the first step, going to the 3-dimensional boundaries, we only turn off one Plücker coordinate. Since there are six Plücker coordinates that can be turned off, we would naively expect six different 3-dimensional boundaries. Instead, as shown in Figure 4.11, there are only four of them. This is because once we restrict the Δ_I's to be positive, two of these would-be boundaries are inconsistent with the Plücker relations. For example, killing Δ_{13} gives

$$\Delta_{12}\Delta_{34} + \Delta_{23}\Delta_{14} = 0\,, \tag{5.3.2}$$

  which can only be satisfied if we do not restrict ourselves to the strictly positive domain. This is the first example of positivity killing boundaries "by hand".

This phenomenon was already studied in §4 and emerged naturally from the methods therein. We note that this is not imposing extended positivity yet, which imposes compatibility of relations from different loops; this is positivity at a single loop level.

- For several 2-dimensional boundaries some extra Δ_I had to be set to zero in order to satisfy the Plücker relation. For example, starting from the boundary with non-vanishing $(12, 13, 14, 24, 34)$, i.e. where we have turned off Δ_{23}, it is not possible to only kill Δ_{12}, because the Plücker relation would then become

$$\Delta_{13}\Delta_{24} = 0\,, \tag{5.3.3}$$

which is not possible on *any* non-zero domain. Note here that positivity is not the issue, it is the violation of the Plücker relation.

- As already mentioned, the boundaries constructed in this way form an Eulerian poset, i.e.

$$\sum_{d=0}^{4}(-1)^d \mathbb{N}^{(d)} = 1\,, \tag{5.3.4}$$

where $\mathbb{N}^{(d)}$ is the number of boundaries of dimension d.

- The full extent of extended positivity never comes into play in this example. Having only one matrix, we never need to consider whether minors of different matrices are compatible. This will however not be the case for the example of $G_+(0, n; L = 2)$.

5.3.2 Non-Minimal Minors

Before developing a practical implementation of our ideas in the coming section, it is illuminating to consider a few explicit examples of the classification of non-minimal minors introduced in §5.2.5.

Let us consider the simple case of $G_+(0, 4; 2)$, which has 12 Plücker coordinates. From Figure 4.11, we see that $G_+(0, 4; 1)$ has 33 boundaries. The square of this positroid stratification then has $33^2 = 1\,089$ configurations, the top-dimensional one being that with all 12 $\Delta_I^{(i)}$'s turned on, giving dimension 8. All these configurations

automatically satisfy the two Plücker relations $\Delta^{(i)}_{12}\Delta^{(i)}_{34} + \Delta^{(i)}_{23}\Delta^{(i)}_{14} = \Delta^{(i)}_{13}\Delta^{(i)}_{24}$ as well as the non-negativity of all Plücker coordinates.

Some of these configurations, however, do not satisfy the extended positivity $\Delta^{(1,2)}_{1234} \geq 0$, with $\Delta^{(1,2)}_{1234}$ given in terms of Plücker coordinates in (5.2.4). One such configuration corresponds to the set of vanishing Plücker coordinates, i.e. label, $\{\Delta^{(2)}_{12}, \Delta^{(2)}_{23}, \Delta^{(2)}_{14}, \Delta^{(2)}_{34}, \Delta^{(2)}_{24}\}$. In this case, we have

$$\Delta^{(1,2)}_{1234} = 0 + 0 + 0 + 0 + 0 - \Delta^{(1)}_{24}\Delta^{(2)}_{13}\,, \tag{5.3.5}$$

which is explicitly negative. We hence conclude that this label does not correspond to a boundary.

Let us now present examples of the three different types of behaviors identified in §5.2.5.

- **Type (i)**: for the label $\{\Delta^{(1)}_{12}, \Delta^{(2)}_{12}, \Delta^{(1)}_{14}, \Delta^{(2)}_{14}, \Delta^{(1)}_{13}, \Delta^{(2)}_{13}\}$, we automatically have

$$\Delta^{(1,2)}_{1234} = 0\,. \tag{5.3.6}$$

- **Type (ii)**: for the label $\{\Delta^{(2)}_{12}, \Delta^{(2)}_{23}, \Delta^{(2)}_{14}, \Delta^{(2)}_{13}, \Delta^{(2)}_{24}\}$, we have

$$\Delta^{(1,2)}_{1234} = \Delta^{(1)}_{12}\Delta^{(2)}_{34} + 0 + 0 + 0 - 0 - 0\,, \tag{5.3.7}$$

  which is strictly positive. We then cannot reach new boundaries by only turning off $\Delta^{(1,2)}_{1234}$.

- **Type (iii)**: for the label $\{\Delta^{(1)}_{12}, \Delta^{(1)}_{34}\}$, we obtain

$$\Delta^{(1,2)}_{1234} = 0 + 0 + \Delta^{(1)}_{23}\Delta^{(2)}_{14} + \Delta^{(1)}_{14}\Delta^{(2)}_{23} - \Delta^{(1)}_{13}\Delta^{(2)}_{24} - \Delta^{(1)}_{24}\Delta^{(2)}_{13}\,, \tag{5.3.8}$$

  which has both positive and negative contributions. This type of non-minimal minor can in principle be turned off without turning off Plücker coordinates. This is possible whenever there are no obstructions coming from relations with other non-minimal minors, which in this particular case do not exist.

In the combinatorial approach we will introduce in the coming sections, the building blocks naturally correspond to entire terms in the non-minimal minors rather than only factors within them.

5.4 The Combinatorics of Extended Positivity

There is a natural, combinatorial implementation of the mini stratification of the loop geometry. This extension includes the more general cases that appear in $G_+(0,n;L)$, for which extended positivity can be systematically incorporated as explained in §5.4. The combinatorial structures discussed in this section only depend on labels and hence correspond to the mini stratification.

5.4.1 Multi-Loop Geometry and Hyper Perfect Matchings

The natural approach for treating the $k = 0$, L-loop geometry $G_+(0,n;L)$ is to introduce one bipartite graph associated to the top dimensional cell of $G_+(2,n)$ per loop, and to regard the union of these L identical disjoint graphs as a unified object in its own right.

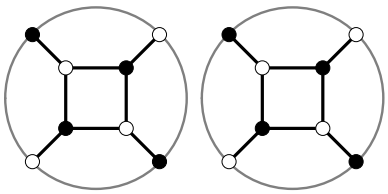

Figure 5.2: The starting graph for the stratification of two loops is simply two separate identical planar graphs for the top-dimensional cell of $G_+(2,n)$ (here $n = 4$), each representing one loop.

As for $G_+(k,n)$, perfect matchings of the multi-component bipartite graph play a central role. In order to emphasize the disjoint nature of the underlying graphs we will refer to them as *hyper perfect matchings*, reserving the term perfect matching for those on each component. Denoting p_i the perfect matchings on the first component, q_j the ones on the second component, and so on, a hyper perfect matching takes the form

$$P_{i,j,k,\ldots} = p_i q_j r_k \ldots . \tag{5.4.1}$$

The first step, before incorporating the effect of extended positivity, is to produce the L^{th} power of the 1-loop stratification, as done in §5.3.2. This can be done in

two ways:

- Performing the combinatorial stratification introduced in Chapter 4 of the L-component graph, considered as a unified object. This involves constructing the face lattice of the matching polytope and identifying hyper perfect matchings that correspond to the same point in the matroid polytope.

- Taking L copies of the 1-loop stratification in which perfect matchings from different loops are given a distinct name and multiplying them together. Effectively, this is equivalent to directly taking the L^{th} power of the 1-loop result, whilst keeping track of which graph component perfect matchings belong to.

The second method is computationally much easier to implement and faster to execute, and will therefore be adopted from here on. However, it is often conceptually useful to think in terms of the first one.

Like the positroid stratification of the positive Grassmannian, its L^{th} power automatically gives rise to a poset with Euler number $\mathcal{E} = 1$. This can be understood in different ways. First, as we mentioned above, this is in fact the positroid stratification of a graph made out of L disjoint components. Alternatively, one can understand this by thinking that there are L nested Eulerian posets. Our explicit results in §5.5, §5.6 and §5.8 confirm this general result.

Let us see how these ideas work for $G_+(0,4;2)$. In this case, we need to consider two graphs for the top-dimensional cell of $G_+(2,4)$ as shown in Figure 5.2. Each of them has 7 perfect matchings, which we call p_i and q_j, $i,j = 1,\ldots,7$. The combined graph thus has $7^2 = 49$ hyper perfect matchings $P_{i,j} = p_i q_j$. The matroid identification of perfect matchings on each loop, $p_6 \leftrightarrow p_7$ and $q_6 \leftrightarrow q_7$, implies the identification of hyper perfect matchings $P_{6,j} \leftrightarrow P_{7,j}$ and $P_{i,6} \leftrightarrow P_{i,7}$.

5.4.2 Hyper Perfect Matchings: Good, Bad and Neutral

The hyper perfect matchings automatically implement the Plücker relations and the positivity of the $\Delta_I^{(i)}$'s, but not yet the full extended positivity. The next step of the process is to shrink the poset we have just generated by eliminating those points which violate extended positivity.

Before introducing a combinatorial approach, let us revisit our discussion of extended positivity from §5.2.2 and the observations made for explicit examples in §5.3. Boundaries can be associated to labels, i.e. to lists of vanishing minors, generally of different dimensions, $\Delta_J^{(i_1,\ldots,i_m)}$, $m = 1, \ldots, L$. Extended positivity demands the non-vanishing ones to be strictly positive. The $\Delta_J^{(i_1,\ldots,i_m)}$'s, are polynomials in which every term is an order m product of $\Delta_I^{(i)}$'s coming from different loops. For illustration purposes, consider the single 4×4 minor that exists for $G_+(0,4;2)$, which was presented in (5.2.4). It is given by

$$\Delta_{1234}^{(1,2)} = \Delta_{12}^{(1)}\Delta_{34}^{(2)} + \Delta_{23}^{(1)}\Delta_{14}^{(2)} + \Delta_{34}^{(1)}\Delta_{12}^{(2)} + \Delta_{14}^{(1)}\Delta_{23}^{(2)} - \Delta_{13}^{(1)}\Delta_{24}^{(2)} - \Delta_{24}^{(1)}\Delta_{13}^{(2)}. \quad (5.4.2)$$

We see that there is a rather obvious distinction between those terms which appear with a positive sign, appear with a negative sign or do not appear. The different types of contributions to a given minor can be translated into a classification of hyper perfect matchings.

We recall that there is a correspondence between Plücker coordinates $\Delta_{\ell_a\ell_b}^{(i)}$ in $G_+(2,n)$ and perfect matchings: the Plücker coordinate associated to a given perfect matching is determined by the source set of the corresponding perfect orientation. Since every term in a $2m \times 2m$ minor is a product of m Plücker coordinates coming from different loops, the previous map implies that every such term can be identified with a hyper perfect matching.[10] For $m > 1$, however, the sign of terms vary, as e.g. in (5.4.2).

For every non-minimal minor, we will thus define the following classification of hyper perfect matchings:

- **Good:** it corresponds to a positive term in the minor.
- **Bad:** it corresponds to a negative term in the minor.
- **Neutral:** it does not appear in the minor.

[10]Extending what we did for perfect matchings, here we also discuss hyper perfect matchings after identifications following from the matroid polytope or, equivalently, distinguishing them only by their external edge content.

Let us investigate in more detail how these concepts work for the example in (5.4.2). The corresponding graph is shown in Figure 5.2 and the map between perfect matchings for each loop and Plücker coordinates is given in (4.3.5). In terms of perfect matchings and hyper perfect matchings, we have

$$\Delta^{(1,2)}_{1234} = \Delta^{(1)}_{12}\Delta^{(2)}_{34} + \Delta^{(1)}_{23}\Delta^{(2)}_{14} + \Delta^{(1)}_{34}\Delta^{(2)}_{12} + \Delta^{(1)}_{14}\Delta^{(2)}_{23} - \Delta^{(1)}_{13}\Delta^{(2)}_{24} - \Delta^{(1)}_{24}\Delta^{(2)}_{13} \ .$$

$$\begin{array}{cccccc} p_3\, q_2 & p_5\, q_4 & p_2\, q_3 & p_4\, q_5 & p_1\, q_6 & p_6\, q_1 \\ P_{3,2} & P_{5,4} & P_{2,3} & P_{4,5} & P_{1,6} & P_{6,1} \end{array} \tag{5.4.3}$$

For this minor, we thus have:

- **Good:** $P_{3,2}$, $P_{5,4}$, $P_{2,3}$, $P_{4,5}$
- **Bad:** $P_{1,6}$, $P_{6,1}$

while all other hyper perfect matchings are neutral.

We now have a powerful technology for incorporating extended positivity into our stratification. For a given minor to be positive, some of its good hyper perfect matchings must survive. Conversely, a minor violates positivity if only bad hyper perfect matchings are present. We can also see how to, in the language of §5.2.5, go from Γ_0 to Γ_1 by turning off $m > 1$ minors. Such minors can vanish *without sending to zero additional Plücker coordinates* only if both good and bad hyper perfect matchings are simultaneously present. Note that this condition is necessary but not sufficient.

Practical Implementation. In cases with multiple $m > 1$ minors, a good approach for implementing extended positivity is as follows:

- For every minor, determine whether a given hyper perfect matching P_i is good, bad or neutral. For each hyper perfect matching, this information is easily stored in a vector whose length is the number of non-minimal minors. If P_i is bad for a given minor, the corresponding entry is set to be the complex number i; if P_i is good, the entry is set to 1; if P_i is neutral, the entry is 0.
- We then generate a single vector for each boundary, by adding the vectors associated to all hyper perfect matchings in it.

- If in the final vector the argument of the complex number in any entry is $\pi/2$, the boundary has at least one relation with only negative terms turned on, so it violates extended positivity and should be removed. If the argument is 0, the corresponding minor has only positive terms turned on or none at all, and hence cannot be further turned off to go to a lower dimensional boundary.

It is straightforward to implement this method with any algebraic manipulation software. We stress that sticking to this method is however not strictly necessary to obtain the stratification. For it, only knowledge of vanishing minors is necessary and, as we have just seen, hyper perfect matchings provide a highly efficient language for dealing with them.

5.4.3 Classification of Hyper Perfect Matchings Using Permutations

We shall now demonstrate a very efficient method for determining whether a hyper perfect matching is good, bad or neutral with respect to a given $m > 1$ minor.

Consider a hyper perfect matching $P_{i,j,k,\ldots} = p_i q_j r_k \ldots$. Let us call $\{s_i, t_i\}$, $\{s_j, t_j\}$, $\{s_k, t_k\}, \ldots$ the pairs of sources for each of the constituent perfect matchings. The union of these source sets determines which term in the minor corresponds to $P_{i,j,k,\ldots}$, as in (5.4.3). The classification of the hyper perfect matching is determined by the parity of the number of crossings in the source set. Let us denote a_1, a_2 the ordered source set for the first loop under consideration, b_1, b_2 the ordered source set for the second loop, etc. Then, define $\epsilon^{a_1 a_2 b_1 b_2 \cdots}$ to be the ordinary antisymmetric tensor, with the slight modification that the ordered indices are not necessarily consecutive, but do need to be monotonically increasing. For example, $\epsilon^{1256} = \epsilon^{1234} = 1$ and $\epsilon^{5739} = 1$ but $\epsilon^{2648} = -1$ and $\epsilon^{4849} = 0$. The classification of hyper perfect matchings then reduces to:

$$\epsilon^{a_1 a_2 b_1 b_2 \cdots} = \begin{cases} 1 \Rightarrow & \text{good} \\ -1 \Rightarrow & \text{bad} \\ 0 \Rightarrow & \text{neutral} \end{cases} \tag{5.4.4}$$

Let us discuss in further detail the graphical implementation of extended posi-

tivity. For doing so, we draw a line connecting the pairs of sources for each perfect matching in a given hyper perfect matching and superimpose them on a single graph.

Bad hyper perfect matchings. Bad hyper perfect matchings are those for which the lines between sources intersect an odd number of times in the interior of the graph, and no edges touch at external nodes. Figure 5.3 shows an example of a bad perfect matching for the $n = 4$, 2-loop case, $P_{1,6} = p_1 q_6$.[11] The sources for p_1 are $\{1, 3\}$ and the ones for q_6 are $\{2, 4\}$. Their union occupies all 4 external nodes and hence all the columns in the minor. The lines between sources cross once. Indeed, $\epsilon^{1324} = -1$.

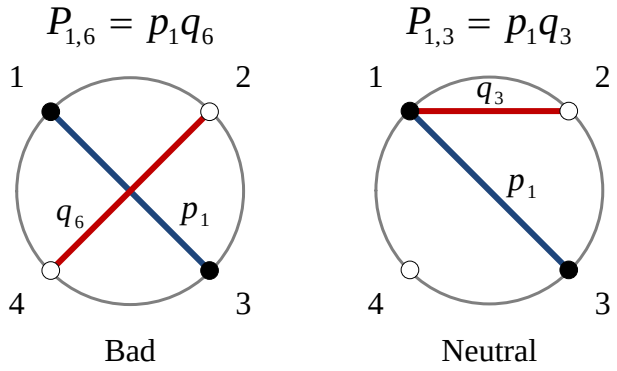

Figure 5.3: $P_{1,6}$ is a bad perfect matching. $P_{1,3}$ is instead neutral, since the crossing does not occur in the interior of the graph. In fact $P_{1,3}$ does not occupy all four external nodes, equivalently all columns in the minor.

Good hyper perfect matchings. They are those whose lines intersect an even number of times in the interior of the graph. Two examples are presented in Figure 5.4.

Neutral hyper perfect matchings. When the lines joining sources touch on external points, the configuration does not occupy all columns in the minor and

[11] Notice that $P_{1,7} = p_1 q_7$ is also a bad perfect matching, but it coincides with $P_{1,6}$ after the matroid polytope identification.

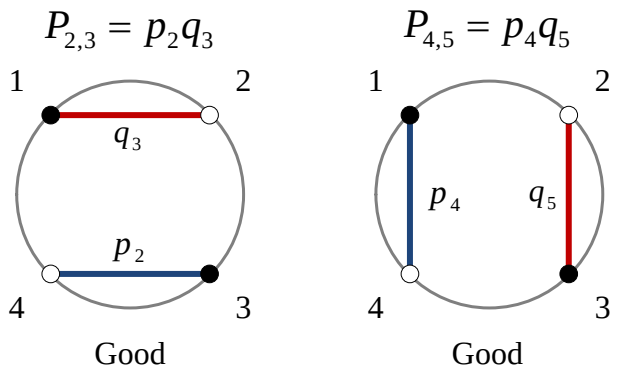

Figure 5.4: $P_{2,3}$ and $P_{4,5}$ are two examples of good perfect matchings.

hence it does not contribute to it. An example is shown in Figure 5.3.

We would like to emphasize that, generally, a hyper perfect matching can be good in regard to a non-minimal minor but bad in regard to another one. An example of this situation is provided in Figure 5.5.

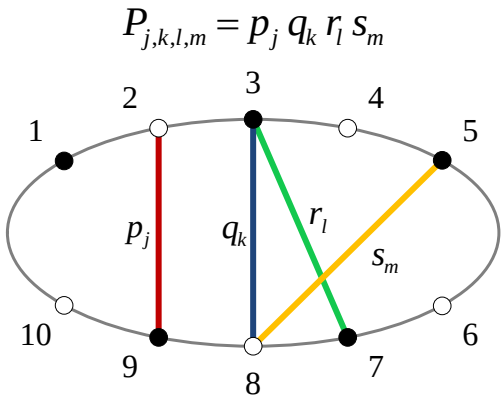

Figure 5.5: This hyper perfect matching is good in regard to the 4×4 minor involving loops p and q and matrix columns $2, 3, 8, 9$ and is bad in regard to loops r and s and columns $3, 5, 7, 8$.

5.5 Two Loops

To illustrate the techniques presented above, we stratify the amplituhedron and the log of the amplitude in the case of $k = 0$ for 4 particles at 2 loops. We first present the mini stratification introduced in §5.5.1. As a cross-check, the results have been derived both in terms of hyper perfect matchings and directly using Plücker coordinates and the relations between them. The full stratification, accounting for all solutions arising from factorization, is presented in §5.5.2.

5.5.1 Mini Stratification

Let us begin our analysis by classifying boundaries according to their labels.

The Amplituhedron

For $G_+(0, n; 2)$, the starting point is the graph in Figure 5.2, which has $7^2 = 49$ hyper perfect matchings. The 1-loop stratification was obtained in Chapter 4. To square it, we produce an equivalent set of boundaries for the second graph; the boundaries of both are summarized in Table 5.1. Every boundary in the left table must be

Dim	Boundaries of graph 1
4	$\{p_1, p_2, p_3, p_4, p_5, p_6\}$
3	$\{p_1, p_2, p_3, p_4, p_6\}, \{p_1, p_2, p_3, p_5, p_6\},$ $\{p_1, p_2, p_4, p_5, p_6\}, \{p_1, p_3, p_4, p_5, p_6\}$
2	$\{p_1, p_2, p_4\}, \{p_1, p_2, p_5\}, \{p_1, p_3, p_4\},$ $\{p_1, p_3, p_5\}, \{p_1, p_2, p_3, p_6\},$ $\{p_1, p_4, p_5, p_6\}, \{p_2, p_4, p_6\},$ $\{p_2, p_5, p_6\}, \{p_3, p_4, p_6\}, \{p_3, p_5, p_6\}$
1	$\{p_1, p_2\}, \{p_1, p_4\}, \{p_1, p_3\}, \{p_1, p_5\},$ $\{p_2, p_4\}, \{p_2, p_5\}, \{p_3, p_4\}, \{p_3, p_5\},$ $\{p_2, p_6\}, \{p_3, p_6\}, \{p_4, p_6\}, \{p_5, p_6\}$
0	$\{p_1\}, \{p_2\}, \{p_3\}, \{p_4\}, \{p_5\}, \{p_6\}$

Dim	Boundaries of graph 2
4	$\{q_1, q_2, q_3, q_4, q_5, q_6\}$
3	$\{q_1, q_2, q_3, q_4, q_6\}, \{q_1, q_2, q_3, q_5, q_6\},$ $\{q_1, q_2, q_4, q_5, q_6\}, \{q_1, q_3, q_4, q_5, q_6\}$
2	$\{q_1, q_2, q_4\}, \{q_1, q_2, q_5\}, \{q_1, q_3, q_4\},$ $\{q_1, q_3, q_5\}, \{q_1, q_2, q_3, q_6\},$ $\{q_1, q_4, q_5, q_6\}, \{q_2, q_4, q_6\},$ $\{q_2, q_5, q_6\}, \{q_3, q_4, q_6\}, \{q_3, q_5, q_6\}$
1	$\{q_1, q_2\}, \{q_1, q_4\}, \{q_1, q_3\}, \{q_1, q_5\},$ $\{q_2, q_4\}, \{q_2, q_5\}, \{q_3, q_4\}, \{q_3, q_5\},$ $\{q_2, q_6\}, \{q_3, q_6\}, \{q_4, q_6\}, \{q_5, q_6\}$
0	$\{q_1\}, \{q_2\}, \{q_3\}, \{q_4\}, \{q_5\}, \{q_6\}$

Table 5.1: List of boundaries, in terms of perfect matchings, for each component of the graph in Figure 5.2.

multiplied by all boundaries in the right table. This automatically accounts for the Plücker relations and the positivity of all Plücker coordinates $\Delta_I^{(i)} > 0$. Organizing these boundaries according to their dimension we obtain the results summarized in the first column of Table 5.2, where we show the number of boundaries $\mathbb{N}$ of each dimension. This corresponds to performing step (1) in §5.2.5.

Dim	$\mathbb{N}$	$\boldsymbol{\mathcal{N}_M}$	$\boldsymbol{\mathfrak{N}_M}$
8	1	1	1
7	8	8	9
6	36	36	44
5	104	104	140
4	208	178	274
3	288	224	330
2	264	216	264
1	144	128	136
0	36	34	34

Table 5.2: Number of boundaries $\mathfrak{N}_M$ of the $n = 4$, 2-loop amplituhedron, of various dimensions. $\mathbb{N}$ is the number of boundaries before the positivity of $\Delta_{1234}^{(1,2)}$ is implemented. $\mathcal{N}_M$ is the surviving number of boundaries after this condition is enforced, but before the non-trivial vanishing of $\Delta_{1234}^{(1,2)}$ is considered. We use a subindex M to emphasize quantities which are computed in the mini stratification.

In agreement with our general statement in §5.4.1, the poset for the square of the positroid stratification of $G_+(2,4)$ is Eulerian:

$$\sum_{i=0}^{8}(-1)^i\,\mathbb{N}^{(i)} = 36 - 144 + 264 - \ldots - 8 + 1 = 1 \quad . \tag{5.5.1}$$

Extended positivity only imposes one additional condition: that the 4×4 minor $\Delta_{1234}^{(1,2)} \geq 0$. The bad perfect matchings here are quickly found to be the one shown in Figure 5.3 and the one where p and q are swapped, i.e. $P_{1,6}$ and $P_{6,1}$; the good perfect matchings are those shown in Figure 5.4 and their $p \leftrightarrow q$ counterparts, i.e. $P_{2,3}, P_{4,5}, P_{3,2}$ and $P_{5,4}$, cf. (5.4.3).

Next, we remove all boundaries containing $P_{1,6}$ or $P_{6,1}$, unless they also contain any of $P_{2,3}, P_{4,5}, P_{3,2}$ or $P_{5,4}$. This procedure corresponds to performing step (2) in §5.2.5 and yields the middle column in Table 5.2. It is very interesting to see that this column also forms an Eulerian poset:

$$\sum_{i=0}^{8}(-1)^i\mathcal{N}_M^{(i)} = 34 - 128 + 216 - \ldots - 8 + 1 = 1 \quad . \tag{5.5.2}$$

This is in general not true at higher loops. However, we will later observe in §5.8.1 that this is also the case at 4-loops.

Finally, we construct new boundaries by further imposing the vanishing of the 4×4 minor $\Delta_{1234}^{(1,2)}$ on those boundaries on which it is possible and not automatic due to the vanishing of Plücker coordinates. Its expression in terms of Plücker coordinates is given in (5.4.2). This corresponds to steps (3) and (4) in §5.2.5. For every boundary in the $\mathcal{N}_M$ column of Table 5.2 for which it is possible to impose the equality in (5.4.3), we get an additional boundary of one dimension less. The final answer for the total number of boundaries of the amplituhedron is displayed in the right-hand column in Table 5.2. The poset is no longer Eulerian:

$$\sum_{i=0}^{8}(-1)^i\mathfrak{N}_M^{(i)} = 34 - 136 + 264 - \ldots - 9 + 1 = 2 \quad . \tag{5.5.3}$$

Remarkably, in §5.7 we will reproduce the right column of Table 5.2 by studying the singularities of the integrand.

The Log of the Amplitude

Let us now investigate the geometric properties of another object related to the amplitude. While the fundamental object of interest in field theory is the amplitude, in order to make a connection with the S-matrix we are really interested in its *log*, $S \sim \log(A)$. Writing the loop expansion of A as

$$A = 1 + gA_1 + g^2A_2 + \ldots \,, \tag{5.5.4}$$

where A_L is the L-loop contribution, and expanding $\log(A)$ we find the second-order correction to the log of the amplitude to be $g^2(A_2 - \frac{A_1^2}{2})$.

Physically, the log of the amplitude is a very interesting object. All amplitudes are IR divergent, with the divergence going as $\frac{1}{\epsilon^{2L}}$ for the L-loop contribution, in dimensional regularization. However, the divergence of the log of the amplitude has a fixed order, always going as $\frac{1}{\epsilon^2}$. In the 2-loop case this manifests itself in an exact cancellation of higher order divergences between the A_2 and $\frac{A_1^2}{2}$ terms.

Let us continue focusing on $k = 0$, $n = 4$ and $L = 2$. The amplitude A_2 can be viewed as two $D_{(i)} \in G_+(2,4)$ with the additional condition that the 4×4 minor $\Delta_{1234}^{(1,2)} \geq 0$. On the other hand, A_1^2 is simply the square of the 1-loop amplitude, and corresponds to two $D_{(i)} \in G_+(2,4)$ with no extra condition imposed (the factor of $\frac{1}{2}$ corresponds to the symmetrization of loop variables and is of no geometric importance). Then, the *difference* between these two objects is clearly given by two $D_{(i)}$ with $\Delta_{1234}^{(1,2)} \leq 0$. We thus conclude that, from a geometric standpoint, the log of the amplitude at 2-loops can be seen as a complement of the amplitude. At higher loops the story is more complicated, so we shall here only focus on understanding the geometric significance of the complement of the 2-loop amplituhedron.

It is straightforward to modify our combinatorial methods to incorporate the change from $\Delta_{1234}^{(1,2)} \geq 0$ to $\Delta_{1234}^{(1,2)} \leq 0$. The results of the stratification of the log of the amplitude are summarized in Table 5.3. Very interestingly, $\mathcal{E}$ is once again

$$\sum_{i=0}^{8}(-1)^i \mathfrak{N}_{M,\text{Log}}^{(i)} = 32 - 120 + 220 - \ldots - 9 + 1 = 2 \quad . \tag{5.5.5}$$

Gluing the Amplitude to its Log

The amplitude and its log are characterized by having $\Delta_{1234}^{(1,2)} \geq 0$ and $\Delta_{1234}^{(1,2)} \leq 0$, respectively. Their gluing corresponds to the square of the positroid stratification of $G_+(2,4)$, since it is obtained by not imposing any restriction on $\Delta_{1234}^{(1,2)}$. Here we discuss in detail the emergence of this simple geometric object from its components.

The 7-dimensional gluing subspace is characterized by $\Delta_{1234}^{(1,2)} = 0$. We can study its structure by demanding $\Delta_{1234}^{(1,2)} = 0$ and proceeding with our standard stratification. The numbers of boundaries at different dimensions $\mathfrak{N}_{M,\Delta^{(1,2)}=0}$ are given in Table 5.4. These boundaries can be divided into two disjoint categories:

Dim	$\mathfrak{N}_{M,\text{Log}}$
8	1
7	9
6	44
5	132
4	240
3	274
2	220
1	120
0	32

Table 5.3: Number of boundaries $\mathfrak{N}_{M,\text{Log}}$ of various dimensions of the log of the $k = 0$, $n = 4$, 2-loop amplituhedron.

- Boundaries on which the condition $\Delta^{(1,2)}_{1234} = 0$ imposes a constraint on 2×2 minors.
- Boundaries on which the condition $\Delta^{(1,2)}_{1234} = 0$ is trivially satisfied because at least six of the 2×2 minors vanish, cf. (5.4.2).

The first category corresponds to boundaries of both the amplitude and its log, but which are not present in the square of the positroid stratification of $G_+(2,4)$. It is given by the first column on the left of Table 5.4. The second category consists of boundaries of the amplitude, its log, and the square of the positroid stratification of $G_+(2,4)$. The corresponding number of boundaries is simply the difference of the two columns in this table. Note that the first category also represents the difference between the last two columns of Table 5.2, and for this reason we have denoted it $\mathfrak{N}_M - \mathcal{N}_M$.

Let us investigate the interplay among the boundaries of the two components and the gluing region. One should be particularly careful in not double counting boundaries which are present in both the amplitude and its log. Moreover, there are boundaries of the gluing subspace which are not boundaries of the square of the positroid stratification of $G_+(2,4)$. Table 5.5 presents a useful classification of the

Dim	$\mathfrak{N}_M - \mathcal{N}_M$	$\mathfrak{N}_{M,\boldsymbol{\Delta}^{(1,2)}=\mathbf{0}}$
7	1	1
6	8	8
5	36	36
4	96	104
3	106	162
2	48	164
1	8	104
0	0	30

Dim	$(\mathfrak{N}_M - \mathcal{N}_M)^{(+1)}$
8	1
7	8
6	36
5	96
4	106
3	48
2	8
1	0
0	0

Table 5.4: On the left: number of boundaries $\mathfrak{N}_{M,\Delta^{(1,2)}=0}$ for the space with $\Delta^{(1,2)}_{1234} = 0$ in the $n = 4$, 2-loop case. The first column $\mathfrak{N}_M - \mathcal{N}_M$ lists those boundaries where the condition $\Delta^{(1,2)}_{1234} = 0$ imposes a non-trivial constraint among the 2×2 minors. On the right: the list of boundaries $\mathfrak{N}_M - \mathcal{N}_M$ considered as of one dimension larger, following the explanation in the text.

boundaries of all the objects under consideration based on the properties of the 4×4 minor.

The last row in Table 5.5 corresponds to the $(\mathfrak{N}_M - \mathcal{N}_M)$ boundaries of Table 5.4. The first row in the table specifies those boundaries for which $\Delta^{(1,2)}_{1234}$ contains both positive and negative terms but it is not set to zero. Starting from such configurations, $\Delta^{(1,2)}_{1234}$ can be turned off non-trivially, reducing the dimension by one and producing the boundaries in the last row of Table 5.5. We thus conclude that the list of the boundaries in the first row is also equal to $(\mathfrak{N}_M - \mathcal{N}_M)$, but where the dimension of the boundaries is increased by 1. We denote this set $(\mathfrak{N}_M - \mathcal{N}_M)^{(+1)}$ and show it on the right of Table 5.4.

Given the structure shown in Table 5.5, the relation between the number of boundaries *at each dimension* is

$$\mathbb{N} = \mathfrak{N}_M + \mathfrak{N}_{M,\text{Log}} - \mathfrak{N}_{M,\Delta^{(1,2)}=0} - (\mathfrak{N}_M - \mathcal{N}_M) - (\mathfrak{N}_M - \mathcal{N}_M)^{(+1)} \,. \tag{5.5.6}$$

The validity of this equation can be explicitly checked using Tables 5.2, 5.3 and 5.4.

$\Delta^{(1,2)}_{1234}$ **property**	**Square of** $G_+(2,4)$ $\mathbb{N}$	**Amplitude** $\mathfrak{N}_M$	**Log** $\mathfrak{N}_{M,\text{Log}}$	**Gluing space** $\mathfrak{N}_{M,\Delta^{(1,2)}=0}$
$\neq 0$, (+) and (−) terms	×	×	×	
> 0, only (+) terms	×	×		
< 0, only (−) terms	×		×	
$= 0$ trivially	×	×	×	×
$= 0$ non-trivially		×	×	×

Table 5.5: Boundaries of the different geometries, classified in terms of the properties of $\Delta^{(1,2)}_{1234}$: whether it is vanishing (trivially or not once vanishing Plücker coordinates have been fixed), and if it contains positive, negative or both types of Plücker coordinates, cf. (5.4.2).

For instance, at dimension 4 we have $274+240-104-96-106 = 208$. The relation extends to the Euler numbers of the different objects. $\mathcal{E} = 2$ for $\mathfrak{N}_M$ and $\mathfrak{N}_{M,\text{Log}}$, the Euler numbers of $(\mathfrak{N}_M - \mathcal{N}_M)$ and $(\mathfrak{N}_M - \mathcal{N}_M)^{(+1)}$ are opposite by construction and cancel in (5.5.6), while $\mathcal{E} = 3$ for $\mathfrak{N}_{M,\Delta^{(1,2)}=0}$. The combination of all these pieces beautifully produces the $\mathcal{E} = 1$ for the square of the positroid stratification of $G_+(2,4)$.

5.5.2 Full Stratification

Let us now consider the full stratification of $G_+(0,4;2)$. As explained in §5.2.4, the full stratification refines the mini stratification by distinguishing the different regions satisfying each positivity condition. In the $G_+(0,4;2)$ case, the positivity condition being satisfied in different regions is the extended positivity of the 4×4 minor $\Delta^{(1,2)}_{1234}$, and the domains are characterized by additional inequalities imposed on (combinations of) 2×2 Plücker coordinates. In this way, each boundary is specified by a list of minors, and by a set of inequalities for the 2×2 minors.

The refinement to obtain the full stratification changes the mini stratification in two ways:

- The boundaries in Γ_0 are now distinguished by the set of vanishing Plücker

coordinates and the region. For every set of vanishing Plücker coordinates, the minor $\Delta^{(1,2)}_{1234}$ may or may not be trivially zero; if it is not, the separate regions are generated by the condition $\Delta^{(1,2)}_{1234} > 0$ which can be satisfied on disjoint regions of the $\Delta^{(i)}_I$ parameter space. If instead $\Delta^{(1,2)}_{1234} = 0$ trivially, there may still be multiple regions: they descend from higher-dimensional configurations where the 4×4 minor is different from zero and splits into separate regions. Of course, it is also possible that $\Delta^{(1,2)}_{1234} = 0$ trivially and we only have a single region. We will illustrate explicit examples of each of these phenomena in the examples below.

- The structure of Γ_1, which is obtained by setting $\Delta^{(1,2)}_{1234} = 0$ non-trivially when it is possible to do so, changes in general. The new Γ_1 takes into account the explicit form of the regions in Γ_0.

For convenience we again reproduce the expression for the only 4×4 minor present at 2-loops, expressed in terms of the 2×2 Plücker coordinates:

$$\Delta^{(1,2)}_{1234} = \Delta^{(1)}_{12}\Delta^{(2)}_{34} + \Delta^{(1)}_{34}\Delta^{(2)}_{12} + \Delta^{(1)}_{23}\Delta^{(2)}_{14} + \Delta^{(1)}_{14}\Delta^{(2)}_{23} - \Delta^{(1)}_{13}\Delta^{(2)}_{24} - \Delta^{(1)}_{24}\Delta^{(2)}_{13}\,. \quad (5.5.7)$$

By using the Plücker relations this may be turned into the convenient form

$$\begin{aligned}\Delta^{(1,2)}_{1234} \;=\; & \frac{1}{\Delta^{(1)}_{24}\Delta^{(2)}_{24}}\Big[(\Delta^{(1)}_{23}\Delta^{(2)}_{24} - \Delta^{(1)}_{24}\Delta^{(2)}_{23})(\Delta^{(2)}_{14}\Delta^{(1)}_{24} - \Delta^{(2)}_{24}\Delta^{(1)}_{14}) + \\ & (\Delta^{(1)}_{12}\Delta^{(2)}_{24} - \Delta^{(1)}_{24}\Delta^{(2)}_{12})(\Delta^{(2)}_{34}\Delta^{(1)}_{24} - \Delta^{(2)}_{24}\Delta^{(1)}_{34})\Big]\,. \quad (5.5.8)\end{aligned}$$

An equivalent expression exists where all $\{24\}$ indices are replaced by $\{13\}$ indices; this simply amounts to solving for the Plücker relations in terms of $\Delta^{(i)}_{13}$ instead of $\Delta^{(i)}_{24}$. To avoid ambiguity, when the Plücker relations are non-trivial we shall always explicitly solve for them, and plug the answer into $\Delta^{(1,2)}_{1234}$, in a form similar to (5.5.8).

The inequalities that characterize the full stratification only involve the factors in the expression for $\Delta^{(1,2)}_{1234}$ shown in (5.5.8). Explicitly, the inequalities specifying the regions can only be one or more of the following:

$$\begin{aligned}&(\Delta^{(1)}_{23}\Delta^{(2)}_{24} - \Delta^{(1)}_{24}\Delta^{(2)}_{23}) \gtrless 0 \qquad && (\Delta^{(2)}_{14}\Delta^{(1)}_{24} - \Delta^{(2)}_{24}\Delta^{(1)}_{14}) \gtrless 0 \\ &(\Delta^{(1)}_{12}\Delta^{(2)}_{24} - \Delta^{(1)}_{24}\Delta^{(2)}_{12}) \gtrless 0 \qquad && (\Delta^{(2)}_{34}\Delta^{(1)}_{24} - \Delta^{(2)}_{24}\Delta^{(1)}_{34}) \gtrless 0 \quad (5.5.9)\end{aligned}$$

or their equivalent counterparts where $\Delta^{(i)}_{24}$ is replaced by $\Delta^{(i)}_{13}$. The choice of whether we need to consider the expressions with $\Delta^{(i)}_{13}$ or $\Delta^{(i)}_{24}$ is determined by which ones are equal to zero: if any $\Delta^{(i)}_{13} = 0$ we need to use the expression with $\Delta^{(i)}_{24}$'s, and vice-versa. If both $\Delta^{(i)}_{13} = \Delta^{(j)}_{24} = 0$ are zero (where $i = 1, 2$ and $j = 1, 2$), there are no non-trivial inequalities which we may consider. When there are no non-trivial inequalities, we only have a single region for the label in question.

Given a set of vanishing Plücker coordinates, the full list of cases for which there cannot be any non-trivial inequalities is the following:

- Configurations where the expression (5.5.7) for $\Delta^{(1,2)}_{1234}$ only has positive terms.
- Configurations where $\Delta^{(i)}_{13} = \Delta^{(j)}_{24} = 0$, where i and j are individually free to be 1 or 2.
- Configurations where the following combination of 2×2 minors is vanishing: $\Delta^{(i)}_{12} = \Delta^{(j)}_{14} = \Delta^{(k)}_{23} = \Delta^{(l)}_{34} = 0$, where i, j, k, l are individually free to be 1 or 2. These configurations ruin all 4 inequalities in (5.5.9).

For these cases, the construction of Γ_1 is identical to that of the mini stratification.

For the remaining cases we now identify eight prototypical configurations, which exhaust all possibilities which may arise at 2-loops. In each separate case, we specify the Γ_1 structure, and in this way construct the full stratification. We indicate with $(\ldots)$ the factors in the 4×4 determinant which are "non-trivial", e.g. $(\Delta^{(1)}_{23}\Delta^{(2)}_{24} - \Delta^{(1)}_{24}\Delta^{(2)}_{23})$, and which may thus define a region through the inequalities (5.5.9). We indicate with k_i a positive quantity made up of a product of 2×2 Plücker coordinates, e.g. $k = (\Delta^{(1)}_{24}\Delta^{(2)}_{24})$.

The eight possible configurations are the following:

1. Cases where the 4×4 is different from zero and has the expression[12]

$$\Delta^{(1,2)} = \frac{1}{k}\Big[\,(\ldots)\,(\ldots) + (\ldots)\,(\ldots)\,\Big]\,.$$

[12]For notational convenience we suppress the subindex of the 4×4 minor, since for four particles it can only be $\{1234\}$.

At 2-loops there is in fact only one such case in Γ_0, which is the 8-dimensional element. Here $\Delta^{(1,2)} > 0$ specifies a single region, with a single boundary at $\Delta^{(1,2)} = 0$. Thus, Γ_1 only gives rise to one additional boundary of dimension 7, precisely as in the mini stratification.

2. Cases where the 4×4 is different from zero and has the expression

$$\Delta^{(1,2)} = \frac{1}{k_1}\Big[\,(\dots)\,(\dots) + k_2\,(\dots)\Big]\,.$$

All 7-dimensional elements in Γ_0 are of this type, e.g. the configuration with $\Delta^{(1)}_{23} = 0$. $\Delta^{(1,2)} > 0$ specifies a single region, with a single 6-dimensional boundary at $\Delta^{(1,2)} = 0$, similarly to the case above.

3. Cases where the 4×4 is different from zero and has the expression

$$\Delta^{(1,2)} = \frac{1}{k_1}\Big[\,(\dots)\,(\dots) - k_2\Big]\,.$$

Here $\Delta^{(1,2)} > 0$ is divided into two regions, each bounded by a hyperbolic curve, as explained in §5.2.4. The regions are specified by the parentheses being both positive or both negative. The condition $\Delta^{(1,2)} = 0$ gives rise to two boundaries of one dimension less, because we can solve $\Delta^{(1,2)} = 0$ on these two different regions, each region being one of the two hyperbolic curves. An example of this type is $\Delta^{(1)}_{23} = \Delta^{(1)}_{14} = 0$.

4. Cases where the 4×4 is different from zero and has the expression

$$\Delta^{(1,2)} = \frac{1}{k_1}\Big[\,(\dots)\,(\dots) + k_2\Big]\,.$$

This is a single connected region, bounded by two hyperbolic curves. Hence, the condition $\Delta^{(1,2)} = 0$ gives rise to two extra boundaries of one dimension less. As an example for this category, consider the case

$$\Delta^{(1)}_{12} = \Delta^{(2)}_{34} = 0\,.$$

Using (5.5.8), the region with $\Delta^{(1,2)} > 0$ is defined by the inequality

$$(\Delta^{(1)}_{23}\Delta^{(2)}_{24} - \Delta^{(1)}_{24}\Delta^{(2)}_{23})(\Delta^{(2)}_{14}\Delta^{(1)}_{24} - \Delta^{(2)}_{24}\Delta^{(1)}_{14}) > -(\Delta^{(1)}_{24}\Delta^{(2)}_{12})(\Delta^{(2)}_{24}\Delta^{(1)}_{34})\,.$$

Parametrizing $x = (\Delta^{(1)}_{23}\Delta^{(2)}_{24} - \Delta^{(1)}_{24}\Delta^{(2)}_{23})$, $y = (\Delta^{(2)}_{14}\Delta^{(1)}_{24} - \Delta^{(2)}_{24}\Delta^{(1)}_{14})$ and $k = (\Delta^{(1)}_{24}\Delta^{(2)}_{12})(\Delta^{(2)}_{24}\Delta^{(1)}_{34})$, this is the connected region in the xy plane inside the hyperbola $xy = -k$. The two extra boundaries of one dimension less are the two branches of the hyperbola.

5. Cases where the 4×4 is different from zero and factorizes as

$$\Delta^{(1,2)} = \frac{1}{k}\Big[\,(\dots)\,(\dots)\,\Big]\,.$$

This type of configuration is a bit more subtle, as it is the limit of the hyperbolic cases above where the two branches of the hyperbola meet at the origin. Parametrizing the first $(\dots)$ as x and the second one as y, the $\Delta^{(1,2)} > 0$ condition is satisfied in the first and third quadrant of the xy plane, thus giving rise to two regions. Here there are four boundaries of one dimension less, where $\Delta^{(1,2)} = 0$, corresponding to the positive and negative x and y axes. The origin corresponds to a single boundary of two dimensions less. These boundaries may be seen as setting $x = 0$ while remembering that $y \neq 0$ was composed of two separate regions, or setting $y = 0$ and $x \neq 0$, and finally setting $x = y = 0$. An example for this category is

$$\Delta^{(1)}_{12} = \Delta^{(2)}_{12} = 0\,.$$

6. Cases where the 4×4 is different from zero and does not contain parentheses $(\dots)$ that are multiplied together, i.e.

$$\Delta^{(1,2)} = \frac{1}{k_1}\Big[\,(\dots)\,k_2 + (\dots)\,k_3\Big] \text{ or } \Delta^{(1,2)} = \frac{1}{k_1}\Big[\,(\dots)\,k_2 \pm k_3\Big] \text{ or } \Delta^{(1,2)} = (\dots)\,k\,.$$

Each of these cases consist of a single region and the condition $\Delta^{(1,2)} = 0$ gives rise to a single boundary of one dimension less. This can most clearly be seen by studying the xy plane as done above. An example of this category is

$$\Delta^{(1)}_{12} = \Delta^{(2)}_{23} = 0\,.$$

7. Cases where the 4×4 trivially vanishes but two of the four inequalities in (5.5.9) (or their $\{13\} \leftrightarrow \{24\}$ counterparts) remain untouched. This is most transparently written as

$$\Delta^{(1,2)} = \frac{1}{k}\Big[0 \times (\dots) + 0 \times (\dots)\,\Big]\,.$$

These cases are the most subtle of all. Although the 4×4 minor vanishes, we still have four separate regions, specified by the two possible inequalities which are still present in each $(\ldots)$. To see why this is the case, we need to know how these configurations arose from higher dimensional ones: here the path taken to reach this configuration will specify the region.

To this end, let us denote the first bracket as x and the second one as y. A detailed investigation shows that all these cases arise from Type 5 cases described above, where additionally one of the brackets is trivially shut off by turning off some $\Delta_I^{(i)}$'s. Here, the remaining bracket is still split into two regions, while the brackets that do not appear in Type 5 are completely free.

Thus, the only possibilities are as follows: either x is split into two regions while y is free, or y is split into two regions while x is free. In total we then have four regions.

From these four regions descend two extra boundaries of one dimension less: either $x = 0$ and y is free, or $y = 0$ and x is free. From here there are no further boundaries, as we may not set a free variable to zero.

An example for this category is given by the following set of vanishing Plücker coordinates

$$\Delta_{12}^{(1)} = \Delta_{23}^{(1)} = \Delta_{13}^{(1)} = \Delta_{12}^{(2)} = \Delta_{23}^{(2)} = \Delta_{13}^{(2)} = 0\,.$$

Here the four 4-dimensional regions are

$$\begin{aligned} &\text{Regions 1 and 2:} \qquad (\Delta_{14}^{(2)}\Delta_{24}^{(1)} - \Delta_{24}^{(2)}\Delta_{14}^{(1)}) \gtrless 0 \\ &\text{Regions 3 and 4:} \qquad (\Delta_{34}^{(2)}\Delta_{24}^{(1)} - \Delta_{24}^{(2)}\Delta_{34}^{(1)}) \gtrless 0 \end{aligned}$$

while the two extra lower dimensional boundaries of dimension 3 are characterized by the conditions

$$\begin{aligned} &\text{Region A:} \qquad (\Delta_{14}^{(2)}\Delta_{24}^{(1)} - \Delta_{24}^{(2)}\Delta_{14}^{(1)}) = 0 \\ &\text{Region B:} \qquad (\Delta_{34}^{(2)}\Delta_{24}^{(1)} - \Delta_{24}^{(2)}\Delta_{34}^{(1)}) = 0\,. \end{aligned}$$

8. Cases where the 4×4 trivially vanishes but one of the four inequalities in

(5.5.9) can be imposed. These are most transparently written as

$$\Delta^{(1,2)} = \frac{1}{k_1}\Big[0 \times (\dots) + k_2 \times 0\Big] \qquad \text{or} \qquad \Delta^{(1,2)} = \frac{1}{k_1}\Big[0 \times (\dots)\Big]$$

and can be obtained from the Type 7, above. These cases consist of two regions, determined by the sign of the non-vanishing parenthesis. They give rise to one extra boundary of one dimension less, when we saturate the inequality.

The results of the full stratification are summarized in Table 5.6. To give an example of how these numbers are obtained, let us discuss in detail the 6-dimensional boundaries of $\mathfrak{N}_F$. At dimension 6, there are four possible sets of vanishing Plücker coordinates which are cases of Type 3, four cases of Type 4, four cases of Type 5, and 24 cases of Type 6. On top of that, there are 8 other boundaries descending from 8 7-dimensional configurations of Type 2, where we have imposed $\Delta^{(1,2)} = 0$. In total this gives the entry at dimension 6 in Table 5.6, i.e. $4 \times 2 + 4 + 4 \times 2 + 24 + 8 = 52$.

We can then adopt the same strategy to obtain the full stratification of the log of the amplitude; the only difference is that we have to impose $\Delta^{(1,2)} \leq 0$ to identify the different regions. This modification takes a very simple form on the classification described here: we only need to interchange Types 3 and 4. Table 5.6 also shows the results for the log of the amplitude, as well as the gluing region defined by $\Delta^{(1,2)} = 0$, which is obtained in a very similar way.

We note that for the full stratification, the relation (5.5.6) which connects the amplitude, the log and the gluing region is no longer valid.

The Euler numbers for the full stratification of the different spaces can be easily computed to be:

- $\mathfrak{N}_F$: $\mathcal{E} = 8$,
- $\mathfrak{N}_{F,\text{Log}}$: $\mathcal{E} = 8$,
- $\mathfrak{N}_{F,\Delta^{(1,2)}=0}$: $\mathcal{E} = 7$

Interestingly, the Euler number of the amplitude and of the log of the amplitude coincide; the reason for this is that there is an equal number of cases of Types 3 and 4.

Dim	$\mathfrak{N}_F$	$\mathfrak{N}_{F,\text{Log}}$	$\mathfrak{N}_{F,\Delta^{(1,2)}=0}$
8	1	1	0
7	9	9	1
6	52	52	8
5	168	160	56
4	328	294	156
3	392	336	224
2	306	262	206
1	144	128	112
0	34	32	30

Table 5.6: Full stratification of the $n = 4$, 2-loop amplituhedron. $\mathfrak{N}_F$ gives the number of boundaries for the amplitude. $\mathfrak{N}_{F,\text{Log}}$ gives the number of boundaries for the log of the amplitude, and $\mathfrak{N}_{F,\Delta^{(1,2)}=0}$ describes the full stratification of the gluing space.

5.6 Three loops

In this section we initiate the investigation of $L = 3$, for which we construct the mini stratification. Our results should be valuable for any future study of this geometry.

5.6.1 Mini Stratification

The matrix $\mathcal{C}$ takes the form

$$\mathcal{C} = \begin{pmatrix} D_{(1)} \\ D_{(2)} \\ D_{(3)} \end{pmatrix} . \tag{5.6.1}$$

Its largest minors are 4×4 and we have three of them. $\mathcal{C}$ has $3 \times 4 = 12$ degrees of freedom.

Taking three identical copies of the graph in Figure 4.8 and doing the decomposition followed by identification as done in §4.5, we obtain the left-hand column of Table 5.7. This is the same as taking the 3^{rd} power of the 1-loop stratification. In total we get $33^3 = 35\,937$ different boundaries. At this stage extended positivity has

not yet been fully implemented; we have only performed step (1) in §5.2.5. Again, we note in agreement with the general discussion in §5.4.1, we obtain an Eulerian poset:

$$\sum_{i=0}^{12}(-1)^i\mathbb{N}^{(i)} = 216 - 1296 + \ldots - 12 + 1 = 1\,. \tag{5.6.2}$$

Dim	$\mathbb{N}$	$\boldsymbol{\mathcal{N}_M}$	$\boldsymbol{\mathfrak{N}_M}$
12	1	1	1
11	12	12	15
10	78	78	117
9	340	340	611
8	1 086	1 002	2 244
7	2 640	2 160	5 908
6	4 960	3 490	10 996
5	7 200	4 440	13 956
4	7 956	4 656	12 044
3	6 480	3 960	7 488
2	3 672	2 520	3 504
1	1 296	1 008	1 128
0	216	186	186

Table 5.7: Number of boundaries $\mathfrak{N}_M$ of $G_+(0,4;3)$, of various dimensions. $\mathbb{N}$ is the number of boundaries before the extended positivity conditions on the larger minors are implemented, and $\mathcal{N}_M$ is the surviving number of boundaries after these conditions are enforced, but before taking into account the boundaries arising from the $\Delta_I^{(i,j)} \geq 0$.

Next, we need to impose three additional conditions from extended positivity: $\Delta_I^{(1,2)} \geq 0$, $\Delta_I^{(1,3)} \geq 0$ and $\Delta_I^{(2,3)} \geq 0$, where $I = 1234$ as in the rest of this section. This can be done either by checking them individually or employing the method expounded in §5.4. Deleting the boundaries that violate extended positivity gives the second column in Table 5.7. We note that this column does not correspond to

an Eulerian poset:

$$\sum_{i=0}^{12}(-1)^i\mathcal{N}_M^{(i)} = 186 - 1008 + \ldots - 12 + 1 = 13\,. \tag{5.6.3}$$

Let us now perform a complete classification of the possible Γ_1 sub-posets in the mini stratification of $G_+(0,4;3)$, i.e. the new structure arising from turning off 4×4 minors. Points in Γ_0 can be discriminated according to the number of $\Delta_I^{(i,j)}$'s with both positive and negative terms, i.e. of type (iii) in the discussion of §5.2.5. We denote the three possibilities as $N\Delta_I^{(i,j)}$, where $N = 1, 2, 3$.

Figure 5.6 shows the possible Γ_1's emanating from $1\Delta_I^{(i,j)}$ and $2\Delta_I^{(i,j)}$ points. This is a result of careful analysis which shows that in both cases, all type (iii) $\Delta_I^{(i,j)}$ can be independently turned off.

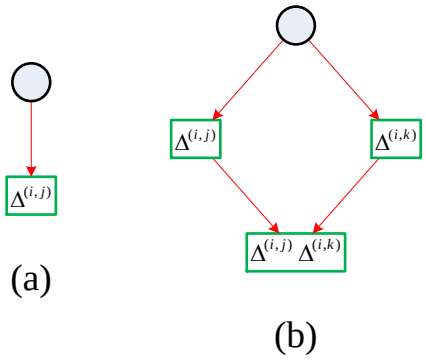

Figure 5.6: The general structure of Γ_1's emanating from: (a) $1\Delta_I^{(i,j)}$ and (b) $2\Delta_I^{(i,j)}$ points

The possible structures become far richer for $3\Delta_I^{(i,j)}$ points. In general the determination of Γ_1's is challenging, because it requires solving equations in which variables and certain combinations of them are restricted to the positive domain. To illustrate the subtleties involved, let us consider a $3\Delta_I^{(i,j)}$ example, i.e. one in which it naively seems possible that any of the three 4×4 minors can be turned off, but this is not the case once relations are properly taken into account. For example, if we have a relation like

$$\Delta_I^{(1,3)} = a\,\Delta_I^{(1,2)} - b\,\Delta_I^{(2,3)}\,, \quad a, b > 0\,, \tag{5.6.4}$$

we see that it is not possible to turn off $\Delta_I^{(1,2)}$ while keeping both $\Delta_I^{(1,3)}$ and $\Delta_I^{(2,3)}$ positive. In this expression, a and b are functions of non-vanishing Plücker coordinates. We also see that it is not possible to turn off only two of the three $\Delta_I^{(i,j)}$. From any boundary that has a reduced set of Plücker coordinates from the maximum possible, such that the larger minors $\Delta_I^{(i,j)}$ satisfy the relation above, we expect a Γ_1 as in Figure 5.7 Type A.

Other structures in Figure 5.7 result from relations of the following general forms

$$\begin{aligned}
&\text{Type B:} \quad \Delta_I^{(i,j)} = a\,\Delta_I^{(j,k)} - b\,\Delta_I^{(i,k)} - c\,, && a,b,c \;>\; 0 \\
&\text{Type C:} \quad \Delta_I^{(i,k)} = k\left(a\,\Delta_I^{(i,j)} - b\,\Delta_I^{(j,k)}\right)\,, && a,b \;>\; 0, \quad k \text{ free} \\
&\text{Type D:} \quad \Delta_I^{(i,k)} = k\left(a\,\Delta_I^{(i,j)} - b\,\Delta_I^{(j,k)}\right) - c\,, && a,b,c \;>\; 0, \quad k \text{ free}
\end{aligned} \tag{5.6.5}$$

and so on. Here a, b, c and k represent functions of non-vanishing Plücker coordinates. For Type H structures, all the $\Delta_I^{(i,j)}$'s may be turned off completely independently. In §5.8 we consider an explicit example of these relations and discuss it in more detail.

Figure 5.7 provides a comprehensive treatment of $3\Delta_I^{(i,j)}$ boundaries. We stress that all the boundaries in a given Γ_1 have the same set of non-vanishing Plücker coordinates; different sites only differ by $\Delta^{(i,j)}$'s that have been set to zero.

Table 5.8 shows the number of boundaries of each dimension with the structures in Figure 5.7, and the added contribution to the total number of boundaries. This contribution must be added to those boundaries in column $\mathcal{N}_M$ of Table 5.7, to yield the total $\mathfrak{N}_M$, also quoted in Table 5.7. This procedure implements step (4) in §5.2.5.

We can use these results to compute an Euler number, which is

$$\mathcal{E} = \sum_{i=0}^{12} (-1)^i \mathfrak{N}_M^{(i)} = 186 - 1128 + \ldots - 15 + 1 = -14\,. \tag{5.6.6}$$

This, however, should only be interpreted as a possible characterization of the space based on the mini stratification. It should not be assigned much geometric significance beyond this. In fact, as we have seen for $L = 2$, the value of $\mathcal{E}$ associated to the full stratification will most likely be different.

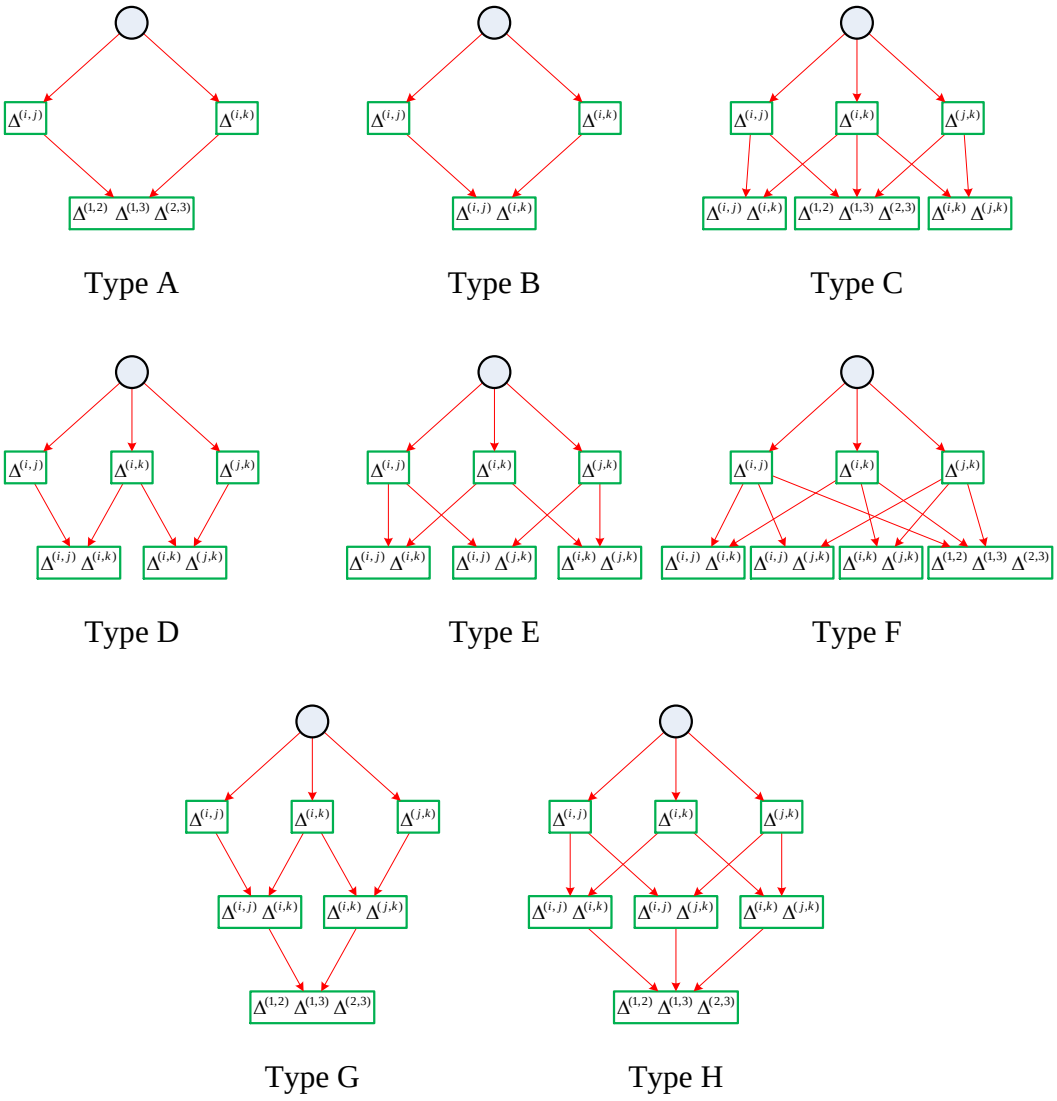

Figure 5.7: Full classification of possible Γ_1's emanating from $3\Delta_I^{(i,j)}$ points in Γ_0 in the mini stratification of $G_+(0,4;3)$. In each green box we indicate which 4×4 minors have been set to zero. Interestingly, for Type A it is not possible to turn off only two of them due to positivity. Furthermore, for types B, D and E it is also impossible to turn off the three 4×4 minors.

	$3\ \Delta_I^{(i,j)}$								$2\ \Delta_I^{(i,j)}$	$1\ \Delta_I^{(i,j)}$	Total
Dim	**A**	**B**	**C**	**D**	**E**	**F**	**G**	**H**			**contribution**
12	0	0	0	0	0	0	0	1	0	0	+0
11	0	0	0	0	0	0	0	12	0	0	+3
10	0	0	0	0	0	0	0	78	0	0	+39
9	0	0	0	0	0	4	0	324	0	12	+271
8	0	12	48	0	0	12	0	726	96	108	+1 242
7	48	96	144	96	48	12	12	600	576	528	+3 748
6	144	120	144	96	0	2	0	144	1 080	1 584	+7 506
5	144	0	24	0	0	0	0	0	792	2 424	+9 516
4	24	0	0	0	0	0	0	0	240	1 848	+7 388
3	0	0	0	0	0	0	0	0	24	672	+3 528
2	0	0	0	0	0	0	0	0	0	96	+984
1	0	0	0	0	0	0	0	0	0	0	+120
0	0	0	0	0	0	0	0	0	0	0	+0

Table 5.8: Number of boundaries with $N = 1, 2, 3$ number of 4×4 minors which have both positive and negative terms, and may hence be set to zero non-trivially. The cases with $3\ \Delta_I^{(i,j)}$ are refined according to which type they are, cf. Figure 5.7. The final column contains the added contribution to the total number of boundaries.

5.7 An Alternative Path to Stratification: Integrand Poles

The amplituhedron was introduced as a geometric object whose properties replicate those of the amplitude integrand. In particular, boundaries of the amplituhedron directly correspond to singularities of the integrand. The same holds for the log of the amplitude. This implies that the corresponding integrands provide an alternative way of obtaining the stratification of these spaces.

In this section we will focus on $n = 4$ and $L = 2$ and discuss how the stratification of the amplitude and its log can be derived from the corresponding integrands. In particular, we will manage to obtain the entire mini stratifications for the two

objects. The full agreement with the ones attained via the amplituhedron constitutes substantial non-trivial evidence for the amplituhedron conjecture. It should be straightforward to extend our analysis to the full stratification. It may be possible that agreement at the level of the mini stratifications implies agreement of the full stratifications. While very interesting, investigating this claim is beyond the scope of this chapter.

We stress that looking for poles of the integrand is a substantially different approach to the one adopted in previous sections involving minors and positivity, and it is very satisfactory to see that the two methods agree beautifully. From the integrand perspective, positivity is not an ingredient that is introduced by hand; the integrand accounts for positivity in an automatic way, and positivity emerges as a result.

5.7.1 The Amplitude

For the amplitude, the integrand in question is

$$\frac{\langle AB34\rangle\langle CD12\rangle + \langle AB23\rangle\langle CD14\rangle + \langle AB14\rangle\langle CD23\rangle + \langle AB12\rangle\langle CD34\rangle}{\langle ABCD\rangle\langle AB12\rangle\langle AB14\rangle\langle AB23\rangle\langle AB34\rangle\langle CD12\rangle\langle CD14\rangle\langle CD23\rangle\langle CD34\rangle}\,. \quad (5.7.1)$$

The stratification results from looking for poles of this integrand.

We have seen in previous sections that positivity eliminates many of the potential boundaries which one might naively expect from just taking the square of the positroid stratification of $G_+(2,4)$. The integrand achieves this through the presence of a nontrivial numerator, which for certain would-be boundaries cancels with factors in the denominator, to eliminate those poles which would violate positivity. Conversely, positivity eliminates configurations for which the integrand is non-singular.

It is useful to highlight that for $n = 4$ at arbitrary L there is a very simple map between brackets and minors, as shown in [80]. For $L = 2$ it is

$$\begin{array}{llll} \langle AB12\rangle = \Delta^{(1)}_{34} & \langle AB13\rangle = \Delta^{(1)}_{24} & \langle CD12\rangle = \Delta^{(2)}_{34} & \langle CD13\rangle = \Delta^{(2)}_{24} \\ \langle AB14\rangle = \Delta^{(1)}_{23} & \langle AB23\rangle = \Delta^{(1)}_{14} & \langle CD14\rangle = \Delta^{(2)}_{23} & \langle CD23\rangle = \Delta^{(2)}_{14} \\ \langle AB24\rangle = \Delta^{(1)}_{13} & \langle AB34\rangle = \Delta^{(1)}_{12} & \langle CD24\rangle = \Delta^{(2)}_{13} & \langle CD34\rangle = \Delta^{(2)}_{12} \end{array}$$
$$\langle ABCD\rangle = \Delta^{(1,2)}_{1234} \quad (5.7.2)$$

This map generalizes in the obvious way for higher loops. In this language, (5.2.4) translates into an expression for $\langle ABCD\rangle$ in terms of $\langle ABij\rangle$ and $\langle CDij\rangle$ brackets:

$$\begin{aligned}\langle ABCD\rangle &= \langle AB34\rangle\langle CD12\rangle - \langle AB24\rangle\langle CD13\rangle + \langle AB23\rangle\langle CD14\rangle \\ &+ \langle AB14\rangle\langle CD23\rangle - \langle AB13\rangle\langle CD24\rangle + \langle AB12\rangle\langle CD34\rangle\,. \quad (5.7.3)\end{aligned}$$

Similarly, (5.2.5), which was obtained by using Plücker relations, becomes

$$\begin{aligned}\langle ABCD\rangle &= \frac{\Big(\langle AB24\rangle\langle CD34\rangle - \langle AB34\rangle\langle CD24\rangle\Big)\Big(\langle AB12\rangle\langle CD24\rangle - \langle AB24\rangle\langle CD12\rangle\Big)}{\langle AB24\rangle\langle CD24\rangle} \\ &+ \frac{\Big(\langle AB24\rangle\langle CD23\rangle - \langle AB23\rangle\langle CD24\rangle\Big)\Big(\langle AB14\rangle\langle CD24\rangle - \langle AB24\rangle\langle CD14\rangle\Big)}{\langle AB24\rangle\langle CD24\rangle}\,.\end{aligned} \quad (5.7.4)$$

It is possible to use the integrand to construct both the mini and the full stratifications. As usual, for the latter it is necessary to properly account for the possible factorization of $\langle ABCD\rangle$. This can be done exactly as explained in §5.5.2.

When going to poles by shutting off brackets, it is necessary to take into account the Plücker relations associated to each of the 2-loops. In bracket language, they become

$$\begin{aligned}\langle AB14\rangle\langle AB23\rangle &+ \langle AB12\rangle\langle AB34\rangle &&= \langle AB13\rangle\langle AB24\rangle \\ \langle CD14\rangle\langle CD23\rangle &+ \langle CD12\rangle\langle CD34\rangle &&= \langle CD13\rangle\langle CD24\rangle\end{aligned} \quad (5.7.5)$$

We do not substitute these relations explicitly, but account for them *implicitly*, by only shutting off allowed combinations of brackets. For example, when shutting off $\langle AB12\rangle = 0$ and $\langle AB14\rangle = 0$ we see that we are forced to also shut off $\langle AB13\rangle = 0$ and/or $\langle AB24\rangle = 0$.

The main result of this section is that we have implemented the procedure described above and, focusing on labels, reproduced the entire mini stratification of $G_+(0,4;2)$ given by the third column of Table 5.2 starting from (5.7.1). It is important to emphasize that we have not only reproduced the counting of boundaries obtained from the amplituhedron, but have managed to establish a *one-to-one* map between all boundaries constructed with both methods. In order to illustrate this, in Appendix B.1 we present representative subsets of the boundaries at each dimension. The examples have been chosen to showcase the conceptually different

scenarios that might arise. Each of them is presented in geometric and integrand language.

The procedures for deriving the mini stratification based on the integrand and the amplituhedron are path-independent: the order in which minors are turned off to arrive at a given boundary is irrelevant. However, in a few cases, it is logically simpler to arrive at a given boundary using one route rather than another. In particular, it is usually preferable to set $\langle ABCD\rangle \to 0$ as late as possible.

5.7.2 The Log of the Amplitude

Let us now investigate the log of the amplitude in terms of the integrand. Using the integrand for A_2 given in (5.7.1) and the square of the 1-loop

$$\frac{1}{\langle AB12\rangle\langle AB14\rangle\langle AB23\rangle\langle AB34\rangle\langle CD12\rangle\langle CD14\rangle\langle CD23\rangle\langle CD34\rangle}\,, \tag{5.7.6}$$

the integrand for the 2-loop log of the amplitude becomes

$$\begin{aligned}&\frac{\langle AB34\rangle\langle CD12\rangle + \langle AB23\rangle\langle CD14\rangle + \langle AB14\rangle\langle CD23\rangle + \langle AB12\rangle\langle CD34\rangle - \langle ABCD\rangle}{\langle ABCD\rangle\langle AB12\rangle\langle AB14\rangle\langle AB23\rangle\langle AB34\rangle\langle CD12\rangle\langle CD14\rangle\langle CD23\rangle\langle CD34\rangle}\\ &= \frac{\langle AB13\rangle\langle CD24\rangle + \langle AB24\rangle\langle CD13\rangle}{\langle ABCD\rangle\langle AB12\rangle\langle AB14\rangle\langle AB23\rangle\langle AB34\rangle\langle CD12\rangle\langle CD14\rangle\langle CD23\rangle\langle CD34\rangle}\,.\end{aligned} \tag{5.7.7}$$

We still have the two Plücker relations (5.7.5). For convenience, we shall usually use the form in (5.7.7); this makes it explicit that once $\langle ABCD\rangle$ is zero, the singularities of the log integrand are the same as those of the ordinary integrand.

As in the previous section, we obtain the singularities by setting to zero brackets which explicitly appear in the denominator of the integrand. Due to Plücker relations, this may force other brackets to turn off. Again, we stress that the order in which we turn off minors to arrive at a given singularity is irrelevant. But as previously done, it is often simpler to set $\langle ABCD\rangle \to 0$ as late as possible.

Using the singularities of (5.7.7), we have managed to derive the mini stratification of the log of the amplitude previously obtained by geometric methods and summarized in Table 5.3. As for the amplitude, we stress that we have not only reproduced the counting of boundaries, but have managed to establish a one-to-one map between all boundaries constructed with both methods. This matching provides additional strong support for the amplituhedron conjecture.

5.8 The Deformed $G_+(0,n;L)$

A remarkable property of cells in the positive Grassmannian is that they are topologically balls. In other words, it is possible to prove that the posets encoding the positroid stratification of the Grassmannian are Eulerian, i.e. have $\mathcal{E}=1$ [126]. The same is true for the L^{th} power of the positroid stratification, i.e. the initial step for the stratification $G_+(0,n;L)$.

Given the detailed information on the boundary structure of the amplituhedron (or more precisely of $G_+(0,n;L)$ when discussing general values of n) we have gathered it is natural to ask whether general statements regarding the topology of the amplituhedron can be made.

In this section we would like to report on some striking experimental evidence based on explicit examples suggesting that there is a simple generalization of $G_+(0,n;L)$ which might exhibit a remarkably simple topology.

Let us introduce the *deformed* $G_+(k,n;L)$. It is convenient to define it through its stratification as we explain below. For our purposes, it is equivalent to think we are considering not the original $G_+(k,n;L)$, but a modified or deformed stratification. All the discussion in this section will be in the context of the mini stratification.[13]

Recalling the general discussion in §5.2.5, given a point in Γ_0, which is defined by a list of vanishing Plücker coordinates, we can identify non-minimal minors of type (iii). These are minors that, at least initially, can be turned off. In fact, in general, sometimes some of these minors cannot be switched off due to relations. For example, turning off one of them might impose a relation that forces another one to be strictly non-zero, or might be forbidden because it would force another minor to violate positivity. We have already encountered this kind of restriction in §5.6.1, when constructing the mini stratification of $G_+(0,4;3)$. The deformed $G_+(0,n;L)$ corresponds to assuming that *all* such minors can be independently switched off at will in the Γ_1 that emanates from that point in Γ_0. Of course we know that this is not true for $G_+(0,n;L)$: as we turn off non-minimal minors, relations between them

[13] It would be interesting to investigate how the full stratification is affected by the deformation. In order to do this, however, a more detailed definition of the deformation is necessary.

generally become important and determine the actual structure of Γ_1.

Example. Let us demonstrate the difference between the deformed and standard stratifications with an explicit example from $G_+(0,4;3)$, for which a general discussion of all possible relations which can arise between non-minimal minors was presented in §5.6.1. Consider the point in Γ_0 corresponding to the vanishing of

$$\begin{array}{c} \Delta^{(1)}_{14}, \Delta^{(1)}_{23}, \Delta^{(1)}_{24}, \Delta^{(1)}_{34} \\ \Delta^{(2)}_{12}, \Delta^{(2)}_{13}, \Delta^{(2)}_{14}, \Delta^{(2)}_{23} \\ \Delta^{(3)}_{14}, \Delta^{(3)}_{23} \end{array} \tag{5.8.1}$$

with all other Plücker coordinates being non-zero. In this case, only the Plücker relation associated to the third loop remains non-trivial and reduces to

$$\Delta^{(3)}_{12}\Delta^{(3)}_{34} = \Delta^{(3)}_{13}\Delta^{(3)}_{24}\,. \tag{5.8.2}$$

The 4×4 minors become

$$\begin{aligned} \Delta^{(1,2)}_{1234} &= \Delta^{(1)}_{12}\Delta^{(2)}_{34} - \Delta^{(1)}_{13}\Delta^{(2)}_{24} \\ \Delta^{(1,3)}_{1234} &= \Delta^{(1)}_{12}\Delta^{(3)}_{34} - \Delta^{(1)}_{13}\Delta^{(3)}_{24} \\ \Delta^{(2,3)}_{1234} &= \Delta^{(2)}_{34}\Delta^{(3)}_{12} - \Delta^{(2)}_{24}\Delta^{(3)}_{13}\,. \end{aligned} \tag{5.8.3}$$

The three of them are of type (iii) in the classification of §5.2.5, i.e. they contain both positive and negative contributions and it naively appears that any of them can be independently set to zero while preserving extended positivity. However, this is not the case. Imagine we set to zero only $\Delta^{(1,2)}_{1234}$. In this case, the remaining 4×4 minors take the form

$$\begin{aligned} \Delta^{(1,3)}_{1234} &= \frac{\Delta^{(1)}_{13}}{\Delta^{(2)}_{34}}\left(\Delta^{(2)}_{24}\Delta^{(3)}_{34} - \Delta^{(2)}_{34}\Delta^{(3)}_{24}\right) \\ \Delta^{(2,3)}_{1234} &= \frac{\Delta^{(3)}_{12}}{\Delta^{(3)}_{24}}\left(\Delta^{(2)}_{34}\Delta^{(3)}_{24} - \Delta^{(2)}_{24}\Delta^{(3)}_{34}\right) \end{aligned} \tag{5.8.4}$$

We have rewritten the first one using $\Delta^{(1,2)}_{1234}=0$ and the second one using (5.8.2). Since the prefactors are positive, we conclude it is impossible for $\Delta^{(1,3)}_{1234}$ and $\Delta^{(2,3)}_{1234}$ to be simultaneously positive.

An alternative way of reaching the same conclusion is as follows. Using (5.8.2) to rewrite $\Delta^{(2,3)}_{1234}$ as before, it is possible to prove the relation

$$\Delta^{(1,2)}_{1234} = \frac{\Delta^{(2)}_{24}}{\Delta^{(3)}_{24}}\,\Delta^{(1,3)}_{1234} + \frac{\Delta^{(1)}_{12}}{\Delta^{(2)}_{12}}\,\Delta^{(2,3)}_{1234}\,. \tag{5.8.5}$$

This is an explicit realization of the relations of Type C of (5.6.5). Once again, we see we cannot turn off $\Delta^{(1,2)}_{1234}$ while preserving the positivity of the other two 4×4 minors. We conclude that the Γ_1 emanating from this point in the underformed mini stratification does not contain a point in which only $\Delta^{(1,2)}_{1234}$ vanishes. In contrast, the deformed stratification is precisely defined such that all type (iii) minors can be independently turned off in Γ_1.

This example illustrates why we refer to the object defined by the new stratification as a *deformation*. The relaxation of the constraint imposed by each relation between non-minimal minors can be regarded as the introduction of a new degree of freedom, i.e. a *deformation parameter*. Very schematically, each relation gets an independent deformation of the form[14]

$$R(\Delta_I^{(i,j)}) = 0 \qquad \to \qquad R(\Delta_I^{(i,j)}) = \epsilon \tag{5.8.6}$$

Similar deformations are possible in the presence of higher dimensional minors. In what follows, we assume all relations between non-minimal minors can be independently relaxed. Determining how many independent deformation parameters are necessary for achieving this for each geometry is certainly an interesting problem that we will not pursue here.

As a result of the relaxation of relations in the deformed stratification, the structure of Γ_1's is considerably simplified. Figure 5.8 shows the Γ_1's for the cases of 1, 2 and 3 type (iii) $\Delta_I^{(i,j)}$s. They coincide with types (a) and (b) of Figure 5.6 and type H of Figure 5.7, from the mini stratification of the undeformed $G_+(0,4,3)$. We see the deformation substantially reduces the number of possible Γ_1's.

[14] As in (5.8.5), these relations generally depend on smaller minors, too.

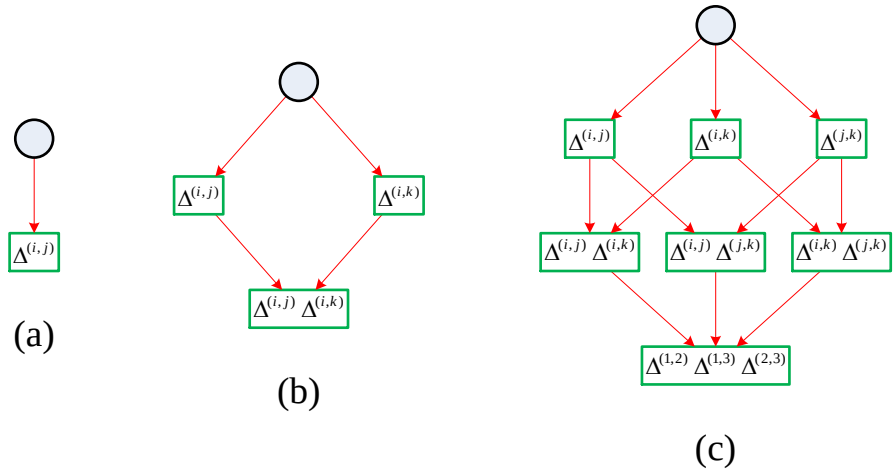

Figure 5.8: Γ_1's for the deformed $G_+(0,n;L)$ in the cases of 1, 2 and 3 type (iii) Δ_I^{ij}'s.

5.8.1 Examples

We will now stratify the deformed $G_+(0,4;L)$ for $1 \leq L \leq 4$. Taking an experimental approach, we will observe that the resulting data gives rise to a natural conjecture about the topology.

1-loop

For $L = 1$, there are no non-minimal minors and hence the deformed $G_+(0,4;1)$ is equal to the standard $G_+(0,4;1) \equiv G_+(2,4)$, which was discussed in detail in §5.3.1 and Chapter 4. The resulting poset has $\mathcal{E} = 1$.

2-loops

$G_+(0,4;2)$ coincides with its deformation, since this example contains a single 4×4 minor $\Delta_{1234}^{(1,2)}$. Then, the right-hand column of Table 5.2 also gives the boundaries of the deformed $G_+(0,4;2)$, which we reproduce in Table 5.9 for easy reference. The total number of boundaries is 1232. As noted in (5.5.3), the Euler number is equal to 2:

$$\mathcal{E} = \sum_{i=0}^{8} (-1)^i \mathfrak{N}_M^{(i)} = 34 - 136 + 264 - \ldots - 9 + 1 = 2\,. \tag{5.8.7}$$

Dim	$\mathfrak{N}_{M,\text{deformed}}$
8	1
7	9
6	44
5	140
4	274
3	330
2	264
1	136
0	34

Table 5.9: Number of boundaries at each dimension for $G_+(0,4;2)$, which coincides with its deformation.

3-loops

It is straightforward to directly construct the stratification of the deformed $G_+(0,4;3)$. However, for illustration, here we take a shortcut and derive it from a detailed analysis of the undeformed mini stratification presented in §5.6.1. In the deformation, we simply assume that the non-minimal minors $\Delta_I^{(i,j)}$ are completely independent. Thus, we just need to know how many $\Delta_I^{(i,j)}$ naively appear to be tunable to zero, i.e. the total number of $N\Delta_I^{(i,j)}$'s. We can determine this by just collapsing the various types of $3\Delta_I^{(i,j)}$'s in Table 5.8 into a single total number. The boundaries in this column are assigned the structure of Type H in Figure 5.7. The remaining two columns do not change, and give rise to the same additional contributions as before.

The result of this modification is displayed in Table 5.10. The fourth column adds up all of the contributions from the first three columns. Adding these contributions to the $\mathcal{N}_M$ column in Table 5.7 will indeed give the number of boundaries $\mathfrak{N}_{M,\text{deformed}}$ of the deformed $G_+(0,4;3)$. The total number of boundaries is 61 354 and, once again, the Euler number is

$$\sum_{i=0}^{12}(-1)^i\mathfrak{N}^{(i)}_{M,\text{deformed}} = 186 - 1152 + 3720 - \ldots - 15 + 1 = 2\,. \tag{5.8.8}$$

Dim	**3** $\boldsymbol{\Delta_I^{(i,j)}}$	**2** $\boldsymbol{\Delta_I^{(i,j)}}$	**1** $\boldsymbol{\Delta_I^{(i,j)}}$	**Total contribution**	$\boldsymbol{\mathfrak{N}_{M,\text{deformed}}}$
12	1	0	0	+0	1
11	12	0	0	+3	15
10	78	0	0	+39	117
9	328	0	12	+271	611
8	798	96	108	+1 242	2 244
7	1 056	576	528	+3 756	5 916
6	650	1 080	1 584	+7 666	11 156
5	168	792	2 424	+10 236	14 676
4	24	240	1 848	+8 598	13 254
3	0	24	672	+4 346	8 306
2	0	0	96	+1 200	3 720
1	0	0	0	+144	1 152
0	0	0	0	+0	186

Table 5.10: Number of boundaries with $N = 1, 2, 3$ number of 4×4 minors which have both positive and negative terms, and the corresponding added contribution to the total number of boundaries, obtained by assuming these minors to be completely independent and setting them to zero. The final column shows the number of boundaries $\mathfrak{N}_{M,\text{deformed}}$ of the deformed $G_+(0,4;3)$.

4-loops

Let us now consider the deformed $G_+(0,4;4)$. In this case there are six 4×4 minors $\Delta_{1234}^{(i,j)}$. As usual, the first step is to obtain the 4^{th} power of the positroid stratification of $G_+(2,4)$. This contains a total of $33^4 = 1\,185\,921$ potential boundaries, which are stratified as shown in the first column $\mathbb{N}$ of Table 5.11. In agreement with the general result, this has Euler number equal to 1:

$$\sum_{i=0}^{16}(-1)^i\mathbb{N}^{(i)} = 1296 - 10368 + \ldots - 16 + 1 = 1\,. \tag{5.8.9}$$

Many of these boundaries explicitly violate the positivity of some $\Delta_I^{(i,j)}$, as can be easily found using the methods of §5.4.3. Keeping only those boundaries which satisfy extended positivity, we obtain the column labeled $\mathcal{N}_M$ in Table 5.11. Inter-

estingly, similarly to the $L = 2$ case this again has Euler number equal to 1:

$$\sum_{i=0}^{16}(-1)^i \mathcal{N}_M^{(i)} = 994 - 6976 + \ldots - 16 + 1 = 1\,. \tag{5.8.10}$$

For each of these boundaries it is then necessary to classify which $\Delta_I^{(i,j)}$ may be turned off without turning off any 2×2 minors; this corresponds to step (3) in §5.2.5 and is also easily implemented as in §5.4.3. The additional boundaries which stem from the boundaries in the column $\mathcal{N}_M$ are added assuming that the $\Delta_I^{(i,j)}$ are completely independent. For example, if it is possible to turn off all six $\Delta_I^{(i,j)}$, we see that a large number of boundaries is added: $\binom{6}{1} = 6$ boundaries of one dimension lower, $\binom{6}{2} = 15$ boundaries of two dimensions lower, and so on; this will add a total of $\sum_{i=1}^{6}\binom{6}{i} = 63$ boundaries. The result of adding the boundaries from the $\Delta_I^{(i,j)}$ is the deformed $G_+(0,4;4)$, whose boundaries are shown in the right-hand column of Table 5.11. Remarkably, there is a total of 4 828 226 boundaries, but cancellations are such that the Euler number is again

$$\sum_{i=0}^{16}(-1)^i \mathfrak{N}_{M,\text{deformed}}^{(i)} = 1162 - 10880 + \ldots - 22 + 1 = 2 \quad . \tag{5.8.11}$$

The explicit examples presented in this section hint that the deformed $G_+(0,n;L)$ might have a remarkably simple geometry. Summarizing our findings for $G_+(0,4;L)$, we obtained $\mathcal{E} = 1$ for $L = 1$ and $\mathcal{E} = 2$ for $2 \leq L \leq 4$. If such simplicity is indeed general, it would be interesting to understand how the complicated geometry of Γ_0 that arises after demanding extended positivity on the L^{th} power of positroid stratification gets "fixed" by the deformed Γ_1's. These questions certainly deserve further study.

5.9 Conclusions and Outlook

The amplituhedron is a new geometric formulation of scattering amplitudes in planar $\mathcal{N} = 4$ Super Yang-Mills theory which can potentially lead to a completely new, geometric formulation of quantum field theory. In this chapter we initiated a systematic investigation of the geometry of the amplituhedron. To do so, we introduced a stratification for it and developed a combinatorial implementation based

Dim	$\mathbb{N}$	$\mathcal{N}_M$	$\mathfrak{N}_{M,\text{deformed}}$
16	1	1	1
15	16	16	22
14	136	136	247
13	784	784	1 860
12	3 376	3 212	10 243
11	11 392	9 856	42 846
10	30 928	23 288	138 421
9	68 512	43 616	346 320
8	124 552	67 626	666 654
7	185 664	88 128	974 212
6	225 312	96 496	1 061 154
5	219 456	90 720	843 992
4	167 616	73 144	480 870
3	96 768	47 744	193 980
2	39 744	22 944	55 362
1	10 368	6 976	10 880
0	1 296	994	1 162

Table 5.11: Stratification of the deformed $G_+(0,4;4)$.

on graphs and hyper perfect matchings. The stratification of the amplituhedron considerably generalizes the positroid stratification of the positive Grassmannian and its graphical implementation [84, 101]. Extended positivity plays a central role in the definition of the amplituhedron. Our stratification efficiently takes care of it. Furthermore, we explained how extended positivity is beautifully captured by permutations.

We then proceeded to the stratification of explicit examples, focusing on $k = 0$ and $n = 4$. We first considered a *mini stratification* which lists boundaries with distinct labels—lists of vanishing Plücker coordinates and non-minimal minors (in this case 4×4 determinants). This is an interesting simplification of the structure which follows from the definition of the amplituhedron. To capture all boundaries

we have to consider the *full stratification* which uses extended labels—not only listing all vanishing Plücker coordinates and non-minimal minors but also additional conditions between Plücker coordinates which come from factorizing non-minimal minors.

We first studied the amplitude at 2-loops. In the mini stratification, it contains 1 232 boundaries which interplay to produce an extremely simple topology with $\mathcal{E} = 2$. We repeated the analysis for the log of the amplitude at 2-loops, which has 1 072 boundaries and, once again, found $\mathcal{E} = 2$. We also discussed how these two objects beautifully combine into the square of the positroid stratification of $G_+(2, 4)$. In the full stratification there are 1 434 boundaries in the amplitude and 1 274 boundaries in the log and both have $\mathcal{E} = 8$, while the gluing region has $\mathcal{E} = 7$. This shows that the topology is substantially different from the square of $G_+(2, 4)$.

We also performed the mini stratification of the $L = 3$ amplitude. Unlike the 2-loop result, we obtained a rather large Euler number (in absolute value), $\mathcal{E} = -14$ which also shows that the topology is much more involved than $[G_+(2, 4)]^3$. The fact that a relatively complicated topology can in general arise from the simple definition of the amplituhedron is certainly a logical possibility and, perhaps, the most natural expectation. Note that the available Euler numbers for the mini stratification are even Catalan numbers. It would not be surprising if this persists at higher loops, as Catalan numbers play an important role in the positive Grassmannian, so it is tempting to conjecture that for $L = 4$ we should get $\mathcal{E} = 132$. We should of course warn that this conjecture is based on extrapolation from very limited data.

We rederived the entire mini stratifications of the $L = 2$ amplitude and its log in terms of the integrand. It is important to remark that the computations involved in this approach are completely different from the ones based on the amplituhedron. In particular, this method is based on looking for singularities of a function and makes no reference to positivity. We succeeded in not only reproducing the counting of boundaries at each dimension but also in explicitly verifying that the identities of all boundaries obtained by the two methods match. This is a very important piece of explicit evidence supporting the amplituhedron conjecture and which supplements the direct triangulation provided in [80].

Finally, we introduced the deformed amplituhedron, which corresponds to deforming the relations between non-minimal minors in order to make them independent. The stratification of this object is considerably simpler than the one for the ordinary amplituhedron. We computed several explicit examples and, quite remarkably, they exhibit an extremely simple topology: $\mathcal{E} = 1$ for $L = 1$ and $\mathcal{E} = 2$ for $2 \leq L \leq 4$.

There are several directions worth investigating in the future, among them:

- One of the main questions we expect to address in future work is how to exploit the combinatorial tools we developed for triangulating the amplituhedron. Different triangulations should correlate with the different forms the integrand can take.

- Another natural next step is to study how our ideas need to be extended to deal with $k > 0$ and $n > 4$. In this cases, positivity becomes more involved due to the addition of a tree-level contribution to the matrix $\mathcal{C}$ and the importance of external data, respectively.

- As a mathematical question, it would be interesting to investigate the geometry of $G_+(0, n; L)$ for $n > 4$. Notice that, contrary to the amplituhedron, $G_+(0, n; L)$ does not have additional positivity constraints involving external data for $n > 4$. In fact, the mini stratification and its combinatorial implementation can be applied without modifications to this geometry for arbitrary n and L and provide a powerful handle on it.

- The amplituhedron is just one example inside a large list of spaces which are related to it by relaxing some of the extended positivity conditions [128]. For example, for $k = 0$ and $n = 4$ the parent of all these spaces corresponds to the L^{th} power of the positroid stratification of $G_+(2, 4)$. Dealing with extended positivity is straightforward in our stratification, so our tools can be readily extended for the stratification of these spaces. These geometries are relatively simpler than that of the amplituhedron and it is expected that they can be exploited to constrain or even infer the structure of the integrand [128]. It would also be interesting to investigate whether the deformed amplituhedron,

which similarly results from the relaxation of some relations, can likewise be used for determining the integrand.

- From a purely mathematical standpoint, it would be interesting to investigate whether the simplicity of the deformed stratification we have observed in explicit examples holds more generally. If so, it would interesting to understand the underlying reason for this. It is important to keep in mind that the general definition of deformation might turn out to be more sophisticated than the one we have considered. On a related note, it is possible that the deformations of relations cannot be arbitrary but must obey a certain structure in order to preserve a simple geometry. Further exploration of these questions can potentially uncover a rather rich story. It would also be interesting to investigate whether the deformed stratification has any physical significance.

- Similarly to the story for 4d $\mathcal{N} = 4$ SYM, a connection between scattering amplitudes in the planar ABJM theory in 3d [129] and the positive orthogonal Grassmannian has been established in [130, 131]. It would be interesting to investigate whether something like the amplituhedron exists for this theory and, if so, how our ideas extend to it.

Chapter 6

Non-Planar On-Shell Diagrams

In this chapter we shall use the machinery developed in Chapters 2 and 4 to compute the integrand associated to non-planar on-shell diagrams. We'll find that the generalized face variables of Chapter 2 make the $d\log$ form of the on-shell form explicit, and we'll use the boundary measurement of Chapter 4 to compute the integrand for non-planar diagrams. We shall also introduce a completely different approach to obtaining the same answer, through a prescription applicable beyond the MHV case for writing the on-shell form as a function of minors directly from the graph. Finally, we present a discussion of equivalence and reductions for non-planar diagrams in terms of the matching and matroid polytopes. We'll explicitly see that non-planar diagrams exhibit novel phenomena, such as the emergence of constraints on Plücker coordinates beyond Plücker relations when deleting edges.

6.1 Non-Planar On-Shell Diagrams and Non-Adjacent BCFW Shifts

Before embarking on a fully general investigation of non-planar on-shell diagrams in the coming sections, we would like to collect a few thoughts about a concrete scenario in which non-planar on-shell diagrams appear and are important: the computation of tree-level amplitudes in $\mathcal{N}=4$ SYM via non-adjacent BCFW shifts [44].

It is a well known fact that there is a one-to-one correspondence between the quadruple cut of a two-mass-hard box and a BCFW diagram with adjacent shifts

[132], as shown in Figure 6.1. In fact, this is how the BCFW recursion relations for tree-level amplitudes were originally derived in [43]. As emphasized in the figure, one can further recursively express the tree-level amplitudes entering the two massive corners of the box in terms of two-mass-hard boxes, obtaining a representation of the BCFW diagram with adjacent BCFW shifts in terms of on-shell diagrams.

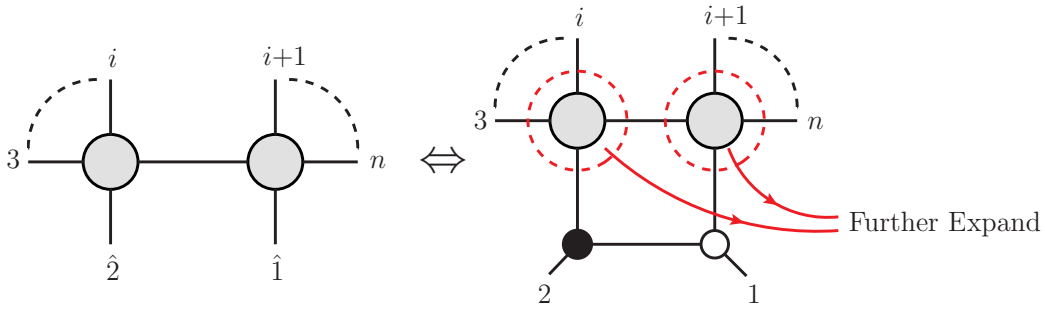

Figure 6.1: A one-to-one correspondence between a BCFW diagram with an adjacent shift and a two-mass-hard box. The tree-level amplitudes in the two massive corners can be further expanded into two-mass-hard boxes until reaching an on-shell diagram representation of the BCFW diagram.

Since tree-level amplitudes can also be expressed in terms of BCFW diagrams with non-adjacent shifts, it is natural to wonder whether there is a corresponding on-shell diagram representation. Indeed, such a representation exists and the resulting objects are precisely non-planar on-shell diagrams. Similarly to what happens for BCFW diagrams with adjacent shifts, there is a one-to-one correspondence between a BCFW diagram with non-adjacent shifts and a non-planar two-mass-hard box, as shown in Figure 6.2. Once again, the tree-level amplitudes in the two massive corners can be further expanded into two-mass-hard boxes, either planar or non-planar. Doing this recursively, we can express any BCFW diagram with non-adjacent shifts in terms of non-planar on-shell diagrams.

It is possible to represent a given amplitude in terms of different on-shell diagrams obtained via different BCFW shifts. This procedure thus generates interesting identities between on-shell diagrams. We present an example of such an identity in Figure 6.3, where we provide two alternative expressions for the tree-level five-point MHV amplitude $\mathcal{A}_5^{\text{MHV}}$. One of the expressions involves two non-planar diagrams

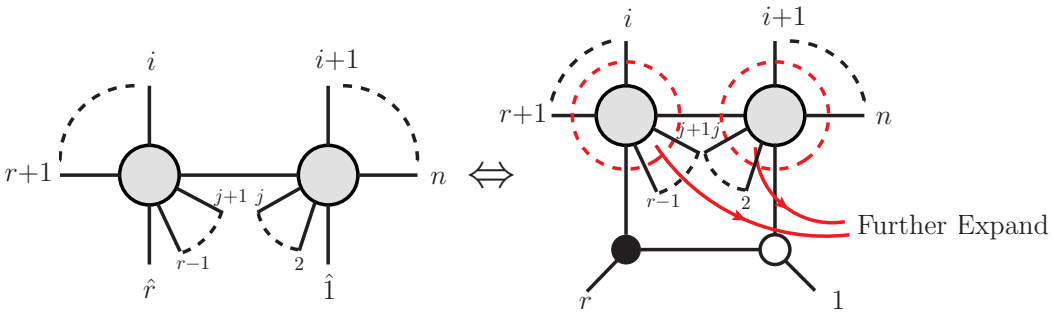

Figure 6.2: A one-to-one correspondence between a BCFW diagram with non-adjacent shifts and a non-planar two-mass-hard box. The tree-level amplitudes at two massive corners can be further expanded into either non-planar or planar two-mass-hard boxes until reaching an on-shell diagram representation of the BCFW diagram.

and the other one involves a single planar diagram. Furthermore, it is known that there are additional relations between BCFW diagrams with non-adjacent shifts due to the so-called bonus relations [133–135]; it would be interesting to explore their application to non-planar on-shell diagrams. Finally, it would be interesting to investigate how general the construction of non-planar on-shell diagrams in terms of non-adjacent BCFW shifts can be.

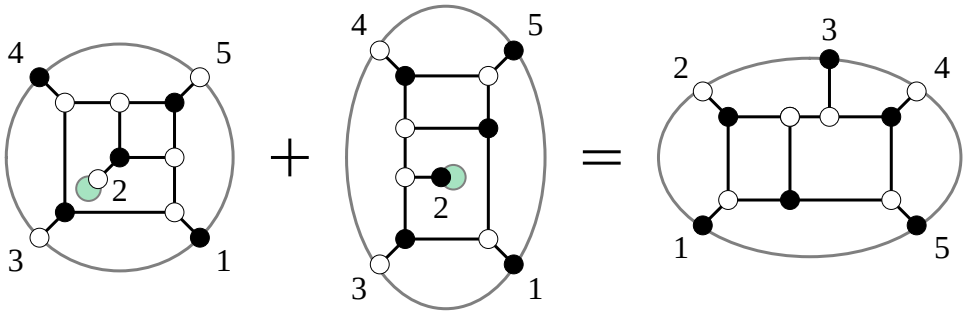

Figure 6.3: Tree-level five-point MHV amplitude in terms of non-planar on-shell diagrams (left) and a planar on-shell diagram (right).

6.2 Face Variables and the $d$log Form

In this section we will discuss the $d$log form using generalized face variables. We recall that in order to use face variables, we need to embed the on-shell diagram into a bordered Riemann surface. While only the connectivity of an on-shell diagram matters, choosing an embedding will turn out to be very convenient. Given a graph, the choice of embedding is not unique. However we will later see that, as expected from the embedding-independence of the boundary measurement, physical results are independent of it.

It is interesting to notice that a choice of embedding is already implicit in the usual discussion of planar diagrams. Indeed, face variables are not an intrinsic property of planar graphs, but arise when imagining them to be embedded on a disk.

As we recall from §4.2.2, another feature of generalized face variables is that they precisely contain all of the degrees of freedom d of a general on-shell diagram, which is simply determined by

$$d \;=\; F + B + 2g - 2\,. \tag{6.2.1}$$

There is a simple, alternative way of understanding the origin of this expression. Notice that for an on-shell diagram with E edges and N internal nodes, we have $d = E - N$. Now, let us consider an embedding of the diagram with Euler characteristic χ, such that the diagram gives rise to F faces. Since $\chi = F - E + N$, we obtain the compact expression

$$d = F - \chi\,, \tag{6.2.2}$$

which agrees with (6.2.1).

6.2.1 The $d$log Form

An important feature of on-shell diagrams is the $d\log$ form of the on-shell form, which arises automatically when using generalized face variables, without the need for solving for the GL(1) redundancies associated to internal nodes when using edge

variables.[1] For planar diagrams, it is simply given by

$$\Omega = \prod_{i=1}^{F-1} \frac{df_i}{f_i}. \tag{6.2.3}$$

For arbitrary diagrams, this expression beautifully generalizes to

$$\Omega = \prod_{i=1}^{F-1} \frac{df_i}{f_i} \prod_{a=1}^{B-1} \frac{db_a}{b_a} \prod_{m=1}^{g} \frac{d\alpha_m}{\alpha_m} \frac{d\beta_m}{\beta_m} \tag{6.2.4}$$

when using generalized face variables. The general form in (6.2.4) is an embedding-independent statement, since ultimately it is only the connectivity of the graph which is of importance.

Appendix C.1 illustrates embedding independence in a very simple example: a box diagram embedded on a disk and on an annulus. By flipping an external leg, we lose the internal face but give rise to an additional boundary, which in turn produces a new cut. The independent set of generalized face variables then goes from $\{f_1, f_2, f_3, f_4\}$ to $\{f_1, f_2, f_3, b_1\}$. The on-shell form, in both sets of variables, becomes

$$\frac{df_1}{f_1}\frac{df_2}{f_2}\frac{df_3}{f_3}\frac{df_4}{f_4} = \frac{df_1}{f_1}\frac{df_2}{f_2}\frac{df_3}{f_3}\frac{db_1}{b_1}\,. \tag{6.2.5}$$

If instead of using generalized face variables we are interested in expressing the on-shell form in terms of minors of C, which is only possible for reduced graphs, it takes the generic form

$$\Omega \;=\; \frac{d^{k\times n}C}{\mathrm{Vol}(\mathrm{GL}(k))}\,\frac{1}{(1\cdots k)(2\cdots k+1)\cdots(n\cdots k-1)} \times \mathcal{F}, \tag{6.2.6}$$

where the non-trivial factor $\mathcal{F}$ accounts for the non-planarity of the on-shell diagram.[2] Explicit examples with non-trivial $\mathcal{F}$ factors will be presented in §6.3.

A Genus-One Example. Let us verify (6.2.4) in the explicit example shown in Figure 6.4, which already appeared in Figure 4.6.

Since the diagram is embedded into a torus, additionally to the face variables there is a pair of variables α and β corresponding to its fundamental directions, and

[1] The expression of the on-shell form in terms of edge variables (4.2.6) remains valid for non-planar diagrams.

[2] We remind the reader of the standard notation $(i_1, \ldots, i_k) \equiv \Delta_{i_1,\ldots,i_k}$.

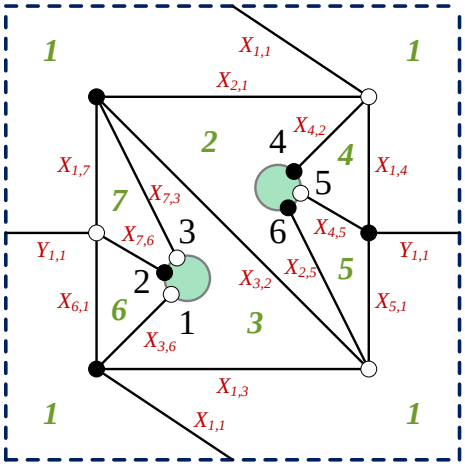

Figure 6.4: A reduced on-shell diagram embedded into a torus with two boundaries. This graph has already appeared in Figure 4.6 and is reproduced here for convenience.

a path b connecting the two boundaries. Figure 6.5 shows a possible set of these variables; as we mentioned earlier, the choice of these paths is not unique. In terms of edges, the generalized face variables are given by

$$f_1 = \frac{\alpha_{2,1}\alpha_{5,1}\alpha_{6,1}}{\alpha_{1,3}\alpha_{1,4}\alpha_{1,7}} \quad f_2 = \frac{\alpha_{3,2}\alpha_{4,2}}{\alpha_{2,5}\alpha_{2,1}} \quad f_3 = \frac{\alpha_{7,3}\alpha_{1,3}}{\alpha_{3,2}\alpha_{3,6}} \quad f_4 = \frac{\alpha_{1,4}}{\alpha_{4,2}\alpha_{4,5}} \quad f_5 = \frac{\alpha_{4,5}\alpha_{2,5}}{\alpha_{5,1}}$$
$$f_6 = \frac{\alpha_{3,6}}{\alpha_{6,1}\alpha_{7,6}} \quad f_7 = \frac{\alpha_{1,7}}{\alpha_{7,6}\alpha_{7,3}} \quad \alpha = \frac{\alpha_{1,7}\alpha_{1,4}}{\alpha'_{1,1}\alpha_{2,1}} \quad \beta = \frac{\alpha_{1,1}\alpha_{1,7}}{\alpha_{6,1}\alpha_{2,1}} \quad b = \frac{\alpha_{7,3}\alpha_{2,5}}{\alpha_{3,2}} \,. \tag{6.2.7}$$

The faces satisfy $\prod_{i=1}^{7} f_i = 1$ so, without loss of generality, we can discard f_7.

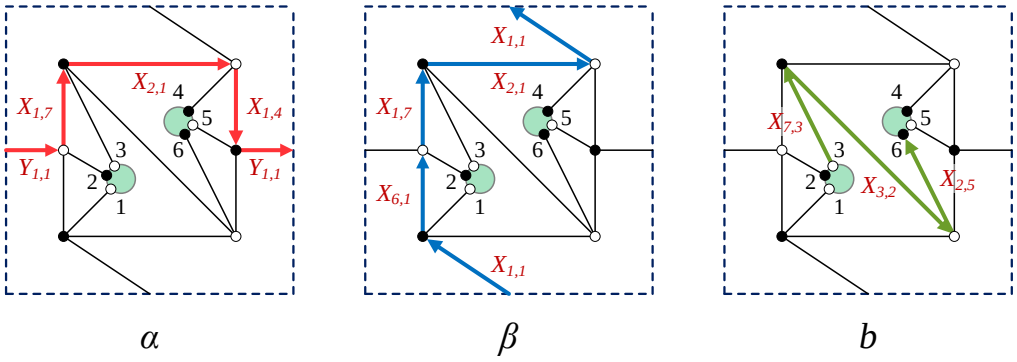

Figure 6.5: Possible choices of the α, β and b variables.

Let us first construct the $d$log form in terms of edge variables. It is possible to gauge fix the GL(1) redundancies of the 6 internal nodes by setting to 1 one edge for each of them. One consistent way of picking these edges corresponds to setting[3]

$$X_{7,6} = X_{3,6} = X_{4,5} = X_{4,2} = X_{1,3} = X_{1,7} = 1. \tag{6.2.8}$$

The remaining edges are

$$X_{1,1},\ X_{1,4},\ X_{2,1},\ X_{2,5},\ X_{3,2},\ X_{5,1},\ X_{6,1},\ X_{7,3},\ Y_{1,1}. \tag{6.2.9}$$

We thus conclude that this on-shell diagram has $d = 9$ degrees of freedom. This counting of course agrees with the one based on generalized face variables: we have 7 faces (6 of which are independent), an α and a β cycle from being on a torus and $B - 1 = 1$ path b.

After this gauge fixing, the independent generalized face variables become

$$\begin{aligned} &f_1 = \frac{\alpha_{2,1}\alpha_{5,1}\alpha_{6,1}}{\alpha_{1,4}} \quad f_2 = \frac{\alpha_{3,2}}{\alpha_{2,5}\alpha_{2,1}} \quad f_3 = \frac{\alpha_{7,3}}{\alpha_{3,2}} \qquad f_4 = \alpha_{1,4} \qquad f_5 = \frac{\alpha_{2,5}}{\alpha_{5,1}} \\ &f_6 = \frac{1}{\alpha_{6,1}} \qquad\quad \alpha = \frac{\alpha_{1,4}}{\alpha'_{1,1}\alpha_{2,1}} \quad \beta = \frac{\alpha_{1,1}}{\alpha_{6,1}\alpha_{2,1}} \quad b = \frac{\alpha_{7,3}\alpha_{2,5}}{\alpha_{3,2}} \quad . \end{aligned} \tag{6.2.10}$$

Let us now translate the on-shell form from the edge variables in (6.2.9) to generalized face variables. It becomes

$$\begin{aligned} \Omega &= \frac{d\alpha_{1,1}}{\alpha_{1,1}}\frac{d\alpha_{1,4}}{\alpha_{1,4}}\frac{d\alpha_{2,1}}{\alpha_{2,1}}\frac{d\alpha_{2,5}}{\alpha_{2,5}}\frac{d\alpha_{3,2}}{\alpha_{3,2}}\frac{d\alpha_{5,1}}{\alpha_{5,1}}\frac{d\alpha_{6,1}}{\alpha_{6,1}}\frac{d\alpha_{7,3}}{\alpha_{7,3}}\frac{d\alpha'_{1,1}}{\alpha'_{1,1}} \\ &= \frac{f_1^2 f_2 f_4^4 f_5}{\alpha^2 f_3}\ \frac{\alpha}{b\beta f_1^3 f_2^2 f_4^5 f_5^2 f_6}\ df_1\ df_2\ df_3\ df_4\ df_5\ df_6\ d\alpha\ d\beta\ db \\ &= \frac{df_1}{f_1}\frac{df_2}{f_2}\frac{df_3}{f_3}\frac{df_4}{f_4}\frac{df_5}{f_5}\frac{df_6}{f_6}\frac{d\alpha}{\alpha}\frac{d\beta}{\beta}\frac{db}{b} \end{aligned} \tag{6.2.11}$$

where, in the middle line, the first factor comes from the Jacobian of the variable transformation and the second factor comes from the product of edge variables, expressed in terms of face variables. We see that the on-shell form takes the general

[3]For planar diagrams, this way of fixing the gauge fits nicely into the construction of the diagrams in terms of BCFW bridges [34]. It is interesting to mention that other natural ways of gauge fixing exist. For example, it is possible to treat all edges symmetrically by demanding that the product of edges at every internal node is equal to 1.

form in (6.2.4). In other words, generalized variables can be used to directly write the on-shell form in $d\log$ form without having to work through the GL(1) gauge fixing that is necessary for arriving at (6.2.9).

It is also easy to verify that the $d\log$ form of the on-shell form is independent of the explicit choice of generalized face variables. For example, we could trade α for another path α' also wrapping the torus along the horizontal direction, such as the one shown in Figure 6.6. Once again, the Jacobian of the change of variables is such that the $d\log$ form is preserved.

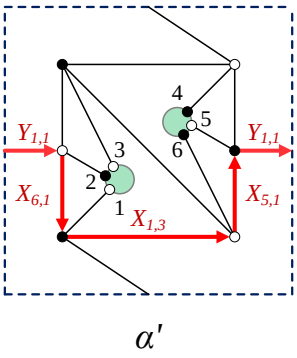

Figure 6.6: An alternative choice for one of the fundamental cycles of the torus. The Jacobian of the change of variables is such that the on-shell form preserves its $d\log$ in terms of generalized face variables.

Finally, let us see how face variables appear in the boundary measurement. It is straightforward to check that (4.3.9) can be rewritten using (6.2.7) into the form

$$C = \left(\begin{array}{c|cccccc} & 1 & 2 & 3 & 4 & 5 & 6 \\ \hline 1 & 1 & 0 & -\frac{1}{f_3} & 0 & \frac{b}{f_3 f_5} & \frac{b}{f_3} \\ 2 & 0 & 1 & \frac{1}{f_1 f_2 f_3 f_4 f_5 f_6} + \frac{1}{f_3 f_6} & 0 & -\frac{b}{f_1 f_3 f_5 f_6 \alpha} - \frac{b}{f_3 f_5 f_6} & -\frac{b}{f_3 f_6} \\ 4 & 0 & 0 & \frac{1}{f_2 b} - \frac{f_1 f_4 f_5 \beta}{b} & 1 & f_4 + f_1 f_4 \beta & f_1 f_4 f_5 \beta \end{array}\right). \tag{6.2.12}$$

From this expression it is particularly transparent that the 9 degrees of freedom of C, corresponding to the 9 non-trivial entries, are the same 9 degrees of freedom contained by the face variables. Utilizing this will be the topic of the next section.

6.3 The Non-Planar On-Shell Form

We shall now study the differential form associated to each non-planar on-shell diagram. As we have already seen, there are multiple ways of expressing it:

- Using edge variables, which straightforwardly extends to non-planar graphs. This has the advantage of manifestly displaying the $d\log$ form of the on-shell form. A disadvantage is that it depends on the choice of GL(1) gauge at every internal node, which needs to be taken into account to identify d independent edges.

- Using generalized face variables as in (6.2.4). This approach has the advantage of both displaying the $d\log$ form as well as being independent of the choice of GL(1)'s. The determination of generalized face variables naturally involves an embedding of the diagram.

- Using the minors of the Grassmannian, i.e. Plücker coordinates, such as in (6.2.6). While this representation hides the $d\log$ form and has a GL(k) redundancy, it has the advantage of having a more direct connection to the geometry of $G(k,n)$, naturally expressed in terms of Plücker coordinates.

In this section we will primarily be concerned with the third point. In particular, the on-shell forms obtained in this section correspond to having non-trivial factors $\mathcal{F}$ in (6.2.6). While the discussion in the previous sections applies to general on-shell diagrams, here we focus on reduced ones. This is physically motivated by being interested in leading singularities, which imply the diagrams are reduced. Formally, it is also required by a dimensionality argument: in order to express the on-shell form in terms of minors, its rank needs to match the number of independent Plücker coordinates, implying the diagram must be reduced.

6.3.1 From Generalized Face Variables to Minors

A possible way of obtaining the on-shell form in term of minors of C is to use generalized face variables and the boundary measurement. More explicitly, starting with the form in (6.2.4), we can use the boundary measurement from Chapter 4 to

obtain the map between Plücker coordinates and generalized face variables. Solving for the generalized face variables will then yield the desired expression:

$$\prod_{i=1}^{F-1}\frac{df_i}{f_i}\prod_{j=1}^{B-1}\frac{db_j}{b_j}\prod_{m=1}^{g}\frac{d\alpha_m}{\alpha_m}\frac{d\beta_m}{\beta_m} = |\mathcal{J}|\, d^{\dim}C \prod_{i,j,m}\frac{1}{f_i(\Delta)b_j(\Delta)\alpha_m(\Delta)\beta_m(\Delta)}\,, \quad (6.3.1)$$

where Δ is the relevant set of Plücker coordinates, and $\mathcal{J}$ is the Jacobian for the transformation between entries in the Grassmannian and generalized face variables.[4]

Example. We shall now illustrate how this works in practice in a top-dimensional example in $G(3,6)$ with two boundaries, shown in Figure 6.7.

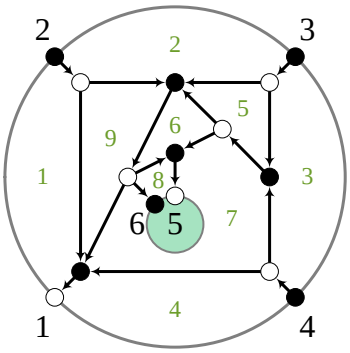

Figure 6.7: A top-dimensional on-shell diagram in $G(3,6)$ embedded on an annulus. The selected perfect orientation has source set $\{2,3,4\}$.

This example has 9 independent generalized face variables: 8 independent f_i variables and one b_j. In terms of oriented edge weights, the generalized face variables are given by

$$f_1 = \frac{\alpha_{9,1}}{\alpha_{1,2}\alpha_{1,4}} \quad f_2 = \frac{\alpha_{5,2}\alpha_{1,2}}{\alpha_{2,3}\alpha_{2,9}} \quad f_3 = \frac{\alpha_{7,3}\alpha_{2,3}}{\alpha_{3,4}\alpha_{3,5}} \quad f_4 = \frac{\alpha_{1,4}\alpha_{3,4}}{\alpha_{4,7}} \quad f_5 = \frac{\alpha_{6,5}\alpha_{3,5}}{\alpha_{5,7}\alpha_{5,2}}$$
$$f_6 = \frac{\alpha_{7,6}\alpha_{9,6}}{\alpha_{6,8}\alpha_{6,5}} \quad f_7 = \frac{\alpha'_{8,7}\alpha_{5,7}\alpha_{4,7}\alpha_{8,7}}{\alpha_{7,6}\alpha_{7,3}\alpha_{7,9}} \quad f_8 = \frac{\alpha_{6,8}}{\alpha_{8,7}\alpha'_{8,7}} \quad f_9 = \frac{\alpha_{2,9}\alpha_{7,9}}{\alpha_{9,6}\alpha_{9,1}} \quad b_1 = \frac{\alpha_{1,4}\alpha_{8,7}}{\alpha_{7,9}} \quad (6.3.2)$$

[4]Of course it is possible to do a similar thing starting from the on-shell form in terms of edge weights and using the boundary measurement to connect it to Plücker coordinates. The advantage of using generalized face variables is that they automatically produce the starting point (6.2.4).

Eliminating f_4 using $\prod_{i=1}^{9} f_i = 1$ we obtain the on-shell form

$$\Omega = \frac{db_1}{b_1} \prod_{i\neq 4}^{9} \frac{df_i}{f_i}. \tag{6.3.3}$$

Using the boundary measurement in Chapter 4, we obtain the following matrix

$$C = \left(\begin{array}{c|cccccc} & 1 & 2 & 3 & 4 & 5 & 6 \\ \hline 2 & f_1(1+f_9) & 1 & 0 & 0 & b_1 f_1 f_8 f_9 & b_1 f_1 f_9 \\ 3 & -f_1 f_2 (1+f_5) f_9 & 0 & 1 & 0 & -b_1 f_1 f_2 (1+f_5+f_5 f_6) f_8 f_9 & -b_1 f_1 f_2 (1+f_5) f_9 \\ 4 & f_1 f_2 f_3 f_5 (1+f_6 f_7 f_8) f_9 & 0 & 0 & 1 & b_1 f_1 f_2 f_3 f_5 (1+f_6) f_8 f_9 & b_1 f_1 f_2 f_3 f_5 f_9 \end{array}\right). \tag{6.3.4}$$

The variable transformation from generalized face variables to elements of the above matrix, i.e. to $\prod_{i=1}^{9} dc_i \equiv d^9 C$, carries a Jacobian, which can also be expressed in terms of the generalized face variables. For this example $c_1 = f_1(1+f_9)$, ..., $c_9 = b_1 f_1 f_2 f_3 f_5 f_9$.

Using (6.3.4) we can express the Plücker coordinates in terms of generalized face variables. Solving for the generalized face variables, we obtain the following differential form:

$$\Omega = \prod_{i\neq 4}^{9} \frac{df_i}{f_i} \frac{db_1}{b_1} = d^9 C \frac{(246)^2}{(234)(345)(456)(612)(124)(146)(236)(256)} . \tag{6.3.5}$$

An important remark is that the resulting expression in terms of minors is independent of the chosen embedding. The simple example in Appendix C.1 illustrates this point.

6.3.2 A Combinatorial Method

In this section we present an alternative systematic procedure for computing the non-planar on-shell form in terms of Plücker coordinates for any MHV degree k, which allows us to construct it without the need to compute the boundary measurement.[5] This is a generalization of the method developed in [124] for general non-planar MHV leading singularities. We will begin by quickly reviewing the procedure in [124], and

[5]Since we are again dealing with on-shell diagrams, we shall use the definition for k as used in Chapter 4, as opposed to that in Chapter 5: here $k = 2$ is MHV.

then propose its generalization to any k. As a consistency check, all results in this section have also been obtained using the method in §6.3.1, providing substantial support for our proposal.

MHV Leading Singularities

A general method for obtaining non-planar MHV leading singularities was recently introduced in [124]. We now review this method with a simple example, shown in Figure 6.8.

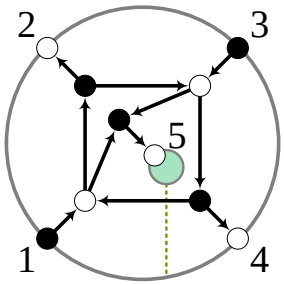

Figure 6.8: A five-point MHV on-shell diagram with two boundaries.

A general feature of MHV leading singularities is that every internal black vertex can be associated to a set of three external legs. These legs are those that are connected to the black node either directly or through a sequence of edges and internal white nodes. The previous sentence applies also to non-bipartite on-shell diagrams. As explained earlier, every on-shell diagram can be turned into a bipartite one. We will continue focusing on bipartite diagrams, for which it is clear that there can only be at most one internal white node connecting an internal black node to an external leg.[6] The fact that for MHV leading singularities this rule precisely gives

[6]It is natural to speculate that this basic observation can be turned into a new quantitative characterization of reduced graphs. It seems to suggest that a necessary condition for a bipartite on-shell diagram to be reduced is that all internal black nodes must be at a distance equal or smaller than 2 (as measured in terms of edges following our prescription) from some external node. Not surprisingly, this would tell us that reduced graphs need to be "small" or "narrow" in some sense. We leave a more detailed investigation of this thought for future work.

rise to three end points for every internal black node is indeed a rather non-trivial graph-combinatorial result.

The procedure for obtaining the differential form is as follows:

1. For each internal black node, we find the three external legs associated to it. Then we construct a $n_B \times 3$ matrix T, where n_B is the number of black nodes. Each row in T contains the labels of the three external nodes associated to each black node. For the example in Figure 6.8, T is given by

$$T = \begin{pmatrix} 1 & 2 & 3 \\ 1 & 3 & 5 \\ 1 & 3 & 4 \end{pmatrix}. \tag{6.3.6}$$

2. Next, we construct an $n_B \times n$ matrix M, where n is the number of external nodes, in the following manner. For each row $\{i, j, k\}$ in T we construct a corresponding row in M by inserting $(i\,j)$ at position k, $(j\,k)$ at position i, $(k\,i)$ at j, and zero for the remaining entries. For our example, we get

$$M = \begin{pmatrix} (23) & (31) & (12) & 0 & 0 \\ (35) & 0 & (51) & 0 & (13) \\ (34) & 0 & (41) & (13) & 0 \end{pmatrix}. \tag{6.3.7}$$

3. We delete two arbitrary columns a and b from the matrix M, to obtain the square matrix $\widehat{M}_{a,b}$ of size $n_B \times (n-2) = n_B \times n_B$. We then compute $\det(\widehat{M}_{a,b})/(ab)$. This quantity turns out to be independent of the choice of a and b. For the case at hand, we have $\det(\widehat{M}_{a,b}/(ab)) = -(13)^2$.

4. Finally, the on-shell form corresponding to a diagram for which

$$T = \begin{pmatrix} i_1^{(1)} & i_2^{(1)} & i_3^{(1)} \\ i_1^{(2)} & i_2^{(2)} & i_3^{(2)} \\ \vdots & \vdots & \vdots \\ i_1^{(n_B)} & i_2^{(n_B)} & i_3^{(n_B)} \end{pmatrix} \tag{6.3.8}$$

is given by

$$\Omega = \frac{d^{2\times n}C}{\mathrm{Vol}(\mathrm{GL}(2))} \left(\frac{\det(\widehat{M}_{i,j})}{(i\,j)}\right)^2 \frac{1}{\mathrm{PT}^{(1)}\mathrm{PT}^{(2)}\cdots\mathrm{PT}^{(n_B)}}, \tag{6.3.9}$$

where we denote by $\mathrm{PT}^{(i)}$ the Parke-Taylor-like product corresponding to each row i of T; for instance in (6.3.8), $\mathrm{PT}^{(1)} = (i_1^{(1)} i_2^{(1)})(i_2^{(1)} i_3^{(1)})(i_3^{(1)} i_1^{(1)})$. For the example in Figure 6.8, the differential form obtained from the above procedure is

$$\Omega = \frac{d^{2\times 5}C}{\mathrm{Vol}(\mathrm{GL}(2))} \frac{(13)^4}{(12)(23)(31)(13)(35)(51)(13)(34)(41)} \,. \tag{6.3.10}$$

The original rules [124] are formulated in terms of spinor brackets $\langle i\, j\rangle$; for MHV leading singularities these are equivalent to $(i\, j)$ on the support of the kinematic constraints. Writing them in terms of minors hints at an appropriate generalization to N^{k-2}MHV diagrams, for which the minors are $k \times k$, which we now investigate.

Generalization to N^{k-2}MHV On-Shell Diagrams

Here we propose a generalization of the procedure shown above to $k > 2$. Subsequent sections will illustrate its inner workings with some non-trivial examples. In [6] we prove the method for certain subclasses of diagrams.

MHV leading singularities only require us to take into account on-shell diagrams with trivalent black vertices, but for $k > 2$ we will need to consider more general bipartite graphs. The complications arising when $k > 2$ are twofold:

- In order to have $k \times k$ minors we need a T matrix with $k+1$ columns. For $k > 2$ it is possible that some internal black nodes do not connect to $k+1$ external legs in the way described for $k = 2$.

- The number of black nodes may exceed $(n-k)$, forcing $\widehat{M}$ to have more rows than columns, thus preventing us from taking its determinant.

The first point is related to the valency v of internal black nodes. There are two possible reasons why internal black nodes might fail to connect to $k+1$ external ones. The first one is that the valency of the node is $v > k+1$. Generally, performing a square move changes the valency of nodes in a diagram. In what follows we will assume that it is always possible to perform a series of equivalence moves to turn a diagram into one where every black node has $v \leq k+1$. An example of this procedure is given in Figure 6.9.

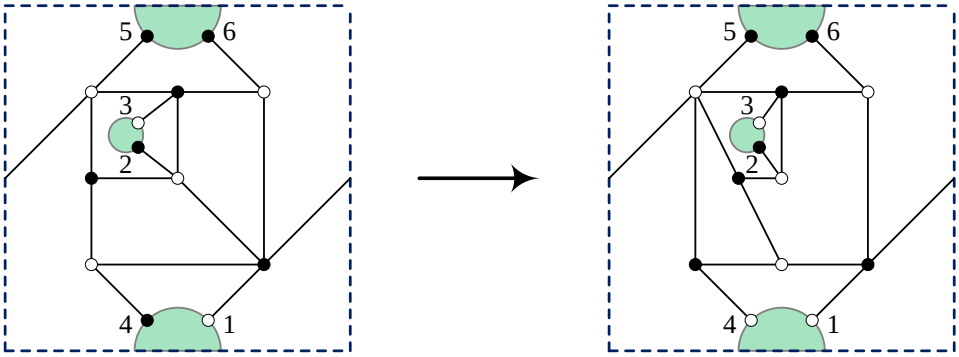

Figure 6.9: On the left, an NMHV diagram where the black node attached to external node 1 has valency $v > k+1$. This is resolved by performing a square move, leading to the diagram on the right, where all nodes have $v \leq k+1$.

If, on the other hand, the valency of an internal black node is $v < k+1$, we assign the first entries of the corresponding row in T to the external nodes to which the black node connects, ordered clockwise,[7] and leave the remaining entries free:

$$\{i_1, \ldots, i_v, *_{v+1}, \cdots *_{k+1}\} \ . \tag{6.3.11}$$

We then fill these additional entries with external labels, chosen arbitrarily from the set of nodes that do not already appear in the row, i.e. $*_j \notin \{i_1, \ldots, i_v\}$. Finally, we need to order the new entries $*_j$ among the $\{i_1, \ldots, i_v\}$, such that $\det(\widehat{M}_{a_1,\ldots,a_k})/(a_1 \cdots a_k)$ is independent of $\{a_1 \cdots a_k\}$, up to an overall sign $(-1)^{\sum_{j=1}^{k} a_j}$. In all cases we have considered, it is always possible to do this, but it would be interesting to understand better how to determine the correct ordering in the T matrix in general.

The second complication listed above, regarding the total number of black nodes, typically arises when the diagram has internal white nodes which are completely surrounded by black nodes. Notice that for bipartite graphs, this is always the case, except when the internal white nodes are directly connected to some external leg. In

[7] Defining a clockwise ordering requires considering an embedding. In practice, this is how we have dealt with the examples in §6.3.4. Since the result should be independent of any embedding, it would be interesting to understand what notion generalizes the ordering in its absence.

the examples we have studied, it appears that $n_B = n-k+\alpha$, where α is the number of such white nodes in the diagram. This issue is resolved by adding an auxiliary external leg to every internal white node contributing to α.[8] Once the form has been obtained, through the generalization of the steps taken for MHV diagrams which we will outline shortly, we integrate over the extra variables C_{ij}, $j = n+1, \ldots, n+\alpha$ around $C_{ij} = 0$. We will see this done in detail in several examples.

In summary, the procedure to obtain the differential form for general N^{k-2}MHV on-shell diagrams is as follows:

1. If any internal black node is connected to more than $k+1$ external nodes either directly or through a succession of edges and internal white nodes, perform a series of equivalence moves until all internal black nodes only connect to $k+1$ or fewer external nodes. Also, if $n_B > n-k$, add auxiliary external legs to the internal white nodes which are totally surrounded by internal black nodes, until $n_B = n-k$.

2. Construct the $n_B \times (k+1)$ matrix T where each row corresponds to an internal black node. Every time there is an internal black node that connects to fewer than $k+1$ external nodes, choose the remaining entries freely as described above; the correct ordering will be determined by point 4, below.

3. Construct the $n_B \times n$ matrix M in the same way as for the MHV case. For each row $\{i_1, \ldots, i_j, \ldots, i_{k+1}\}$ in T we populate the same row in M: at each position i_j, insert the minor $(i_{j+1} \cdots i_{k+1} i_1 \cdots i_{j-1})$ formed by removing i_j; all other entries are zero.

4. Remove k columns from M, chosen arbitrarily, to form $\widehat{M}_{a_1,\ldots,a_k}$. Then compute the ratio $\det(\widehat{M}_{a_1,\ldots,a_k})/(a_1 \cdots a_k)$. We emphasize that this quantity must be independent of the choice of $\{a_1 \cdots a_k\}$; if this is not the case, the ordering

[8] It is interesting to notice that, when thinking in terms of an embedding, this operation can generate new boundary components. In addition, if applied to a reducible graph it can turn it into a reduced one. This is related to our comment in footnote 6.

of the rows in T was chosen incorrectly, i.e. the position of the free entries $*_j$ must be modified.

5. The on-shell form corresponding to a diagram for which

$$T = \begin{pmatrix} i_1^{(1)} & i_2^{(1)} & \cdots & i_{k+1}^{(1)} \\ i_1^{(2)} & i_2^{(2)} & \cdots & i_{k+1}^{(2)} \\ \vdots & & & \vdots \\ i_1^{(n_B)} & i_2^{(n_B)} & \cdots & i_{k+1}^{(n_B)} \end{pmatrix} \tag{6.3.12}$$

is given by

$$\Omega = \frac{d^{k\times n}C}{\mathrm{Vol}(\mathrm{GL}(k))} \left(\frac{\det(\widehat{M}_{a_1,\ldots,a_k})}{(a_1,\ldots,a_k)}\right)^k \frac{1}{\mathrm{PT}^{(1)}\mathrm{PT}^{(2)}\cdots\mathrm{PT}^{(n_B)}}\,, \tag{6.3.13}$$

where we denote by $\mathrm{PT}^{(i)}$ the Parke-Taylor-like product corresponding to each row i of T, for instance in (6.3.12), $\mathrm{PT}^{(1)} = (i_1^{(1)}\cdots i_k^{(1)})\cdots(i_{k+1}^{(1)}\cdots i_{k-1}^{(1)})$. If there was no need for introducing auxiliary external legs, this is the final answer.

6. In the presence of auxiliary legs, we now need to integrate over the extra variables C_{ij}, $j = n+1,\ldots,n+\alpha$ around $C_{ij} = 0$. Below we present various examples in which this is done.

6.3.3 The Meaning of $*$

In (6.3.11) we proposed that when an internal black node in an N^{k-2}MHV on-shell diagram has valency $v < k+1$, this leads to arbitrary entries on the matrix T, denoted by $*$. In this section we want to address the physical meaning of this freedom of choice: a row in T of the form $\{i_1,\ldots,i_v,*_{v+1},\cdots *_{k+1}\}$ implies that the columns $\vec{c}_{i_1},\ldots,\vec{c}_{i_v}$ of the matrix $C \in G(k,n)$ are linearly dependent vectors, which implies that $(i_1,\ldots,i_v) = 0$.

This is a general statement that can be understood by splitting the original diagram into two sub-diagrams: C_R containing the black node in question and all possible internal white nodes and external legs attached to it, and C_L, the rest of the diagram. The original diagram is obtained by "amalgamating" C_L and C_R, cf.

§3 of [34]. The main purpose of splitting the diagram is that the minors of C can be written in terms of products of minors of C_L and C_R. Importantly, the diagram C_R has $k_R < k$, therefore every $k \times k$ minor of C with labels that belong entirely to external nodes in C_R will be expressed as a product of a $k_R \times k_R$ minor from C_R, and a $k_L \times k_L$ minor from C_L but which contains labels from C_R. In other words, the $k_L \times k_L$ minor has labels which are not present in C_L, and must hence be zero.

Example. To illustrate this argument let us consider a leading singularity in $G(3, 6)$ presented in Figure 6.11, and split it as shown in Figure 6.10.

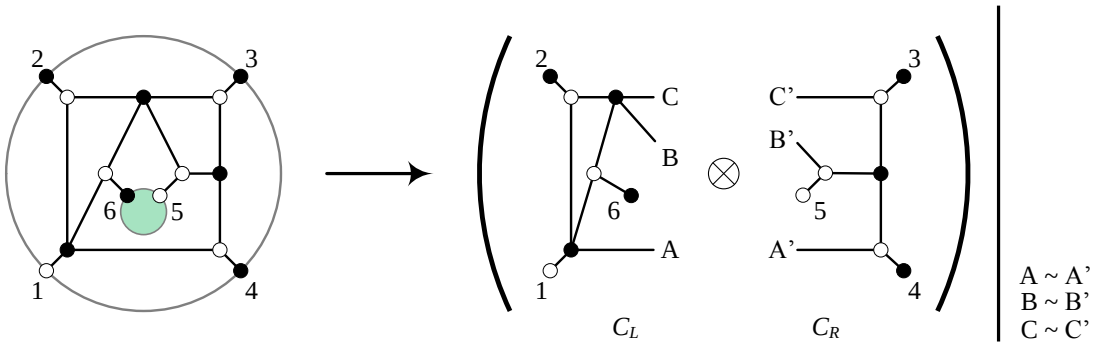

Figure 6.10: On the left, NMHV leading singularity corresponding to $(345) = 0$. This diagram can be obtained by the two diagrams on the right upon direct product and projection of the edges $A \sim A'$, $B \sim B'$, $C \sim C'$.

Notice that $k_L = 4$ and $k_R = 2$, thus the minors of the matrix C of the original diagram can be related to the minors of C_L and C_R as

$$(345)\Big|_C = (ABC3)\Big|_{C_L}(45)\Big|_{C_R} + (ABC4)\Big|_{C_L}(53)\Big|_{C_R} + (ABC5)\Big|_{C_L}(34)\Big|_{C_R} = 0 \ , \tag{6.3.14}$$

since 3,4, and 5 only appear in C_R, so $(ABC3)\Big|_{C_L} = (ABC4)\Big|_{C_L} = (ABC5)\Big|_{C_L} = 0$.

In diagrams with $\alpha > 0$, the T matrix may gain $*$ entries when introducing auxiliary external edges. These will only impose the vanishing of minors containing the auxiliary edges, however.

6.3.4 Examples

We now illustrate the rules introduced in the previous section on various explicit examples.

NMHV with Low Valency

Our first example illustrates how to deal with cases when we need to introduce $*$ into the matrix T. The diagram is shown in Figure 6.11. We will also show that this diagram is decomposable into a sum of Parke-Taylor factors through the use of Kleiss-Kuijf relations [136], thus independently confirming the answer.

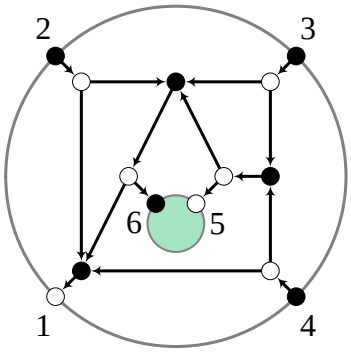

Figure 6.11: NMHV leading singularity with $(345) = 0$.

Since $n_B = n - k$ and all internal black nodes connect to a maximum of $k+1 = 4$ external nodes, no manipulations of the diagram are required. The T matrix is given by

$$T = \begin{pmatrix} 1 & 2 & 6 & 4 \\ 2 & 3 & 5 & 6 \\ 5 & 3 & 4 & * \end{pmatrix}, \tag{6.3.15}$$

where we may choose $* = 1$, 2 or 6. The final answer is independent of this choice, and in the following we choose $* = 2$. From the bottom row we can also immediately read off that the minor $(345) = 0$, as proven in §6.3.3.

We shall now construct the matrix M. We have

$$T = \begin{pmatrix} 1 & 2 & 6 & 4 \\ 2 & 3 & 5 & 6 \\ 5 & 3 & 4 & 2 \end{pmatrix} \rightarrow M = \begin{pmatrix} (264) & (641) & 0 & (126) & 0 & (412) \\ 0 & (356) & (562) & 0 & (623) & (235) \\ 0 & (534) & (425) & (253) & (342) & 0 \end{pmatrix}. \tag{6.3.16}$$

Deleting columns 2, 3, and 4 we get

$$\widehat{M}_{2,3,4} = \begin{pmatrix} (264) & 0 & (412) \\ 0 & (623) & (235) \\ 0 & (342) & 0 \end{pmatrix} \quad \Rightarrow \quad \frac{\det \widehat{M}_{2,3,4}}{(234)} = -(264)(235). \tag{6.3.17}$$

Thus, the on-shell form corresponding to the leading singularity in Figure 6.11 is given by

$$\Omega = \frac{d^{3\times 6}C}{\mathrm{Vol}(\mathrm{GL}(3))} \frac{(264)^2(235)}{(126)(641)(412)(356)(562)(623)(342)(425)(345)}\bigg|_{(345)=0}. \tag{6.3.18}$$

Although we do not have a general proof for the independence of the choice of $*$ and the deleted rows of M, this example provides strong evidence to believe this is indeed the case. For the example at hand, we have checked explicitly that this result agrees with the differential form in terms of edge or generalized face variables for any choice of GL(3) gauge fixing, deleted rows, as well as for $* = 1$ or 6. For this particular example, (6.3.18) can be explicitly confirmed to be correct: this leading singularity can be written in terms of planar integrals, with the help of the Kleiss-Kuijf relations [136] on the four-point nodes present in the diagram in Figure 6.11. Explicitly, using Plücker relations at the pole $(345) = 0$ one may rewrite the ratio in (6.3.18) as

$$\begin{aligned} &\frac{(264)^2(235)}{(126)(641)(412)(356)(562)(623)(342)(425)(345)}\bigg|_{(345)=0} \\ &= I(1,6,2,3,5,4) + I(1,6,2,5,3,4) + I(1,2,6,3,5,4) + I(1,2,6,5,3,4), \end{aligned} \tag{6.3.19}$$

where $I(i_1, i_2, i_3, i_4, i_5, i_6)$ stands for the planar integrals with ordering indicated by their arguments:

$$I(i_1, i_2, i_3, i_4, i_5, i_6) = \frac{1}{(i_1 i_2 i_3)(i_2 i_3 i_4)(i_3 i_4 i_5)(i_4 i_5 i_6)(i_5 i_6 i_1)(i_6 i_1 i_2)}. \tag{6.3.20}$$

For MHV diagrams, [124] showed that every non-planar leading singularity can be re-expressed as a sum of Parke-Taylor factors with coefficients +1. This is not a general feature of N^{k-2}MHV leading singularities, as will become clear with the final example in this section. In Appendix C.2 we present a similar, higher genus, example.

NMHV with Too Many Black Nodes

Let us now consider diagrams with $n_B > n-k$. An example of this type is provided in Figure 6.12, which is obtained by adding a BCFW bridge to legs 5 and 6 in Figure 6.11. Hence, the two examples must agree on the pole $(345) = 0$, which provides us with an additional check of the validity of the procedure in §6.3.2.

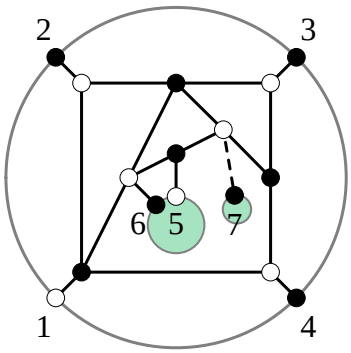

Figure 6.12: NMHV leading singularity with $n_B > n-k$. This requires the introduction of an auxiliary leg, indicated by a dashed line and numbered 7.

This example has $\alpha = 1$. Following §6.3.2, we must introduce an auxiliary leg as shown in Figure 6.12. This new diagram yields the T matrix

$$T = \begin{pmatrix} 1 & 2 & 6 & 4 \\ 2 & 3 & 7 & 6 \\ 7 & 3 & 4 & * \\ 5 & 6 & 7 & * \end{pmatrix} \xrightarrow{\text{Choice of } *} T = \begin{pmatrix} 1 & 2 & 6 & 4 \\ 2 & 3 & 7 & 6 \\ 7 & 3 & 4 & 2 \\ 5 & 6 & 7 & 2 \end{pmatrix} . \tag{6.3.21}$$

Notice how from the last two rows of T we learn that $(734) = (567) = 0$.

This gives the following matrix M

$$M = \begin{pmatrix} (264) & (641) & 0 & (126) & 0 & (412) & 0 \\ 0 & (376) & (762) & 0 & 0 & (237) & (623) \\ 0 & (734) & (427) & (273) & 0 & 0 & (342) \\ 0 & (567) & 0 & 0 & (672) & (725) & (256) \end{pmatrix}, \tag{6.3.22}$$

which results in the on-shell form

$$\Omega = \frac{d^{3\times 7}C}{\mathrm{Vol}(\mathrm{GL}(3))} \frac{(264)^2}{(126)(641)(412)(623)(234)(256)} \times I|_7 \,, \tag{6.3.23}$$

where $I|_7$ stands for the piece containing the dependence on the auxiliary external node 7 and must be evaluated at the poles $(347) = (567) = 0$. On these poles, it can be recast as

$$I|_7 = \frac{(256)}{(456)(347)(567)(725)}. \tag{6.3.24}$$

The final step is to remove the effect of the auxiliary edge. This is done by taking a generic element of the "extended" Grassmannian $G(k, n+1)$ and integrating the extra variables C_{i7} around $C_{i7} = 0$. To do so, we write a generic 3×7 matrix C and compute the residues of $I|_7$ around $C_{i7} = 0$, $i = 1, 2, 3$. We obtain

$$\Omega = \frac{d^{3\times 6}C}{\mathrm{Vol}(\mathrm{GL}(3))} \frac{(246)^2}{(234)(345)(456)(612)(124)(146)(236)(256)}. \tag{6.3.25}$$

As expected, this result agrees with the leading singularity (6.3.18) on the support of $(345) = 0$.

With the previous two examples, we have illustrated the full set of our tools. As an additional demonstration of the power of this procedure, in Appendix C.3 we compute a highly non-trivial N^2MHV example.

NMHV with a New Type of Pole

We shall now apply our tools to computing a top-dimensional example in $G(3, 6)$ which exhibits a novel feature: a differential form with a singularity which is not of the form $(ijk) = 0$. This fact ultimately prohibits the diagram from being able to be written as a sum of planar terms. The on-shell diagram is shown in Figure

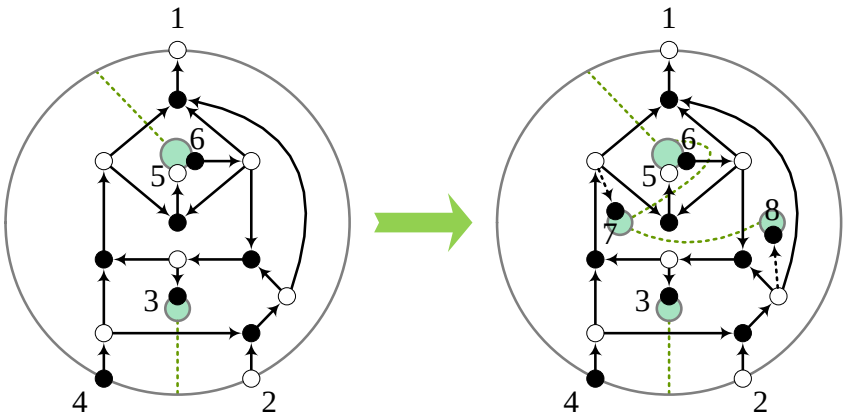

Figure 6.13: Left: a NMHV top-dimensional diagram in $G(3,6)$. Right: this diagram requires the addition of two auxiliary legs, here shown with dashed arrows and terminating on external nodes 7 and 8. This example has a non-standard singularity when $(124)(346)(365) - (456)(234)(136) = 0$.

6.13. This example will also be revisited in §6.4, where the consequences of such a peculiar differential form will be studied in detail.

The T matrix is

$$T = \begin{pmatrix} 1 & 8 & 6 & 7 \\ 5 & 6 & 7 & * \\ 6 & 8 & 3 & * \\ 8 & 2 & 4 & * \\ 7 & 3 & 4 & * \end{pmatrix} \xrightarrow{\text{Choice of } *} T = \begin{pmatrix} 1 & 8 & 6 & 7 \\ 5 & 6 & 7 & 2 \\ 6 & 8 & 3 & 2 \\ 8 & 2 & 4 & 6 \\ 7 & 3 & 4 & 2 \end{pmatrix}, \tag{6.3.26}$$

from which we can immediately read off that

$$(347) = (567) = (368) = (248) = 0. \tag{6.3.27}$$

From T, we construct the matrix M

$$M = \begin{pmatrix} (867) & 0 & 0 & 0 & 0 & (718) & (186) & (671) \\ 0 & (567) & 0 & 0 & (672) & (725) & (256) & 0 \\ 0 & (683) & (268) & 0 & 0 & (832) & 0 & (326) \\ 0 & (468) & 0 & (682) & 0 & (824) & 0 & (246) \\ 0 & (734) & (427) & (273) & 0 & 0 & (342) & 0 \end{pmatrix}. \tag{6.3.28}$$

The resulting on-shell form can be simplified on the poles $(567) = (368) = (248) = (347) = 0$ to

$$\Omega = \frac{d^{3\times 8}C}{\text{Vol}(\text{GL}(3))} \frac{(346)^2(356)}{(234)(345)(456)(561)(136)(236)} \times I|_{7,8} \tag{6.3.29}$$

where $I|_{7,8}$ encodes all the dependence on the extra legs 7 and 8,

$$I|_{7,8} = \frac{1}{(781)(567)(368)(248)(347)}. \tag{6.3.30}$$

As in the previous examples, we now compute the residues of $I|_{7,8}$ around $C_{i7} = C_{i8} = 0$ for $i = 1, 2, 3$ and obtain

$$I|_{7,8} \to \frac{1}{(124)(346)(365) - (456)(234)(136)}. \tag{6.3.31}$$

Thus we find that the on-shell form of the six-point diagram in Figure 6.13 is given by

$$\Omega = \frac{d^{3\times 6}C}{\text{Vol}(\text{GL}(3))} \frac{(346)^2(356)}{(234)(345)(456)(561)(136)(236)\left((124)(346)(365) - (456)(234)(136)\right)}. \tag{6.3.32}$$

The appearance of the factor $(124)(346)(365)-(456)(234)(136)$ in the denominator through this process is rather non-trivial and shows that this diagram, unlike the NMHV leading singularity (6.3.18), cannot be written as a linear combination of planar diagrams. This example thus provides concrete evidence for a behavior already announced in [124], that already for $k = 3$ and $n = 6$ not all leading singularities can be expressed as linear combinations of planar ones. This diagram certainly deserves further study, and we will come back to it in §6.4.1. There we will use a matroid polytope perspective to fully understand reducibility in the context of non-planar diagrams. For this diagram we will indeed find an edge which, when removed, does not set any Plücker coordinates to zero but instead relates Plücker coordinates to each other, i.e. it will impose the relation $(124)(346)(365) - (456)(234)(136) = 0$. The leading singularity that arises through the removal of this edge is fully computed in [6].

6.4 Novel Features of Non-Planar Reductions

In §4.4 we discussed reductions and reducibility of on-shell diagrams and introduced a combinatorial framework that can be used to study edge removal. In this section we will work out an example in detail. We will construct its matching and matroid polytopes, establish the precise connection between points in the matroid polytope and Plücker coordinates using the boundary measurement and investigate its reducibility. The example has been chosen to illustrate a new phenomenon that can occur when removing an edge from a non-planar diagram: the set of non-vanishing Plücker coordinates can remain the same while new non-Plücker constraints are generated. This has a direct impact on the issue of reducibility. If a new constraint arises, the new diagram does not cover the same region of the Grassmannian as the original one and hence it is not a reduction.

This story has an interesting counterpart in terms of the on-shell form. The killing of degrees of freedom associated to removing an edge corresponds to taking the residue of the form at the pole where that degree of freedom goes to zero. On-shell forms for planar diagrams have a particularly simple structure; they are just one over a product of Plücker coordinates. Every pole of the on-shell form thus corresponds to setting some Plücker coordinate to zero. New things can, however, happen for non-planar diagrams: the on-shell form can have poles at which no Plücker coordinate vanishes.

Non-Plücker constraints should also be taken into account when determining whether two diagrams cover the same region of the Grassmannian. We leave a more detailed investigation of on-shell diagrams with constraints for future work. They certainly arise, as we explicitly show, as limits of more standard diagrams. At present we do not have any argument indicating that they should not be physical.

6.4.1 An Example

Let us consider the example on the left of Figure 6.13. For convenience, the on-shell diagram is reproduced in Figure 6.14. The perfect orientation is the one corresponding to the perfect matching $\tilde{p}_{\text{ref}} = \alpha_{1,3}\alpha_{1,7}\alpha_{4,5}\alpha_{6,7}\alpha_{8,3}\alpha_{8,7}\alpha'_{4,5}$. The new possibilities

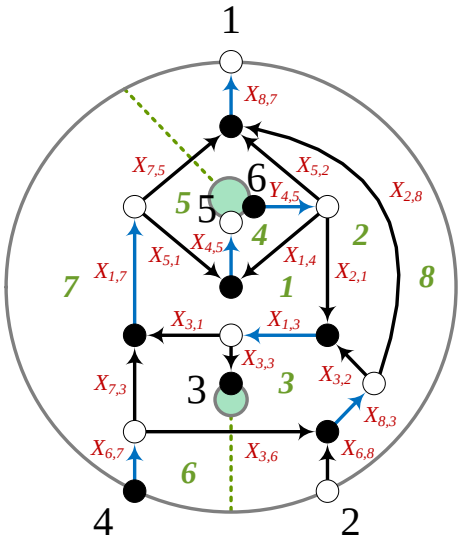

Figure 6.14: An on-shell diagram embedded on a genus-0 surface with three boundaries. Faces are labeled in green, external nodes in black and edges in red.

might be anticipated by looking at the denominator of the on-shell form (6.3.32), which contains a factor $((124)(346)(365) - (456)(234)(136))$. This means that there is a pole when this factor vanishes, which can be reached without shutting off any Plücker coordinate. Furthermore, we expect that this can be achieved by deleting edges in the graph. Notice that $((124)(346)(365) - (456)(234)(136)) = 0$ does not kill any minors but instead imposes a new constraint on them.[9] We shall now see how this happens.

The perfect matching matrix P for this graph is given in (6.4.1), below, where we have organized the rows such that the final six correspond to external edges. We have also highlighted the row corresponding to $X_{5,2}$ for future convenience. It is straightforward to check, e.g. by shifting the coordinates such that one of them lies at the origin and then row-reducing P, that the matching polytope is a 9-dimensional object. This fact nicely matches the counting in terms of generalized face variables:

[9]It is interesting to point out that this is very reminiscent of the detailed discussion of boundaries of the amplituhedron presented in [5], in which certain boundaries correspond to setting combinations of minors to zero. In that case, too, all boundaries can be mapped to poles of the on-shell form.

there are 8 faces f_i (7 of which are independent) and $B-1=2$ variables b_j, which totals 9 degrees of freedom. This will become important later.

$$P = \left(\begin{array}{c|cccccccccccccccccccccccccccccccccccc}
X_{1,3} & 1&1&1&1&1&1&1&1&1&1&1&0&0&0&0&0&0&0&0&0&0&0&0&0&0&0&0&0&0&0&0&0&0&0&0&0&0&0&0&0 \\
X_{1,4} & 1&1&1&1&0&0&0&0&0&0&0&0&1&1&1&1&1&0&0&0&0&0&0&0&0&0&0&0&0&0&0&0&0&0&0&0&0&0&0&0 \\
X_{1,7} & 1&1&1&0&1&1&1&1&0&0&0&0&1&1&0&0&0&1&1&1&1&1&1&1&0&0&0&0&0&0&0&0&0&0&0&0&0&0&0&0 \\
X_{2,8} & 1&1&0&0&1&1&0&0&1&0&0&0&0&0&0&0&0&1&1&0&0&0&0&0&1&1&1&0&0&0&0&0&0&0&0&0&0&0&0&0 \\
X_{3,6} & 1&0&0&0&1&0&0&0&0&0&0&0&1&0&1&0&0&1&0&1&1&0&0&0&1&0&0&1&1&1&0&0&0&0&0&0&0&0&0&0 \\
X_{3,1} & 0&0&0&0&0&0&0&0&0&0&0&0&0&0&1&1&0&0&0&0&0&0&0&0&0&1&1&0&1&1&1&1&1&1&1&1&0&0&0&0&0&0 \\
X_{3,2} & 0&0&0&0&0&0&0&0&0&0&0&0&1&1&1&1&1&0&0&1&1&1&1&0&0&0&0&1&1&1&1&1&1&0&0&1&1&1&0&0 \\
X_{5,1} & 0&0&0&0&0&0&0&0&1&1&1&0&0&0&0&0&0&0&0&0&0&0&0&0&0&0&0&1&1&1&1&1&0&1&1&0&1&0&1&1&0&1&0 \\
\boldsymbol{X_{5,2}} & 0&0&0&0&0&0&1&0&0&1&0&0&0&0&0&0&0&0&0&1&0&1&0&0&0&0&0&1&0&0&1&0&0&0&0&1&0&0&0&0 \\
X_{7,5} & 0&0&0&1&0&0&0&0&0&0&0&1&0&0&1&1&1&0&0&0&0&0&0&0&0&0&0&0&0&1&0&0&1&0&1&0&0&1&0&1 \\
X_{7,3} & 0&0&0&1&0&0&0&0&1&1&1&1&0&0&0&0&1&0&0&0&0&0&0&0&0&0&1&0&0&0&0&0&0&0&0&1&1&1&1&1 \\
X_{8,3} & 0&0&1&1&0&0&1&1&0&1&1&1&0&0&0&0&0&0&0&0&0&0&0&0&0&1&0&0&0&0&0&0&0&0&1&1&0&0&0&1&1 \\
Y_{2,1} & 0&0&0&0&0&0&0&0&0&0&0&0&0&0&0&0&0&0&0&1&1&0&0&0&0&1&1&1&1&0&0&0&0&0&0&1&1&0&0&0&1&1 \\
\hline
X_{3,3} & 0&0&0&0&0&0&0&0&0&0&0&0&0&1&1&0&0&1&1&1&1&1&1&1&1&0&0&1&0&0&0&0&0&0&0&0&1&1&1&1&1 \\
X_{6,7} & 0&1&1&0&0&1&1&1&0&0&0&0&0&1&0&1&0&0&1&0&0&1&1&1&0&1&0&0&0&0&1&1&1&1&0&0&0&0&0 \\
X_{6,8} & 0&1&0&0&0&1&0&0&1&0&0&0&0&1&0&1&1&0&1&0&0&1&1&0&0&1&1&0&0&0&1&1&1&0&0&1&1&1&0&0 \\
X_{8,7} & 0&0&1&0&0&0&0&1&0&0&1&0&1&1&0&0&0&0&0&0&1&0&1&1&0&0&0&0&1&0&0&1&0&1&0&0&1&0&1&0 \\
X_{4,5} & 0&0&0&0&1&1&1&1&0&0&0&1&0&0&0&0&0&1&1&1&1&1&1&1&0&0&0&0&0&1&0&0&1&0&1&0&0&1&0&1 \\
Y_{4,5} & 0&0&0&0&1&1&0&1&1&0&1&1&0&0&0&0&0&0&0&0&1&0&1&0&0&0&0&0&1&1&0&1&1&0&0&0&1&1&0&0
\end{array}\right) \tag{6.4.1}$$

The matroid polytope is obtained by taking (6.4.1) and keeping only the 6 coordinates associated to the external edges. Doing this projects multiple perfect matchings down to the same point in the matroid polytope. The points in the matroid polytope are summarized in (6.4.2), where for every point we list the corresponding perfect matchings and Plücker coordinate.

0	0	0	0	0	0	0	0	0	1
0	1	1	0	1	1	1	0	0	0
0	1	0	0	1	0	0	1	0	0
0	0	1	0	0	0	1	0	1	1
0	0	0	1	1	1	1	0	0	0
0	0	0	1	1	0	1	1	1	0
p_1, p_4 p_{10}, p_{15} p_{25}, p_{28}	p_2, p_{16} p_{26}, p_{31}	p_3, p_{34}	p_5, p_{12} p_{30}	p_6, p_{33}	p_7, p_{35}	p_8	p_9	p_{11}, p_{29}	p_{13}, p_{39}
$\Delta_{1,2,5}$	$\Delta_{1,4,5}$	$\Delta_{2,4,5}$	$\Delta_{1,2,6}$	$\Delta_{1,4,6}$	$\Delta_{1,2,4}$	$\Delta_{2,4,6}$	$\Delta_{1,5,6}$	$\Delta_{2,5,6}$	$\Delta_{2,3,5}$

1	1	1	1	1	1	1	1	1	1
1	0	0	1	0	1	1	1	0	0
1	1	0	1	0	1	0	1	1	1
1	0	0	0	1	1	1	1	1	0
0	0	1	1	1	1	1	0	0	1
0	0	0	0	1	1	0	1	1	1
p_{14}	p_{17}, p_{27} p_{36}	p_{18}, p_{20} p_{40}	p_{19}, p_{22}	p_{21}	p_{23}	p_{24}	p_{32}	p_{37}	p_{38}
$\Delta_{3,4,5}$	$\Delta_{1,3,5}$	$\Delta_{1,2,3}$	$\Delta_{1,3,4}$	$\Delta_{2,3,6}$	$\Delta_{3,4,6}$	$\Delta_{2,3,4}$	$\Delta_{4,5,6}$	$\Delta_{3,5,6}$	$\Delta_{1,3,6}$

(6.4.2)

Using (6.4.1) it is straightforward to check that there is a single edge, $X_{5,2}$, which can be removed without killing any point in the matroid polytope. Eliminating this edge removes all perfect matchings that contain it, i.e. $p_7, p_{10}, p_{20}, p_{22}, p_{28}, p_{31}, p_{36}$, which are shown in red in (6.4.2). Following our previous discussion, none of the Plücker coordinates are set to zero. We now investigate what happens to them in more detail, by considering the effect on the boundary measurement.

Boundary Measurement for the Original Diagram. Before removing $X_{5,2}$, the matrix C associated to Figure 6.14 is

$$C \equiv \left(\begin{array}{c|cccccc} & 1 & 2 & 3 & 4 & 5 & 6 \\ \hline 2 & c_1 & 1 & c_2 & 0 & c_3 & 0 \\ 4 & c_4 & 0 & c_5 & 1 & c_6 & 0 \\ 6 & c_7 & 0 & c_8 & 0 & c_9 & 1 \end{array}\right)$$

$$= \left(\begin{array}{cccccc} \frac{\alpha_{6,8}\alpha_{2,8}}{\alpha_{8,3}\alpha_{8,7}} + \frac{\alpha_{6,8}\alpha_{3,2}\alpha_{3,1}\alpha_{7,5}}{\alpha_{8,3}\alpha_{1,3}\alpha_{1,7}\alpha_{8,7}} & 1 & \frac{\alpha_{6,8}\alpha_{3,2}\alpha_{3,3}}{\alpha_{8,3}\alpha_{1,3}} & 0 & \cdots \\ -\frac{\alpha_{3,6}\alpha_{2,8}}{\alpha_{6,7}\alpha_{8,3}\alpha_{8,7}} - \frac{\alpha_{3,6}\alpha_{3,2}\alpha_{3,1}\alpha_{7,5}}{\alpha_{6,7}\alpha_{8,3}\alpha_{1,3}\alpha_{1,7}\alpha_{8,7}} - \frac{\alpha_{7,3}\alpha_{7,5}}{\alpha_{6,7}\alpha_{1,7}\alpha_{8,7}} & 0 & -\frac{\alpha_{3,6}\alpha_{3,2}\alpha_{3,3}}{\alpha_{6,7}\alpha_{8,3}\alpha_{1,3}} & 1 & \cdots \\ \frac{\alpha_{5,2}}{\alpha'_{4,5}\alpha_{8,7}} - \frac{\alpha_{2,1}\alpha_{3,1}\alpha_{7,5}}{\alpha'_{4,5}\alpha_{1,3}\alpha_{1,7}\alpha_{8,7}} & 0 & -\frac{\alpha_{2,1}\alpha_{3,3}}{\alpha'_{4,5}\alpha_{1,3}} & 0 & \cdots \end{array}\right.$$

$$\left.\begin{array}{c} -\frac{\alpha_{6,8}\alpha_{3,2}\alpha_{3,1}\alpha_{5,1}}{\alpha_{8,3}\alpha_{1,3}\alpha_{1,7}\alpha_{4,5}} \\ \cdots \quad \frac{\alpha_{7,3}\alpha_{5,1}}{\alpha_{6,7}\alpha_{1,7}\alpha_{4,5}} + \frac{\alpha_{3,6}\alpha_{3,2}\alpha_{3,1}\alpha_{5,1}}{\alpha_{6,7}\alpha_{8,3}\alpha_{1,3}\alpha_{1,7}\alpha_{4,5}} \\ \frac{\alpha_{1,4}}{\alpha'_{4,5}\alpha_{4,5}} + \frac{\alpha_{2,1}\alpha_{3,1}\alpha_{5,1}}{\alpha'_{4,5}\alpha_{1,3}\alpha_{1,7}\alpha_{4,5}} \end{array}\right) \begin{array}{c} 0 \\ 0 \\ 1 \end{array} \Bigg). \tag{6.4.3}$$

All minors of this matrix are generally non-zero:

$$\begin{aligned}
\Delta_{1,2,3} &= -\mathfrak{p}_{18} - \mathfrak{p}_{20} - \mathfrak{p}_{40} & \Delta_{2,3,4} &= \mathfrak{p}_{24} \\
\Delta_{1,2,4} &= \mathfrak{p}_{7} - \mathfrak{p}_{35} & \Delta_{2,3,5} &= \mathfrak{p}_{39} - \mathfrak{p}_{13} \\
\Delta_{1,2,5} &= \mathfrak{p}_{1} + \mathfrak{p}_{4} + \mathfrak{p}_{10} + \mathfrak{p}_{15} + \mathfrak{p}_{25} + \mathfrak{p}_{28} & \Delta_{2,3,6} &= -\mathfrak{p}_{21} \\
\Delta_{1,2,6} &= \mathfrak{p}_{5} + \mathfrak{p}_{12} + \mathfrak{p}_{30} & \Delta_{2,4,5} &= \mathfrak{p}_{3} + \mathfrak{p}_{34} \\
\Delta_{1,3,4} &= \mathfrak{p}_{19} + \mathfrak{p}_{22} & \Delta_{2,4,6} &= 1 \\
\Delta_{1,3,5} &= \mathfrak{p}_{17} + \mathfrak{p}_{27} + \mathfrak{p}_{36} & \Delta_{2,5,6} &= \mathfrak{p}_{11} + \mathfrak{p}_{29} \\
\Delta_{1,3,6} &= \mathfrak{p}_{38} & \Delta_{3,4,5} &= \mathfrak{p}_{14} \\
\Delta_{1,4,5} &= \mathfrak{p}_{2} + \mathfrak{p}_{16} + \mathfrak{p}_{26} + \mathfrak{p}_{31} & \Delta_{3,4,6} &= \mathfrak{p}_{23} \\
\Delta_{1,4,6} &= \mathfrak{p}_{6} + \mathfrak{p}_{33} & \Delta_{3,5,6} &= \mathfrak{p}_{37} \\
\Delta_{1,5,6} &= \mathfrak{p}_{9} & \Delta_{4,5,6} &= \mathfrak{p}_{32}
\end{aligned} \tag{6.4.4}$$

The flows for perfect matchings containing $X_{5,2}$ are shown in red. In total we have 9 independent minors, which tells us that C is in the top cell of $G(3,6)$. Thus, we see that if generalized face variables are to parametrize all degrees of freedom of C, we cannot lose any f_i or b_j, as we already have the minimal number possible to account for a 9-dimensional C. Naively, this is in tension with the fact that edge $X_{5,2}$ can be removed without eliminating points in the matroid polytope, i.e. without setting Plücker coordinates to zero. As we now explain, while this is true, the removal of $X_{5,2}$ does not kill any Δ_I, but it removes a degree of freedom in such a way as to create a new constraint on the Δ_I, independent from the Plücker relations. We then conclude that the graph is *not* reducible.

Boundary Measurement After Removing $X_{5,2}$. Let us understand in detail how the new constraint arises. We will do so from the perspective of the boundary measurement and the matching polytopes. If we remove $X_{5,2}$, i.e. set $X_{5,2} = 0$, the only entry in C that is affected is c_7.[10] The Plücker coordinates now become

[10]Let us say a few words on how to eliminate edges that appear in the denominator of entries in the boundary measurement. Once a perfect orientation is chosen, a given oriented edge weight appears either *only* in numerators (as is the case for X_{52} in this example) or denominators. This is determined by whether the perfect orientation coincides or is opposed to the conventional orientation we picked for the edge under consideration. If we want to remove an edge appearing in denominators, all we need to do is to send the corresponding edge weight to infinity. The fact that

$$
\begin{aligned}
\Delta_{1,2,3} &= -\mathfrak{p}_{18} - \mathfrak{p}_{40} & \Delta_{2,3,4} &= \mathfrak{p}_{24} \\
\Delta_{1,2,4} &= -\mathfrak{p}_{35} & \Delta_{2,3,5} &= \mathfrak{p}_{39} - \mathfrak{p}_{13} \\
\Delta_{1,2,5} &= \mathfrak{p}_1 + \mathfrak{p}_4 + \mathfrak{p}_{15} + \mathfrak{p}_{25} & \Delta_{2,3,6} &= -\mathfrak{p}_{21} \\
\Delta_{1,2,6} &= \mathfrak{p}_5 + \mathfrak{p}_{12} + \mathfrak{p}_{30} & \Delta_{2,4,5} &= \mathfrak{p}_3 + \mathfrak{p}_{34} \\
\Delta_{1,3,4} &= \mathfrak{p}_{19} & \Delta_{2,4,6} &= 1 \\
\Delta_{1,3,5} &= \mathfrak{p}_{17} + \mathfrak{p}_{27} & \Delta_{2,5,6} &= \mathfrak{p}_{11} + \mathfrak{p}_{29} \\
\Delta_{1,3,6} &= \mathfrak{p}_{38} & \Delta_{3,4,5} &= \mathfrak{p}_{14} \\
\Delta_{1,4,5} &= \mathfrak{p}_2 + \mathfrak{p}_{16} + \mathfrak{p}_{26} & \Delta_{3,4,6} &= \mathfrak{p}_{23} \\
\Delta_{1,4,6} &= \mathfrak{p}_6 + \mathfrak{p}_{33} & \Delta_{3,5,6} &= \mathfrak{p}_{37} \\
\Delta_{1,5,6} &= \mathfrak{p}_9 & \Delta_{4,5,6} &= \mathfrak{p}_{32}
\end{aligned}
\tag{6.4.5}
$$

These equations can also be directly obtained from (6.4.4) by removing the red flows. In addition, that same information, up to signs, can be directly obtained from the matroid polytope encoded in (6.4.2).

Here we see the new situation we anticipated from our knowledge of the matroid polytope: no Plücker coordinates are shut off despite losing a face variable.

Let us now consider the generalized face variables. In addition to the ordinary faces, we will use the paths

$$
b_1 = \frac{\alpha_{1,3}\alpha_{8,3}}{\alpha_{3,3}\alpha_{3,2}\alpha_{6,8}} \qquad b_2 = \frac{\alpha_{4,5}\alpha_{7,5}}{\alpha_{5,1}\alpha_{8,7}}. \tag{6.4.6}
$$

At this point, a natural question is whether it is even possible to express all paths in the matrix C using the generalized face variables that remain at our disposal. The answer is yes: we have

$$
\begin{aligned}
c_1 &= \frac{1}{f_3 f_6 f_7} + \frac{1}{f_1 f_3 f_4 f_{2/5} f_6 f_7} & c_4 &= -\frac{1}{f_7} - \frac{1}{f_3 f_7} - \frac{1}{f_1 f_3 f_4 f_{2/5} f_7} & c_7 &= -b_2 f_1 f_4 \\
c_2 &= \frac{1}{b_1} & c_5 &= -\frac{f_6}{b_1} & c_8 &= -\frac{b_2 f_1 f_3 f_4 f_6 f_7}{b_1} \\
c_3 &= -\frac{1}{b_2 f_3 f_6 f_7} & c_6 &= \frac{1}{b_2 f_3 f_7} + \tfrac{1}{b_2 f_7} & c_9 &= f_1 f_4 + f_4
\end{aligned}
\tag{6.4.7}
$$

We see that only the 8 variables f_1, $f_{2/5}$, f_3, f_4, f_6, f_7, b_1 and b_2 are used, where $f_{2/5} \equiv f_2 f_5$ indicates the combination of f_2 and f_5. It is possible to invert this map

some edges are removed by sending them to zero while other ones are removed by sending them to infinity is thus a matter of conventions and another reflection of the symmetry of on-shell diagrams under the inversion of the edge weights.

without using c_7, obtaining

$$\begin{aligned} f_1 &= \frac{c_3 c_8}{c_2 c_9 - c_3 c_8} & f_4 &= \frac{c_2 c_9 - c_3 c_8}{c_2} & f_6 &= -\frac{c_5}{c_2} & b_1 &= \frac{1}{c_2} \\ f_3 &= \frac{c_2 c_6 - c_3 c_5}{c_3 c_5} & f_{2/5} &= \frac{c_1 c_5 - c_2 c_4}{c_8(c_3 c_4 - c_1 c_6)} & f_7 &= \frac{c_2}{c_1 c_5 - c_2 c_4} & b_2 &= \frac{c_1 c_5 - c_2 c_4}{c_2 c_6 - c_3 c_5}\,. \end{aligned} \tag{6.4.8}$$

This implies that c_7 can indeed be expressed in terms of the other c_i's as follows

$$c_7 = -b_2 f_1 f_4 = \frac{c_8 c_3 (c_2 c_4 - c_1 c_5)}{c_2 (c_2 c_6 - c_3 c_5)}. \tag{6.4.9}$$

We have just shown that although it appears that all 9 entries of the matrix C are independent, this is not the case. This condition can be translated into a constraint on the Plücker coordinates, by noting that

$$\begin{aligned} c_1 &= \Delta_{1,4,6} & c_4 &= -\Delta_{1,2,6} & c_7 &= \Delta_{1,2,4} \\ c_2 &= \Delta_{3,4,6} & c_5 &= \Delta_{2,3,6} & c_8 &= -\Delta_{2,3,4} \\ c_3 &= -\Delta_{4,5,6} & c_6 &= \Delta_{2,5,6} & c_9 &= \Delta_{2,4,5} \end{aligned} \tag{6.4.10}$$

Hence, (6.4.9) becomes

$$\begin{aligned} \Delta_{1,2,4} = \frac{\Delta_{2,3,4}\Delta_{4,5,6}(-\Delta_{3,4,6}\Delta_{1,2,6} - \Delta_{1,4,6}\Delta_{2,3,6})}{\Delta_{3,4,6}(\Delta_{3,4,6}\Delta_{2,5,6} + \Delta_{4,5,6}\Delta_{2,3,6})} = -\frac{\Delta_{2,3,4}\Delta_{4,5,6}(\Delta_{1,3,6}\Delta_{2,4,6})}{\Delta_{3,4,6}(\Delta_{3,5,6}\Delta_{2,4,6})} \\ \Leftrightarrow \quad \Delta_{1,2,4}\Delta_{3,4,6}\Delta_{3,5,6} = -\Delta_{2,3,4}\Delta_{4,5,6}\Delta_{1,3,6} \end{aligned} \tag{6.4.11}$$

where we used two Plücker relations to simplify the expression. This constraint is equivalent to the one we expected from the denominator $((124)(346)(365) - (456)(234)(136))$.

We then see a novel and interesting feature appearing in non-planar graphs: by removing an edge we have created a constraint on the Plücker coordinates that is independent of the Plücker relations. We conclude that the original graph was indeed reduced. Irreducibility can manifest when deleting edges as the vanishing of Plücker coordinates (as for planar graphs) or as the emergence of new constraints on them.

This constraint can alternatively be simply determined by using (6.4.1) and (6.4.2), because it just reflects the linear dependencies of vectors in the matching

polytope. From (6.4.2) we see that (6.4.11) is

$$p_{35}\, p_{23}\, p_{37} = p_{24}\, p_{32}\, p_{38}$$

$$\Leftrightarrow \quad \begin{pmatrix} 0\\0\\0\\0\\0\\1\\0\\0\\0\\1\\0\\1\\1\\0\\1\\0\\0\\1\\0 \end{pmatrix} + \begin{pmatrix} 0\\0\\1\\0\\0\\0\\1\\0\\0\\0\\0\\0\\0\\1\\1\\1\\1\\1\\1 \end{pmatrix} + \begin{pmatrix} 0\\0\\0\\0\\0\\0\\1\\1\\0\\0\\1\\0\\0\\1\\0\\1\\1\\0\\1 \end{pmatrix} = \begin{pmatrix} 0\\0\\1\\0\\0\\0\\0\\0\\0\\0\\1\\1\\1\\1\\0\\1\\1\\0 \end{pmatrix} + \begin{pmatrix} 0\\0\\0\\0\\0\\1\\1\\1\\0\\0\\0\\0\\0\\1\\1\\1\\0\\1 \end{pmatrix} + \begin{pmatrix} 0\\0\\0\\0\\0\\0\\1\\1\\0\\0\\0\\0\\0\\1\\0\\1\\0\\1 \end{pmatrix} \tag{6.4.12}$$

Now we understand how the new constraint arises. While (6.4.12) is always true, we need to set $X_{5,2} = 0$ in order to translate it into a constraint on Plücker coordinates Δ_I. Phrased differently, before removing $X_{5,2}$, (6.4.11) would imply that $(p_{35} - p_7)\, p_{23}\, p_{37} = p_{24}\, p_{32}\, p_{38}$, which is not true. Once $X_{5,2}$ has been removed, however, p_7 disappears and (6.4.11) becomes equivalent to the known relation among perfect matchings (6.4.12).

6.4.2 A Systematic Approach to Reducibility

One lesson we should draw from the previous section is that for non-planar graphs the preservation of the matroid polytope under edge removal is a necessary but not sufficient condition for reducibility. It is nonetheless possible to establish a systematic procedure for determining whether a non-planar graph is reducible or not, which goes as follows. Simply remove as many edges as possible while preserving the matroid polytope, and count the degrees of freedom of the generalized face variables f_i and b_j in the resulting graph.[11] This number should be compared to the expected number of degrees of freedom based on the surviving points of the matroid polytope,

[11] Generally, multiple combinations of removed edges are possible at this step. In addition, these combinations might involve different numbers of edges.

i.e. a naive counting of dimensions of C that assumes the absence of constraints other than the Plücker relations. Two scenarios may occur:

- The surviving points of the matroid polytope suggest a dimension that is *equal* to the number of independent generalized face variables. This means that the graph is now maximally reduced, and there are no new constraints on the Δ_I.

- The surviving points of the matroid polytope suggest a dimension that is *larger* than the number of independent generalized face variables. This means that the collection of removed edges, which did not affect the matroid polytope, has reduced the graph "more than the maximal amount". The difference δ between the naive and actual dimensions gives the number of new constraints on non-vanishing Plücker coordinates which have been generated. Whenever $\delta > 0$, it means that too many edges have been removed and the graph was already reduced after deleting a subset of them.

For illustration, let us reconsider the graph in Figure 6.14. As we saw, it is possible to remove the edge $X_{5,2}$ while preserving the matroid polytope. The number of points in the matroid polytope after this operation is 20, which for $G(3,6)$ suggests a naive dimension equal to 9 (i.e. as many dimensions as the top cell). However, we only have $6+2=8$ independent generalized face variables, so $\delta = 9-8 = 1$. We conclude that the original graph was already reduced and by deleting $X_{5,2}$ we generate a new constraint on Plücker coordinates.

These operations are very simple to implement algorithmically on a computer and thus provide a quick check for whether a graph is reduced or not.

6.4.3 Discovering Non-Plücker Constraints

As mentioned above, $\delta > 0$ indicates the existence of constraints on the Δ_I that are independent from the Plücker relations. It is natural to want to find these constraints. To this end, we suggest the following strategy:

- Solve the linear relations among column vectors in P to obtain all constraints on linear combinations of these vectors.

- Solve the Plücker relations.
- Rewrite the perfect matchings in terms of Plücker coordinates, by inverting the map in (6.4.4).
- Plug the expressions of perfect matchings into the constraints obtained from the first point, to obtain the corresponding constraints in terms of Plücker coordinates.
- Insert the solution of the Plücker relations into these constraints. The number of new constraints that do not trivialize should be δ.

6.5 Conclusions

We have established several concepts and machinery to undertake the study of non-planar on-shell diagrams. Some of our main results are: the use of generalized face variables together with the boundary measurement to obtain the on-shell form for general non-planar diagrams, a generalization of the prescription of [124] for obtaining the on-shell form in terms of minors that applies beyond the MHV case, and a thorough study of reducibility of non-planar diagrams.

The natural goal of this general program is to achieve a level of understanding of non-planar diagrams similar to the existing one for planar diagrams. As we have repeatedly witnessed in this chapter, the non-planar realm is far richer.

In addition, there are several concrete questions for future investigation, and we now mention a few of them. First, it would be interesting to investigate in further detail the interplay between our combinatorial tools and the classification of diagrams based on equivalence moves. For example, a concrete problem is to classify the on-shell diagrams associated to all permutation inequivalent top-dimensional cells for various $G(k, n)$'s. It would be interesting to find an algorithm to construct non-planar on-shell diagrams. Similar methods exist for constructing planar on-shell diagrams from permutations [34] and for constructing dimer models from toric diagrams [19, 107]. It would be worth studying whether the stratification of non-planar on-shell diagrams hints at some interesting topologies of the associated geometries

and, if so, what its physical significance is.[12] It is also natural to investigate whether there are non-planar counterparts for some of the objects which followed on-shell diagrams in planar $\mathcal{N} = 4$ SYM, such as deformed on-shell diagrams [67–70, 137–139] and the amplituhedron [79, 80]. Another question to explore is whether there is a non-planar generalization of the connection between scattering amplitudes in the 3d ABJM theory [129] and the positive orthogonal Grassmannian [130, 131].

[12]Here we have in mind the approach to stratification introduced in Chapter 4, based on the matching and matroid polytopes.

Bibliography

[1] S. Franco, D. Galloni, and R.-K. Seong, *New Directions in Bipartite Field Theories*, *JHEP* **1306** (2013) 032, [arXiv:1211.5139].

[2] S. Franco, D. Galloni, and Y.-H. He, *Towards the Continuous Limit of Cluster Integrable Systems*, *JHEP* **1209** (2012) 020, [arXiv:1203.6067].

[3] S. Franco, D. Galloni, and A. Mariotti, *The Geometry of On-Shell Diagrams*, *JHEP* **1408** (2014) 038, [arXiv:1310.3820].

[4] S. Franco, D. Galloni, and A. Mariotti, *Bipartite Field Theories, Cluster Algebras and the Grassmannian*, *J.Phys.* **A47** (2014), no. 47 474004, [arXiv:1404.3752].

[5] S. Franco, D. Galloni, A. Mariotti, and J. Trnka, *Anatomy of the Amplituhedron*, arXiv:1408.3410.

[6] S. Franco, D. Galloni, B. Penante, and C. Wen, *Non-Planar On-Shell Diagrams*, arXiv:1502.0203.

[7] N. Seiberg, *Electric - magnetic duality in supersymmetric nonAbelian gauge theories*, *Nucl.Phys.* **B435** (1995) 129–146, [hep-th/9411149].

[8] P. C. Argyres and N. Seiberg, *S-duality in N=2 supersymmetric gauge theories*, *JHEP* **0712** (2007) 088, [arXiv:0711.0054].

[9] K. A. Intriligator and N. Seiberg, *Mirror symmetry in three-dimensional gauge theories*, *Phys.Lett.* **B387** (1996) 513–519, [hep-th/9607207].

[10] S. Franco, *Bipartite Field Theories: from D-Brane Probes to Scattering Amplitudes*, *JHEP* **1211** (2012) 141, [arXiv:1207.0807].

[11] J. J. Heckman, C. Vafa, D. Xie, and M. Yamazaki, *String Theory Origin of Bipartite SCFTs*, *JHEP* **1305** (2013) 148, [arXiv:1211.4587].

[12] S. Franco, *Cluster Transformations from Bipartite Field Theories*, *Phys.Rev.* **D88** (2013), no. 10 105010, [arXiv:1301.0316].

[13] S. Franco and A. Uranga, *Bipartite Field Theories from D-Branes*, *JHEP* **1404** (2014) 161, [arXiv:1306.6331].

[14] D. Xie and M. Yamazaki, *Network and Seiberg Duality*, *JHEP* **1209** (2012) 036, [arXiv:1207.0811].

[15] A. Hanany and K. D. Kennaway, *Dimer models and toric diagrams*, hep-th/0503149.

[16] S. Franco, A. Hanany, K. D. Kennaway, D. Vegh, and B. Wecht, *Brane dimers and quiver gauge theories*, *JHEP* **0601** (2006) 096, [hep-th/0504110].

[17] S. Franco, A. Hanany, D. Martelli, J. Sparks, D. Vegh, et al., *Gauge theories from toric geometry and brane tilings*, *JHEP* **0601** (2006) 128, [hep-th/0505211].

[18] K. D. Kennaway, *Brane Tilings*, *Int.J.Mod.Phys.* **A22** (2007) 2977–3038, [arXiv:0706.1660].

[19] B. Feng, Y.-H. He, K. D. Kennaway, and C. Vafa, *Dimer models from mirror symmetry and quivering amoebae*, *Adv.Theor.Math.Phys.* **12** (2008) 489–545, [hep-th/0511287].

[20] A. Butti, D. Forcella, and A. Zaffaroni, *The Dual superconformal theory for L**pqr manifolds*, *JHEP* **0509** (2005) 018, [hep-th/0505220].

[21] J. Davey, A. Hanany, and J. Pasukonis, *On the Classification of Brane Tilings*, *JHEP* **1001** (2010) 078, [arXiv:0909.2868].

[22] A. Hanany and R.-K. Seong, *Brane Tilings and Reflexive Polygons*, *Fortsch.Phys.* **60** (2012) 695–803, [arXiv:1201.2614].

[23] I. R. Klebanov and A. A. Tseytlin, *Gravity duals of supersymmetric SU(N) x SU(N+M) gauge theories*, *Nucl.Phys.* **B578** (2000) 123–138, [hep-th/0002159].

[24] I. R. Klebanov and M. J. Strassler, *Supergravity and a confining gauge theory: Duality cascades and chi SB resolution of naked singularities*, *JHEP* **0008** (2000) 052, [hep-th/0007191].

[25] A. Hanany and J. Walcher, *On duality walls in string theory*, *JHEP* **0306** (2003) 055, [hep-th/0301231].

[26] S. Franco, A. Hanany, Y.-H. He, and P. Kazakopoulos, *Duality walls, duality trees and fractional branes*, hep-th/0306092.

[27] S. Franco, A. Hanany, and A. M. Uranga, *Multi-flux warped throats and cascading gauge theories*, *JHEP* **0509** (2005) 028, [hep-th/0502113].

[28] F. Marchesano, G. Shiu, and A. M. Uranga, *F-term Axion Monodromy Inflation*, *JHEP* **1409** (2014) 184, [arXiv:1404.3040].

[29] S. Franco, D. Galloni, A. Retolaza, and A. Uranga, *On axion monodromy inflation in warped throats*, *JHEP* **1502** (2015) 086, [arXiv:1405.7044].

[30] S. Franco, *Dimer Models, Integrable Systems and Quantum Teichmuller Space*, *JHEP* **1109** (2011) 057, [arXiv:1105.1777].

[31] R. Eager, S. Franco, and K. Schaeffer, *Dimer Models and Integrable Systems*, *JHEP* **1206** (2012) 106, [arXiv:1107.1244].

[32] A. Amariti, D. Forcella, and A. Mariotti, *Integrability on the Master Space*, *JHEP* **1206** (2012) 053, [arXiv:1203.1616].

[33] A. Goncharov and R. Kenyon, *Dimers and cluster integrable systems*, *Annales scientifiques de l'ENS* **46** (2013) 747–813, [arXiv:1107.5588].

[34] N. Arkani-Hamed, J. L. Bourjaily, F. Cachazo, A. B. Goncharov, A. Postnikov, and J. Trnka, *Scattering Amplitudes and the Positive Grassmannian*, arXiv:1212.5605.

[35] A. Amariti and D. Forcella, *Scattering Amplitudes and Toric Geometry*, *JHEP* **1309** (2013) 133, [arXiv:1305.5252].

[36] C. Closset, *Toric geometry and local Calabi-Yau varieties: An Introduction to toric geometry (for physicists)*, arXiv:0901.3695.

[37] O. Aharony, A. Hanany, and B. Kol, *Webs of (p,q) five-branes, five-dimensional field theories and grid diagrams*, *JHEP* **9801** (1998) 002, [hep-th/9710116].

[38] Z. Bern, L. J. Dixon, D. C. Dunbar, and D. A. Kosower, *One loop n point gauge theory amplitudes, unitarity and collinear limits*, *Nucl.Phys.* **B425** (1994) 217–260, [hep-ph/9403226].

[39] Z. Bern, L. J. Dixon, D. C. Dunbar, and D. A. Kosower, *Fusing gauge theory tree amplitudes into loop amplitudes*, *Nucl.Phys.* **B435** (1995) 59–101, [hep-ph/9409265].

[40] Z. Bern, L. J. Dixon, and V. A. Smirnov, *Iteration of planar amplitudes in maximally supersymmetric Yang-Mills theory at three loops and beyond*, *Phys.Rev.* **D72** (2005) 085001, [hep-th/0505205].

[41] F. Cachazo, P. Svrcek, and E. Witten, *MHV vertices and tree amplitudes in gauge theory*, *JHEP* **0409** (2004) 006, [hep-th/0403047].

[42] R. Britto, F. Cachazo, and B. Feng, *Generalized unitarity and one-loop amplitudes in N=4 super-Yang-Mills*, *Nucl.Phys.* **B725** (2005) 275–305, [hep-th/0412103].

[43] R. Britto, F. Cachazo, and B. Feng, *New recursion relations for tree amplitudes of gluons*, *Nucl.Phys.* **B715** (2005) 499–522, [hep-th/0412308].

[44] R. Britto, F. Cachazo, B. Feng, and E. Witten, *Direct proof of tree-level recursion relation in Yang-Mills theory*, *Phys.Rev.Lett.* **94** (2005) 181602, [hep-th/0501052].

[45] L. J. Dixon, *Calculating scattering amplitudes efficiently*, hep-ph/9601359.

[46] N. Beisert, C. Ahn, L. F. Alday, Z. Bajnok, J. M. Drummond, et al., *Review of AdS/CFT Integrability: An Overview*, *Lett.Math.Phys.* **99** (2012) 3–32, [arXiv:1012.3982].

[47] J. Drummond, *Tree-level amplitudes and dual superconformal symmetry*, *J.Phys.* **A44** (2011) 454010, [arXiv:1107.4544].

[48] H. Elvang and Y.-t. Huang, *Scattering Amplitudes*, arXiv:1308.1697.

[49] Z. Bern, M. Czakon, L. J. Dixon, D. A. Kosower, and V. A. Smirnov, *The Four-Loop Planar Amplitude and Cusp Anomalous Dimension in Maximally Supersymmetric Yang-Mills Theory*, *Phys.Rev.* **D75** (2007) 085010, [hep-th/0610248].

[50] Z. Bern, J. Carrasco, H. Johansson, and D. Kosower, *Maximally supersymmetric planar Yang-Mills amplitudes at five loops*, *Phys.Rev.* **D76** (2007) 125020, [arXiv:0705.1864].

[51] J. L. Bourjaily, A. DiRe, A. Shaikh, M. Spradlin, and A. Volovich, *The Soft-Collinear Bootstrap: N=4 Yang-Mills Amplitudes at Six and Seven Loops*, *JHEP* **1203** (2012) 032, [arXiv:1112.6432].

[52] N. Arkani-Hamed, J. L. Bourjaily, F. Cachazo, S. Caron-Huot, and J. Trnka, *The All-Loop Integrand For Scattering Amplitudes in Planar N=4 SYM*, *JHEP* **1101** (2011) 041, [arXiv:1008.2958].

[53] N. Arkani-Hamed, J. L. Bourjaily, F. Cachazo, and J. Trnka, *Local Integrals for Planar Scattering Amplitudes*, *JHEP* **1206** (2012) 125, [arXiv:1012.6032].

[54] L. J. Dixon, J. M. Drummond, and J. M. Henn, *Analytic result for the two-loop six-point NMHV amplitude in N=4 super Yang-Mills theory*, *JHEP* **1201** (2012) 024, [arXiv:1111.1704].

[55] L. J. Dixon, J. M. Drummond, M. von Hippel, and J. Pennington, *Hexagon functions and the three-loop remainder function*, *JHEP* **1312** (2013) 049, [arXiv:1308.2276].

[56] L. J. Dixon, J. M. Drummond, C. Duhr, M. von Hippel, and J. Pennington, *Bootstrapping six-gluon scattering in planar $\mathcal{N} = 4$ super-Yang-Mills theory*, arXiv:1407.4724.

[57] L. F. Alday and J. M. Maldacena, *Gluon scattering amplitudes at strong coupling*, *JHEP* **0706** (2007) 064, [arXiv:0705.0303].

[58] J. Drummond, J. Henn, V. Smirnov, and E. Sokatchev, *Magic identities for conformal four-point integrals*, *JHEP* **0701** (2007) 064, [hep-th/0607160].

[59] J. M. Drummond, J. M. Henn, and J. Plefka, *Yangian symmetry of scattering amplitudes in N=4 super Yang-Mills theory*, *JHEP* **0905** (2009) 046, [arXiv:0902.2987].

[60] N. Beisert and M. Staudacher, *The N=4 SYM integrable super spin chain*, *Nucl.Phys.* **B670** (2003) 439–463, [hep-th/0307042].

[61] N. Beisert, B. Eden, and M. Staudacher, *Transcendentality and Crossing*, *J.Stat.Mech.* **0701** (2007) P01021, [hep-th/0610251].

[62] N. Arkani-Hamed, F. Cachazo, C. Cheung, and J. Kaplan, *A Duality For The S Matrix*, *JHEP* **1003** (2010) 020, [arXiv:0907.5418].

[63] N. Arkani-Hamed, F. Cachazo, and C. Cheung, *The Grassmannian Origin Of Dual Superconformal Invariance*, *JHEP* **1003** (2010) 036, [arXiv:0909.0483].

[64] J. Kaplan, *Unraveling L(n,k): Grassmannian Kinematics*, *JHEP* **1003** (2010) 025, [arXiv:0912.0957].

[65] L. Mason and D. Skinner, *Dual Superconformal Invariance, Momentum Twistors and Grassmannians*, *JHEP* **0911** (2009) 045, [arXiv:0909.0250].

[66] N. Arkani-Hamed, J. Bourjaily, F. Cachazo, and J. Trnka, *Unification of Residues and Grassmannian Dualities*, *JHEP* **1101** (2011) 049, [arXiv:0912.4912].

[67] L. Ferro, T. Lukowski, C. Meneghelli, J. Plefka, and M. Staudacher, *Harmonic R-matrices for Scattering Amplitudes and Spectral Regularization*, *Phys.Rev.Lett.* **110** (2013), no. 12 121602, [arXiv:1212.0850].

[68] L. Ferro, T. ukowski, C. Meneghelli, J. Plefka, and M. Staudacher, *Spectral Parameters for Scattering Amplitudes in N=4 Super Yang-Mills Theory*, *JHEP* **1401** (2014) 094, [arXiv:1308.3494].

[69] N. Beisert, J. Broedel, and M. Rosso, *On Yangian-invariant regularisation of deformed on-shell diagrams in N=4 super-Yang-Mills theory*, arXiv:1401.7274.

[70] L. Ferro, T. Lukowski, and M. Staudacher, *N=4 Scattering Amplitudes and the Deformed Grassmannian*, arXiv:1407.6736.

[71] T. Bargheer, Y.-t. Huang, F. Loebbert, and M. Yamazaki, *Integrable Amplitude Deformations for N=4 Super Yang–Mills and ABJM Theory*, arXiv:1407.4449.

[72] Z. Bern, J. Rozowsky, and B. Yan, *Two loop four gluon amplitudes in N=4 superYang-Mills*, *Phys.Lett.* **B401** (1997) 273–282, [hep-ph/9702424].

[73] Z. Bern, J. Carrasco, L. J. Dixon, H. Johansson, D. Kosower, et al., *Three-Loop Superfiniteness of N=8 Supergravity*, *Phys.Rev.Lett.* **98** (2007) 161303, [hep-th/0702112].

[74] Z. Bern, J. Carrasco, L. J. Dixon, H. Johansson, and R. Roiban, *The Complete Four-Loop Four-Point Amplitude in N=4 Super-Yang-Mills Theory*, *Phys.Rev.* **D82** (2010) 125040, [arXiv:1008.3327].

[75] J. J. Carrasco and H. Johansson, *Five-Point Amplitudes in N=4 Super-Yang-Mills Theory and N=8 Supergravity*, *Phys.Rev.* **D85** (2012) 025006, [arXiv:1106.4711].

[76] Z. Bern, J. Carrasco, H. Johansson, and R. Roiban, *The Five-Loop Four-Point Amplitude of N=4 super-Yang-Mills Theory*, *Phys.Rev.Lett.* **109** (2012) 241602, [arXiv:1207.6666].

[77] N. Arkani-Hamed, J. L. Bourjaily, F. Cachazo, and J. Trnka, *Singularity Structure of Maximally Supersymmetric Scattering Amplitudes*, *Phys.Rev.Lett.* **113** (2014), no. 26 261603, [arXiv:1410.0354].

[78] Z. Bern, E. Herrmann, S. Litsey, J. Stankowicz, and J. Trnka, *Logarithmic Singularities and Maximally Supersymmetric Amplitudes*, arXiv:1412.8584.

[79] N. Arkani-Hamed and J. Trnka, *The Amplituhedron*, *JHEP* **1410** (2014) 30, [arXiv:1312.2007].

[80] N. Arkani-Hamed and J. Trnka, *Into the Amplituhedron*, *JHEP* **1412** (2014) 182, [arXiv:1312.7878].

[81] T. Lam, *Amplituhedron cells and Stanley symmetric functions*, arXiv:1408.5531.

[82] Y. Bai and S. He, *The Amplituhedron from Momentum Twistor Diagrams*, arXiv:1408.2459.

[83] N. Arkani-Hamed, A. Hodges, and J. Trnka, *Positive Amplitudes In The Amplituhedron*, arXiv:1412.8478.

[84] A. Postnikov, *Total positivity, Grassmannians, and networks*, *ArXiv Mathematics e-prints* (2006) [math/0609764].

[85] A. Ishii and K. Ueda, *On moduli spaces of quiver representations associated with dimer models*, *ArXiv e-prints* (Oct., 2007) [arXiv:0710.1898].

[86] S. Benvenuti, S. Franco, A. Hanany, D. Martelli, and J. Sparks, *An Infinite family of superconformal quiver gauge theories with Sasaki-Einstein duals*, *JHEP* **0506** (2005) 064, [hep-th/0411264].

[87] A. Hanany and R.-K. Seong, *Brane Tilings and Specular Duality*, *JHEP* **1208** (2012) 107, [arXiv:1206.2386].

[88] S. Cremonesi, A. Hanany, and R.-K. Seong, *Double Handled Brane Tilings*, *JHEP* **1310** (2013) 001, [arXiv:1305.3607].

[89] Y.-H. He and M. van Loon, *Gauge Theories, Tessellations & Riemann Surfaces*, *JHEP* **1406** (2014) 053, [arXiv:1402.3846].

[90] R. Kenyon, A. Okounkov, and S. Sheffield, *Dimers and amoebae*, *Ann.Math.* **163** (2006) 1019–1056, [math-ph/0311005].

[91] S. Franco and D. Vegh, *Moduli spaces of gauge theories from dimer models: Proof of the correspondence*, *JHEP* **0611** (2006) 054, [hep-th/0601063].

[92] A. Hanany, *Counting BPS operators in the chiral ring: The plethystic story*, *AIP Conf.Proc.* **939** (2007) 165–175.

[93] A. Butti, D. Forcella, A. Hanany, D. Vegh, and A. Zaffaroni, *Counting Chiral Operators in Quiver Gauge Theories*, *JHEP* **0711** (2007) 092, [arXiv:0705.2771].

[94] B. Feng, A. Hanany, and Y.-H. He, *Counting gauge invariants: The Plethystic program*, *JHEP* **0703** (2007) 090, [hep-th/0701063].

[95] S. Benvenuti, B. Feng, A. Hanany, and Y.-H. He, *Counting BPS Operators in Gauge Theories: Quivers, Syzygies and Plethystics*, *JHEP* **0711** (2007) 050, [hep-th/0608050].

[96] D. Forcella, A. Hanany, Y.-H. He, and A. Zaffaroni, *The Master Space of N=1 Gauge Theories*, *JHEP* **0808** (2008) 012, [arXiv:0801.1585].

[97] D. Forcella, A. Hanany, Y.-H. He, and A. Zaffaroni, *Mastering the Master Space*, *Lett.Math.Phys.* **85** (2008) 163–171, [arXiv:0801.3477].

[98] A. Hanany and A. Zaffaroni, *The master space of supersymmetric gauge theories*, *Adv.High Energy Phys.* **2010** (2010) 427891.

[99] B. Feng, S. Franco, A. Hanany, and Y.-H. He, *Symmetries of toric duality*, *JHEP* **0212** (2002) 076, [hep-th/0205144].

[100] B. Feng, A. Hanany, and Y.-H. He, *D-brane gauge theories from toric singularities and toric duality*, *Nucl.Phys.* **B595** (2001) 165–200, [hep-th/0003085].

[101] A. Postnikov, D. Speyer, and L. Williams, *Matching polytopes, toric geometry, and the non-negative part of the Grassmannian*, *Journal of Algebraic Combinatorics* **30** (2009) 173–191, [arXiv:0706.2501].

[102] B. Feng, A. Hanany, and Y.-H. He, *Phase structure of D-brane gauge theories and toric duality*, *JHEP* **0108** (2001) 040, [hep-th/0104259].

[103] B. Feng, A. Hanany, Y.-H. He, and A. M. Uranga, *Toric duality as Seiberg duality and brane diamonds*, *JHEP* **0112** (2001) 035, [hep-th/0109063].

[104] C. E. Beasley and M. R. Plesser, *Toric duality is Seiberg duality*, *JHEP* **0112** (2001) 001, [hep-th/0109053].

[105] S. Franco, A. Hanany, and Y.-H. He, *A Trio of dualities: Walls, trees and cascades*, *Fortsch.Phys.* **52** (2004) 540–547, [hep-th/0312222].

[106] B. Feng, S. Franco, A. Hanany, and Y.-H. He, *UnHiggsing the del Pezzo*, *JHEP* **0308** (2003) 058, [hep-th/0209228].

[107] A. Hanany and D. Vegh, *Quivers, tilings, branes and rhombi*, *JHEP* **0710** (2007) 029, [hep-th/0511063].

[108] N. Broomhead, *Dimer models and Calabi-Yau algebras*, arXiv:0901.4662.

[109] C. Romelsberger, *Counting chiral primaries in N = 1, d=4 superconformal field theories*, *Nucl.Phys.* **B747** (2006) 329–353, [hep-th/0510060].

[110] J. Kinney, J. M. Maldacena, S. Minwalla, and S. Raju, *An Index for 4 dimensional super conformal theories*, *Commun.Math.Phys.* **275** (2007) 209–254, [hep-th/0510251].

[111] Y. Terashima and M. Yamazaki, *Emergent 3-manifolds from 4d Superconformal Indices*, *Phys.Rev.Lett.* **109** (2012) 091602, [arXiv:1203.5792].

[112] O. Aharony and A. Hanany, *Branes, superpotentials and superconformal fixed points*, *Nucl.Phys.* **B504** (1997) 239–271, [hep-th/9704170].

[113] W. Fulton, *Introduction to toric varieties*. Annals of mathematics studies. Princeton Univ. Press, Princeton, NJ, 1993.

[114] M. R. Douglas, B. R. Greene, and D. R. Morrison, *Orbifold resolution by D-branes*, *Nucl.Phys.* **B506** (1997) 84–106, [hep-th/9704151].

[115] C. Beasley, B. R. Greene, C. Lazaroiu, and M. Plesser, *D3-branes on partial resolutions of Abelian quotient singularities of Calabi-Yau threefolds*, *Nucl.Phys.* **B566** (2000) 599–640, [hep-th/9907186].

[116] I. Garcia-Etxebarria, F. Saad, and A. M. Uranga, *Quiver gauge theories at resolved and deformed singularities using dimers*, *JHEP* **0606** (2006) 055, [hep-th/0603108].

[117] D. Orlando and S. Reffert, *Combinatorics of the Dimer Model on a Strip*, *ArXiv e-prints* (Sept., 2007) [arXiv:0709.1546].

[118] A. Postnikov, "Positive grassmannian." http://www-math.mit.edu/~ahmorales/18.318lecs/lectures.pdf, 2013.

[119] K. Talaska and L. Williams, *Network Parameterizations for the Grassmannian*, *ArXiv e-prints* (2012) [arXiv:1210.5433].

[120] J. Oxley, *Matroid Theory*. Oxford graduate texts in mathematics. Oxford University Press, 2006.

[121] A. R. Fink, "Matroid polytope subdivisions and valuations." `http://www.maths.qmul.ac.uk/~fink/thesis.pdf`, 2010.

[122] K. Talaska, *A formula for Plücker coordinates associated with a planar network*, *International Mathematics Research Notices* **2008** (2008) [`arXiv:0801.4822`].

[123] M. Gekhtman, M. Shapiro, and A. Vainshtein, *Poisson Geometry of Directed Networks in an Annulus*, *Journal of the European Mathematical Society* **14** (2012) 541–570, [`arXiv:0901.0020`].

[124] N. Arkani-Hamed, J. L. Bourjaily, F. Cachazo, A. Postnikov, and J. Trnka, *On-Shell Structures of MHV Amplitudes Beyond the Planar Limit*, `arXiv:1412.8475`.

[125] E. Gawrilow and M. Joswig, *polymake: a framework for analyzing convex polytopes*, in *Polytopes Combinatorics and Computation* (G. Kalai and G. Ziegler, eds.), vol. 29 of *DMV Seminar*, pp. 43–73. Birkhuser Basel, 2000.

[126] L. K. Williams, *Shelling totally nonnegative flag varieties*, *J. Reine Angew. Math.* **609** (2007) 001, [`0509129`].

[127] M. Enciso, *Volumes of Polytopes Without Triangulations*, `arXiv:1408.0932`.

[128] J. Trnka, *Work in progress*, .

[129] O. Aharony, O. Bergman, D. L. Jafferis, and J. Maldacena, *N=6 superconformal Chern-Simons-matter theories, M2-branes and their gravity duals*, *JHEP* **0810** (2008) 091, [`arXiv:0806.1218`].

[130] Y.-T. Huang and C. Wen, *ABJM amplitudes and the positive orthogonal grassmannian*, *JHEP* **1402** (2014) 104, [`arXiv:1309.3252`].

[131] Y.-t. Huang, C. Wen, and D. Xie, *The Positive orthogonal Grassmannian and loop amplitudes of ABJM*, `arXiv:1402.1479`.

[132] R. Roiban, M. Spradlin, and A. Volovich, *Dissolving N=4 loop amplitudes into QCD tree amplitudes*, *Phys.Rev.Lett.* **94** (2005) 102002, [hep-th/0412265].

[133] N. Arkani-Hamed, F. Cachazo, and J. Kaplan, *What is the Simplest Quantum Field Theory?*, *JHEP* **1009** (2010) 016, [arXiv:0808.1446].

[134] M. Spradlin, A. Volovich, and C. Wen, *Three Applications of a Bonus Relation for Gravity Amplitudes*, *Phys.Lett.* **B674** (2009) 69–72, [arXiv:0812.4767].

[135] B. Feng, R. Huang, and Y. Jia, *Gauge Amplitude Identities by On-shell Recursion Relation in S-matrix Program*, *Phys.Lett.* **B695** (2011) 350–353, [arXiv:1004.3417].

[136] R. Kleiss and H. Kuijf, *Multi - Gluon Cross-sections and Five Jet Production at Hadron Colliders*, *Nucl.Phys.* **B312** (1989) 616.

[137] N. Kanning, T. Lukowski, and M. Staudacher, *A shortcut to general tree-level scattering amplitudes in $\mathcal{N} = 4$ SYM via integrability*, *Fortsch.Phys.* **62** (2014) 556–572, [arXiv:1403.3382].

[138] J. Broedel, M. de Leeuw, and M. Rosso, *A dictionary between R-operators, on-shell graphs and Yangian algebras*, *JHEP* **1406** (2014) 170, [arXiv:1403.3670].

[139] J. Broedel, M. de Leeuw, and M. Rosso, *Deformed one-loop amplitudes in $\mathcal{N} = 4$ super-Yang-Mills theory*, *JHEP* **1411** (2014) 091, [arXiv:1406.4024].

Appendix A

Appendices to Chapter 4: "The Geometry of On-Shell Diagrams"

A.1 The Path Matrix

In this appendix we describe an efficient algorithm to extract the paths for a given perfect orientation of a bipartite diagram, planar or non-planar. This is an important step of the boundary measurement which maps bipartite graphs to elements of the Grassmannian. The path matrix $\mathcal{M}$ is an $n_v \times n_v$ matrix, where n_v is the number of vertices in the diagram. Given a perfect orientation, each entry $\mathcal{M}_{ab}$ contains the sum of edge weights for all oriented paths connecting vertices a and b. We shall now show how this matrix can be obtained using the Kasteleyn matrix.

The perfect orientation is determined in terms of a reference perfect matching p_{ref} as explained in §2.3. We now construct two matrices as follows: we define K^r as the Kasteleyn matrix where we have set to zero the edge weights $X_{i,j} \in p_{\text{ref}}$ and replaced all other $X_{i,j} \to \alpha_{i,j}$; we define $\tilde{K}^r$ as the Kasteleyn matrix where we have set to zero all the edge weights not belonging to p_{ref}, and sent $X_{i,j} \to 1/\alpha_{i,j}$ for the edge weights $X_{i,j} \in p_{\text{ref}}$. We then arrange the following $n_v \times n_v$ matrix:

$$C = \begin{pmatrix} \mathbb{I}_{n_w \times n_w} & -K^r \\ -(\tilde{K}^r)^T & \mathbb{I}_{n_b \times n_b} \end{pmatrix} , \tag{A.1.1}$$

where n_w and n_b is the number of white and black nodes, respectively. The path

matrix is $\mathcal{M} = C^{-1}$. The $k \times n$ dimensional matrix $\mathcal{M}^C$ is simply a sub-matrix of $\mathcal{M}$, obtained by extracting those entries that correspond to sources flowing to external nodes.

The entries $\mathcal{M}_{ab}$ are generally sums of ratios of edge weights $\alpha_{i,j}$, where the denominator contains those $\alpha_{i,j}$ in $\tilde{p}_{\text{ref}}$ which are relevant to the path. We remind the reader that an edge in the numerator signifies that the direction of that edge is from the white node to the black node, an edge in the denominator signifies the opposite direction.

Sometimes a path from a vertex a to a vertex b contains a loop. This results in an infinite number of paths from a to b, which differ in the number of times the path runs over the loop. The entry $\mathcal{M}_{ab}$ will thus contain the infinite sum of paths: $(1-\text{loop})^{-1} = 1 + \text{loop} + (\text{loop})^2 + \dots$. Explicit examples of the construction of $\mathcal{M}$ can be found in the appendices of [3].

A.2 A Genus-Two Example

Let us now apply our boundary measurement prescription to an on-shell diagram embedded into a genus-2 surface with a single boundary. This example admits an alternative embedding into a genus-0 surface with multiple boundaries, which allows for a non-trivial check of our proposal. Genus-2 surfaces have four fundamental cycles: α_1, β_1, α_2, β_2. The diagram is shown in Figure A.1, where we present the fundamental cell of the surface and segments on its perimeter are periodically identified according to their color and orientation. We pick a perfect orientation corresponding to the perfect matching $\tilde{p}_{\text{ref}} = \alpha_{1,2}\alpha_{1,3}\alpha_{4,2}\alpha_{4,3}\alpha_{5,1}\alpha_{5,2}\alpha'_{5,2}$.

Let us now determine the boundary measurement. To do so, we first list all flows and their source sets.

$$\mathfrak{p}_1 = \frac{\alpha_{1,5}\alpha_{3,1}\alpha_{4,1}\alpha_{4,5}}{\alpha_{1,2}\alpha_{1,3}\alpha_{4,3}\alpha_{5,1}\alpha_{5,2}\alpha'_{5,2}} \quad \{1,2,3\}$$

$$\mathfrak{p}_2 = \frac{\alpha_{1,5}\alpha_{2,4}\alpha_{3,1}\alpha_{4,1}}{\alpha_{1,2}\alpha_{1,3}\alpha_{4,3}\alpha_{5,2}\alpha'_{5,2}} \quad \{1,3,5\}$$

$$\mathfrak{p}_3 = \frac{\alpha_{1,4}\alpha_{1,5}\alpha_{2,4}\alpha_{3,1}}{\alpha_{1,2}\alpha_{4,3}\alpha_{5,1}\alpha_{5,2}\alpha'_{5,2}} \quad \{1,3,4\}$$

$$\mathfrak{p}_4 = \frac{\alpha_{1,5}\alpha_{2,3}\alpha_{4,1}\alpha_{4,5}\alpha'_{1,4}}{\alpha_{1,2}\alpha_{1,3}\alpha_{4,2}\alpha_{4,3}\alpha_{5,1}\alpha_{5,2}\alpha'_{5,2}} \quad \{1,2,3\}$$

$$\mathfrak{p}_{15} = \frac{\alpha_{2,1}\alpha_{3,1}\alpha_{3,4}\alpha_{4,5}\alpha'_{2,1}}{\alpha_{1,2}\alpha_{1,3}\alpha_{4,2}\alpha_{4,3}\alpha_{5,1}\alpha_{5,2}\alpha'_{5,2}} \quad \{1,2,3\}$$

$$\mathfrak{p}_{16} = \frac{\alpha_{1,4}\alpha_{2,1}\alpha_{3,1}\alpha_{3,4}}{\alpha_{1,2}\alpha_{1,3}\alpha_{4,2}\alpha_{4,3}\alpha_{5,1}\alpha'_{5,2}} \quad \{1,2,3\}$$

$$\mathfrak{p}_{17} = \frac{\alpha_{2,1}\alpha_{2,4}\alpha_{3,1}\alpha_{3,4}\alpha'_{2,1}}{\alpha_{1,2}\alpha_{1,3}\alpha_{4,2}\alpha_{4,3}\alpha_{5,2}\alpha'_{5,2}} \quad \{1,3,5\}$$

$$\mathfrak{p}_{18} = \frac{\alpha_{2,1}\alpha_{2,3}\alpha_{4,1}}{\alpha_{1,2}\alpha_{1,3}\alpha_{4,2}\alpha'_{5,2}} \quad \{1,2,5\}$$

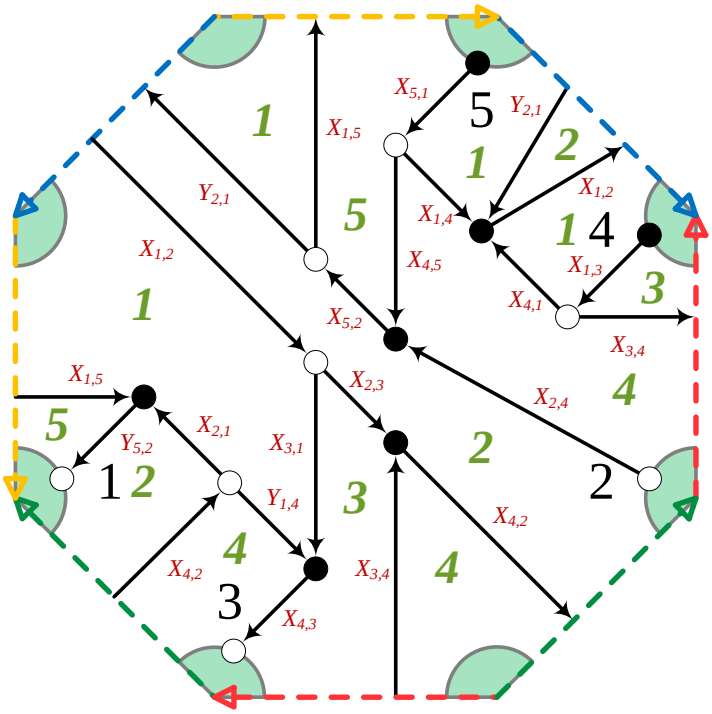

Figure A.1: An on-shell diagram embedded into a genus-2 surface with a single boundary. The unit cell is an octagon. Dashed arrows of the same color are identified respecting their orientation. Faces are labeled in green, external nodes in black and edges in red.

$$
\begin{aligned}
\mathfrak{p}_5 &= \frac{\alpha_{1,5}\alpha_{2,3}\alpha_{2,4}\alpha_{4,1}\alpha'_{1,4}}{\alpha_{1,2}\alpha_{1,3}\alpha_{4,2}\alpha_{4,3}\alpha_{5,2}\alpha'_{5,2}} && \{1,3,5\} & \mathfrak{p}_{19} &= \frac{\alpha_{2,3}\alpha_{4,1}\alpha'_{1,4}}{\alpha_{1,2}\alpha_{1,3}\alpha_{4,2}\alpha_{4,3}} && \{2,3,5\}\\
\mathfrak{p}_6 &= \frac{\alpha_{1,5}\alpha_{4,5}}{\alpha_{5,1}\alpha_{5,2}\alpha'_{5,2}} && \{1,2,4\} & \mathfrak{p}_{20} &= 1 && \{2,4,5\}\\
\mathfrak{p}_7 &= \frac{\alpha_{1,5}\alpha_{2,4}}{\alpha_{5,2}\alpha'_{5,2}} && \{1,4,5\} & \mathfrak{p}_{21} &= \frac{\alpha_{2,1}\alpha_{2,3}\alpha_{4,5}\alpha'_{2,1}}{\alpha_{1,2}\alpha_{4,2}\alpha_{5,1}\alpha_{5,2}\alpha'_{5,2}} && \{1,2,4\}\\
\mathfrak{p}_8 &= \frac{\alpha_{1,5}\alpha_{3,4}\alpha_{4,5}\alpha'_{1,4}}{\alpha_{1,3}\alpha_{4,2}\alpha_{4,3}\alpha_{5,1}\alpha_{5,2}\alpha'_{5,2}} && \{1,2,3\} & \mathfrak{p}_{22} &= \frac{\alpha_{2,3}\alpha_{4,5}\alpha'_{1,4}\alpha'_{2,1}}{\alpha_{1,2}\alpha_{4,2}\alpha_{4,3}\alpha_{5,1}\alpha_{5,2}} && \{2,3,4\}\\
\mathfrak{p}_9 &= \frac{\alpha_{1,4}\alpha_{1,5}\alpha_{2,3}\alpha_{2,4}\alpha'_{1,4}}{\alpha_{1,2}\alpha_{4,2}\alpha_{4,3}\alpha_{5,1}\alpha_{5,2}\alpha'_{5,2}} && \{1,3,4\} & \mathfrak{p}_{23} &= \frac{\alpha_{1,4}\alpha_{2,1}\alpha_{2,3}}{\alpha_{1,2}\alpha_{4,2}\alpha_{5,1}\alpha'_{5,2}} && \{1,2,4\}\\
\mathfrak{p}_{10} &= \frac{\alpha_{1,5}\alpha_{2,4}\alpha_{3,4}\alpha'_{1,4}}{\alpha_{1,3}\alpha_{4,2}\alpha_{4,3}\alpha_{5,2}\alpha'_{5,2}} && \{1,3,5\} & \mathfrak{p}_{24} &= \frac{\alpha_{1,4}\alpha_{2,3}\alpha'_{1,4}}{\alpha_{1,2}\alpha_{4,2}\alpha_{4,3}\alpha_{5,1}} && \{2,3,4\}\\
\mathfrak{p}_{11} &= \frac{\alpha_{3,1}\alpha_{4,1}}{\alpha_{1,2}\alpha_{1,3}\alpha_{4,3}} && \{2,3,5\} & \mathfrak{p}_{25} &= \frac{\alpha_{2,1}\alpha_{3,4}}{\alpha_{1,3}\alpha_{4,2}\alpha'_{5,2}} && \{1,2,5\}\\
\mathfrak{p}_{12} &= \frac{\alpha_{3,1}\alpha_{4,5}\alpha'_{2,1}}{\alpha_{1,2}\alpha_{4,3}\alpha_{5,1}\alpha_{5,2}} && \{2,3,4\} & \mathfrak{p}_{26} &= \frac{\alpha_{2,1}\alpha_{2,3}\alpha_{2,4}\alpha'_{2,1}}{\alpha_{1,2}\alpha_{4,2}\alpha_{5,2}\alpha'_{5,2}} && \{1,4,5\}\\
\mathfrak{p}_{13} &= \frac{\alpha_{1,4}\alpha_{3,1}}{\alpha_{1,2}\alpha_{4,3}\alpha_{5,1}} && \{2,3,4\} & \mathfrak{p}_{27} &= \frac{\alpha_{3,4}\alpha'_{1,4}}{\alpha_{1,3}\alpha_{4,2}\alpha_{4,3}} && \{2,3,5\}\\
\mathfrak{p}_{14} &= \frac{\alpha_{2,4}\alpha_{3,1}\alpha'_{2,1}}{\alpha_{1,2}\alpha_{4,3}\alpha_{5,2}} && \{3,4,5\} & \mathfrak{p}_{28} &= \frac{\alpha_{2,3}\alpha_{2,4}\alpha'_{1,4}\alpha'_{2,1}}{\alpha_{1,2}\alpha_{4,2}\alpha_{4,3}\alpha_{5,2}} && \{3,4,5\}
\end{aligned}
\tag{A.2.1}
$$

Including the $(-1)^{s(i,j)}$ signs, we obtain the following matrix

$$\left(\begin{array}{c|ccccc} & 1 & 2 & 3 & 4 & 5 \\ \hline 2 & \mathfrak{p}_7+\mathfrak{p}_{26} & 1 & \mathfrak{p}_{14}+\mathfrak{p}_{28} & 0 & 0 \\ 4 & -\mathfrak{p}_{18}-\mathfrak{p}_{25} & 0 & \mathfrak{p}_{11}+\mathfrak{p}_{19}+\mathfrak{p}_{27} & 1 & 0 \\ 5 & \mathfrak{p}_6+\mathfrak{p}_{21}+\mathfrak{p}_{23} & 0 & -\mathfrak{p}_{12}-\mathfrak{p}_{13}-\mathfrak{p}_{22}-\mathfrak{p}_{24} & 0 & 1 \end{array}\right). \tag{A.2.2}$$

The minors of this matrix cannot be written as a sum of flows. It is sufficient to determine the combinatorial signs for only those flows appearing in the matrix, which are shown in Figure A.2 along with their respective signs. This then yields

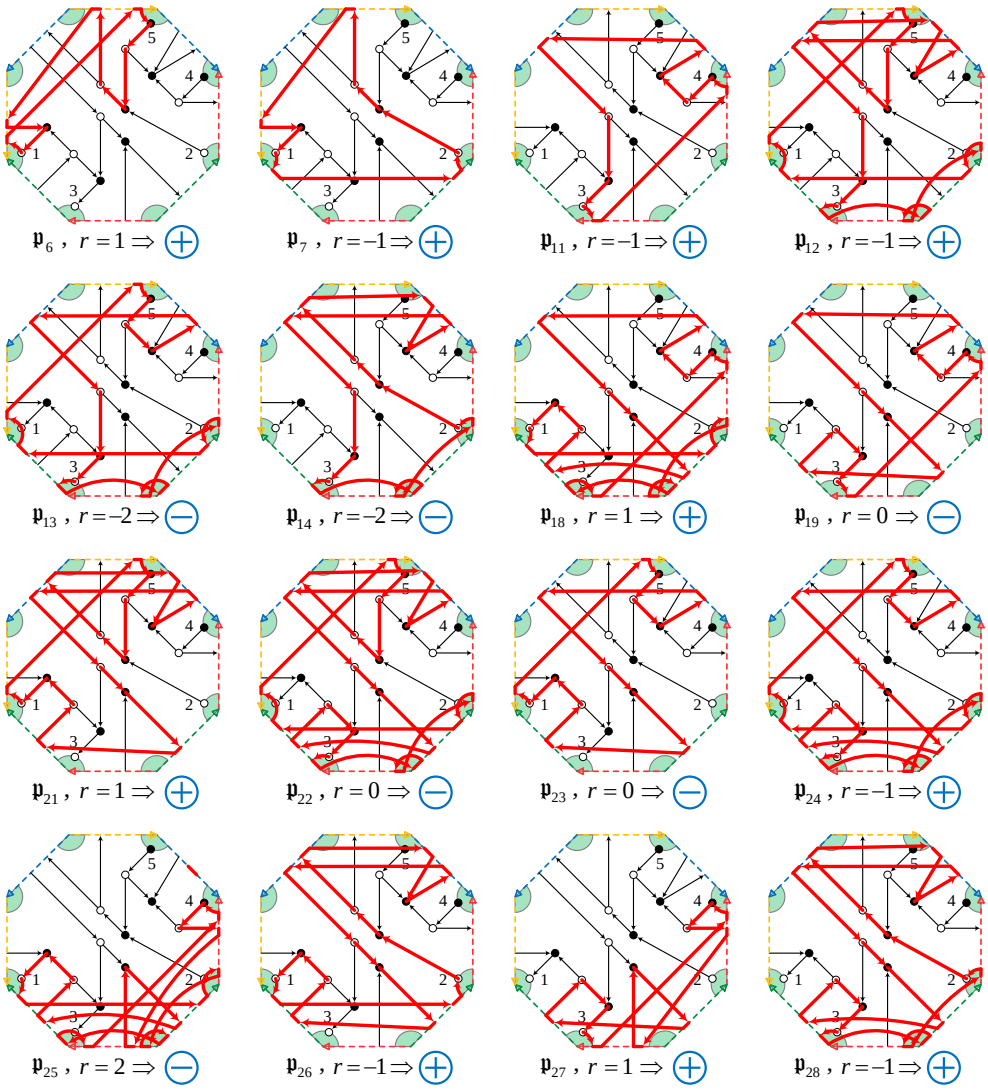

Figure A.2: Flows contributing to (A.2.2) completed to loops within the unit cell, the corresponding rotation numbers and the resulting signs.

the Grassmannian matrix

$$C = \left(\begin{array}{c|ccccc} & 1 & 2 & 3 & 4 & 5 \\ \hline 2 & \mathfrak{p}_7 + \mathfrak{p}_{26} & 1 & -\mathfrak{p}_{14} + \mathfrak{p}_{28} & 0 & 0 \\ 4 & -\mathfrak{p}_{18} + \mathfrak{p}_{25} & 0 & \mathfrak{p}_{11} - \mathfrak{p}_{19} + \mathfrak{p}_{27} & 1 & 0 \\ 5 & \mathfrak{p}_6 + \mathfrak{p}_{21} - \mathfrak{p}_{23} & 0 & -\mathfrak{p}_{12} + \mathfrak{p}_{13} + \mathfrak{p}_{22} - \mathfrak{p}_{24} & 0 & 1 \end{array}\right). \tag{A.2.3}$$

Interestingly, here we observe a new phenomenon, exclusive to higher genus. For genus-0, in the absence of closed loops in the perfect orientation, all flows whose source and sink lie on the same boundary do not pick up any $(-1)^{r+1}$ signs. This is because they do not use cuts to be completed into loops, which in this case are the only possible sources of self-intersections. On the contrary, despite the fact that this example has only one boundary, several flows pick up this type of minus sign. This effect is precisely tuned such that the minors of C are subject to important cancellations that result in the simple expressions

$$\begin{aligned} \Delta_{1,2,3} &= \mathfrak{p}_1 - \mathfrak{p}_4 + \mathfrak{p}_8 + \mathfrak{p}_{15} - \mathfrak{p}_{16} & \Delta_{1,4,5} &= \mathfrak{p}_7 + \mathfrak{p}_{26} \\ \Delta_{1,2,4} &= \mathfrak{p}_6 + \mathfrak{p}_{21} - \mathfrak{p}_{23} & \Delta_{2,3,4} &= \mathfrak{p}_{12} - \mathfrak{p}_{13} - \mathfrak{p}_{22} + \mathfrak{p}_{24} \\ \Delta_{1,2,5} &= \mathfrak{p}_{18} - \mathfrak{p}_{25} & \Delta_{2,3,5} &= \mathfrak{p}_{11} - \mathfrak{p}_{19} + \mathfrak{p}_{27} \\ \Delta_{1,3,4} &= \mathfrak{p}_9 - \mathfrak{p}_3 & \Delta_{2,4,5} &= 1 \\ \Delta_{1,3,5} &= \mathfrak{p}_2 - \mathfrak{p}_5 + \mathfrak{p}_{10} + \mathfrak{p}_{17} & \Delta_{3,4,5} &= \mathfrak{p}_{28} - \mathfrak{p}_{14} \end{aligned} \tag{A.2.4}$$

We would like to stress how non-trivial this example is. Not only were we required to introduce signs for paths that start and end on the same boundary, but the signs in (A.2.3) seem not to have any particular pattern, yet they magically produce the cancellations required to obtain (A.2.4). Based on the examples presented, it is reasonable to conjecture that we have identified the full set of rules for constructing the boundary measurement for on-shell diagrams embedded on surfaces with arbitrary number of boundaries and genus. It would be interesting to confirm that this is the case and to find a formal derivation of our proposal.

A.3 Matroid Stratification from Multiple Graphs

As already explained in §4.5.2, the combinatorial decomposition yields a subset of the matroid stratification: only certain strata appear in the decomposition. It is

then natural to ask whether it is possible to extend it such that it produces the full matroid stratification. This leads us to the following reasonable conjecture:

- **Conjecture:** The full matroid stratification can be obtained by *simultaneously* considering the combinatorial decomposition of *multiple* bipartite graphs associated to Grassmannian elements with a maximal number of degrees of freedom. Some of these graphs are non-planar. The matroid stratification is given by the union of the resulting strata.

This proposal follows from the definition of the matroid stratification in §4.1.5. Analogously to the positroid stratification, where we take the common refinement of n *cyclically permuted* Schubert cells, hence n cyclic permutations, the matroid stratification is in general the refinement over *all* $n!$ permutations. Here we remind the reader that every permutation specifies a lexicographic order that characterizes the Schubert cell, analogously to §4.1.3. The distribution of external nodes over boundaries gives rise, following the discussion in §4.3.3, to different orderings, which we map to these permutations.

In essence, to access all the permutations and hence all the matroids, we have to consider permutations which cannot be obtained by cyclic rotations of $1, 2, \ldots, n$, which are the only ones that can be realized on planar graphs. The other permutations can be obtained only by introducing new boundaries, thus making the graphs non-planar.

To illustrate this idea, let us consider the decomposition of the diagram in Figure 4.2(b) which, after introducing an additional boundary and the corresponding cut, is the same as the square box but with ordering 1243. The decomposition is obtained through the procedure explained in §4.5 and is shown in Figure A.3, where the matroid label is given in dark green and the positroid label is in light green. The matroid labels are identical to those of Figure 4.8, but with 3 and 4 interchanged. The fact that we no longer have the positroid stratification is confirmed by the fact that the positroid stratum $\{C \in G(2,4) \mid \Delta_{12} \neq 0, \Delta_{23} \neq 0, \Delta_{34} \neq 0, \Delta_{14} \neq 0\}$ has multiple representatives, and some positroid strata are missing, e.g. $\{C \in G(2,4) \mid \Delta_{12} \neq 0, \Delta_{24} \neq 0, \Delta_{34} \neq 0, \Delta_{14} \neq 0\}$. However, we note that the decomposition just obtained is precisely the same as that of §4.1.4 but where each component is the

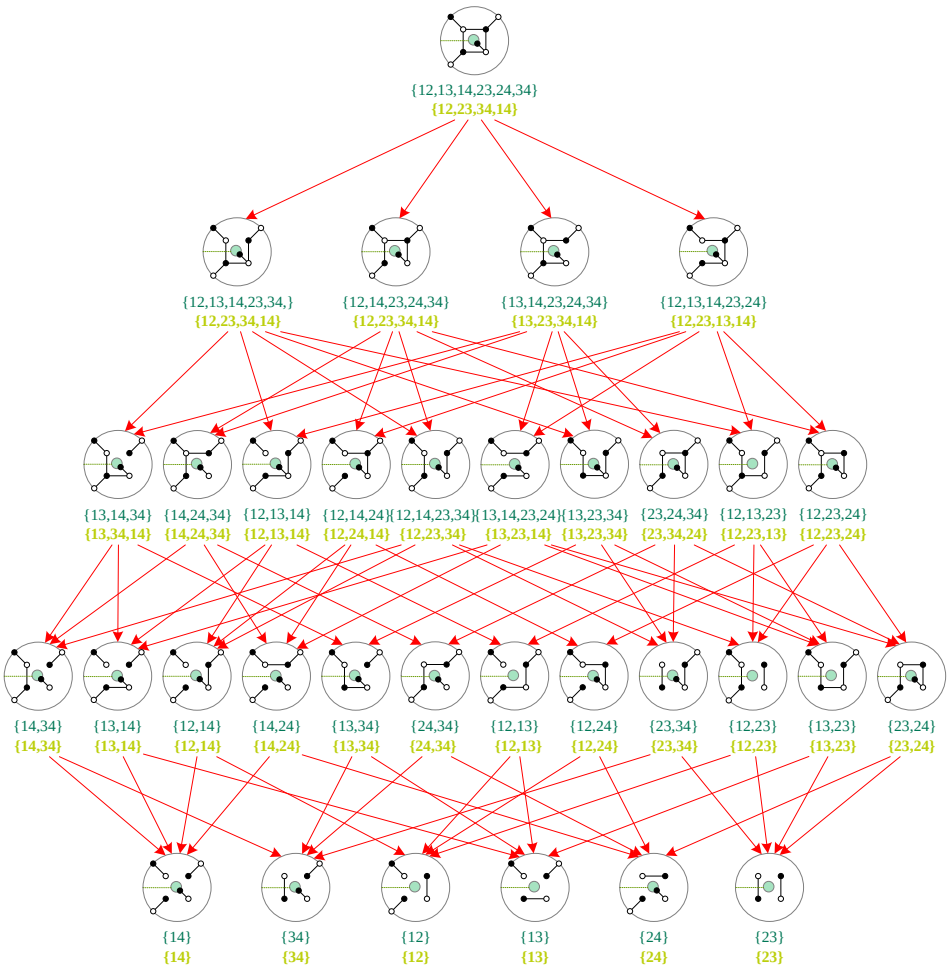

Figure A.3: Decomposition of the square box with flipped legs and two boundaries. It corresponds to the permutation 1243. The dark green label indicates the matroid stratum corresponding to the graph, the light green label indicates the positroid stratum.

simultaneous refinement of 4 cyclically permuted Schubert cells with respect to the lexicographic order specified by the permutation 1243.

In the decomposition of the non-planar graph, the matroid strata that were missing from the decomposition of the planar case with ordering 1234, as described in §4.5.2, are now present. Hence we conclude that the union of the matroid strata of the decomposition in Figure 4.8 and Figure A.3 gives the entire matroid stratification, at least at the combinatorial level. We provide in Figure A.4 a depiction

of how the two decompositions together form the entire matroid stratification. The matroid strata are marked by a green circle, where the matroid labels have been included underneath.

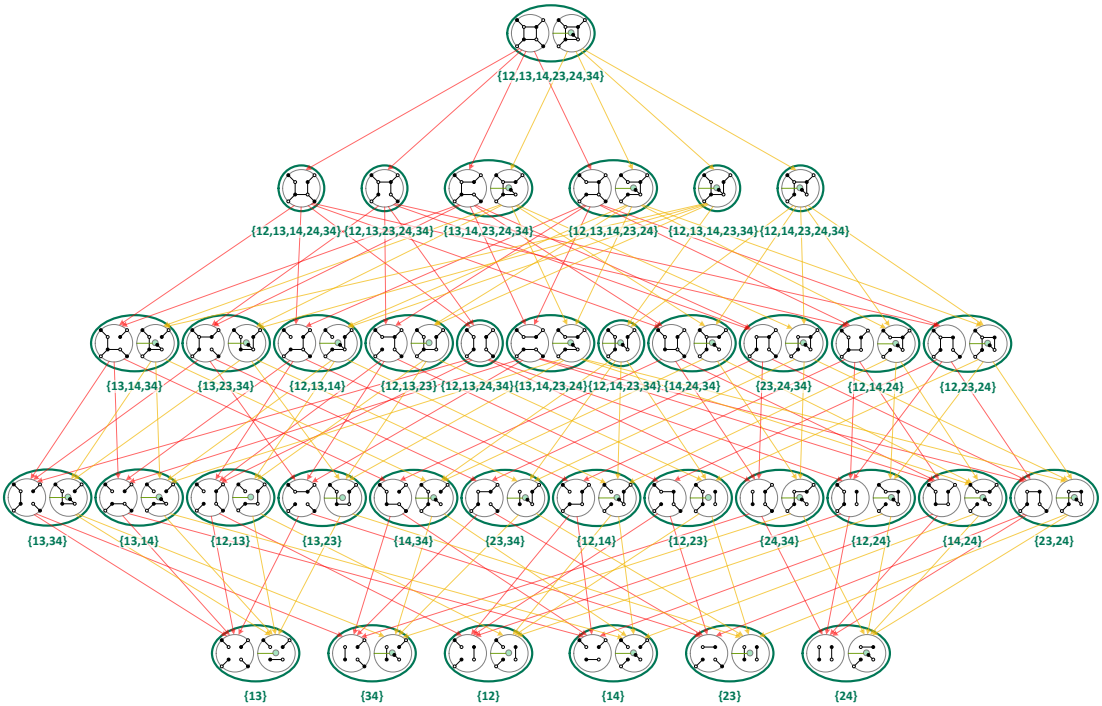

Figure A.4: Matroid stratification of $G(2,4)$ via a pair of graphs, both planar and non-planar. Matroid strata are indicated by green circles. Red and yellow arrows belong to the combinatorial decompositions of the planar and non-planar graphs, respectively.

Generally, including all $n!$ permutations of external edges modulo cyclicity will include all matroid strata, but in practice it can be sufficient to consider fewer permutations.

Let us explain why this is the case and show how to determine the diagrams required for the matroid stratification in the case of $G(2,4)$, whose matroid contains the 6 bases 12, 13, 14, 23, 24 and 34. We begin by only discussing the problem in terms of permutations and lexicographic orders, and explain how the graphs fit into this picture at a secondary stage.

Each permutation of $1, 2, 3, 4$ specifies a lexicographic order, to which we can associate a Schubert cell analogously to the definition in §4.1.3. The positroid stratification uses n permutations, related to each other by cyclic shifts, and the corresponding Schubert cells, and is then specified by n entries. To put a label in each entry, we select the lexicographically minimal non-zero element with respect to the permutation in question. For example, the permutation 2413 will select the matroid element (24), if present, otherwise select (21), if present, etc.

The matroid stratification generally uses $n!$ permutations. However, in order to find all the strata, it is sufficient to refine over the set of Schubert cells such that for each base there exists a Schubert cell whose lexicographic order has that base as minimal element. Thus, to specify all matroids in the example at hand, we will need 6 permutations, each permutation having a different lexicographically minimal order of the form:

$$12XX, \quad 13XX, \quad 14XX, \quad 23XX, \quad 24XX, \quad 34XX, \tag{A.3.1}$$

where XX may be any order of the remaining two digits, e.g. it does not matter whether we choose 1342 or 1324. For example, the first lexicographic order will always find the matroid base 12, regardless of the presence or absence of other bases; the second one will always find 13 regardless of the other matroid bases, and so on. Strictly speaking the order of the first two digits is also irrelevant, since either order specifies the same matroid element. In this way, each matroid base, if present, will appear in one of the six entries associated to the different lexicographic orders. A set of 6 permutations as in (A.3.1) is sufficient for labeling all matroids with the correct matroid labels.

Graphs fit into this picture as follows. Each graph specifies an ordering, dictated by the arrangement of the external edges. Because of cyclicity of the starting point, the graph actually specifies n orderings, related to each other by cyclic shifts. In this example, the planar graph has the ordering 1234, which specifies the permutations

$$1234, \quad 2341, \quad 3412, \quad 4123, \tag{A.3.2}$$

which simply differ in which edge of the graph we call "1". We see that such a graph contains 4 of the required lexicographic orders.[1] We are however still missing a permutation of the form $13XX$ and one of the form $24XX$. If we introduce a second graph with the ordering 1243, we obtain the permutations

$$1243, \quad 2431, \quad 4312, \quad 3124, \tag{A.3.3}$$

which contain the lexicographic orders given by 3124 and 2431 as desired, and two more which were already covered by the previous graph. Thus, we see that the two graphs with ordering 1234 and 1243 are sufficient to cover all lexicographic orders and corresponding Schubert cells which are required to specify the matroids. We then argue that their decomposition will cover the combinatoric structure of the entire matroid stratification.

As a check at the first level, we indeed see that the decomposition of the two diagrams does indeed overlap in the matroids obtained by removing 12 or removing 34, which are precisely the lexicographically minimal sets of those permutations which in the arguments above were covered by both orders 1234 and 1243, and by 3412 and 4312, respectively. Likewise, at the first level the decompositions do not overlap precisely on the matroid labels which are lexicographically minimal to those permutations which do not overlap for the two orderings. This is also true at the second level, where $\{12, 13, 24, 34\}$ is missing 14 and 23, which are precisely those which are not lexicographically minimal of any permutation in equation (A.3.3). Also, $\{12, 14, 23, 34\}$ is missing 13 and 24, which are precisely those which are not lexicographically minimal of any permutation in equation (A.3.2).

It is reasonable to expect that it might be possible to find which graphs are necessary to cover the entire matroid stratification by simply listing the set of all possible matroid elements, a set of permutations for which these elements are the lexicographically minimal subsets, and finding graphs whose ordering can achieve these permutations. We leave a detailed study of this interesting possibility for future investigation.

[1] We again remind the reader that it does not matter whether it is 4123 or 1423: either way the lexicographically minimal element will be the one corresponding to the Plücker coordinate Δ_{14}.

Appendix B

Appendices to Chapter 5: "Anatomy of the Amplituhedron"

B.1 Geometric Versus Integrand Stratification: Explicit Examples

In §5.7.1 we obtained the mini stratification of $G_+(0,4;2)$ using the integrand. We have explicitly verified the one-to-one agreement of all boundaries obtained with the stratifications based on the integrand and the amplituhedron. In this appendix we collect several explicit examples of this precise match for illustration purposes. They have been chosen to provide a good representation of all qualitatively different cases that arise.

Strictly speaking, the language used in this study is the one of labels, i.e. the mini stratification. As explained in §5.2.3, labels really correspond to classes of boundaries. In particular, for every label in which the 4×4 minor vanishes, there can be multiple boundaries, i.e. different integrands. Furthermore, these boundaries in general have different dimensions. For these cases, the table below provides the integrand corresponding to the maximal vanishing of the 4×4 minor. As in the mini stratification, we list this configuration at the highest dimension at which the 4×4 vanishes. All other integrands corresponding to the same labels can be easily constructed.

Dimension 8. There is only one 8-dimensional boundary, which is the top dimensional one. It is the integrand (5.7.1), where the lines AB and CD are completely free. In the table below, we compare the integrand and geometric methods. The same format will be used for all other examples. The first two rows show the integrand and the restrictions on the lines. The comparison with our other method is seen in the last two rows, where we specify the set of Plücker coordinates and hyper perfect matchings present. The hyper perfect matchings contributing to the 4×4 minor $\langle ABCD\rangle$ are highlighted in color, with the ones contributing positively (P_{23}, P_{32}, P_{45}, P_{54}) in blue and the ones contributing negatively (P_{16}, P_{61}) in red. Notice that $\langle ABCD\rangle$ can vanish while some of them are present due to cancellations. However, if none of these perfect matchings are present, $\langle ABCD\rangle$ is forced to automatically vanish.

Integrand	$\frac{\langle AB34\rangle\langle CD12\rangle+\langle AB23\rangle\langle CD14\rangle+\langle AB14\rangle\langle CD23\rangle+\langle AB12\rangle\langle CD34\rangle}{\langle ABCD\rangle\langle AB12\rangle\langle AB14\rangle\langle AB23\rangle\langle AB34\rangle\langle CD12\rangle\langle CD14\rangle\langle CD23\rangle\langle CD34\rangle}$
Constraints on AB and CD	Free
Plücker coordinates turned on	$\Delta^{(1,2)}_{1234}, \Delta^{(1)}_{12}, \Delta^{(1)}_{13}, \Delta^{(1)}_{14}, \Delta^{(1)}_{23}, \Delta^{(1)}_{24}, \Delta^{(1)}_{34}$, $\Delta^{(2)}_{12}, \Delta^{(2)}_{13}, \Delta^{(2)}_{14}, \Delta^{(2)}_{23}, \Delta^{(2)}_{24}, \Delta^{(2)}_{34}$
Hyper perfect matchings present	$P_{1,1}, P_{1,2}, P_{1,3}, P_{1,4}, P_{1,5}, \mathbf{P_{1,6}}, P_{2,1}, P_{2,2}, \mathbf{P_{2,3}}, P_{2,4}$, $P_{2,5}, P_{2,6}, P_{3,1}, \mathbf{P_{3,2}}, P_{3,3}, P_{3,4}, P_{3,5}, P_{3,6}, P_{4,1}, P_{4,2}$, $P_{4,3}, P_{4,4}, \mathbf{P_{4,5}}, P_{4,6}, P_{5,1}, P_{5,2}, P_{5,3}, \mathbf{P_{5,4}}, P_{5,5}, P_{5,6}$, $\mathbf{P_{6,1}}, P_{6,2}, P_{6,3}, P_{6,4}, P_{6,5}, P_{6,6}$

Dimension 7. There are 9 integrands corresponding to 7-dimensional boundaries. We present all of them below.

$\frac{\langle AB34\rangle\langle CD12\rangle+\langle AB23\rangle\langle CD14\rangle+\langle AB14\rangle\langle CD23\rangle+\langle AB12\rangle\langle CD34\rangle}{\langle AB12\rangle\langle AB14\rangle\langle AB23\rangle\langle AB34\rangle\langle CD12\rangle\langle CD14\rangle\langle CD23\rangle\langle CD34\rangle}$	$\frac{\langle AB34\rangle\langle CD12\rangle+\langle AB23\rangle\langle CD14\rangle+\langle AB14\rangle\langle CD23\rangle}{\langle ABCD\rangle\langle AB14\rangle\langle AB23\rangle\langle AB34\rangle\langle CD12\rangle\langle CD14\rangle\langle CD23\rangle\langle CD34\rangle}$
$\langle ABCD\rangle \to 0$	$\langle AB12\rangle \to 0$
$\Delta^{(1)}_{12}, \Delta^{(1)}_{13}, \Delta^{(1)}_{14}, \Delta^{(1)}_{23}, \Delta^{(1)}_{24}, \Delta^{(1)}_{34}$, $\Delta^{(2)}_{12}, \Delta^{(2)}_{13}, \Delta^{(2)}_{14}, \Delta^{(2)}_{23}, \Delta^{(2)}_{24}, \Delta^{(2)}_{34}$	$\Delta^{(1,2)}_{1234}, \Delta^{(1)}_{12}, \Delta^{(1)}_{13}, \Delta^{(1)}_{14}, \Delta^{(1)}_{23}, \Delta^{(1)}_{24}$, $\Delta^{(2)}_{12}, \Delta^{(2)}_{13}, \Delta^{(2)}_{14}, \Delta^{(2)}_{23}, \Delta^{(2)}_{24}, \Delta^{(2)}_{34}$
$P_{1,1}, P_{1,2}, P_{1,3}, P_{1,4}, P_{1,5}, \mathbf{P_{1,6}}, P_{2,1}, P_{2,2}, \mathbf{P_{2,3}}, P_{2,4}$, $P_{2,5}, P_{2,6}, P_{3,1}, \mathbf{P_{3,2}}, P_{3,3}, P_{3,4}, P_{3,5}, P_{3,6}, P_{4,1}, P_{4,2}$, $P_{4,3}, P_{4,4}, \mathbf{P_{4,5}}, P_{4,6}, P_{5,1}, P_{5,2}, P_{5,3}, \mathbf{P_{5,4}}, P_{5,5}, P_{5,6}$, $\mathbf{P_{6,1}}, P_{6,2}, P_{6,3}, P_{6,4}, P_{6,5}, P_{6,6}$	$P_{1,1}, P_{1,2}, P_{1,3}, P_{1,4}, P_{1,5}, \mathbf{P_{1,6}}, P_{3,1}, \mathbf{P_{3,2}}, P_{3,3}, P_{3,4}$, $P_{3,5}, P_{3,6}, P_{4,1}, P_{4,2}, P_{4,3}, P_{4,4}, \mathbf{P_{4,5}}, P_{4,6}, P_{5,1}, P_{5,2}$, $P_{5,3}, \mathbf{P_{5,4}}, P_{5,5}, P_{5,6}, \mathbf{P_{6,1}}, P_{6,2}, P_{6,3}, P_{6,4}, P_{6,5}, P_{6,6}$

$\frac{\langle AB34\rangle\langle CD12\rangle+\langle AB23\rangle\langle CD14\rangle+\langle AB12\rangle\langle CD34\rangle}{\langle ABCD\rangle\langle AB12\rangle\langle AB23\rangle\langle AB34\rangle\langle CD12\rangle\langle CD14\rangle\langle CD23\rangle\langle CD34\rangle}$	$\frac{\langle AB34\rangle\langle CD12\rangle+\langle AB14\rangle\langle CD23\rangle+\langle AB12\rangle\langle CD34\rangle}{\langle ABCD\rangle\langle AB12\rangle\langle AB14\rangle\langle AB34\rangle\langle CD12\rangle\langle CD14\rangle\langle CD23\rangle\langle CD34\rangle}$
$\langle AB14\rangle \to 0$	$\langle AB23\rangle \to 0$
$\Delta^{(1,2)}_{1234}, \Delta^{(1)}_{12}, \Delta^{(1)}_{13}, \Delta^{(1)}_{14}, \Delta^{(1)}_{24}, \Delta^{(1)}_{34}, \Delta^{(2)}_{12}, \Delta^{(2)}_{13}, \Delta^{(2)}_{14}, \Delta^{(2)}_{23}, \Delta^{(2)}_{24}, \Delta^{(2)}_{34}$	$\Delta^{(1,2)}_{1234}, \Delta^{(1)}_{12}, \Delta^{(1)}_{13}, \Delta^{(1)}_{23}, \Delta^{(1)}_{24}, \Delta^{(1)}_{34}, \Delta^{(2)}_{12}, \Delta^{(2)}_{13}, \Delta^{(2)}_{14}, \Delta^{(2)}_{23}, \Delta^{(2)}_{24}, \Delta^{(2)}_{34}$
$P_{1,1}, P_{1,2}, P_{1,3}, P_{1,4}, P_{1,5}, \mathbf{P_{1,6}}, P_{2,1}, P_{2,2}, \mathbf{P_{2,3}}, P_{2,4}, P_{2,5}, P_{2,6}, P_{3,1}, \mathbf{P_{3,2}}, P_{3,3}, P_{3,4}, P_{3,5}, P_{3,6}, P_{4,1}, P_{4,2}, P_{4,3}, P_{4,4}, \mathbf{P_{4,5}}, P_{4,6}, \mathbf{P_{6,1}}, P_{6,2}, P_{6,3}, P_{6,4}, P_{6,5}, P_{6,6}$	$P_{1,1}, P_{1,2}, P_{1,3}, P_{1,4}, P_{1,5}, \mathbf{P_{1,6}}, P_{2,1}, P_{2,2}, \mathbf{P_{2,3}}, P_{2,4}, P_{2,5}, P_{2,6}, P_{3,1}, \mathbf{P_{3,2}}, P_{3,3}, P_{3,4}, P_{3,5}, P_{3,6}, P_{5,1}, P_{5,2}, P_{5,3}, \mathbf{P_{5,4}}, P_{5,5}, P_{5,6}, \mathbf{P_{6,1}}, P_{6,2}, P_{6,3}, P_{6,4}, P_{6,5}, P_{6,6}$

$\frac{\langle AB23\rangle\langle CD14\rangle+\langle AB14\rangle\langle CD23\rangle+\langle AB12\rangle\langle CD34\rangle}{\langle ABCD\rangle\langle AB12\rangle\langle AB14\rangle\langle AB23\rangle\langle CD12\rangle\langle CD14\rangle\langle CD23\rangle\langle CD34\rangle}$	$\frac{\langle AB23\rangle\langle CD14\rangle+\langle AB14\rangle\langle CD23\rangle+\langle AB12\rangle\langle CD34\rangle}{\langle ABCD\rangle\langle AB12\rangle\langle AB14\rangle\langle AB23\rangle\langle AB34\rangle\langle CD14\rangle\langle CD23\rangle\langle CD34\rangle}$
$\langle AB34\rangle \to 0$	$\langle CD12\rangle \to 0$
$\Delta^{(1,2)}_{1234}, \Delta^{(1)}_{12}, \Delta^{(1)}_{13}, \Delta^{(1)}_{14}, \Delta^{(1)}_{23}, \Delta^{(1)}_{24}, \Delta^{(1)}_{34}, \Delta^{(2)}_{12}, \Delta^{(2)}_{13}, \Delta^{(2)}_{14}, \Delta^{(2)}_{23}, \Delta^{(2)}_{24}, \Delta^{(2)}_{34}$	$\Delta^{(1,2)}_{1234}, \Delta^{(1)}_{12}, \Delta^{(1)}_{13}, \Delta^{(1)}_{14}, \Delta^{(1)}_{23}, \Delta^{(1)}_{24}, \Delta^{(1)}_{34}, \Delta^{(2)}_{12}, \Delta^{(2)}_{13}, \Delta^{(2)}_{14}, \Delta^{(2)}_{23}, \Delta^{(2)}_{24}$
$P_{1,1}, P_{1,2}, P_{1,3}, P_{1,4}, P_{1,5}, \mathbf{P_{1,6}}, P_{2,1}, P_{2,2}, \mathbf{P_{2,3}}, P_{2,4}, P_{2,5}, P_{2,6}, P_{4,1}, P_{4,2}, P_{4,3}, P_{4,4}, \mathbf{P_{4,5}}, P_{4,6}, P_{5,1}, P_{5,2}, P_{5,3}, \mathbf{P_{5,4}}, P_{5,5}, P_{5,6}, \mathbf{P_{6,1}}, P_{6,2}, P_{6,3}, P_{6,4}, P_{6,5}, P_{6,6}$	$P_{1,1}, P_{1,3}, P_{1,4}, P_{1,5}, \mathbf{P_{1,6}}, P_{2,1}, \mathbf{P_{2,3}}, P_{2,4}, P_{2,5}, P_{2,6}, P_{3,1}, P_{3,3}, P_{3,4}, P_{3,5}, P_{3,6}, P_{4,1}, P_{4,3}, P_{4,4}, \mathbf{P_{4,5}}, P_{4,6}, P_{5,1}, P_{5,3}, \mathbf{P_{5,4}}, P_{5,5}, P_{5,6}, \mathbf{P_{6,1}}, P_{6,3}, P_{6,4}, P_{6,5}, P_{6,6}$

$\frac{\langle AB34\rangle\langle CD12\rangle+\langle AB14\rangle\langle CD23\rangle+\langle AB12\rangle\langle CD34\rangle}{\langle ABCD\rangle\langle AB12\rangle\langle AB14\rangle\langle AB23\rangle\langle AB34\rangle\langle CD12\rangle\langle CD23\rangle\langle CD34\rangle}$	$\frac{\langle AB34\rangle\langle CD12\rangle+\langle AB23\rangle\langle CD14\rangle+\langle AB12\rangle\langle CD34\rangle}{\langle ABCD\rangle\langle AB12\rangle\langle AB14\rangle\langle AB23\rangle\langle AB34\rangle\langle CD12\rangle\langle CD14\rangle\langle CD34\rangle}$
$\langle CD14\rangle \to 0$	$\langle CD23\rangle \to 0$
$\Delta^{(1,2)}_{1234}, \Delta^{(1)}_{12}, \Delta^{(1)}_{13}, \Delta^{(1)}_{14}, \Delta^{(1)}_{23}, \Delta^{(1)}_{24}, \Delta^{(1)}_{34}, \Delta^{(2)}_{12}, \Delta^{(2)}_{13}, \Delta^{(2)}_{14}, \Delta^{(2)}_{24}, \Delta^{(2)}_{34}$	$\Delta^{(1,2)}_{1234}, \Delta^{(1)}_{12}, \Delta^{(1)}_{13}, \Delta^{(1)}_{14}, \Delta^{(1)}_{23}, \Delta^{(1)}_{24}, \Delta^{(1)}_{34}, \Delta^{(2)}_{12}, \Delta^{(2)}_{13}, \Delta^{(2)}_{23}, \Delta^{(2)}_{24}, \Delta^{(2)}_{34}$
$P_{1,1}, P_{1,2}, P_{1,3}, P_{1,4}, \mathbf{P_{1,6}}, P_{2,1}, P_{2,2}, \mathbf{P_{2,3}}, P_{2,4}, P_{2,6}, P_{3,1}, \mathbf{P_{3,2}}, P_{3,3}, P_{3,4}, P_{3,6}, P_{4,1}, P_{4,2}, P_{4,3}, P_{4,4}, P_{4,6}, P_{5,1}, P_{5,2}, P_{5,3}, \mathbf{P_{5,4}}, P_{5,6}, \mathbf{P_{6,1}}, P_{6,2}, P_{6,3}, P_{6,4}, P_{6,6}$	$P_{1,1}, P_{1,2}, P_{1,3}, P_{1,5}, \mathbf{P_{1,6}}, P_{2,1}, P_{2,2}, \mathbf{P_{2,3}}, P_{2,5}, P_{2,6}, P_{3,1}, \mathbf{P_{3,2}}, P_{3,3}, P_{3,5}, P_{3,6}, P_{4,1}, P_{4,2}, P_{4,3}, \mathbf{P_{4,5}}, P_{4,6}, P_{5,1}, P_{5,2}, P_{5,3}, P_{5,5}, P_{5,6}, \mathbf{P_{6,1}}, P_{6,2}, P_{6,3}, P_{6,5}, P_{6,6}$

$\frac{\langle AB34\rangle\langle CD12\rangle+\langle AB23\rangle\langle CD14\rangle+\langle AB14\rangle\langle CD23\rangle}{\langle ABCD\rangle\langle AB12\rangle\langle AB14\rangle\langle AB23\rangle\langle AB34\rangle\langle CD12\rangle\langle CD14\rangle\langle CD23\rangle}$
$\langle CD34\rangle \to 0$
$\Delta^{(1,2)}_{1234}, \Delta^{(1)}_{12}, \Delta^{(1)}_{13}, \Delta^{(1)}_{14}, \Delta^{(1)}_{23}, \Delta^{(1)}_{24}, \Delta^{(1)}_{34}, \Delta^{(2)}_{13}, \Delta^{(2)}_{14}, \Delta^{(2)}_{23}, \Delta^{(2)}_{24}, \Delta^{(2)}_{34}$
$P_{1,1}, P_{1,2}, P_{1,4}, P_{1,5}, \mathbf{P_{1,6}}, P_{2,1}, P_{2,2}, P_{2,4}, P_{2,5}, P_{2,6}, P_{3,1}, \mathbf{P_{3,2}}, P_{3,4}, P_{3,5}, P_{3,6}, P_{4,1}, P_{4,2}, P_{4,4}, \mathbf{P_{4,5}}, P_{4,6}, P_{5,1}, P_{5,2}, \mathbf{P_{5,4}}, P_{5,5}, P_{5,6}, \mathbf{P_{6,1}}, P_{6,2}, P_{6,4}, P_{6,5}, P_{6,6}$

Dimension 6. There are 44 integrands corresponding to 6-dimensional boundaries. We present some examples below.

$\frac{\langle AB34\rangle\langle CD12\rangle+\langle AB23\rangle\langle CD14\rangle+\langle AB14\rangle\langle CD23\rangle}{\langle AB14\rangle\langle AB23\rangle\langle AB34\rangle\langle CD12\rangle\langle CD14\rangle\langle CD23\rangle\langle CD34\rangle}$	$\frac{\langle AB23\rangle\langle CD14\rangle+\langle AB14\rangle\langle CD23\rangle}{\langle AB14\rangle\langle AB23\rangle\langle ABCD\rangle\langle CD12\rangle\langle CD14\rangle\langle CD23\rangle\langle CD34\rangle}$
$\langle ABCD\rangle \to 0, \langle AB12\rangle \to 0$	$\langle AB12\rangle \to 0, \langle AB34\rangle \to 0$
$\Delta^{(1)}_{12}, \Delta^{(1)}_{13}, \Delta^{(1)}_{14}, \Delta^{(1)}_{23}, \Delta^{(1)}_{24}, \Delta^{(2)}_{12}, \Delta^{(2)}_{13}, \Delta^{(2)}_{14}, \Delta^{(2)}_{23}, \Delta^{(2)}_{24}, \Delta^{(2)}_{34}$	$\Delta^{(1,2)}_{1234}, \Delta^{(1)}_{13}, \Delta^{(1)}_{14}, \Delta^{(1)}_{23}, \Delta^{(1)}_{24}, \Delta^{(2)}_{12}, \Delta^{(2)}_{13}, \Delta^{(2)}_{14}, \Delta^{(2)}_{23}, \Delta^{(2)}_{24}, \Delta^{(2)}_{34}$
$P_{1,1}, P_{1,2}, P_{1,3}, P_{1,4}, P_{1,5}, \mathbf{P_{1,6}}, P_{3,1}, \mathbf{P_{3,2}}, P_{3,3}, P_{3,4}, P_{3,5}, P_{3,6}, P_{4,1}, P_{4,2}, P_{4,3}, P_{4,4}, \mathbf{P_{4,5}}, P_{4,6}, P_{5,1}, P_{5,2}, P_{5,3}, \mathbf{P_{5,4}}, P_{5,5}, P_{5,6}, \mathbf{P_{6,1}}, P_{6,2}, P_{6,3}, P_{6,4}, P_{6,5}, P_{6,6}$	$P_{1,1}, P_{1,2}, P_{1,3}, P_{1,4}, P_{1,5}, \mathbf{P_{1,6}}, P_{4,1}, P_{4,2}, P_{4,3}, P_{4,4}, \mathbf{P_{4,5}}, P_{4,6}, P_{5,1}, P_{5,2}, P_{5,3}, \mathbf{P_{5,4}}, P_{5,5}, P_{5,6}, \mathbf{P_{6,1}}, P_{6,2}, P_{6,3}, P_{6,4}, P_{6,5}, P_{6,6}$

$\frac{\langle AB23\rangle\langle CD14\rangle+\langle AB14\rangle\langle CD23\rangle}{\langle AB14\rangle\langle AB23\rangle\langle AB34\rangle\langle ABCD\rangle\langle CD14\rangle\langle CD23\rangle\langle CD34\rangle}$	$\frac{\langle AB14\rangle\langle CD23\rangle+\langle AB23\rangle\langle CD14\rangle+\langle AB34\rangle\langle CD12\rangle}{\langle AB14\rangle\langle AB23\rangle\langle AB34\rangle\langle ABCD\rangle\langle CD12\rangle\langle CD14\rangle\langle CD23\rangle}$
$\langle AB12\rangle \to 0, \langle CD12\rangle \to 0$	$\langle AB12\rangle \to 0, \langle CD34\rangle \to 0$
$\Delta^{(1,2)}_{1234}, \Delta^{(1)}_{12}, \Delta^{(1)}_{13}, \Delta^{(1)}_{14}, \Delta^{(1)}_{23}, \Delta^{(1)}_{24}$ $\Delta^{(2)}_{12}, \Delta^{(2)}_{13}, \Delta^{(2)}_{14}, \Delta^{(2)}_{23}, \Delta^{(2)}_{24}$	$\Delta^{(1,2)}_{1234}, \Delta^{(1)}_{12}, \Delta^{(1)}_{13}, \Delta^{(1)}_{14}, \Delta^{(1)}_{23}, \Delta^{(1)}_{24}$ $\Delta^{(2)}_{13}, \Delta^{(2)}_{14}, \Delta^{(2)}_{23}, \Delta^{(2)}_{24}, \Delta^{(2)}_{34}$
$P_{1,1}, P_{1,3}, P_{1,4}, P_{1,5}, \mathbf{P_{1,6}}, P_{3,1}, P_{3,3}, P_{3,4}, P_{3,5}, P_{3,6},$ $P_{4,1}, P_{4,3}, P_{4,4}, \mathbf{P_{4,5}}, P_{4,6}, P_{5,1}, P_{5,3}, \mathbf{P_{5,4}}, P_{5,5}, P_{5,6},$ $\mathbf{P_{6,1}}, P_{6,3}, P_{6,4}, P_{6,5}, P_{6,6}$	$P_{1,1}, P_{1,2}, P_{1,4}, P_{1,5}, \mathbf{P_{1,6}}, P_{3,1}, \mathbf{P_{3,2}}, P_{3,4}, P_{3,5}, P_{3,6},$ $P_{4,1}, P_{4,2}, P_{4,4}, \mathbf{P_{4,5}}, P_{4,6}, P_{5,1}, P_{5,2}, \mathbf{P_{5,4}}, P_{5,5}, P_{5,6},$ $\mathbf{P_{6,1}}, P_{6,2}, P_{6,4}, P_{6,5}, P_{6,6}$

$\frac{\langle AB34\rangle\langle CD12\rangle+\langle AB23\rangle\langle CD14\rangle}{\langle AB23\rangle\langle AB34\rangle\langle ABCD\rangle\langle CD12\rangle\langle CD14\rangle\langle CD23\rangle\langle CD34\rangle}$
$\langle AB12\rangle \to 0, \langle AB13\rangle \to 0, \langle AB14\rangle \to 0$
$\Delta^{(1,2)}_{1234}, \Delta^{(1)}_{12}, \Delta^{(1)}_{13}, \Delta^{(1)}_{14}, \Delta^{(2)}_{12}, \Delta^{(2)}_{13}, \Delta^{(2)}_{14}, \Delta^{(2)}_{23}, \Delta^{(2)}_{24}, \Delta^{(2)}_{34}$
$P_{1,1}, P_{1,2}, P_{1,3}, P_{1,4}, P_{1,5}, \mathbf{P_{1,6}}, P_{3,1}, \mathbf{P_{3,2}}, P_{3,3}, P_{3,4}, P_{3,5}, P_{3,6}, P_{4,1}, P_{4,2}, P_{4,3}, P_{4,4}, \mathbf{P_{4,5}}, P_{4,6}$

Dimension 5. There are 140 integrands corresponding to 5-dimensional boundaries. We present some examples below.

$\frac{\langle AB23\rangle\langle CD14\rangle+\langle AB14\rangle\langle CD23\rangle}{\langle AB14\rangle\langle AB23\rangle\langle CD12\rangle\langle CD14\rangle\langle CD23\rangle\langle CD34\rangle}$	$\frac{\langle AB23\rangle\langle CD14\rangle+\langle AB14\rangle\langle CD23\rangle}{\langle AB14\rangle\langle AB23\rangle\langle AB34\rangle\langle CD14\rangle\langle CD23\rangle\langle CD34\rangle}$
$\langle ABCD\rangle \to 0, \langle AB12\rangle \to 0, \langle AB34\rangle \to 0$	$\langle ABCD\rangle \to 0, \langle AB12\rangle \to 0, \langle CD12\rangle \to 0$
$\Delta^{(1)}_{13}, \Delta^{(1)}_{14}, \Delta^{(1)}_{23}, \Delta^{(1)}_{24}$ $\Delta^{(2)}_{12}, \Delta^{(2)}_{13}, \Delta^{(2)}_{14}, \Delta^{(2)}_{23}, \Delta^{(2)}_{24}, \Delta^{(2)}_{34}$	$\Delta^{(1)}_{12}, \Delta^{(1)}_{13}, \Delta^{(1)}_{14}, \Delta^{(1)}_{23}, \Delta^{(1)}_{24}$ $\Delta^{(2)}_{12}, \Delta^{(2)}_{13}, \Delta^{(2)}_{14}, \Delta^{(2)}_{23}, \Delta^{(2)}_{24}$
$P_{1,1}, P_{1,2}, P_{1,3}, P_{1,4}, P_{1,5}, \mathbf{P_{1,6}}, P_{4,1}, P_{4,2}, P_{4,3}, P_{4,4},$ $\mathbf{P_{4,5}}, P_{4,6}, P_{5,1}, P_{5,2}, P_{5,3}, \mathbf{P_{5,4}}, P_{5,5}, P_{5,6}, \mathbf{P_{6,1}}, P_{6,2},$ $P_{6,3}, P_{6,4}, P_{6,5}, P_{6,6}$	$P_{1,1}, P_{1,3}, P_{1,4}, P_{1,5}, \mathbf{P_{1,6}}, P_{3,1}, P_{3,3}, P_{3,4}, P_{3,5}, P_{3,6},$ $P_{4,1}, P_{4,3}, P_{4,4}, \mathbf{P_{4,5}}, P_{4,6}, P_{5,1}, P_{5,3}, \mathbf{P_{5,4}}, P_{5,5}, P_{5,6},$ $\mathbf{P_{6,1}}, P_{6,3}, P_{6,4}, P_{6,5}, P_{6,6}$

$\frac{\langle AB14\rangle\langle CD23\rangle+\langle AB23\rangle\langle CD14\rangle+\langle AB34\rangle\langle CD12\rangle}{\langle AB14\rangle\langle AB23\rangle\langle AB34\rangle\langle CD12\rangle\langle CD14\rangle\langle CD23\rangle}$	$\frac{\langle AB23\rangle\langle CD14\rangle+\langle AB14\rangle\langle CD23\rangle}{\langle AB14\rangle\langle AB23\rangle\langle ABCD\rangle\langle CD14\rangle\langle CD23\rangle\langle CD34\rangle}$
$\langle ABCD\rangle \to 0, \langle AB12\rangle \to 0, \langle CD34\rangle \to 0$	$\langle AB12\rangle \to 0, \langle AB34\rangle \to 0, \langle CD12\rangle \to 0$
$\Delta^{(1)}_{12}, \Delta^{(1)}_{13}, \Delta^{(1)}_{14}, \Delta^{(1)}_{23}, \Delta^{(1)}_{24}$ $\Delta^{(2)}_{13}, \Delta^{(2)}_{14}, \Delta^{(2)}_{23}, \Delta^{(2)}_{24}, \Delta^{(2)}_{34}$	$\Delta^{(1,2)}_{1234}, \Delta^{(1)}_{13}, \Delta^{(1)}_{14}, \Delta^{(1)}_{23}, \Delta^{(1)}_{24}$ $\Delta^{(2)}_{12}, \Delta^{(2)}_{13}, \Delta^{(2)}_{14}, \Delta^{(2)}_{23}, \Delta^{(2)}_{24}$
$P_{1,1}, P_{1,2}, P_{1,4}, P_{1,5}, \mathbf{P_{1,6}}, P_{3,1}, \mathbf{P_{3,2}}, P_{3,4}, P_{3,5}, P_{3,6},$ $P_{4,1}, P_{4,2}, P_{4,4}, \mathbf{P_{4,5}}, P_{4,6}, P_{5,1}, P_{5,2}, \mathbf{P_{5,4}}, P_{5,5}, P_{5,6},$ $\mathbf{P_{6,1}}, P_{6,2}, P_{6,4}, P_{6,5}, P_{6,6}$	$P_{1,1}, P_{1,3}, P_{1,4}, P_{1,5}, \mathbf{P_{1,6}}, P_{4,1}, P_{4,3}, P_{4,4}, \mathbf{P_{4,5}}, P_{4,6},$ $P_{5,1}, P_{5,3}, \mathbf{P_{5,4}}, P_{5,5}, P_{5,6}, \mathbf{P_{6,1}}, P_{6,3}, P_{6,4}, P_{6,5}, P_{6,6}$

$\frac{1}{\langle AB23\rangle\langle ABCD\rangle\langle CD12\rangle\langle CD34\rangle}$	$\frac{\langle AB34\rangle\langle CD12\rangle+\langle AB23\rangle\langle CD14\rangle}{\langle AB23\rangle\langle AB34\rangle\langle CD12\rangle\langle CD14\rangle\langle CD23\rangle\langle CD34\rangle}$
$\langle AB12\rangle \to 0, \langle AB34\rangle \to 0, \langle CD14\rangle \to 0$	$\langle ABCD\rangle \to 0, \langle AB12\rangle \to 0, \langle AB13\rangle \to 0, \langle AB14\rangle \to 0$
$\Delta^{(1,2)}_{1234}, \Delta^{(1)}_{13}, \Delta^{(1)}_{14}, \Delta^{(1)}_{23}, \Delta^{(1)}_{24}$ $\Delta^{(2)}_{12}, \Delta^{(2)}_{13}, \Delta^{(2)}_{14}, \Delta^{(2)}_{24}, \Delta^{(2)}_{34}$	$\Delta^{(1)}_{12}, \Delta^{(1)}_{13}, \Delta^{(1)}_{14}$ $\Delta^{(2)}_{12}, \Delta^{(2)}_{13}, \Delta^{(2)}_{14}, \Delta^{(2)}_{23}, \Delta^{(2)}_{24}, \Delta^{(2)}_{34}$
$P_{1,1}, P_{1,2}, P_{1,3}, P_{1,4}, \mathbf{P_{1,6}}, P_{4,1}, P_{4,2}, P_{4,3}, P_{4,4}, P_{4,6},$ $P_{5,1}, P_{5,2}, P_{5,3}, \mathbf{P_{5,4}}, P_{5,6}, \mathbf{P_{6,1}}, P_{6,2}, P_{6,3}, P_{6,4}, P_{6,6}$	$P_{1,1}, P_{1,2}, P_{1,3}, P_{1,4}, P_{1,5}, \mathbf{P_{1,6}}, P_{3,1}, \mathbf{P_{3,2}}, P_{3,3}, P_{3,4},$ $P_{3,5}, P_{3,6}, P_{4,1}, P_{4,2}, P_{4,3}, P_{4,4}, \mathbf{P_{4,5}}, P_{4,6}$

$\frac{1}{\langle AB23\rangle\langle AB34\rangle\langle CD12\rangle\langle CD14\rangle\langle CD23\rangle\langle CD34\rangle}$	$\frac{1}{\langle ABCD\rangle\langle CD12\rangle\langle CD23\rangle\langle CD34\rangle}$
$\langle AB12\rangle \to 0, \langle AB13\rangle \to 0, \langle AB14\rangle \to 0, \langle AB24\rangle \to 0$	$\langle AB12\rangle \to 0, \langle AB13\rangle \to 0, \langle AB14\rangle \to 0, \langle AB34\rangle \to 0$
$\Delta^{(1,2)}_{1234}, \Delta^{(1)}_{12}, \Delta^{(1)}_{14}$ $\Delta^{(2)}_{12}, \Delta^{(2)}_{13}, \Delta^{(2)}_{14}, \Delta^{(2)}_{23}, \Delta^{(2)}_{24}, \Delta^{(2)}_{34}$	$\Delta^{(1,2)}_{1234}, \Delta^{(1)}_{13}, \Delta^{(1)}_{14}$ $\Delta^{(2)}_{12}, \Delta^{(2)}_{13}, \Delta^{(2)}_{14}, \Delta^{(2)}_{23}, \Delta^{(2)}_{24}, \Delta^{(2)}_{34}$
$P_{3,1}, \mathbf{P_{3,2}}, P_{3,3}, P_{3,4}, P_{3,5}, P_{3,6}, P_{4,1}, P_{4,2}, P_{4,3}, P_{4,4},$ $\mathbf{P_{4,5}}, P_{4,6}$	$P_{1,1}, P_{1,2}, P_{1,3}, P_{1,4}, P_{1,5}, \mathbf{P_{1,6}}, P_{4,1}, P_{4,2}, P_{4,3}, P_{4,4},$ $\mathbf{P_{4,5}}, P_{4,6}$

$\frac{1}{\langle AB34\rangle\langle ABCD\rangle\langle CD23\rangle\langle CD34\rangle}$	$\frac{\langle AB23\rangle\langle CD14\rangle+\langle AB34\rangle\langle CD12\rangle}{\langle AB23\rangle\langle AB34\rangle\langle ABCD\rangle\langle CD12\rangle\langle CD14\rangle\langle CD34\rangle}$
$\langle AB12\rangle \to 0, \langle AB13\rangle \to 0, \langle AB14\rangle \to 0, \langle CD12\rangle \to 0$	$\langle AB12\rangle \to 0, \langle AB13\rangle \to 0, \langle AB14\rangle \to 0, \langle CD23\rangle \to 0$
$\Delta^{(1,2)}_{1234}, \Delta^{(1)}_{12}, \Delta^{(1)}_{13}, \Delta^{(1)}_{14}$ $\Delta^{(2)}_{12}, \Delta^{(2)}_{13}, \Delta^{(2)}_{14}, \Delta^{(2)}_{23}, \Delta^{(2)}_{24}$	$\Delta^{(1,2)}_{1234}, \Delta^{(1)}_{12}, \Delta^{(1)}_{13}, \Delta^{(1)}_{14}$ $\Delta^{(2)}_{12}, \Delta^{(2)}_{13}, \Delta^{(2)}_{23}, \Delta^{(2)}_{24}, \Delta^{(2)}_{34}$
$P_{1,1}, P_{1,3}, P_{1,4}, P_{1,5}, \mathbf{P_{1,6}}, P_{3,1}, P_{3,3}, P_{3,4}, P_{3,5}, P_{3,6},$ $P_{4,1}, P_{4,3}, P_{4,4}, \mathbf{P_{4,5}}, P_{4,6}$	$P_{1,1}, P_{1,2}, P_{1,3}, P_{1,5}, \mathbf{P_{1,6}}, P_{3,1}, \mathbf{P_{3,2}}, P_{3,3}, P_{3,5}, P_{3,6},$ $P_{4,1}, P_{4,2}, P_{4,3}, \mathbf{P_{4,5}}, P_{4,6}$

Dimension 4. There are 274 integrands corresponding to 4-dimensional boundaries. We present some examples below.

$\frac{\langle AB23\rangle\langle CD14\rangle+\langle AB14\rangle\langle CD23\rangle}{\langle AB14\rangle\langle AB23\rangle\langle CD14\rangle\langle CD23\rangle\langle CD34\rangle}$	$\frac{1}{\langle AB23\rangle\langle CD12\rangle\langle CD34\rangle}$
$\langle ABCD\rangle \to 0, \langle AB12\rangle \to 0, \langle AB34\rangle \to 0, \langle CD12\rangle \to 0$	$\langle ABCD\rangle \to 0, \langle AB12\rangle \to 0, \langle AB34\rangle \to 0, \langle CD14\rangle \to 0$
$\Delta^{(1)}_{13}, \Delta^{(1)}_{14}, \Delta^{(1)}_{23}, \Delta^{(1)}_{24}$ $\Delta^{(2)}_{12}, \Delta^{(2)}_{13}, \Delta^{(2)}_{14}, \Delta^{(2)}_{23}, \Delta^{(2)}_{24}$	$\Delta^{(1)}_{13}, \Delta^{(1)}_{14}, \Delta^{(1)}_{23}, \Delta^{(1)}_{24}$ $\Delta^{(2)}_{12}, \Delta^{(2)}_{13}, \Delta^{(2)}_{14}, \Delta^{(2)}_{24}, \Delta^{(2)}_{34}$
$P_{1,1}, P_{1,3}, P_{1,4}, P_{1,5}, \mathbf{P_{1,6}}, P_{4,1}, P_{4,3}, P_{4,4}, \mathbf{P_{4,5}}, P_{4,6},$ $P_{5,1}, P_{5,3}, \mathbf{P_{5,4}}, P_{5,5}, P_{5,6}, \mathbf{P_{6,1}}, P_{6,3}, P_{6,4}, P_{6,5}, P_{6,6}$	$P_{1,1}, P_{1,2}, P_{1,3}, P_{1,4}, \mathbf{P_{1,6}}, P_{4,1}, P_{4,2}, P_{4,3}, P_{4,4}, P_{4,6},$ $P_{5,1}, P_{5,2}, P_{5,3}, \mathbf{P_{5,4}}, P_{5,6}, \mathbf{P_{6,1}}, P_{6,2}, P_{6,3}, P_{6,4}, P_{6,6}$
$\frac{\langle AB23\rangle\langle CD14\rangle+\langle AB14\rangle\langle CD23\rangle}{\langle AB14\rangle\langle AB23\rangle\langle ABCD\rangle\langle CD14\rangle\langle CD23\rangle}$	$\frac{1}{\langle CD14\rangle\langle CD23\rangle\langle CD34\rangle}$
$\langle AB12\rangle \to 0, \langle AB34\rangle \to 0, \langle CD12\rangle \to 0, \langle CD34\rangle \to 0$	$\langle ABCD\rangle \to 0, \langle AB12\rangle \to 0, \langle AB13\rangle \to 0, \langle AB14\rangle \to 0$ $\langle AB23\rangle \to 0$
$\Delta^{(1,2)}_{1234}, \Delta^{(1)}_{13}, \Delta^{(1)}_{14}, \Delta^{(1)}_{23}, \Delta^{(1)}_{24}$ $\Delta^{(2)}_{13}, \Delta^{(2)}_{14}, \Delta^{(2)}_{23}, \Delta^{(2)}_{24}$	$\Delta^{(1)}_{12}, \Delta^{(1)}_{13}$ $\Delta^{(2)}_{12}, \Delta^{(2)}_{13}, \Delta^{(2)}_{14}, \Delta^{(2)}_{23}, \Delta^{(2)}_{24}, \Delta^{(2)}_{34}$
$P_{1,1}, P_{1,4}, P_{1,5}, \mathbf{P_{1,6}}, P_{4,1}, P_{4,4}, \mathbf{P_{4,5}}, P_{4,6}, P_{5,1}, \mathbf{P_{5,4}},$ $P_{5,5}, P_{5,6}, \mathbf{P_{6,1}}, P_{6,4}, P_{6,5}, P_{6,6}$	$P_{1,1}, P_{1,2}, P_{1,3}, P_{1,4}, P_{1,5}, \mathbf{P_{1,6}}, P_{3,1}, \mathbf{P_{3,2}}, P_{3,3}, P_{3,4},$ $P_{3,5}, P_{3,6}$
$\frac{1}{\langle AB34\rangle\langle CD23\rangle\langle CD34\rangle}$	$\frac{\langle AB34\rangle\langle CD12\rangle+\langle AB23\rangle\langle CD14\rangle}{\langle AB23\rangle\langle AB34\rangle\langle CD12\rangle\langle CD14\rangle\langle CD34\rangle}$
$\langle ABCD\rangle \to 0, \langle AB12\rangle \to 0, \langle AB13\rangle \to 0, \langle AB14\rangle \to 0$ $\langle CD12\rangle \to 0$	$\langle ABCD\rangle \to 0, \langle AB12\rangle \to 0, \langle AB13\rangle \to 0, \langle AB14\rangle \to 0$ $\langle CD23\rangle \to 0$
$\Delta^{(1)}_{12}, \Delta^{(1)}_{13}, \Delta^{(1)}_{14}$ $\Delta^{(2)}_{12}, \Delta^{(2)}_{13}, \Delta^{(2)}_{14}, \Delta^{(2)}_{23}, \Delta^{(2)}_{24}$	$\Delta^{(1)}_{12}, \Delta^{(1)}_{13}, \Delta^{(1)}_{14}$ $\Delta^{(2)}_{12}, \Delta^{(2)}_{13}, \Delta^{(2)}_{23}, \Delta^{(2)}_{24}, \Delta^{(2)}_{34}$
$P_{1,1}, P_{1,3}, P_{1,4}, P_{1,5}, \mathbf{P_{1,6}}, P_{3,1}, P_{3,3}, P_{3,4}, P_{3,5}, P_{3,6},$ $P_{4,1}, P_{4,3}, P_{4,4}, \mathbf{P_{4,5}}, P_{4,6}$	$P_{1,1}, P_{1,2}, P_{1,3}, P_{1,5}, \mathbf{P_{1,6}}, P_{3,1}, \mathbf{P_{3,2}}, P_{3,3}, P_{3,5}, P_{3,6},$ $P_{4,1}, P_{4,2}, P_{4,3}, \mathbf{P_{4,5}}, P_{4,6}$
$\frac{1}{\langle AB34\rangle\langle CD12\rangle\langle CD14\rangle\langle CD23\rangle\langle CD34\rangle}$	$\frac{1}{\langle ABCD\rangle\langle CD23\rangle\langle CD34\rangle}$
$\langle AB12\rangle \to 0, \langle AB13\rangle \to 0, \langle AB14\rangle \to 0, \langle AB23\rangle \to 0$ $\langle AB24\rangle \to 0$	$\langle AB12\rangle \to 0, \langle AB13\rangle \to 0, \langle AB14\rangle \to 0, \langle AB23\rangle \to 0$ $\langle CD14\rangle \to 0$
$\Delta^{(1,2)}_{1234}, \Delta^{(1)}_{12}$ $\Delta^{(2)}_{12}, \Delta^{(2)}_{13}, \Delta^{(2)}_{14}, \Delta^{(2)}_{23}, \Delta^{(2)}_{24}, \Delta^{(2)}_{34}$	$\Delta^{(1,2)}_{1234}, \Delta^{(1)}_{12}, \Delta^{(1)}_{13}$ $\Delta^{(2)}_{12}, \Delta^{(2)}_{13}, \Delta^{(2)}_{14}, \Delta^{(2)}_{24}, \Delta^{(2)}_{34}$
$P_{3,1}, \mathbf{P_{3,2}}, P_{3,3}, P_{3,4}, P_{3,5}, P_{3,6}$	$P_{1,1}, P_{1,2}, P_{1,3}, P_{1,4}, \mathbf{P_{1,6}}, P_{3,1}, \mathbf{P_{3,2}}, P_{3,3}, P_{3,4}, P_{3,6}$

$\frac{1}{\langle AB23\rangle\langle AB34\rangle\langle CD14\rangle\langle CD23\rangle\langle CD34\rangle}$	$\frac{1}{\langle AB34\rangle\langle ABCD\rangle\langle CD23\rangle}$
$\langle AB12\rangle \to 0, \langle AB13\rangle \to 0, \langle AB14\rangle \to 0, \langle AB24\rangle \to 0$ $\langle CD12\rangle \to 0$	$\langle AB12\rangle \to 0, \langle AB13\rangle \to 0, \langle AB14\rangle \to 0, \langle CD12\rangle \to 0$ $\langle CD34\rangle \to 0$
$\Delta^{(1,2)}_{1234}, \Delta^{(1)}_{12}, \Delta^{(1)}_{14}$ $\Delta^{(2)}_{12}, \Delta^{(2)}_{13}, \Delta^{(2)}_{14}, \Delta^{(2)}_{23}, \Delta^{(2)}_{24}$	$\Delta^{(1,2)}_{1234}, \Delta^{(1)}_{12}, \Delta^{(1)}_{13}, \Delta^{(1)}_{14}$ $\Delta^{(2)}_{13}, \Delta^{(2)}_{14}, \Delta^{(2)}_{23}, \Delta^{(2)}_{24}$
$P_{3,1}, P_{3,3}, P_{3,4}, P_{3,5}, P_{3,6}, P_{4,1}, P_{4,3}, P_{4,4}, \mathbf{P_{4,5}}, P_{4,6}$	$P_{1,1}, P_{1,4}, P_{1,5}, \mathbf{P_{1,6}}, P_{3,1}, P_{3,4}, P_{3,5}, P_{3,6}, P_{4,1}, P_{4,4},$ $\mathbf{P_{4,5}}, P_{4,6}$
$\frac{1}{\langle AB23\rangle\langle AB34\rangle\langle CD14\rangle\langle CD34\rangle}$	$\frac{1}{\langle AB34\rangle\langle ABCD\rangle\langle CD34\rangle}$
$\langle AB12\rangle \to 0, \langle AB13\rangle \to 0, \langle AB14\rangle \to 0, \langle CD12\rangle \to 0$ $\langle CD13\rangle \to 0, \langle CD23\rangle \to 0$	$\langle AB12\rangle \to 0, \langle AB13\rangle \to 0, \langle AB14\rangle \to 0, \langle CD12\rangle \to 0$ $\langle CD23\rangle \to 0, \langle CD24\rangle \to 0$
$\Delta^{(1,2)}_{1234}, \Delta^{(1)}_{12}, \Delta^{(1)}_{13}, \Delta^{(1)}_{14}$ $\Delta^{(2)}_{12}, \Delta^{(2)}_{13}, \Delta^{(2)}_{23}$	$\Delta^{(1,2)}_{1234}, \Delta^{(1)}_{12}, \Delta^{(1)}_{13}, \Delta^{(1)}_{14}$ $\Delta^{(2)}_{12}, \Delta^{(2)}_{23}, \Delta^{(2)}_{24}$
$P_{1,1}, P_{1,3}, P_{1,5}, P_{3,1}, P_{3,3}, P_{3,5}, P_{4,1}, P_{4,3}, \mathbf{P_{4,5}}$	$P_{1,3}, P_{1,5}, \mathbf{P_{1,6}}, P_{3,3}, P_{3,5}, P_{3,6}, P_{4,3}, \mathbf{P_{4,5}}, P_{4,6}$
$\frac{\langle AB34\rangle\langle CD12\rangle+\langle AB23\rangle\langle CD14\rangle}{\langle AB23\rangle\langle AB34\rangle\langle ABCD\rangle\langle CD12\rangle\langle CD14\rangle}$	$\frac{1}{\langle AB23\rangle\langle AB34\rangle\langle CD23\rangle\langle CD34\rangle}$
$\langle AB12\rangle \to 0, \langle AB13\rangle \to 0, \langle AB14\rangle \to 0, \langle CD23\rangle \to 0$ $\langle CD24\rangle \to 0, \langle CD34\rangle \to 0$	$\langle ABCD\rangle \to 0, \langle AB12\rangle \to 0, \langle AB13\rangle \to 0, \langle AB14\rangle \to 0$ $\langle CD12\rangle \to 0, \langle CD13\rangle \to 0, \langle CD14\rangle \to 0$
$\Delta^{(1,2)}_{1234}, \Delta^{(1)}_{12}, \Delta^{(1)}_{13}, \Delta^{(1)}_{14}$ $\Delta^{(2)}_{23}, \Delta^{(2)}_{24}, \Delta^{(2)}_{34}$	$\Delta^{(1)}_{12}, \Delta^{(1)}_{13}, \Delta^{(1)}_{14}$ $\Delta^{(2)}_{12}, \Delta^{(2)}_{13}, \Delta^{(2)}_{14}$
$P_{1,2}, P_{1,5}, \mathbf{P_{1,6}}, \mathbf{P_{3,2}}, P_{3,5}, P_{3,6}, P_{4,2}, \mathbf{P_{4,5}}, P_{4,6}$	$P_{1,1}, P_{1,3}, P_{1,4}, P_{3,1}, P_{3,3}, P_{3,4}, P_{4,1}, P_{4,3}, P_{4,4}$

Dimension 3. There are 330 integrands corresponding to 3-dimensional boundaries. We present some examples below.

$\frac{\langle AB23\rangle\langle CD14\rangle+\langle AB14\rangle\langle CD23\rangle}{\langle AB14\rangle\langle AB23\rangle\langle CD14\rangle\langle CD23\rangle}$	$\frac{1}{\langle CD23\rangle\langle CD34\rangle}$
$\langle ABCD\rangle \to 0, \langle AB12\rangle \to 0, \langle AB34\rangle \to 0, \langle CD12\rangle \to 0$ $\langle CD34\rangle \to 0$	$\langle ABCD\rangle \to 0, \langle AB12\rangle \to 0, \langle AB13\rangle \to 0, \langle AB14\rangle \to 0$ $\langle AB23\rangle \to 0, \langle CD14\rangle \to 0$
$\Delta^{(1)}_{13}, \Delta^{(1)}_{14}, \Delta^{(1)}_{23}, \Delta^{(1)}_{24}, \Delta^{(2)}_{13}, \Delta^{(2)}_{14}, \Delta^{(2)}_{23}, \Delta^{(2)}_{24}$	$\Delta^{(1)}_{12}, \Delta^{(1)}_{13}, \Delta^{(2)}_{12}, \Delta^{(2)}_{13}, \Delta^{(2)}_{14}, \Delta^{(2)}_{24}, \Delta^{(2)}_{34}$
$P_{1,1}, P_{1,4}, P_{1,5}, \mathbf{P_{1,6}}, P_{4,1}, P_{4,4}, \mathbf{P_{4,5}}, P_{4,6}, P_{5,1}, \mathbf{P_{5,4}},$ $P_{5,5}, P_{5,6}, \mathbf{P_{6,1}}, P_{6,4}, P_{6,5}, P_{6,6}$	$P_{1,1}, P_{1,2}, P_{1,3}, P_{1,4}, \mathbf{P_{1,6}}, P_{3,1}, \mathbf{P_{3,2}}, P_{3,3}, P_{3,4}, P_{3,6}$
$\frac{1}{\langle AB34\rangle\langle CD23\rangle}$	$\frac{1}{\langle AB34\rangle\langle CD12\rangle\langle CD23\rangle\langle CD34\rangle}$
$\langle ABCD\rangle \to 0, \langle AB12\rangle \to 0, \langle AB13\rangle \to 0, \langle AB14\rangle \to 0$ $\langle CD12\rangle \to 0, \langle CD34\rangle \to 0$	$\langle AB12\rangle \to 0, \langle AB13\rangle \to 0, \langle AB14\rangle \to 0, \langle AB23\rangle \to 0$ $\langle AB24\rangle \to 0, \langle CD14\rangle \to 0$
$\Delta^{(1)}_{12}, \Delta^{(1)}_{13}, \Delta^{(1)}_{14}, \Delta^{(2)}_{13}, \Delta^{(2)}_{14}, \Delta^{(2)}_{23}, \Delta^{(2)}_{24}$	$\Delta^{(1,2)}_{1234}, \Delta^{(1)}_{12}, \Delta^{(2)}_{12}, \Delta^{(2)}_{13}, \Delta^{(2)}_{14}, \Delta^{(2)}_{24}, \Delta^{(2)}_{34}$
$P_{1,1}, P_{1,4}, P_{1,5}, \mathbf{P_{1,6}}, P_{3,1}, P_{3,4}, P_{3,5}, P_{3,6}, P_{4,1}, P_{4,4},$ $\mathbf{P_{4,5}}, P_{4,6}$	$P_{3,1}, \mathbf{P_{3,2}}, P_{3,3}, P_{3,4}, P_{3,6}$
$\frac{1}{\langle ABCD\rangle\langle CD34\rangle}$	$\frac{1}{\langle AB23\rangle\langle AB34\rangle\langle CD14\rangle\langle CD23\rangle}$
$\langle AB12\rangle \to 0, \langle AB13\rangle \to 0, \langle AB14\rangle \to 0, \langle AB23\rangle \to 0$ $\langle CD14\rangle \to 0, \langle CD23\rangle \to 0$	$\langle AB12\rangle \to 0, \langle AB13\rangle \to 0, \langle AB14\rangle \to 0, \langle AB24\rangle \to 0$ $\langle CD12\rangle \to 0, \langle CD34\rangle \to 0$
$\Delta^{(1,2)}_{1234}, \Delta^{(1)}_{12}, \Delta^{(1)}_{13}, \Delta^{(2)}_{12}, \Delta^{(2)}_{13}, \Delta^{(2)}_{24}, \Delta^{(2)}_{34}$	$\Delta^{(1,2)}_{1234}, \Delta^{(1)}_{12}, \Delta^{(1)}_{14}, \Delta^{(2)}_{13}, \Delta^{(2)}_{14}, \Delta^{(2)}_{23}, \Delta^{(2)}_{24}$
$P_{1,1}, P_{1,2}, P_{1,3}, \mathbf{P_{1,6}}, P_{3,1}, \mathbf{P_{3,2}}, P_{3,3}, P_{3,6}$	$P_{3,1}, P_{3,4}, P_{3,5}, P_{3,6}, P_{4,1}, P_{4,4}, \mathbf{P_{4,5}}, P_{4,6}$

$\frac{1}{\langle AB34\rangle\langle CD14\rangle\langle CD23\rangle\langle CD34\rangle}$	$\frac{1}{\langle AB34\rangle\langle CD34\rangle}$
$\langle ABCD\rangle \to 0, \langle AB12\rangle \to 0, \langle AB13\rangle \to 0, \langle AB14\rangle \to 0$ $\langle AB23\rangle \to 0, \langle AB24\rangle \to 0, \langle CD12\rangle \to 0$	$\langle ABCD\rangle \to 0, \langle AB12\rangle \to 0, \langle AB13\rangle \to 0, \langle AB14\rangle \to 0$ $\langle CD12\rangle \to 0, \langle CD23\rangle \to 0, \langle CD24\rangle \to 0$
$\Delta_{12}^{(1)}, \Delta_{12}^{(2)}, \Delta_{13}^{(2)}, \Delta_{14}^{(2)}, \Delta_{23}^{(2)}, \Delta_{24}^{(2)}$	$\Delta_{12}^{(1)}, \Delta_{13}^{(1)}, \Delta_{14}^{(1)}, \Delta_{12}^{(2)}, \Delta_{23}^{(2)}, \Delta_{24}^{(2)}$
$P_{3,1}, P_{3,3}, P_{3,4}, P_{3,5}, P_{3,6}$	$P_{1,3}, P_{1,5}, \mathbf{P_{1,6}}, P_{3,3}, P_{3,5}, P_{3,6}, P_{4,3}, \mathbf{P_{4,5}}, P_{4,6}$
$\frac{\langle AB34\rangle\langle CD12\rangle+\langle AB23\rangle\langle CD14\rangle}{\langle AB23\rangle\langle AB34\rangle\langle CD12\rangle\langle CD14\rangle}$	$\frac{1}{\langle AB34\rangle\langle CD12\rangle\langle CD23\rangle}$
$\langle ABCD\rangle \to 0, \langle AB12\rangle \to 0, \langle AB13\rangle \to 0, \langle AB14\rangle \to 0$ $\langle CD23\rangle \to 0, \langle CD24\rangle \to 0, \langle CD34\rangle \to 0$	$\langle AB12\rangle \to 0, \langle AB13\rangle \to 0, \langle AB14\rangle \to 0, \langle AB23\rangle \to 0$ $\langle CD13\rangle \to 0, \langle CD14\rangle \to 0, \langle CD34\rangle \to 0$
$\Delta_{12}^{(1)}, \Delta_{13}^{(1)}, \Delta_{14}^{(1)}, \Delta_{23}^{(2)}, \Delta_{24}^{(2)}, \Delta_{34}^{(2)}$	$\Delta_{1234}^{(1,2)}, \Delta_{12}^{(1)}, \Delta_{13}^{(1)}, \Delta_{13}^{(2)}, \Delta_{14}^{(2)}, \Delta_{34}^{(2)}$
$P_{1,2}, P_{1,5}, \mathbf{P_{1,6}}, \mathbf{P_{3,2}}, P_{3,5}, P_{3,6}, P_{4,2}, \mathbf{P_{4,5}}, P_{4,6}$	$P_{1,1}, P_{1,2}, P_{1,4}, P_{3,1}, \mathbf{P_{3,2}}, P_{3,4}$
$\frac{1}{\langle ABCD\rangle\langle CD23\rangle}$	$\frac{1}{\langle AB23\rangle\langle AB34\rangle\langle CD14\rangle\langle CD34\rangle}$
$\langle AB12\rangle \to 0, \langle AB13\rangle \to 0, \langle AB14\rangle \to 0, \langle AB23\rangle \to 0$ $\langle CD14\rangle \to 0, \langle CD24\rangle \to 0, \langle CD34\rangle \to 0$	$\langle AB12\rangle \to 0, \langle AB13\rangle \to 0, \langle AB14\rangle \to 0, \langle AB24\rangle \to 0$ $\langle CD12\rangle \to 0, \langle CD13\rangle \to 0, \langle CD23\rangle \to 0$
$\Delta_{1234}^{(1,2)}, \Delta_{12}^{(1)}, \Delta_{13}^{(1)}, \Delta_{14}^{(2)}, \Delta_{24}^{(2)}, \Delta_{34}^{(2)}$	$\Delta_{1234}^{(1,2)}, \Delta_{12}^{(1)}, \Delta_{14}^{(1)}, \Delta_{12}^{(2)}, \Delta_{13}^{(2)}, \Delta_{23}^{(2)}$
$P_{1,2}, P_{1,4}, \mathbf{P_{1,6}}, \mathbf{P_{3,2}}, P_{3,4}, P_{3,6}$	$P_{3,1}, P_{3,3}, P_{3,5}, P_{4,1}, P_{4,3}, \mathbf{P_{4,5}}$
$\frac{1}{\langle AB34\rangle\langle CD23\rangle\langle CD34\rangle}$	$\frac{1}{\langle AB23\rangle\langle AB34\rangle\langle CD23\rangle\langle CD34\rangle}$
$\langle ABCD\rangle \to 0, \langle AB12\rangle \to 0, \langle AB13\rangle \to 0, \langle AB14\rangle \to 0$ $\langle AB23\rangle \to 0, \langle CD12\rangle \to 0, \langle CD13\rangle \to 0, \langle CD14\rangle \to 0$	$\langle ABCD\rangle \to 0, \langle AB12\rangle \to 0, \langle AB13\rangle \to 0, \langle AB14\rangle \to 0$ $\langle AB24\rangle \to 0, \langle CD12\rangle \to 0, \langle CD13\rangle \to 0, \langle CD14\rangle \to 0$
$\Delta_{12}^{(1)}, \Delta_{13}^{(1)}, \Delta_{12}^{(2)}, \Delta_{13}^{(2)}, \Delta_{14}^{(2)}$	$\Delta_{12}^{(1)}, \Delta_{14}^{(1)}, \Delta_{12}^{(2)}, \Delta_{13}^{(2)}, \Delta_{14}^{(2)}$
$P_{1,1}, P_{1,3}, P_{1,4}, P_{3,1}, P_{3,3}, P_{3,4}$	$P_{3,1}, P_{3,3}, P_{3,4}, P_{4,1}, P_{4,3}, P_{4,4}$

Dimension 2. There are 264 integrands corresponding to 2-dimensional boundaries. We present some examples below.

$\frac{1}{\langle CD34\rangle}$	$\frac{1}{\langle AB34\rangle\langle CD12\rangle\langle CD34\rangle}$
$\langle ABCD\rangle \to 0, \langle AB12\rangle \to 0, \langle AB13\rangle \to 0, \langle AB14\rangle \to 0$ $\langle AB23\rangle \to 0, \langle CD14\rangle \to 0, \langle CD23\rangle \to 0$	$\langle AB12\rangle \to 0, \langle AB13\rangle \to 0, \langle AB14\rangle \to 0, \langle AB23\rangle \to 0$ $\langle AB24\rangle \to 0, \langle CD14\rangle \to 0, \langle CD23\rangle \to 0$
$\Delta_{12}^{(1)}, \Delta_{13}^{(1)}, \Delta_{12}^{(2)}, \Delta_{13}^{(2)}, \Delta_{24}^{(2)}, \Delta_{34}^{(2)}$	$\Delta_{1234}^{(1,2)}, \Delta_{12}^{(1)}, \Delta_{12}^{(2)}, \Delta_{13}^{(2)}, \Delta_{24}^{(2)}, \Delta_{34}^{(2)}$
$P_{1,1}, P_{1,2}, P_{1,3}, \mathbf{P_{1,6}}, P_{3,1}, \mathbf{P_{3,2}}, P_{3,3}, P_{3,6}$	$P_{3,1}, \mathbf{P_{3,2}}, P_{3,3}, P_{3,6}$
$\frac{1}{\langle AB34\rangle\langle CD14\rangle\langle CD23\rangle}$	$\frac{1}{\langle CD23\rangle}$
$\langle ABCD\rangle \to 0, \langle AB12\rangle \to 0, \langle AB13\rangle \to 0, \langle AB14\rangle \to 0$ $\langle AB23\rangle \to 0, \langle AB24\rangle \to 0, \langle CD12\rangle \to 0, \langle CD34\rangle \to 0$	$\langle ABCD\rangle \to 0, \langle AB12\rangle \to 0, \langle AB13\rangle \to 0, \langle AB14\rangle \to 0$ $\langle AB23\rangle \to 0, \langle CD14\rangle \to 0, \langle CD24\rangle \to 0, \langle CD34\rangle \to 0$
$\Delta_{12}^{(1)}, \Delta_{13}^{(2)}, \Delta_{14}^{(2)}, \Delta_{23}^{(2)}, \Delta_{24}^{(2)}$	$\Delta_{12}^{(1)}, \Delta_{13}^{(1)}, \Delta_{14}^{(2)}, \Delta_{24}^{(2)}, \Delta_{34}^{(2)}$
$P_{3,1}, P_{3,4}, P_{3,5}, P_{3,6}$	$P_{1,2}, P_{1,4}, \mathbf{P_{1,6}}, \mathbf{P_{3,2}}, P_{3,4}, P_{3,6}$
$\frac{1}{\langle AB34\rangle\langle CD12\rangle\langle CD23\rangle}$	$\frac{1}{\langle AB34\rangle\langle CD12\rangle}$
$\langle AB12\rangle \to 0, \langle AB13\rangle \to 0, \langle AB14\rangle \to 0, \langle AB23\rangle \to 0$ $\langle AB24\rangle \to 0, \langle CD13\rangle \to 0, \langle CD14\rangle \to 0, \langle CD34\rangle \to 0$	$\langle AB12\rangle \to 0, \langle AB13\rangle \to 0, \langle AB14\rangle \to 0, \langle AB23\rangle \to 0$ $\langle CD13\rangle \to 0, \langle CD14\rangle \to 0, \langle CD23\rangle \to 0, \langle CD34\rangle \to 0$
$\Delta_{1234}^{(1,2)}, \Delta_{12}^{(1)}, \Delta_{13}^{(2)}, \Delta_{14}^{(2)}, \Delta_{34}^{(2)}$	$\Delta_{1234}^{(1,2)}, \Delta_{12}^{(1)}, \Delta_{13}^{(1)}, \Delta_{13}^{(2)}, \Delta_{34}^{(2)}$
$P_{3,1}, \mathbf{P_{3,2}}, P_{3,4}$	$P_{1,1}, P_{1,2}, P_{3,1}, \mathbf{P_{3,2}}$

$\frac{1}{\langle \text{AB34}\rangle\langle \text{CD12}\rangle\langle \text{CD23}\rangle}$	$\frac{1}{\langle \text{ABCD}\rangle}$
$\langle \text{AB12}\rangle \to 0, \langle \text{AB13}\rangle \to 0, \langle \text{AB14}\rangle \to 0, \langle \text{AB23}\rangle \to 0$ $\langle \text{CD13}\rangle \to 0, \langle \text{CD14}\rangle \to 0, \langle \text{CD24}\rangle \to 0, \langle \text{CD34}\rangle \to 0$	$\langle \text{AB12}\rangle \to 0, \langle \text{AB13}\rangle \to 0, \langle \text{AB14}\rangle \to 0, \langle \text{AB23}\rangle \to 0$ $\langle \text{CD14}\rangle \to 0, \langle \text{CD23}\rangle \to 0, \langle \text{CD24}\rangle \to 0, \langle \text{CD34}\rangle \to 0$
$\Delta^{(1,2)}_{1234}, \Delta^{(1)}_{12}, \Delta^{(1)}_{13}, \Delta^{(2)}_{14}, \Delta^{(2)}_{34}$	$\Delta^{(1,2)}_{1234}, \Delta^{(1)}_{12}, \Delta^{(1)}_{13}, \Delta^{(2)}_{24}, \Delta^{(2)}_{34}$
$P_{1,2}, P_{1,4}, \boldsymbol{P_{3,2}}, P_{3,4}$	$P_{1,2}, \boldsymbol{P_{1,6}}, \boldsymbol{P_{3,2}}, P_{3,6}$
$\frac{1}{\langle \text{AB23}\rangle\langle \text{AB34}\rangle\langle \text{CD14}\rangle\langle \text{CD34}\rangle}$	$\frac{1}{\langle \text{AB34}\rangle\langle \text{CD23}\rangle\langle \text{CD34}\rangle}$
$\langle \text{AB12}\rangle \to 0, \langle \text{AB13}\rangle \to 0, \langle \text{AB14}\rangle \to 0, \langle \text{AB24}\rangle \to 0$ $\langle \text{CD12}\rangle \to 0, \langle \text{CD13}\rangle \to 0, \langle \text{CD23}\rangle \to 0, \langle \text{CD24}\rangle \to 0$	$\langle \text{ABCD}\rangle \to 0, \langle \text{AB12}\rangle \to 0, \langle \text{AB13}\rangle \to 0, \langle \text{AB14}\rangle \to 0$ $\langle \text{AB23}\rangle \to 0, \langle \text{AB24}\rangle \to 0, \langle \text{CD12}\rangle \to 0, \langle \text{CD13}\rangle \to 0$ $\langle \text{CD14}\rangle \to 0$
$\Delta^{(1,2)}_{1234}, \Delta^{(1)}_{12}, \Delta^{(1)}_{14}, \Delta^{(2)}_{12}, \Delta^{(2)}_{23}$	$\Delta^{(1)}_{12}, \Delta^{(2)}_{12}, \Delta^{(2)}_{13}, \Delta^{(2)}_{14}$
$P_{3,3}, P_{3,5}, P_{4,3}, \boldsymbol{P_{4,5}}$	$P_{3,1}, P_{3,3}, P_{3,4}$
$\frac{1}{\langle \text{CD23}\rangle\langle \text{CD34}\rangle}$	$\frac{1}{\langle \text{AB34}\rangle\langle \text{CD34}\rangle}$
$\langle \text{ABCD}\rangle \to 0, \langle \text{AB12}\rangle \to 0, \langle \text{AB13}\rangle \to 0, \langle \text{AB14}\rangle \to 0$ $\langle \text{AB23}\rangle \to 0, \langle \text{AB34}\rangle \to 0, \langle \text{CD12}\rangle \to 0, \langle \text{CD13}\rangle \to 0$ $\langle \text{CD14}\rangle \to 0$	$\langle \text{ABCD}\rangle \to 0, \langle \text{AB12}\rangle \to 0, \langle \text{AB13}\rangle \to 0, \langle \text{AB14}\rangle \to 0$ $\langle \text{AB23}\rangle \to 0, \langle \text{CD12}\rangle \to 0, \langle \text{CD13}\rangle \to 0, \langle \text{CD14}\rangle \to 0$ $\langle \text{CD23}\rangle \to 0$
$\Delta^{(1)}_{13}, \Delta^{(2)}_{12}, \Delta^{(2)}_{13}, \Delta^{(2)}_{14}$	$\Delta^{(1)}_{12}, \Delta^{(1)}_{13}, \Delta^{(2)}_{12}, \Delta^{(2)}_{13}$
$P_{1,1}, P_{1,3}, P_{1,4}$	$P_{1,1}, P_{1,3}, P_{3,1}, P_{3,3}$
$\frac{1}{\langle \text{AB34}\rangle\langle \text{CD23}\rangle\langle \text{CD34}\rangle}$	$\frac{1}{\langle \text{AB23}\rangle\langle \text{AB34}\rangle\langle \text{CD23}\rangle\langle \text{CD34}\rangle}$
$\langle \text{ABCD}\rangle \to 0, \langle \text{AB12}\rangle \to 0, \langle \text{AB13}\rangle \to 0, \langle \text{AB14}\rangle \to 0$ $\langle \text{AB23}\rangle \to 0, \langle \text{CD12}\rangle \to 0, \langle \text{CD13}\rangle \to 0, \langle \text{CD14}\rangle \to 0$ $\langle \text{CD24}\rangle \to 0$	$\langle \text{ABCD}\rangle \to 0, \langle \text{AB12}\rangle \to 0, \langle \text{AB13}\rangle \to 0, \langle \text{AB14}\rangle \to 0$ $\langle \text{AB24}\rangle \to 0, \langle \text{CD12}\rangle \to 0, \langle \text{CD13}\rangle \to 0, \langle \text{CD14}\rangle \to 0$ $\langle \text{CD24}\rangle \to 0$
$\Delta^{(1)}_{12}, \Delta^{(1)}_{13}, \Delta^{(2)}_{12}, \Delta^{(2)}_{14}$	$\Delta^{(1)}_{12}, \Delta^{(1)}_{14}, \Delta^{(2)}_{12}, \Delta^{(2)}_{14}$
$P_{1,3}, P_{1,4}, P_{3,3}, P_{3,4}$	$P_{3,3}, P_{3,4}, P_{4,3}, P_{4,4}$

Dimension 1. There are 136 integrands corresponding to 1-dimensional boundaries. We present some examples below.

1	$\frac{1}{\langle \text{AB34}\rangle\langle \text{CD12}\rangle}$
$\langle \text{ABCD}\rangle \to 0, \langle \text{AB12}\rangle \to 0, \langle \text{AB13}\rangle \to 0, \langle \text{AB14}\rangle \to 0$ $\langle \text{AB23}\rangle \to 0, \langle \text{CD14}\rangle \to 0, \langle \text{CD23}\rangle \to 0, \langle \text{CD24}\rangle \to 0$ $\langle \text{CD34}\rangle \to 0$	$\langle \text{AB12}\rangle \to 0, \langle \text{AB13}\rangle \to 0, \langle \text{AB14}\rangle \to 0, \langle \text{AB23}\rangle \to 0$ $\langle \text{AB24}\rangle \to 0, \langle \text{CD13}\rangle \to 0, \langle \text{CD14}\rangle \to 0, \langle \text{CD23}\rangle \to 0$ $\langle \text{CD34}\rangle \to 0$
$\Delta^{(1)}_{12}, \Delta^{(1)}_{13}, \Delta^{(2)}_{24}, \Delta^{(2)}_{34}$	$\Delta^{(1,2)}_{1234}, \Delta^{(1)}_{12}, \Delta^{(2)}_{13}, \Delta^{(2)}_{34}$
$P_{1,2}, \boldsymbol{P_{1,6}}, \boldsymbol{P_{3,2}}, P_{3,6}$	$P_{3,1}, \boldsymbol{P_{3,2}}$
$\frac{1}{\langle \text{AB34}\rangle\langle \text{CD12}\rangle\langle \text{CD23}\rangle}$	$\frac{1}{\langle \text{AB34}\rangle\langle \text{CD34}\rangle}$
$\langle \text{AB12}\rangle \to 0, \langle \text{AB13}\rangle \to 0, \langle \text{AB14}\rangle \to 0, \langle \text{AB23}\rangle \to 0$ $\langle \text{AB24}\rangle \to 0, \langle \text{CD13}\rangle \to 0, \langle \text{CD14}\rangle \to 0, \langle \text{CD24}\rangle \to 0$ $\langle \text{CD34}\rangle \to 0$	$\langle \text{ABCD}\rangle \to 0, \langle \text{AB12}\rangle \to 0, \langle \text{AB13}\rangle \to 0, \langle \text{AB14}\rangle \to 0$ $\langle \text{AB23}\rangle \to 0, \langle \text{AB24}\rangle \to 0, \langle \text{CD12}\rangle \to 0, \langle \text{CD13}\rangle \to 0$ $\langle \text{CD14}\rangle \to 0, \langle \text{CD23}\rangle \to 0$
$\Delta^{(1,2)}_{1234}, \Delta^{(1)}_{12}, \Delta^{(2)}_{14}, \Delta^{(2)}_{34}$	$\Delta^{(1)}_{12}, \Delta^{(2)}_{12}, \Delta^{(2)}_{13}$
$\boldsymbol{P_{3,2}}, P_{3,4}$	$P_{3,1}, P_{3,3}$

$\frac{1}{\langle \text{AB34}\rangle\langle \text{CD23}\rangle\langle \text{CD34}\rangle}$	$\frac{1}{\langle \text{CD34}\rangle}$
$\langle \text{ABCD}\rangle \to 0, \langle \text{AB12}\rangle \to 0, \langle \text{AB13}\rangle \to 0, \langle \text{AB14}\rangle \to 0$ $\langle \text{AB23}\rangle \to 0, \langle \text{AB24}\rangle \to 0, \langle \text{CD12}\rangle \to 0, \langle \text{CD13}\rangle \to 0$ $\langle \text{CD14}\rangle \to 0, \langle \text{CD24}\rangle \to 0$	$\langle \text{ABCD}\rangle \to 0, \langle \text{AB12}\rangle \to 0, \langle \text{AB13}\rangle \to 0, \langle \text{AB14}\rangle \to 0$ $\langle \text{AB23}\rangle \to 0, \langle \text{AB34}\rangle \to 0, \langle \text{CD12}\rangle \to 0, \langle \text{CD13}\rangle \to 0$ $\langle \text{CD14}\rangle \to 0, \langle \text{CD23}\rangle \to 0$
$\Delta_{12}^{(1)}, \Delta_{12}^{(2)}, \Delta_{14}^{(2)}$	$\Delta_{13}^{(1)}, \Delta_{12}^{(2)}, \Delta_{13}^{(2)}$
$P_{3,3}, P_{3,4}$	$P_{1,1}, P_{1,3}$

Dimension 0. There are 34 integrands corresponding to 0-dimensional boundaries. We present some examples below.

$\frac{1}{\langle \text{AB34}\rangle\langle \text{CD12}\rangle}$	$\frac{1}{\langle \text{AB34}\rangle\langle \text{CD34}\rangle}$
$\langle \text{AB12}\rangle \to 0, \langle \text{AB13}\rangle \to 0, \langle \text{AB14}\rangle \to 0, \langle \text{AB23}\rangle \to 0$ $\langle \text{AB24}\rangle \to 0, \langle \text{CD13}\rangle \to 0, \langle \text{CD14}\rangle \to 0, \langle \text{CD23}\rangle \to 0$ $\langle \text{CD24}\rangle \to 0, \langle \text{CD34}\rangle \to 0$	$\langle \text{ABCD}\rangle \to 0, \langle \text{AB12}\rangle \to 0, \langle \text{AB13}\rangle \to 0, \langle \text{AB14}\rangle \to 0$ $\langle \text{AB23}\rangle \to 0, \langle \text{AB24}\rangle \to 0, \langle \text{CD12}\rangle \to 0, \langle \text{CD13}\rangle \to 0$ $\langle \text{CD14}\rangle \to 0, \langle \text{CD23}\rangle \to 0, \langle \text{CD24}\rangle \to 0$
$\Delta_{1234}^{(1,2)}, \Delta_{12}^{(1)}, \Delta_{34}^{(2)}$	$\Delta_{12}^{(1)}, \Delta_{12}^{(2)}$
$\boldsymbol{P_{3,2}}$	$P_{3,3}$

$\frac{1}{\langle \text{AB34}\rangle}$	1
$\langle \text{ABCD}\rangle \to 0, \langle \text{AB12}\rangle \to 0, \langle \text{AB13}\rangle \to 0, \langle \text{AB14}\rangle \to 0$ $\langle \text{AB23}\rangle \to 0, \langle \text{AB24}\rangle \to 0, \langle \text{CD12}\rangle \to 0, \langle \text{CD13}\rangle \to 0$ $\langle \text{CD14}\rangle \to 0, \langle \text{CD23}\rangle \to 0, \langle \text{CD34}\rangle \to 0$	$\langle \text{ABCD}\rangle \to 0, \langle \text{AB12}\rangle \to 0, \langle \text{AB13}\rangle \to 0, \langle \text{AB14}\rangle \to 0$ $\langle \text{AB23}\rangle \to 0, \langle \text{AB34}\rangle \to 0, \langle \text{CD12}\rangle \to 0, \langle \text{CD13}\rangle \to 0$ $\langle \text{CD14}\rangle \to 0, \langle \text{CD23}\rangle \to 0, \langle \text{CD34}\rangle \to 0$
$\Delta_{12}^{(1)}, \Delta_{13}^{(2)}$	$\Delta_{13}^{(1)}, \Delta_{13}^{(2)}$
$P_{3,1}$	$P_{1,1}$

Appendix C

Appendices to Chapter 6: "Non-Planar On-Shell Diagrams"

C.1 Embedding Independence

Here we illustrate the independence of the embedding of the on-shell diagram with the simple example shown in Figure C.1. It is clear that the non-planarity of this diagram is fake, since it can be embedded on a disk by flipping $X_{1,1}$.

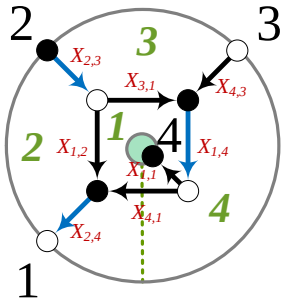

Figure C.1: An on-shell diagram on an annulus. This particular graph can be planarized by flipping the $X_{1,1}$ edge.

Here we have four face variables, three of which are independent, and one path b_1. In terms of oriented edge weights, they are given by

$$f_1 = \frac{\alpha_{3,1}\alpha_{4,1}}{\alpha_{1,2}\alpha_{1,4}}\,, \quad f_2 = \frac{\alpha_{1,2}}{\alpha_{2,3}\alpha_{2,4}}\,, \quad f_3 = \frac{\alpha_{2,3}\alpha_{4,3}}{\alpha_{3,1}}\,, \quad b_1 = \frac{\alpha_{4,1}}{\alpha_{1,1}\alpha_{2,4}}\,. \tag{C.1.1}$$

Let us consider the perfect orientation corresponding to the reference perfect matching $\tilde{p}_{\text{ref}} = \alpha_{1,4}\alpha_{2,3}\alpha_{2,4}$, which has source set $\{2,3\}$. Using our prescription for the boundary measurement, we obtain the Grassmannian matrix

$$C = \left(\begin{array}{c|cccc} & 1 & 2 & 3 & 4 \\ \hline 2 & \frac{\alpha_{1,2}}{\alpha_{2,3}\alpha_{2,4}} + \frac{\alpha_{3,1}\alpha_{4,1}}{\alpha_{1,4}\alpha_{2,3}\alpha_{2,4}} & 1 & 0 & -\frac{\alpha_{1,1}\alpha_{3,1}}{\alpha_{1,4}\alpha_{2,3}} \\ 3 & -\frac{\alpha_{4,1}\alpha_{4,3}}{\alpha_{1,4}\alpha_{2,4}} & 0 & 1 & \frac{\alpha_{1,1}\alpha_{4,3}}{\alpha_{1,4}} \end{array}\right)$$

$$= \left(\begin{array}{c|cccc} & 1 & 2 & 3 & 4 \\ \hline 2 & f_1 f_2 + f_2 & 1 & 0 & -\frac{f_1 f_2}{b_1} \\ 3 & -f_1 f_2 f_3 & 0 & 1 & \frac{f_1 f_2 f_3}{b_1} \end{array}\right). \tag{C.1.2}$$

The on-shell form becomes

$$\Omega = \frac{df_1}{f_1}\frac{df_2}{f_2}\frac{df_3}{f_3}\frac{db_1}{b_1}. \tag{C.1.3}$$

In terms of minors, it becomes

$$\Omega = \frac{d^{2\times 4}C}{\text{Vol}(\text{GL}(2))}\frac{1}{(12)(23)(34)(41)}, \tag{C.1.4}$$

which is simply the form for the planar embedding, i.e. the ordinary square box in Figure 4.1. This illustrates the independence of the on-shell form on the embedding and shows that the generalized face variables maintain a $d\log$ form regardless of its choice.

C.2 On-Shell Form for a Genus-One NMHV Diagram

To show that the method prescribed in §6.3.2 works just as well for graphs with higher genus, we now consider the non-planarizable genus-1 example studied in §6.2, where we choose the perfect orientation shown in Figure 4.6.

Following the prescription in §6.3.2, we find the matrices T and M to be

$$T = \begin{pmatrix} 1 & 6 & 4 & 2 \\ 3 & 2 & 4 & 6 \\ 5 & 4 & 2 & 6 \end{pmatrix}, \quad M = \begin{pmatrix} (642) & (164) & 0 & (216) & 0 & (421) \\ 0 & (463) & (246) & (632) & 0 & (324) \\ 0 & (654) & 0 & (265) & (426) & (542) \end{pmatrix}. \tag{C.2.1}$$

It is easy to see that the simplest way to obtain the on-shell form is by deleting columns {2,4,6},

$$\widehat{M}_{2,4,6} = \begin{pmatrix} (642) & 0 & 0 \\ 0 & (246) & 0 \\ 0 & 0 & (426) \end{pmatrix}, \quad \frac{\det \widehat{M}_{2,4,6}}{(246)} = (246)^2\,, \tag{C.2.2}$$

which gives the on-shell form

$$\Omega = \frac{d^{3\times 6}C}{\mathrm{Vol}(\mathrm{GL}(3))} \frac{(246)^3}{(164)(421)(216)(324)(463)(632)(542)(265)(654)}\,. \tag{C.2.3}$$

We have checked that this result coincides with the result obtained by using the boundary measurement as described in §6.3.1, giving further evidence to both methods as well as to the validity of the boundary measurement in Chapter 4.

C.3 N^{2}MHV Example with Two Auxiliary Edges

Let us consider the N^{2}MHV example in Figure C.2. The T matrix is given by

$$T = \begin{pmatrix} 6 & 1 & 9 & * & * \\ 1 & 7 & 9 & * & * \\ 8 & 10 & 9 & * & * \\ 10 & 3 & 5 & 9 & * \\ 5 & 3 & 8 & 1 & 4 \\ 2 & 3 & 10 & * & * \end{pmatrix} \xrightarrow{\text{Choice of } *} T = \begin{pmatrix} 6 & 1 & 9 & 3 & 8 \\ 1 & 7 & 9 & 3 & 8 \\ 8 & 10 & 9 & 1 & 3 \\ 10 & 3 & 5 & 9 & 1 \\ 5 & 3 & 8 & 1 & 4 \\ 2 & 3 & 10 & 1 & 8 \end{pmatrix}. \tag{C.3.1}$$

This leads to the following matrix M

$$M = \begin{pmatrix} (9386) & 0 & (8619) & 0 & 0 & (1938) & 0 & (6193) & (3861) & 0 \\ (7938) & 0 & (8179) & 0 & 0 & 0 & (9381) & (1793) & (3817) & 0 \\ (38109) & 0 & (81091) & 0 & 0 & 0 & 0 & (10913) & (13810) & (9138) \\ (10359) & 0 & (59110) & 0 & (91103) & 0 & 0 & 0 & (11035) & (3591) \\ (4538) & 0 & (8145) & (5381) & (3814) & 0 & 0 & (1453) & 0 & 0 \\ (82310) & (31018) & (10182) & 0 & 0 & 0 & 0 & (23101) & 0 & (1823) \end{pmatrix}.$$

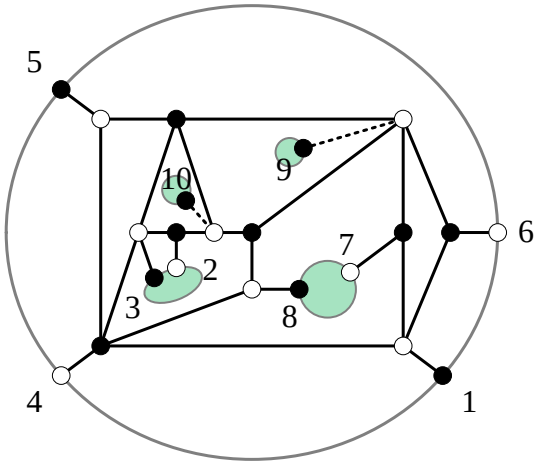

Figure C.2: An N^{2}MHV on-shell diagram for which $n_B = n - k + 2$. In this case it is necessary to add two auxiliary external nodes, 9 and 10, for determining the on-shell form.

The result of the procedure in §6.3.2 gives

$$\Omega = \frac{d^{4\times 10}C}{\mathrm{Vol}(\mathrm{GL}(4))}\frac{(1358)^3(1389)^5(13810)^2(13910)^2}{(1238)(12310)(12810)(1345)(1348)(1359)(13510)(1368)(1369)(1378)(1379)} \times \frac{1}{(1458)(15910)(1689)(1789)(18910)(23810)(3458)(35910)(3689)(3789)(38910)}.$$

This can be simplified using the fact that the points $\{1, 6, 7, 9\}$ are collinear, $\{8, 9, 10\}$ are collinear, $\{2, 3, 10\}$ are collinear and $\{3, 5, 9, 10\}$ are coplanar, as can be read off from (C.3.1). After these simplifications, the dependence on nodes 9 and 10 is encoded in the ratio

$$I|_{9,10} = \frac{1}{(38910)(12310)(1369)(1689)(18910)(23810)}, \tag{C.3.2}$$

which after the residues around $C_{i9} = C_{i10} = 0$ for $i = 1, \ldots 4$ gives

$$I|_{9,10} = \frac{1}{(1368)^2(1238)^2}\,. \tag{C.3.3}$$

Putting everything together, we obtain the following on-shell form

$$\Omega = \frac{d^{4\times 8}C}{\mathrm{Vol}(\mathrm{GL}(4))}\frac{(1358)^3(1386)}{(7812)(1345)(1348)(1356)(1458)(1568)(1376)(6781)(2345)(3528)(3568)(3782)}. \tag{C.3.4}$$

This differential form has been independently confirmed using the boundary measurement procedure from §6.3.1.